

AD-A020 707

PASSIVE NOSETIP TECHNOLOGY (PANT) PROGRAM. VOLUME IX.  
UNSTEADY FLOW ON ABLATED NOSETIP SHAPES - PANT SERIES  
G TEST AND ANALYSIS REPORT

M. J. Abbett, et al

Acurex Corporation

Prepared for:

Space and Missile Systems Organization

December 1973

DISTRIBUTED BY:

**NTIS**

National Technical Information Service  
U. S. DEPARTMENT OF COMMERCE

055039

SAMS0-TR-74-86

(1)

ADA020707

INTERIM REPORT  
PASSIVE NOSETIP TECHNOLOGY  
(PANT) PROGRAM

Volume IX. Unsteady Flow on Ablated Nosetip Shapes -  
PANT Series G Test and Analysis Report

M. J. Abbett  
L. Cooper  
T. J. Dahm  
M. D. Jackson

Aerotherm Division/Acurex Corporation

SAMS0-TR-74-86

December 1973

AEROTHERM REPORT 74-100

DDC  
RECEIVED  
FEB 17 1976  
RILEY  
A

Air Force Space and Missile  
Systems Organization  
Los Angeles, California

Contract F04701-71-C-0027 ✓  
Task 4.2.7.3

Reproduced by  
NATIONAL TECHNICAL  
INFORMATION SERVICE  
U S Department of Commerce  
Springfield VA 22151

DISCONTINUED  
Approved for public release:  
Distribution Unlimited

100-1-1

SAMS0-TR-74-86

C/N 7040.353

INTERIM REPORT  
PASSIVE NOSETIP TECHNOLOGY  
(PANT) PROGRAM

Volume IX. Unsteady Flow on Ablated Nosetip Shapes —  
PANT Series G Test and Analysis Report

M. J. Abbett  
L. Cooper  
T. J. Dahm  
M. D. Jackson

#### ACKNOWLEDGEMENT

In addition to the authors, a number of persons made contributions which were important to the successful completion on this study. The Tunnel 8 test facility staff of the Naval Ordnance Laboratory, under the leadership of Frank Baltakis, did an excellent job in a very tight test schedule. Arnold Galef of TRW reduced the high frequency pressure and accelerometer data and has provided valuable assistance in its interpretation. Duane Baker and Alex Boyd of Aerotherm were instrumental in the entire test phase. Glenn Tickner of Aerotherm was of great assistance in the analysis of random data. Other colleagues, too numerous to acknowledge individually, have participated actively in many technical discussions during this study. We are grateful for the contributions of each of these individuals.

✓  
H. H. H. H. H.  
H. H. H. H. H.  
A



## FOREWORD

This document is Volume IX of the Interim Report series for the Passive Nosetip Technology (PANT) program. A summary of the documents in this series prepared to date is as follows:

- Volume I - Program Overview (U)
- Volume II - Environment and Material Response Procedures for Nosetip Design (U)
- Volume III - Surface Roughness Data
  - Part I - Experimental Data
  - Part II - Roughness Augmented Heating Data Correlation and Analysis (U)
  - Part III - Boundary Layer Transition Data Correlation and Analysis (U)
- Volume IV - Heat Transfer and Pressure Distributions on Ablated Shapes
  - Part I - Experimental Data
  - Part II - Data Correlation
- Volume V - Definition of Shape Change Phenomenology from Low Temperature Ablator Experiments
  - Part I - Experimental Data, Series C (Preliminary Test Series)
  - Part II - Experimental Data, Series D (Final Test Series)
  - Part III - Shape Change Data Correlation and Analysis
- Volume VI - Graphite Ablation Data Correlation and Analysis (U)
- Volume VII - Computer User's Manual, Steady-State Analysis of Ablating Nosetips (SAANT) Program
- Volume VIII - Computer User's Manual, Passive Graphite Ablating Nosetip (PAGAN) Program
- Volume IX - Unsteady Flow on Ablated Nosetip Shapes - PANT Series G Test and Analysis Report

- Volume X - Summary of Experimental and Analytical Results
- Volume XI - Analysis and Review of the ABRES Combustion Test Facility for High Pressure Hyperthermal Reentry Nosetip Systems Tests
- Volume XII - Nosetip Transition and Shape Change Tests in the AFFDL 50 MW RENT Arc - Data Report
- Volume XIII - An Experimental Study to Evaluate Heat Transfer Rates to Scalloped Surfaces - Data Report
- Volume XIV - An Experimental Study to Evaluate the Irregular Nosetip Shape Regime - Data Report
- Volume XV - Roughness Induced Transition Experiments - Data Report

This report was prepared by Aerotherm Division/Acurex Corporation under Contract F04701-71-C-0027. Volumes I through IX covered PANT activities from April 1971 through April 1973. Volumes X through XV represent contract efforts from May 1973 to December 1974. Volume X summarizes the respective test programs and describes improvements in nosetip analysis capabilities. Volume XI presents an evaluation of the ABRES test facility in terms of performing thermostructural and reentry flight simulation testing. Volumes XII through XV are data reports which summarize the experiments performed for the purpose of defining the irregular flight regime. The analysis of these data are presented in Volume X.

This work was administered under the direction of the Space and Missile Systems Organization with Lieutenant A. T. Hopkins and Lieutenant E. G. Taylor as Project Officers with Mr. W. Fortenier and Dr. R. L. Baker of the Aerospace Corporation serving as principal technical monitors. Mr. M. J. Abbett was test engineer and principal Aerotherm investigator for the work described in this volume.

This technical report has been reviewed and is approved.

*E. G. Taylor*

E. G. Taylor, Lt., USAF  
Project Officer  
Aero and Materials Division  
Directorate of Systems Engineering  
Deputy for Reentry Systems

## TABLE OF CONTENTS

<u>Section</u>	<u>Page</u>
1 THE PROBLEM	1-1
2 EXPERIMENTAL PROGRAM	2-1
2.1 Background, Program Objectives, and Approach	2-1
2.2 Model Selection	2-3
2.3 Model Design and Instrumentation	2-4
2.3.1 Models	2-4
2.3.2 Pressure Instrumentation	2-14
2.3.3 Accelerometer Instrumentation	2-18
2.3.4 Photographic Coverage	2-21
2.3.5 Data Acquisition	2-23
2.4 Wind Tunnel	2-24
2.5 Test Matrix	2-24
2.6 Results	2-27
2.6.1 Overview of Findings	2-27
2.6.2 Classification of Flows Observed	2-29
2.6.3 Effect of Geometric and Flow Variables Upon Stability	2-36
2.6.4 Anomalous Types of Flow Behavior	2-39
2.6.5 Quantitative Results	2-43
2.6.6 Preliminary Correlation Results	2-121
3 ANALYTICAL PROGRAM	3-1
4 STABILITY CORRELATION CONSIDERATIONS	4-1
5 CONCLUDING REMARKS	5-1
REFERENCES	R-1
APPENDIX A	A-1

## LIST OF ILLUSTRATIONS

<u>Figure</u>		<u>Page</u>
2-1	Flow Regions for Spiked Cones	2-2
2-2	Schematic of Simplified Model of Nosetip	2-3
2-3	Schematic of Model Design	2-5
2-4	Engineering Drawing of Transition Ring Number 2	2-7
2-5	Interchangeable Nosetip Number 8	2-8
2-6	Interchangeable Nosetip Number 6	2-9
2-7	Interchangeable Nosetip Number 1	2-10
2-8	Interchangeable Nosetip Assembly Drawing	2-11
2-9	Solid Nosetip, Tip Number 10	2-12
2-10	Solid Nosetip Assembly Drawing	2-13
2-11	Specifications of Kulite XTEL-190-100 Pressure Transducer	2-17
2-12	Instrumented Spacer Detail	2-20
2-13	Schematic of Photographic Coverage	2-22
2-14	Nominal Test Points at $M_\infty = 5.0$ in NOL Hypersonic Wind Tunnel	2-25
2-15	Types of Flow Observed During Series G Tests	2-28
2-16	Completely Steady Flow, Type CS	2-31
2-17	Steady Separated Flow, Type SS Run 20 - $\theta_1 = 20^\circ$ , $\theta_2 = 70^\circ$ , $l/D = .534$ , $R_n/D = .95$	2-32
2-18	Fully Pulsating Flow, Type FP Run 2 - $\theta_1 = 20^\circ$ , $\theta_2 = 80^\circ$ , $l/D = .480$	2-34
2-19	Metastable Flow, Type MS Run 19 - $\theta_1 = 20^\circ$ , $\theta_2 = 70^\circ$ , $l/D = .547$ , $R_n/D = 0.0$	2-35
2-20	Effect of Reynolds number $\theta_1 = 20^\circ$ , $\theta_2 = 70^\circ$ , $l/D = .526$	2-38
2-21	Effect of $l/D$ and $\theta_2$ Metastable Flow	2-40
2-22	Nearly Metastable Flow Run 24 - $\theta_1 = 30^\circ$ , $\theta_2 = 70^\circ$ , $l/D = .341$	2-41

# LIST OF ILLUSTRATIONS (Concluded)

<u>Figure</u>		<u>Page</u>
2-23	Unusual Shock Structure	2-42
2-24	Character of K1 Pressure Signal and Axial Accelerometer Signal for Different Types of Flow	2-44
2-25	Four Types of Flow Observed	2-46
2-26.01/ 2-26.49	Pressure PSD	2-47/ 2-96
2-27.01/ 2-27.24	Accelerometer PSD	2-97/ 2-120
2-28	Determination of Effective Angle of Steady Separation	2-122
2-29	Agreement Between Actual and Effective Angles of Separation for Steady Flow Cases	2-123
2-30	Preliminary "Wood Type" Correlation of NOL-8 Series Test Results	2-124
3-1	Schematic of Separation over a Rearward Facing Step and a Forward Facing Ramp	3-2
3-2	Sequence of Free and Forced Interactions for Forward Facing Ramp	3-4
3-3	Schematic of Hypothesized Limit of Separation Length	3-7
3-4	Theory Compared with Observed Flow Behavior on Two- Dimensional Ramps	3-8
3-5	Limits of Instability as Predicted from Theory	3-10
4-1	Comparison of Wood's and NOL-8 Series Test Results - Preliminary Correlation	4-2
4-2	Correlation of Instability Limits Based Upon NOL-8 Series Tests and Data of Wood	

## LIST OF TABLES

<u>Table</u>		<u>Page</u>
2-1	Pressure Tip Locations	2-15
2-2	Calibration of Kulite Pressure Transducers	2-19
2-3	Test Matrix	2-26
2-4	Tabulation of High Frequency Pressure Data (K1)	2-45

# LIST OF SYMBOLS

$C_p$	pressure rise coefficient
$D$	base diameter
$l$	length from nose to shoulder
$L$	length from nose to flare
$l_s$	axial length of separated zone
$l_{sep}$	length of shear layer
$M$	Mach number
$Re$	Reynolds number
$R_f$	flare radius
$R_n$	nose radius
$R_s$	shoulder radius
$S$	Strouhal number
$\alpha$	ramp angle
$\beta$	flare or ramp angle for fully developed shear layer in free interaction
$\beta_{crit}$	maximum flare or ramp angle for attached flow in forced interaction
$\beta_{incip}$	flare or ramp angle that just produces a separation

# LIST OF SYMBOLS (Concluded)

$\delta_o$	boundary layer height ahead of separation
$\Delta\theta$	$\theta_2 - \theta_1$
$\nu$	frequency of pulsation
$\phi$	angle of separation
$\sigma_{eff}$	effective conical body angle
$\sigma_{max}$	maximum conical body angle
$\sigma_{obs}$	effective conical body angle observed from photos
$\theta_1$	tip half angle
$\theta_2$	flare half angle
$\theta_s$	shock angle
$\cdot$	forced interaction



## SECTION 1

### THE PROBLEM

As an ablating nosetip progresses through its trajectory, its surface shape changes continuously. Among the myriad shapes it may assume, there are certain classes of shapes for which the flow field is grossly unsteady, that is, the flow field pulsates with a high frequency. Such shape induced flow field instabilities may seriously compromise the realization of flight objectives, possibly even resulting in structural failure of the nosetip. This report describes the results of an experimental and analytical effort directed toward improving prediction procedures for identifying instability onset and, ultimately, the magnitude and frequency of the pressure fluctuations.

Prior to this study, there were experimental data on such flow field instabilities for idealized shapes, primarily flat faced cylinders and high angle cones with slender spikes. The data were adequate to define, at least roughly, the envelope of instability onset for the idealized shapes. There was no such data base for shapes characteristic of ablating nosetips. The objective of the current experimental program is to fill this void by providing a data base on which a semi-empirical model could be constructed defining the envelope of instability onset for shapes of interest in ablating nosetip technology. An additional objective is to provide data which could be used to correlate pressure pulsation frequencies and magnitudes between ground test and flight configurations.

The analytical study has a two-fold objective: (1) to analytically identify the geometric parameters which are important in defining instability onset and construct a semi-empirical correlation for the envelope of instability onset, and (2) to determine the feasibility of constructing a less empirically dependent flow field model for predicting the onset, frequency, and magnitude of pressure fluctuations resulting from gross flow field pulsations.

The experimental and analytical programs are discussed in Sections 2 and 3, respectively. The results of the two efforts are then synthesized into a correlation for predicting instability onset for nosetip configurations (Section 4). The report is concluded with a summary of the important results.

## SECTION 2

### EXPERIMENTAL PROGRAM

#### 2.1 BACKGROUND, PROGRAM OBJECTIVES, AND APPROACH

As already noted, almost all previous experimental efforts in this area have been focused on idealized shapes. Particularly noteworthy are the studies of Maull<sup>1</sup> and Wood<sup>2</sup> of the hypersonic flow over spiked cones and cylinders. Wood defined five flow regimes depending on the cone half angle and the ratio formed by dividing the spike length by the model base diameter (Figure 2-1).

Wood hypothesized that for very blunt spiked bodies, a necessary condition for instability is that the spike protrude beyond the position that the bow shock would be detached if there were no spike. This hypothesis is consistent with existing experimental data. Maull noted the dependence of the envelope of instability onset to variations in Mach number, aspect ratio, and model shoulder radius. He also noted that the boundary between steady and oscillatory flow correlates with the sharp cone angle for shock detachment. On the basis of a number of shadowgraphs taken during the tests, Maull constructed a physical model of the pulsation cycle in which the flow field instability onset is related to the inability of a separated shear layer to mount the strong adverse pressure gradient associated with the strong shock created at the shoulder when the conical shock detaches from the conical surface.

The geometries tested and correlated by Maull, Wood and most others were spiked cylinders and large angle cones, shapes not representative of configurations encountered by ablating nosetips. Prior to this test series there was a paucity of data about flow instabilities on shapes likely to occur on ablating nosetips.

The nature of these tests is that of a screening program to determine the range of geometric configurations and environmental conditions which result in large-scale flow field pulsations and to determine the frequency and magnitude of the resulting pressure oscillations. This required modeling the ablated nosetip shapes so that they are characterized by an acceptably small number of geometric parameters. Then low temperature ablator data, limited shape change predictions for flight conditions, and Mach number effect considerations were used to determine the range of geometric parameters of interest in this test

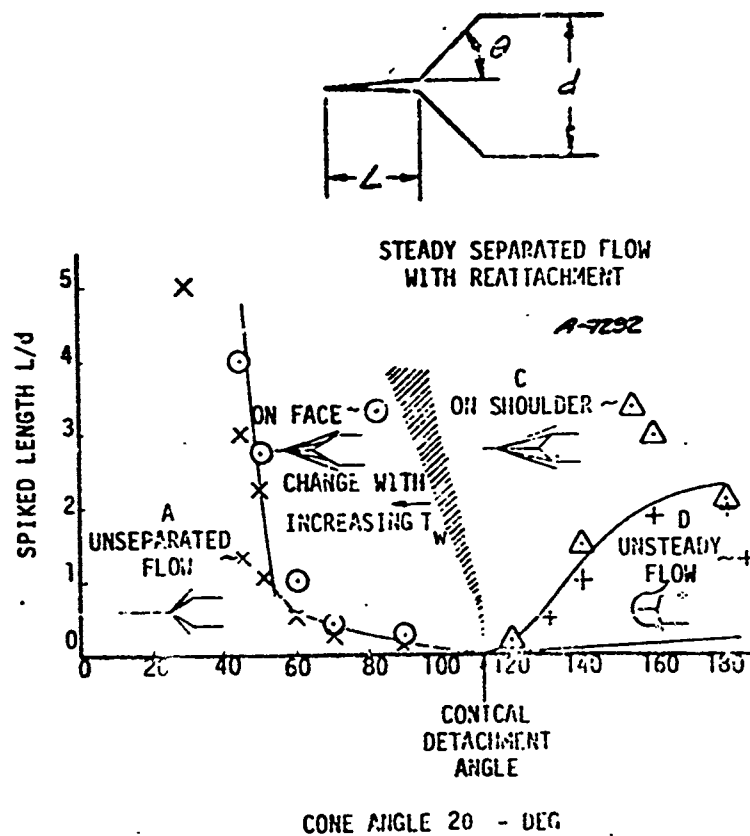


Figure 2-1. Flow Regions for Spiked Cones from Wood<sup>(2)</sup>

$$M_\infty = 10, Re/ft = .81 \times 10^6, T_w = 300^\circ K, T_\infty = 48^\circ K$$

program. A total of 38 different shapes was tested. Since these were screening tests, a few shapes were selected because they were almost certain to pulsate or to remain steady, but most of the configurations were selected because it was uncertain whether or not they would pulsate, and, therefore, the tests provide the needed data base to better define the geometrical configuration boundaries corresponding to instability onset.

The models were tested in the Naval Ordnance Laboratory tunnel number 8 in Silver Spring, Maryland, at  $M_\infty = 5$ . The tips of the models were gritblast roughened to ensure a turbulent boundary layer on the tip if the flow remained attached. Comparative visual and tactile inspection of the roughened tips indicate that the roughness was nominally in the 1-2 mils range. Detailed roughness characterization studies were not conducted.

Each model was instrumented with two high frequency pressure transducers. The sting was instrumented with an axial, a yaw plane, and a pitch plane accelerometer. Pulsed 35 mm still Schlieren (about 4/sec) and 16 mm high speed shadowgraph cinephotography coverage were used on each test.

## 2.2 MODEL SELECTION

It is not easy to model simply the surface geometry of an ablated shape. However, in order to develop and use a correlation which defines the geometrical dependence of instability onset, it is necessary to describe the surface geometry with relatively few parameters. A careful examination of low temperature ablator shapes and shape change prediction results led to the conclusion that the surface geometry can be adequately characterized by the model indicated in Figure 2-2. By varying the parameters\*  $L/D$ ,  $R_n/D$ ,  $R_f/D$ ,  $R_s/D$ ,  $\theta_1$  and  $\theta_2$

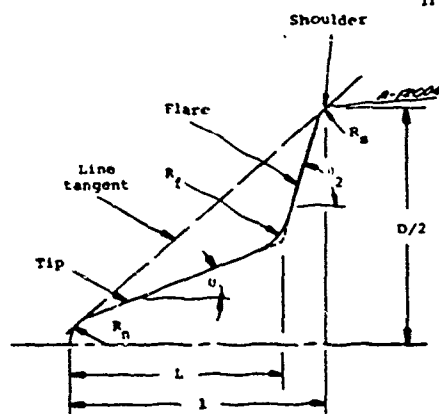


Figure 2-2. Schematic of Simplified Model of Nostip

\* During the data correlation efforts a different definition of  $L$  was determined to better correlate the data. See Section 2.6.3.

through the range of interest determined by examining the low temperature ablator data and published experiments with pulsating flow on spiked bodies, the envelope of instability onset for realistic configurations was determined. With such a large number of parameters, it was unrealistic to test all possible combinations of interest. Therefore, nominal values of  $R_n$ ,  $L/D$ ,  $R_f/D$ ,  $R_s/D$ ,  $\theta_1$ , and  $\theta_2$  were determined. The tests involved varying these parameters about their nominal values to determine the sensitivity of the onset and intensity of flow field instability to departures from the nominal values. The result is that the test objectives were achieved by testing thirty-three different configurations with the following range of parameter variation:

$\theta_1$ : 20°, 30°, 40°

$\theta_2$ : 60°, 70°, 80°, 90°

$L/D$ : 0.1, 0.2, 0.3, 0.4, 0.6

$R_n/D$ : 0.0, 0.15, 0.30

$R_f/D$ : 0.0, 0.05, 0.10, 0.20

$R_s/D$ : 0.0, 0.05, 0.10, 0.20

The test matrix, as run, is given in Table 2-3, Section 2.5.

### 2.3 MODEL DESIGN AND INSTRUMENTATION

As was mentioned in Section 2.2, the nature of the tests described herein is that of a screening program to determine the range of geometric configurations and environmental conditions which result in large scale flow pulsations. A total of 33 different shapes was tested. To accomplish the test objectives while minimizing model expense and test time required that the models be designed so that some geometric variations could be realized without dismounting the entire model. This section, 2.3.1, includes a detailed discussion of model design, Sections 2.3.2 and 2.3.3 discuss pressure and accelerometer instrumentation and finally, photographic coverage and data acquisition is discussed in Sections 2.3.4 and 2.3.5.

#### 2.3.1 Models

In order to minimize model expense and test time, the models were constructed in two parts, a tip and a transition ring, illustrated in Figure 2-3. Table 2-3 defines the pertinent geometric variables for the various transition rings and tips. With the exception of transition ring number 8 and tips 10 and 30, tips are characterized by four geometric variables:  $R_n$ ,  $R_f$ ,  $L$  and  $\theta_1$ , whereas transition rings are characterized by  $R_s$ ,  $\theta_2$  and  $D$  (refer to Figure 2-2 or Table 2-3). Tip numbers 10 and 30 are characterized by:  $R_n$ ,  $R_f$ ,  $L$ ,  $\theta_1$ ,  $R_s$ , and  $\theta_2$ . Transition ring number 8 was merely a cylindrical sleeve. Model base diameter ( $D$ ) was 6.0 inches for all transition rings. The tips and transition

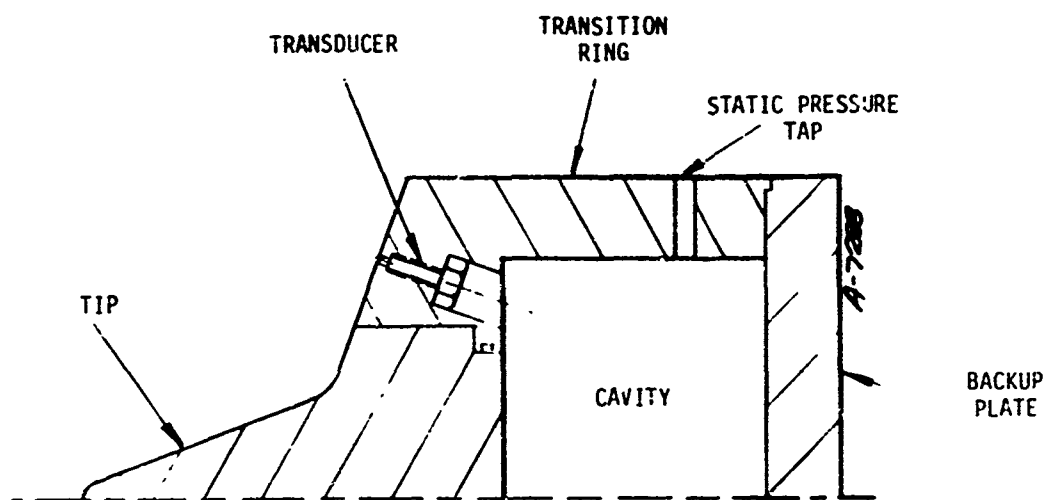


Figure 2-3. Schematic of model Design

rings 2 through 7 were fabricated from a high strength carbon steel (Type 1215); transition ring 8 was fabricated from 6061-T6 aluminum.

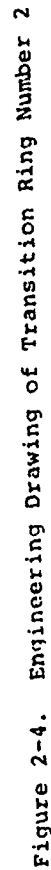
Figure 2-4 illustrates transition ring number 2, and Figures 2-5, 2-6, and 2-7 depict tips 8, 6, and 1, respectively. Some of the important design features illustrated in these figures are:

- Tolerance between tip and transition ring held at a nominal .002 inch.
- O-ring used to seal interior cavity of the transition ring
- Tips held in place via 4 set screws (refer to section B-B, Figure 2-5)
- Pressure ports for 6 static pressure taps and for 2 high frequency pressure transducers were machined only on the transition ring.

Obviously, the model was designed to allow quick changes in configuration. The nosetip, being attached via four set screws, could be changed in approximately five minutes. The transition section, housing, two high frequency pressure transducers and six static pressure taps could be changed in approximately one-half hour.

The assembly drawing (Figure 2-8) illustrates the model wind tunnel sting interface, which includes, from left to right: tip, transition ring, model backplate, model holder, adapter plate, instrumented spacer, and sting. Static pressure tap tubing and electrical wires from the Kulite pressure transducers were placed along the center of parts illustrated in Figure 2-8. Electrical connectors were mounted inside the transition rings so that wiring could be easily connected or disconnected to the high frequency pressure transducers. The capillary tubes from the static pressure taps were connected inside the model holder to tubing which ran through the sting and into a bank of static pressure transducers located outside of the test chamber.

In general, the static and high frequency pressure transducer ports on the face of the transition ring are located as close as possible to the flare so that if there is substantial boundary layer separation the measured pressures will be in the separated flow region. For  $L = 2.4$  inches and  $\theta_1 > 30$  degrees, i.e. tips 10 and 30, it was not practical to construct the models in two parts while still maintaining the pressure ports on the transition ring and locating the pressure ports in the region of potential separated flow. Therefore, tips 10 and 30 were constructed as illustrated in Figure 2-9. Figure 2-10 depicts Tip 27 Transition Ring 8 interfaced with the wind tunnel facility sting.





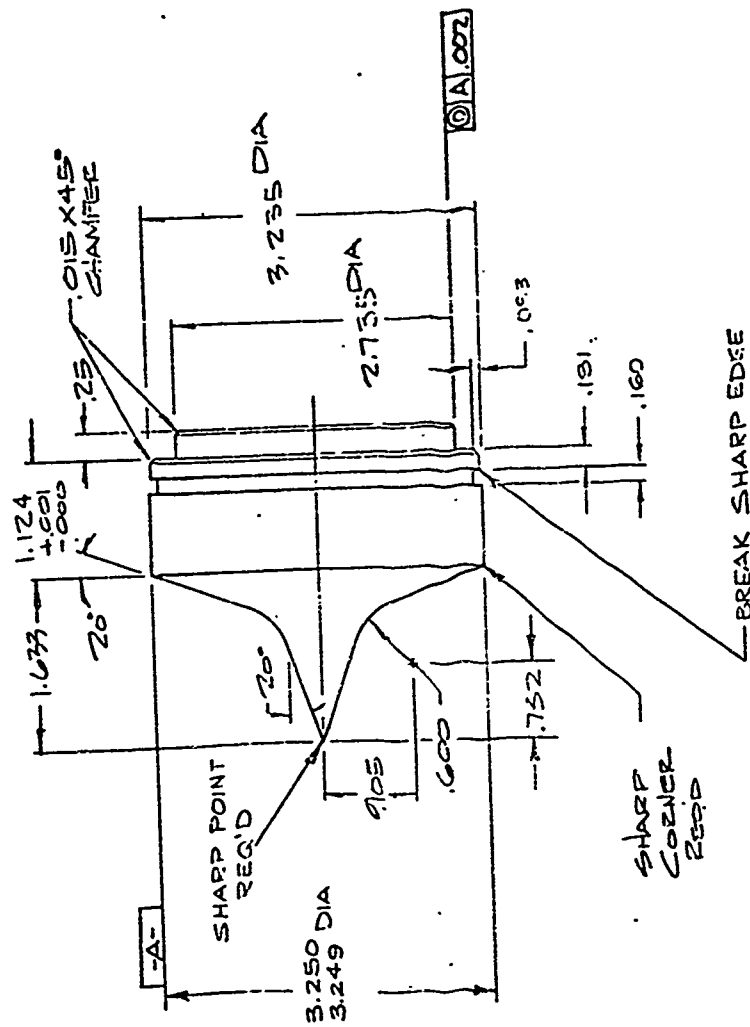
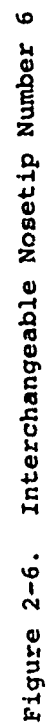


Figure 2-5. Interchangeable Nosetip Number 8



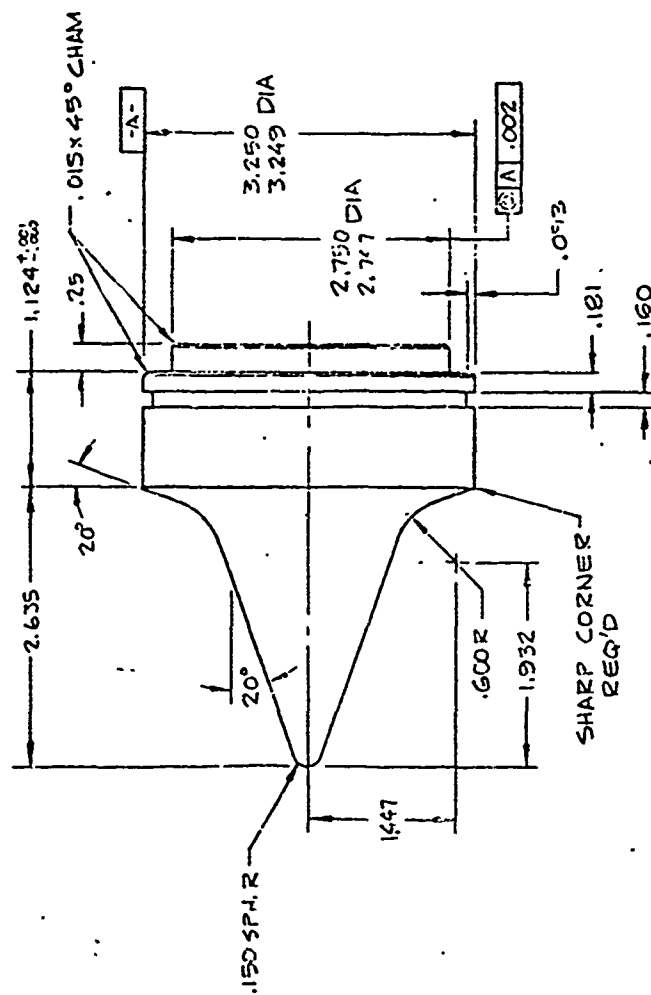


Figure 2-7. Interchangeable Nosetip Number 1

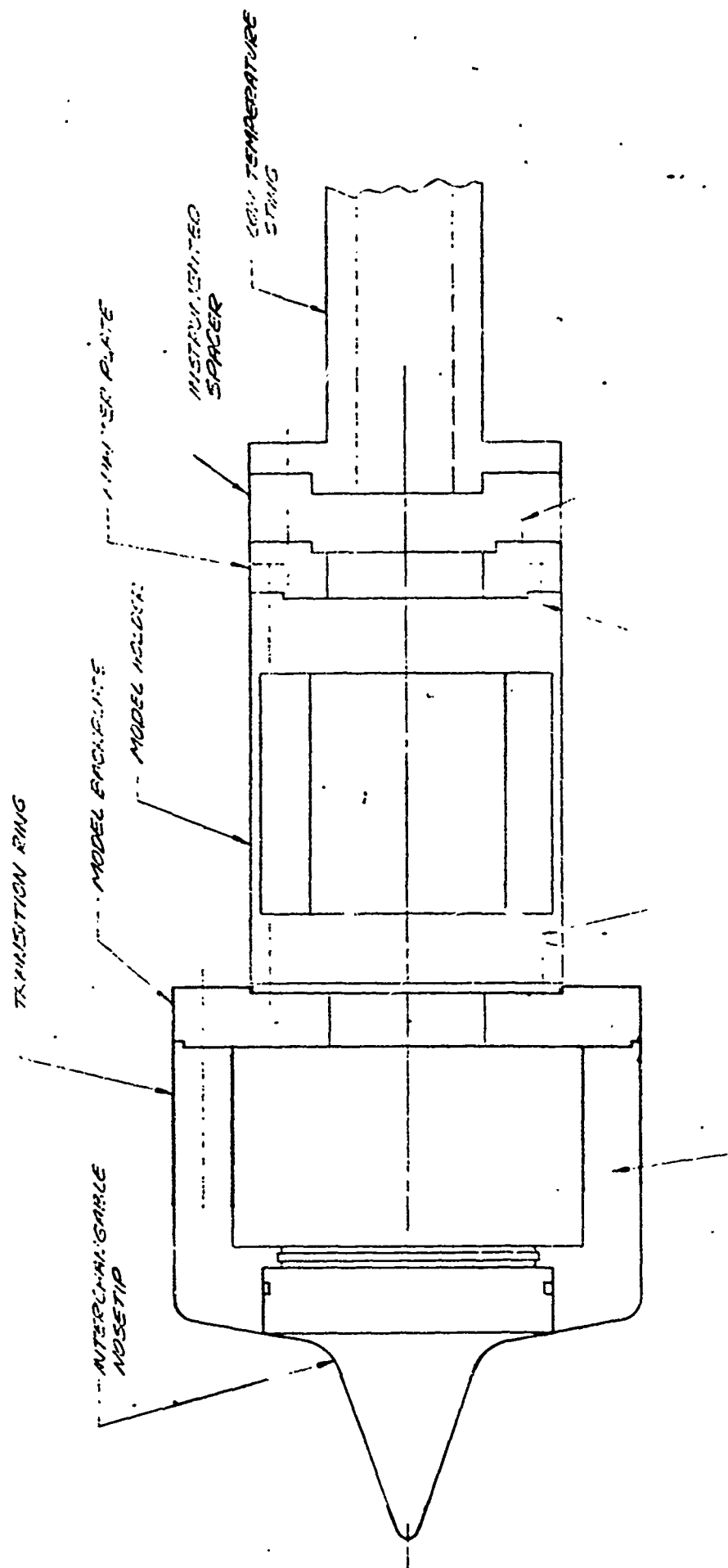


Figure 2-8. Interchangeable Nosetip Assembly Drawing



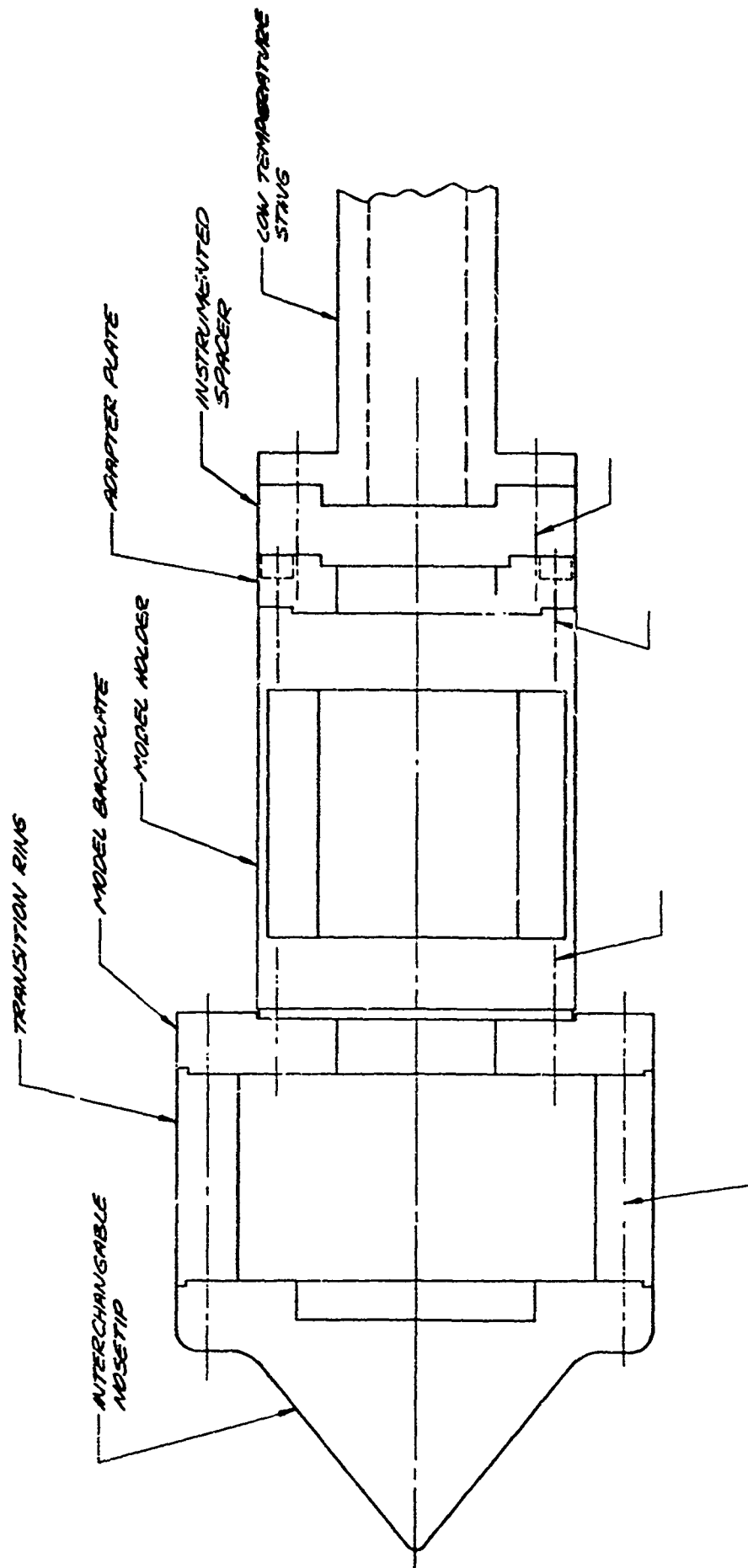


Figure 2-10. Solid Nosetip Assembly Drawing

To insure a turbulent boundary layer by the first shoulder on the model for a nominal free stream unit Reynolds number of  $20 \times 10^6/\text{ft}$ , the model tips were partially roughened. A nominal peak to valley roughness height of 1-2 mils was chosen based on the transition criteria recommended in Reference 3. The 1-2 mils surface roughness was obtained via grit blasting the model tips.

One additional point needs to be made regarding the fit between the tip and transition ring. In general, the surface of a model at the point where the tip and transition ring meet is slightly discontinuous. For transition rings 2, 5, and 6, a step size on the order of 1 to 2 mils resulted from a slight breaking of the material on the sharp corner on the transition ring. Note, however, that this surface discontinuity is of the same order or less than the surface roughness and, therefore, should have had no adverse effect on the results.

### 2.3.2 Pressure Instrumentation

The models tested during this program were instrumented with static pressure taps and high frequency pressure transducers.

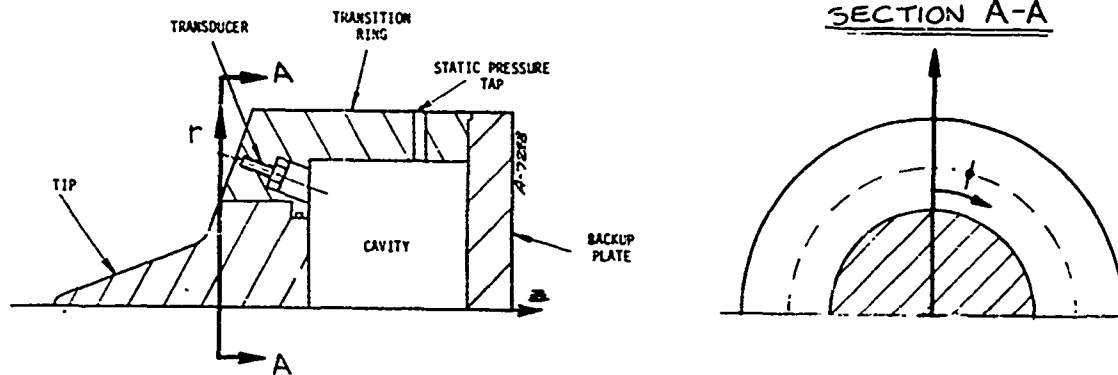
#### Static Pressure Instrumentation

Each transition ring (except transition ring 8) was fitted with 6 pressure tubes: two on the face served as reference pressures for the high frequency transducers, and 4 aft of the shoulder. In addition, one static pressure tube was placed inside the model to monitor the internal pressure.

As illustrated in Figure 2-4 (see Section 2.3.1), the static pressure taps on the face of the transition ring were constructed by drilling a 0.055 inch diameter hole normal to the surface and counterboring a 0.128 inch diameter hole to within 1/4 of an inch from the surface. Stainless steel tubing (outside diameter 0.125 inch, inside diameter 0.095 inch) was then brazed into the 0.128 inch diameter hole. The static pressure tap holes on the cylindrical section of the transition ring were constructed by drilling a 0.096 inch diameter hole and brazing stainless steel tubing having outside and inside diameters of 0.093 inch and 0.061 inch, respectively. In the model holder (c.f. Figure 2-10) the stainless steel tubing originating on the cylindrical section of the transition ring was connected to 0.125 inch OD stainless steel tubing.

Table 2-1 defines the pressure tap locations for all transition rings. The pressure tap holes are referred to as P1 through P6. P1 and P2 are located on the face of the transition ring, in the yaw plane, whereas P3 through P6 are located on the cylindrical section 90 degrees apart. The cylindrical coordinate system used to describe the pressure tap location is illustrated in the sketch associated with Table 2-1. For all transition rings, the origin of

TABLE 2-1  
PRESSURE TIP LOCATIONS



a)

Meridian Angle, $\phi$ (deg)		0	180	90	270	90	180	270	0
Transition Ring	Radial, Axial Distance (inches)	K1	K2	P1	P2	P3	P4	P5	P6
1	r	2.60	2.60	2.60	2.60	3.00	3.00	3.00	3.00
1	z	.43	.43	.43	.43	3.16	3.16	3.16	3.16
2	r	2.28	2.28	2.28	2.28	3.00	3.00	3.00	3.00
2	z	.22	.22	.22	.22	2.94	2.94	2.94	2.94
3	r	2.28	2.28	2.28	2.28	3.00	3.00	3.00	3.00
3	z	.22	.22	.22	.22	2.94	2.94	2.94	2.94
4	r	2.28	2.28	2.28	2.28	3.00	3.00	3.00	3.00
4	z	.22	.22	.22	.22	2.94	2.94	2.94	2.94
5	r	2.09	2.09	2.09	2.09	3.00	3.00	3.00	3.00
	z	.16	.16	.16	.16	2.94	2.94	2.94	2.94
6	r	2.33	2.33	2.33	2.33	3.00	3.00	3.00	3.00
6	z	.79	.79	.79	.79	2.57	2.57	2.57	2.57
7	r	2.25	2.25	2.25	2.25	3.00	3.00	3.00	3.00
7	z	.00	.00	.00	.00	2.38	2.38	2.38	2.38
8	r	--	--	--	--	3.00	3.00	3.00	3.00
8	z	--	--	--	--	1.73 <sup>++</sup>	1.73 <sup>++</sup>	1.73 <sup>++</sup>	1.73 <sup>++</sup>

b)

Meridian Angle, $\phi$ (deg)		0	180	90	270
TIP Number	Radial, Axial Distance (inches)	K1	K2	P1	P2
10	r	1.69	1.69	1.69	1.69
10	z*	2.49 <sup>†</sup>	2.49 <sup>†</sup>	2.49 <sup>†</sup>	2.49 <sup>†</sup>
30	r	1.88	1.88	1.88	1.88
30	z*	2.15 <sup>†</sup>	2.15 <sup>†</sup>	2.15 <sup>†</sup>	2.15 <sup>†</sup>

\* measured from stagnation point

- streamwise distance to these pressure ports for tips 10 and 30 is 2.797 inches and 2.228 inches, respectively

- streamwise distance to these pressure ports for tips 10 and 30 is 4.018 inches and 3.757 inches, respectively



the coordinate system is located at the model centerline at the beginning of the transition ring. The streamwise or axial distance from the model stagnation point can be readily computed for any tip transition ring configuration using the geometric information given in Table 2-3. As discussed in Section 2.3.2, model tips 10 and 30 were solid models and include both static and high frequency pressure taps on the fore-cone of the tip. Table 2-1b defines the location of these pressure taps in terms of radial distance from the model centerline ( $r$ ), meridian angle ( $\phi$ ), and axial distance from model stagnation point. Also included is the streamwise distance to the pressure ports.  $\phi = 0^\circ$  corresponds to the leeward side for the angle of attack runs.

#### Dynamic Pressure Instrumentation

Two high frequency pressure transducers were located on the transition ring face in the pitch plane. Table 2-1 gives the transducer (labeled K1 and K2) locations in terms of the coordinates  $z$ ,  $r$ , and  $\phi$ .

Kulite pressure transducers, manufactured by Kulite Semiconductor Products, Inc., were selected for obtaining the high frequency pressure response on the models. The model number of the Kulite high frequency pressure transducers is XTEL-190-100. Figure 2-11 gives the nominal specifications of the transducers. These transducers are piezoresistive; four piezoresistive elements are diffused on a silicone diaphragm forming a four arm Wheatstone bridge. The transducers have a rated pressure of 100 psi and a maximum pressure of 200 psi. The Kulite transducers are equipped with a one inch reference tube and, therefore, are classified as pressure gauges. As mentioned above, a static pressure tube was positioned inside each model so that the interior pressure could be measured, thus allowing one to obtain a relative comparison between pressures measured via Kulite gauges and capillary tubes.

The operating temperature for the XTEL-90-100 transducer is  $0^\circ\text{F}$  to  $500^\circ\text{F}$ . These transducers are equipped with a thermal compensation unit providing temperature compensation from  $80^\circ\text{F}$  to  $450^\circ\text{F}$ . The electric circuit and external dimensions of the XTEL-90-100, including the thermal compensation unit, is illustrated in Figure 2-11.

The Kulite pressure transducers were mounted in a ported configuration (diameter of port = 0.060 inch, length of port = 0.10 inch), as illustrated in Figures 2-4 and 2-11. Kulite transducers were dynamically tested in a shock tube to determine the transducer response to a step input in pressure (approximately 30 psi). The results of these tests indicate that a Kulite gauge, mounted in the ported configuration given above, experienced output oscillations with a frequency of approximately 13 KHz, with the oscillations being naturally damped in 300 microseconds. Similarly, a Kulite gauge mounted flush in the shock tube

BRIDGE TYPE	Fully active four arm Wheatstone bridge diffused on silicon diaphragm
RATED PRESSURE	100 psi
MAXIMUM PRESSURE	200 psi
SENSITIVITY-NOMINAL	15 mv/psi
EXCITATION	10 vDC (20vDC Maximum)
INPUT IMPEDANCE	2500 ohms (nom.)
OUTPUT IMPEDANCE	1000 ohms (nom.)
ZERO BALANCE	± 5% (rated pressure)
COMBINED NON-LINEARITY AND HYSTERESIS	1% (rated pressure)
REPEATABILITY	0.5%
COMPENSATED TEMPERATURE RANGE	80°F to 450°F
OPERATING TEMPERATURE RANGE	0°F to 500°F
CHANGE OF SENSITIVITY WITH TEMPERATURE	± 5% within the compensated temperature range
CHANGE OF NO-LOAD OUT UT WITH TEMPERATURE	± 10% of rated pressure within the compensated temperature range
NATURAL FREQUENCY	Greater than 100 KHz
ACCELERATION SENSITIVITY	Perpendicular: 0.0005 psi/g Transverse: 0.0005 psi/g.

\*Thermal set is defined as the change in specification due to a thermal cycle from the low end to the high end of the compensated temperature range.

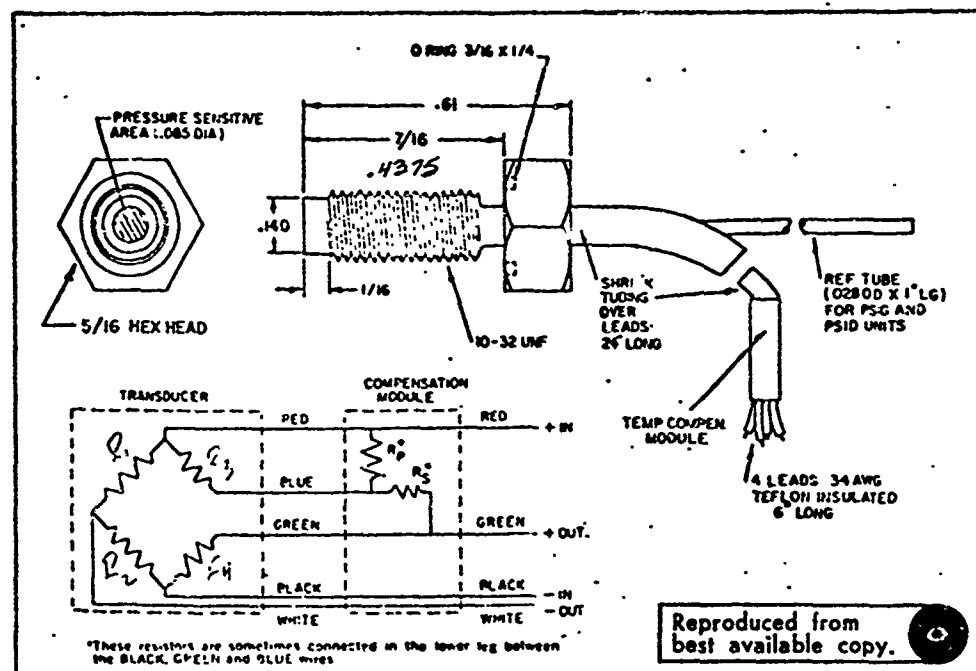


Figure 2-11. Specifications of Kulite XTEL-190-100 Pressure Transducer

results in output oscillations on the order of the natural frequency of the gauge, 100 KHz. Output oscillations damped out after 600 microsecnds in the flush mounted configuration.

#### High Frequency Pressure Instrumentation

The Kulite pressure transducers used during these tests were statically calibrated by the manufacturer and Aerotherm. Both pre and post test calibrations were statically performed at the tunnel facility upon installation in a model. Table 2-2 summarizes the results of the offsite calibrations for transducers D46, D47, D48, D49, and D50. The transducer sensitivity is given in terms of Mv/psi per bridge excitation voltage. These transducers were calibrated with a bridge excitation voltage of 10vDC. Also included in Table 2-2 are (1) the specific transducers which were mounted in the 7 transition rings and two solid nosetips, (2) transducer labels associated with mounting (K1 and K2 refer to 0 and 180 degree meridians, respectively), (3) zero offset of the transducers, (4) estimation of the thermal effect on transducer sensitivity and (5) thermal effect on zero pressure output variation.

In addition to the two Kulite transducers mounted on the model, a Kulite gauge (K3) was flush-mounted on the nozzle wall to obtain pressure fluctuations of the nozzle side wall boundary layer. The data obtained from K3 was to be reduced by NOL personnel in order to quantify the magnitude of noise generated by the turbulent side wall boundary layer.

All three Kulite transducers were attached to a facility D.C. power supply; the nominal input voltage to the transducer was 6.95 volts. Preston model 8300 XWBRC amplifiers were used with the high frequency pressure transducers. The band width on the amplifiers was set at the maximum, 100 KHz, and the gain was adjusted to give an appropriate input signal to the FM tape recorder (the tape recorder is described in Section 2.3.5).

#### 2.3.3 Accelerometer Instrumentation

Three Endevco 2220C high frequency accelerometers were mounted aft of a model in the instrumented spacer, as shown in Figures 2-8 and 2-10. A schematic of the instrumented spacer is given in Figure 2-12. Accelerometers 1, 2 and 3 measured accelerations in the vertical, horizontal and axial directions, respectively. The Endevco 2220C accelerometers have a range from 0 to 5000g and a natural frequency of 50 KHz.

Endevco 2710 charge amplifiers were used to amplify the output of the piezoelectric accelerometers. This Endevco charge amplifier has a frequency range of 2 to 20,000 Hz, with a maximum gain of 10 volts per pico coulomb

TABLE 2-2  
CALIBRATION OF KULITE PRESSURE TRANSDUCERS

Serial Number	Transition Ring Or (TIP) Number	Transducer Label*	Sensitivity† (mv/psi/v)	Thermal** Effect On Sensitivity	Zero Offset (mv)	Thermal** Effect on Zero
2058-5- 1 (D46)	6	K1	.147	< $\pm$ 5%	4.6	< $\pm$ 10%
2058-5- 3 (D47)	1, 3, 5, (10)	K1, K2, K2, K2	.156	Full Scale	.2	Full Scale
2058-5-17 (D48)	6, 2, 4, 7, (30)	K2, K1, K2, K1, K2	.112		.7	
2058-6-28 (D49)	1, 3, 5, (10)	K2, K1, K1, K1	.158		.6	
2058-6-32 (D50)	2, 4, 7, (30)	K2, K1, K2, K1	.153		3.1	

\* See Table 2-1 a and b For Location on Transition Ring or Tip.

† Statically Calibrated For 10VDC Excitation

\*\* Assessed for a Temperature Range From 75°F to 450°F.

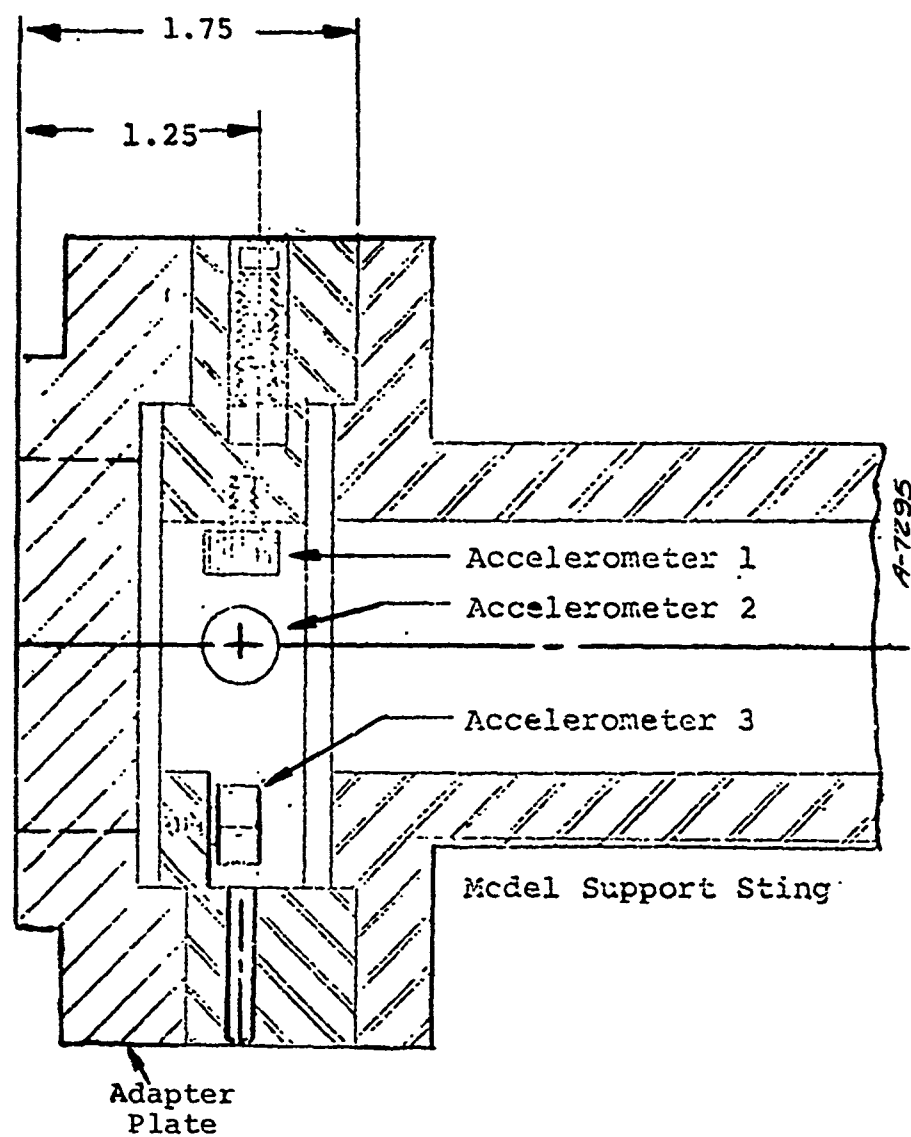


Figure 2-12. Instrumented Spacer Detail

input. For all uses in this test series, the charge amplifiers were set at the maximum frequency response and approximately one half of maximum gain.

#### 2.3.4 Photographic Coverage

Both 35 mm pulsed still Schlieren and 16 mm high speed shadowgraph movie coverage were used in order to visualize large scale flow oscillations and to determine whether boundary layer separation existed when the flow was steady. Figure 2-13 schematically illustrates the camera setup. As shown, two 35 mm pulse cameras were used, one viewing the model pitch plane through the off-axis "Z" Schlieren system,<sup>4</sup> the other photographing a millisecond counter located outside of the tunnel test section. Both 35 mm cameras are Flight Research (Model IV) multi-data cameras which were equipped with a 9 inch lens. The 35mm camera viewing the model through the Schlieren system was synchronized to a pulsed strobe light (General Radio, model 1535) which was interfaced with the Schlieren system. The 35 mm timing camera was also synchronized to the 35 mm viewing camera. Both 35 mm cameras were run at approximately 4 frames per second.

The high speed camera was a 16 mm Hycam movie camera which was run at 20,000 frames per second. The Hycam camera was operated in a half frame mode resulting in a frame size of 0.15 inch by 0.41 inch. This camera was equipped with a 3 inch lens and was focused through the Schlieren system and had the same view of the model as the 35 mm pulse camera. The lighting for the Hycam camera was obtained from the Schlieren system, i.e. from the high pressure mercury vapor lamp, but the lens system was oriented to yield shadowgraph type coverage.

In general, 35 mm pictures were taken during an entire model test, which was typically about 10 seconds. A problem regarding proper synchronizing of the 35 mm pulse cameras and the strobe light was encountered early in the test matrix. This problem resulted in varying frame exposures and incorrect filming of the millisecond counter. Despite varying frame exposures, the 35 mm photographs of the model and flow field were of sufficient quality to accomplish the test objectives. Moreover, an accurate temporal history of the 35 mm photographs was not a necessity in terms of data reduction, and, therefore, the incorrect filming of the millisecond counter did not compromise realization of the program objectives.

High speed movie films were obtained on all runs, except angle of attack runs and variable Reynolds number runs for which the freestream unit Reynolds number was less than  $20 \times 10^6/\text{ft}$ . The Hycam camera was started shortly after model insertion in the test stream, and coverage lasted approximately 1.5 seconds thereafter.

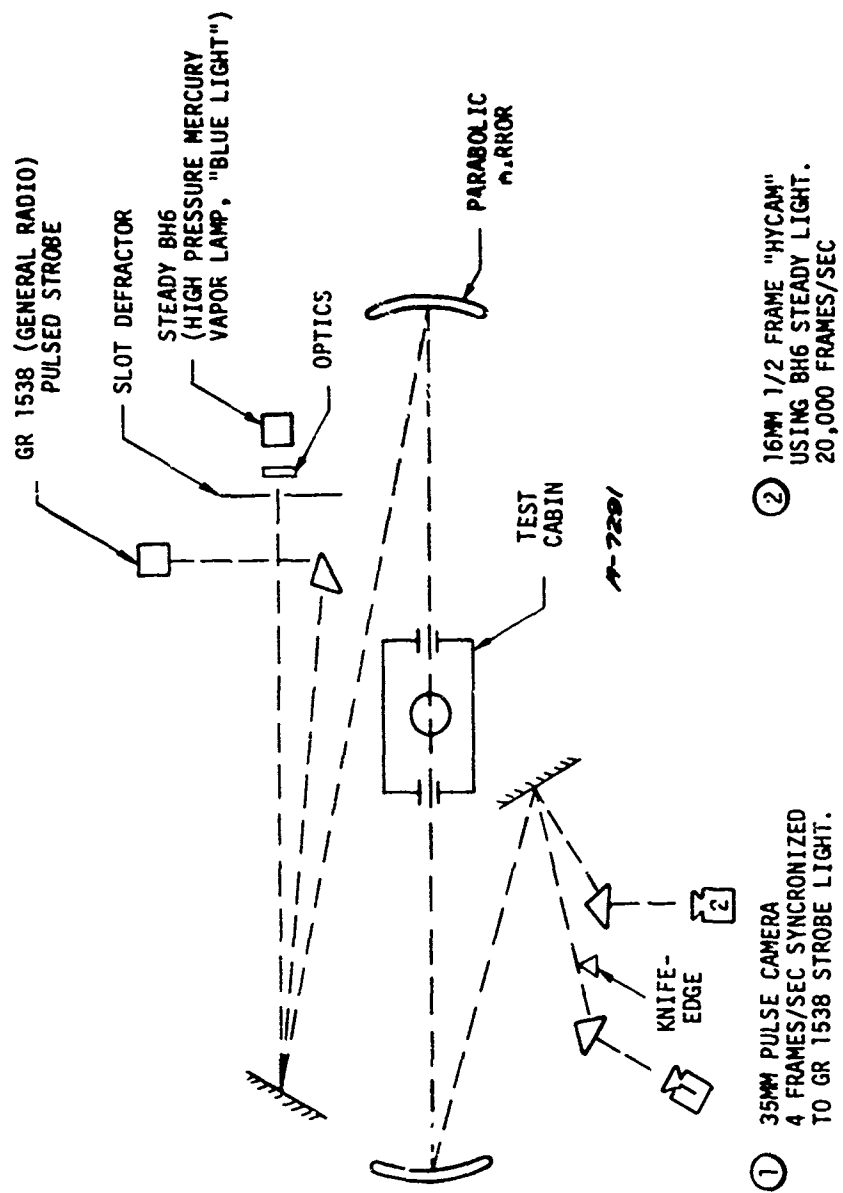


Figure 2-13. Schematic of Photographic Coverage

### 2.3.5 Data Acquisition

As can be inferred from the above sections, recorded data for the Series G wind tunnel tests included:

- Static pressure measurements
- High frequency pressure measurements
- Accelerometer measurements
- 35 mm film coverage
- High speed (20,000 frames/sec) 16mm film coverage

A brief description of the data recording system is presented in the following paragraphs.

At the NOL wind tunnel facility, a 14 channel digital recorder is used for recording the test time, supply pressure, supply temperature and static pressures. This recorder has a sampling or sweep rate of 0.056 second. Test time, supply temperature, supply pressure, and model position are recorded on separate channels, leaving 10 channels available for recording static pressures.

Static pressure tubing from the model was attached to NOL static pressure transducers, which were monitored by the digital recorder. Pressure taps on the aft cone of the model were attached to transducers with a pressure range from 0 to 50 psi, whereas pressure taps on the cylindrical portion of the model were attached to transducers with a pressure range from 0 to 5 psi. The static pressure transducers were calibrated every 2 to 3 runs.

The digital recording system places the data on magnetic tape, which was subsequently reduced according to the calibrations. During each test, digital displacement of pressure transducer emf output as a function of time was available for four channels.

High frequency Kulite pressure transducer and Endevco accelerometer output was amplified and recorded on a 14 channel FR-1300 Ampex tape recorder. This tape recorder was run in a FM mode with a tape drive speed of 60 inches/second which results in a flat frequency response from 0 to 20,000 cycles/second.

In addition to six channels of the tape recorder taken by three Kulite pressure transducers and three Endevco accelerometers, an IRIG B signal and a 50 kHz sine wave were recorded on two of the remaining 8 channels. The IRIG B timer signal generator was manufactured by Datatron, Inc., Model 3000. The sine wave was produced by a Hewlett-Packard wave form generator. An oscilloscope and oscillograph were also available to visualize or play back pressure transducer or accelerometer response.



## 2.4 WIND TUNNEL

The Series G wind tunnel tests were conducted in NOL Tunnel Number 8, which is an intermittent blowdown hypersonic wind tunnel. For this tunnel, air is the working gas and is compressed and stored in high pressure containers. In transit to the nozzle, the air is heated to the desired supply temperature by passing it through a pebble bed heater. The tunnel has an open jet test section and a constant area diffuser. The Mach number for this test series was  $M_\infty = 5$ . The associated nozzle is of rectangular cross section with throat dimensions of 0.6398 inch by 16.00 inches, and exit dimensions of 17.37 inches by 16.97 inches.

At a Mach number of 5, the Reynolds number operating envelope for Tunnel Number 8 is presented in Figure 2-14 as a function of supply temperature ( $T_0$ ) and supply pressure ( $P_0$ ). Superimposed on the figure are the four nominal operation conditions which were run during the test series. The lowest Reynolds number runs were not achieved because of breakdown of the tunnel flow. The actual supply conditions are given in Table 2-3 (see Section 2.5).

Models were aligned in the tunnel test stream by manually checking the angularity of the models in the pitch and yaw plane with a clinometer.

## 2.5 TEST MATRIX

The preliminary data analyses indicated that  $\theta_1$ ,  $\theta_2$ , and  $L/D$  are the most important parameters (verified in these tests), and the test matrix emphasizes variations in those three variables. Effects of  $R_n/D$ ,  $R_f/D$ , and  $R_s/D$  were then determined for nominal values of  $\theta_1$ ,  $\theta_2$ , and  $L/D$ .

One may argue that the important nose radius parameter is  $R_n$  rather than  $R_n/D$  since it is likely that the value of  $R_n$  corresponding to a stable shape is independent of the representative nosetip diameter  $D$ . Consideration of boundary layer transition might lead one to the same conclusion (Section 2.6.3). However, geometric similarity considerations might lead one to conclude that the ratio  $R_n/D$  is more important with respect to instability onset. Nose radius is an important factor, but the precise reason(s) is not well understood.

The tests were run at nominal total temperatures of about 300°F and a free stream unit Reynolds number of  $20 \times 10^6$  per foot. The effect of varying Reynolds number was studied on three geometries by decreasing the free stream unit Reynolds number to 10 and  $5 \times 10^6$  per foot. It was initially intended that data also be obtained at  $Re_\infty/\text{foot} = 2.5 \times 10^6$ , but the tunnel flow broke at that low total pressure. Most configurations were tested only at zero degrees incidence, but three were also tested at  $\alpha = 2\ 1/2^\circ$  and  $5^\circ$  incidence to provide data on the effect of angle of attack on flow instability.

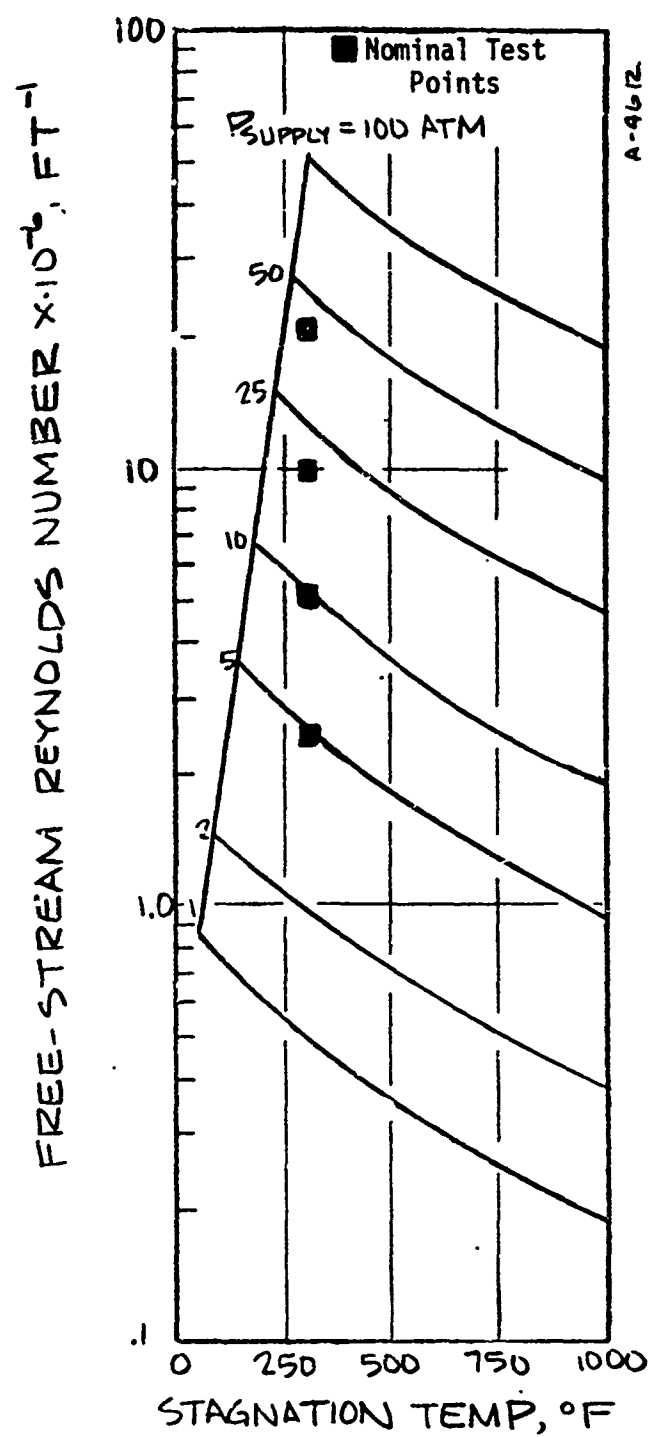


Figure 2-14. Nominal Test Points at  $M_{\infty} = 5.0$  in NOL Hypersonic Wind Tunnel

TABLE 2-3  
TEST MATRIX

Run No.	$\theta_1$ (deg)	$\theta_2$ (deg)	1/D	L/D	$R_H/D$	$R_F/D$	$R_S/D$	$\alpha$ (deg)	$Re_\infty/ft \times 10^{-4}$	Nominal Chamber Conditions		Type <sup>1</sup> Flow
										$T_0$ (°F)	$P_0$ (atm)	
25	20	70	0.540	0.4	0.025	0.10	0.05	0,2-1/2,5	20	300	45	MS
17			0.547			0.0		0	20		45	SS
15						0.05						SS
16												SS
18			0.523			0.20						SS
19			0.547		0.0	0.1						MS
20			0.534		0.05							SS
26			0.367	0.2	0.025			0,2-1/2,5	20		45	MS
22			0.360		0.0			0				FP
23			0.362		0.05							SS
47	30	70	0.507	0.4	0.025							CS
24			0.341	0.2								FP
21			0.277	0.1								CS
27	20	70	0.526	0.4	0.025	0.1	0.0		20		45	SS
28									10		22	MS
29									5		11	--
30												FP
31									2.5		6	--
35			0.554			0.10			20		45	SS
37			0.597			0.20						SS
5	20	30	0.674	0.6	0.025	0.1	0.05					MS
6												MS
7												MS
1			0.480	0.4					10		22	FP
2									20		45	CS
3			0.290	0.2								CS
4												CS
8			0.480	0.4		0.0						FP
9			0.484			0.05						FP
10			0.480			0.2						FP
11	20	60	0.612	0.4	0.025	0.1	0.05					SS
12			0.454	0.2								SS
13	30	60	0.559	0.4								CS
14			0.421	0.2								SS
42	20	90	0.420	0.4	0.025	0.1	0.05	0,2-1/2,5	20		45	FP
43								0,2-1/2,5	10		22	FP
44								0	5		11	FP
45											6	--
39	30	90	0.424						2.5		45	CS
40	40	90	0.316	0.3					20			CS
41			0.212	0.2								CS
46			0.423	0.4								CS
32	20	70	0.367	0.2	0.025	0.1	0.0					MS
33									10		22	MS
34									5		11	MS
36	20	70					0.10		20		45	MS
38	20	70				0.20						MS

<sup>1</sup> SS - Steady separated  
CS - Completely steady  
FP - Fully pulsating  
MS - Metastable  
see Section 2.6.2

The test matrix, as run, is given in Table 2-3. Also included in Table 2-3 is a column summarizing the type of flow field/pressure response observed during the test. Those results are discussed in Section 2.6.2.

## 2.6 RESULTS

The results of the Series G tests are discussed in this section. The discussion begins with an overview of the test results in terms of the basic findings of the experiments. This is followed by a discussion of the different types of flowfields observed in the motion pictures and still photos and how these relate to the mean and fluctuating pressure data. Preliminary attempts to correlate the data are summarized. Further discussions of the correlation efforts and how they are directly affected by theoretical considerations are given in Sections 3 and 4.

### 2.6.1 Overview of Findings

Important objectives of the experiments are to:

- Identify critical parameters which influence flow stability
- Determine effects of Mach number, Reynolds number, and geometry upon stability limits
- Identify ways in which theory can be used to extrapolate to new conditions
- Determine best means of correlating present results and other existing data for application to ablating nosetip technology.

Table 2-3 presents a summary of the test configurations, test conditions, and results for these experiments. Included in this table is a note relating to the type of flow observed at the test conditions of interest. Four such types of flow are noted: completely steady (CS), steady separated (SS), fully pulsating (FP), and metastable (MS). A complete description of each type of flow is discussed in Section 2.6.2; typical pulsed 35 mm Schlieren photographs are shown in Figure 2-15. These flow classifications were determined by observing, in detail, the 16 mm high speed films, the 35 mm photos and the high frequency pressure and accelerometer data. The large body of information contained in the 16 mm films was reduced by recording a running verbal commentary on a tape recorder and simultaneously sketching the significant observations. The recording was later transcribed into a series of notes which could be easily referred to in order to recall the character of the flow.

Completed Steady ( $L/D = .2$ )



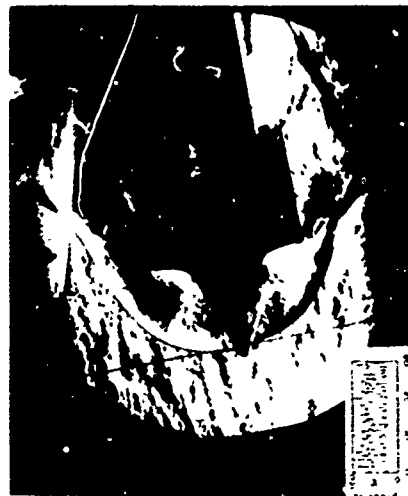
Fully Pulsating ( $L/D = .4$ )



Steady Shock



METASTABLE ( $L/D = .6$ )



Fully Pulsating

Figure 2-15 TYPES OF FLOW OBSERVED DURING SERIES G TESTS

The four types of flows are visually very distinct from each other (Figure 2-15). The frames shown illustrate many of the characteristic details of the flows observed. In addition, the character of the pressure fluctuations felt on the flare face are indicated by the insert in the lower left hand corner of the frames in Figure 2-15.

Before examining the detailed results presented in the next section, the following points represent a summary of the general findings of this study.

- The shape variables  $\theta_1$ ,  $\theta_2$ , and  $l/D$  are of primary importance in determining the limits of stability.
- The variable  $\theta_1$  has special significance in determining the stability limits.
- The fundamental frequency of the strong oscillations present was about 1100 cps which corresponds to a Strouhal number of about .20 which agrees with other data in the literature.
- Many of the MS type flows represent the most severe cases of pressure oscillations on the nosetip with the maximum pressure exceeding the mean by more than a factor of two.
- On an empirical/theoretical basis it was concluded that the stability limits are not strongly affected by free stream Mach number above  $M_\infty = 5$ .
- The effects of Reynolds number and tip radius have some influence on stability, but probably of a secondary nature.
- The effects of flare radius,  $R_f$ , and shoulder radius,  $R_s$ , upon stability limits are weak or negligible for the range of these variables tested.
- The effects of angle of attack are weak or negligible for the range of parameters tested.

#### 2.6.2 Classification of Flows Observed

As mentioned previously four basic types of flow were observed in these experiments:

- Steady separated, SS
- Completely steady, CS
- Fully pulsating, FP
- Metastable, MS

These four basic types of flow possess radically different behavior in terms of

- Visual steadiness
- Magnitude of pressure oscillations
- Magnitude of accelerometer excitation

Each of these four types of flow are discussed in the following paragraphs.

#### 2.6.2.1 Completely Steady (CS)

Completely steady flow means that the shock waves, high frequency pressure transducer response and accelerometer response are all completely steady. Four different runs exhibiting completely steady flow behavior are shown in Figure 2-16. These flows can be subclassed depending on whether the model tip protrudes or does not protrude through the main body bow shock. All cases in which the tip does not protrude through the bow shock are expected to be completely steady. A typical case is run 41, Figure 2-16a.

Usually when the model tip protrudes through the main body bow shock, either the boundary layer separates or the flow pulsates. However, there were three tests in which the boundary layer remained attached and the flow field was apparently completely steady\*. Examples are runs 13, 39, and 40, Figure 2-16.

#### 2.6.2.2 Steady Separated (SS)

The photo shown in Figure 2-17 taken from Run 20 is typical of a steady separated flow. The separation on the tip for this type invariably occurs at a point approximately tangent with a line drawn from the tip to the shoulder of the model. The photograph also shows a demarcation line between the flow in the shear layer and the flow in the separation bubble owing to the density gradient that exists between these two zones. As will be pointed out in a later section this demarcation line position agrees with a prediction of the dividing streamline based upon the shock inclination angle off the tip. For all cases of steady separated flows observed the reattachment occurs at or very near the shoulder, which agrees with the separation model discussed in Section 3.0. Occasionally, for many of the steady separated flows there appeared a very short burst of unsteady flow; however, this only lasted for

---

\*Instrumentation was not adequate to determine very small localized separation at the flare.



a) Run 13 -  $\theta_1 = 30^\circ$ ,  $\theta_2 = 60^\circ$ ,  $1/D = .559$



b) Run 39 -  $\theta_1 = 30^\circ$ ,  $\theta_2 = 90^\circ$ ,  $1/D = .424$



c) Run 40 -  $\theta_1 = 40^\circ$ ,  $\theta_2 = 90^\circ$ ,  $1/D = .316$



d) Run 41 -  $\theta_1 = 40^\circ$ ,  $\theta_2 = 90^\circ$ ,  $1/D = .212$

Figure 2 - 16. Completely Steady Flow, Type CS





Figure 2 - 17. Steady Separated Flow, Type SS  
Run 20 -  $\phi_1 = 20^\circ$ ,  $\phi_2 = 70^\circ$ ,  $1/D = .534$ ,  $R_n/D = .05$

2-5 frames of the high speed movies and the flow quickly recovered, regaining its steady appearance.

#### 2.6.2.3 Fully Pulsating, FP

The basic character of fully pulsating flow is depicted in Figure 2-18 which shows a sequence of 35 mm photos taken during Run 2. A typical sequence of photos was chosen which corresponds essentially to successive frames observed in the 16 mm high speed films. Fully pulsating flow is typified by continuous oscillations and no indication of the flow "trying to become steady". The first picture, Figure 2-18a, shows typically the beginning of the oscillation cycle. The first shock off the tip has separated flow behind it as measured by the local instantaneous shock angle. Such estimates are only approximate since the oblique shock relations apply truly in a moving shock frame of reference. The second frame shows the shock off the tip increasing in inclination due to an expanded growth of the separated region. The third frame, Figure 2-18c, shows the shock off the tip becoming a strong shock as the separation bubble continues to grow. Meanwhile, the secondary shock off the flare has also moved forward as a result of the bubble growth. Eventually, (Figure 2-18d) the first and second shocks nearly merged as they billow off in front of the body. At this point the accumulated mass in the bubble begins to escape by flowing around the shoulder of the body. As this relief occurs, due to the shrinking of the bubble the shock structure begins to collapse, Figure 2-18e. Eventually, the shock structure returns to that shown in Figure 2-18a and the sequence of events is repeated.

#### 2.6.2.4 Metastable (MS)

The sequence of three photos shown in Figure 2-19 illustrates a metastable or separated/fully pulsating flow taken from Run 1<sup>a</sup>. This particular type of flow is characterized by having alternating periods of steady separated flow and fully pulsating flow. The periods of steady separated flow are generally longer in duration. This type of behavior is most difficult to explain on a theoretical or phenomenological basis. Figure 2-19a shows the flow pattern during a period of nearly steady separated flow. At some later instant of time, a ripple in the shock off the tip appears, indicating that some sort of disturbance is present. This disturbance then grows in intensity throughout the shear layer running from the tip to the shoulder. Eventually all semblance of a steady separation breaks down as shown in Figure 2-19b. This flow pattern resembles the start of a full pulsation sequence and, indeed, the oscillatory flow pattern which ensues is fully pulsating in nature as shown by another



a)



c)



b)



d)

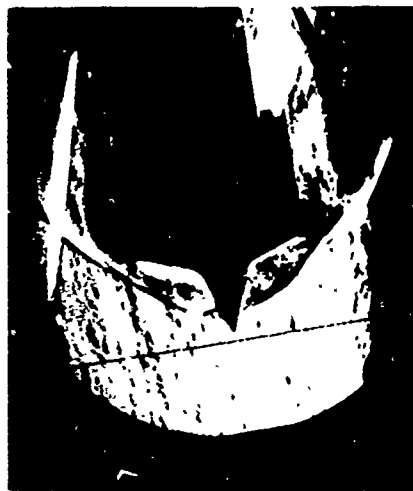


e)

Figure 2 - 18. Fully Pulsating Flow, Type FP  
Run 2 -  $\alpha_1 = 20^\circ$ ,  $\alpha_2 = 80^\circ$ ,  $1/\rho = .480$



a)



b)



c)

Figure 2 - 19. Metastable Flow, Type MS  
Run 19 -  $\Theta_1 \approx 20^\circ$ ,  $\Theta_2 = 70^\circ$ ,  $1/D = .547$ ,  $R_n/D = 0.0$

typical photo from the oscillatory mode in Figure 2-19c. These metastable flows are particularly useful in defining the boundaries between fully pulsating and steady flow.

The preceding remarks describing the four basic types of flow deal primarily with the interpretation of observations that were made with the high speed movies and the still photos. A later section will discuss some of the quantitative data obtained and how it relates to the visually observed flows.

### 2.6.3 Effect of Geometric and Flow Variables Upon Stability

As mentioned previously, a major objective of the present test series is to investigate the effects of several geometric and flow variables upon the stability of the flow. The effect of the various parameters investigated is summarized below.

- $l/D$  - the results of these tests indicated that for small values of  $l/D$ , especially if the tip protrudes not at all or only slightly through the main blunt body shock, the flow is likely to be completely steady (CS). On the other hand if the value of  $l/D$  is sufficiently large, then the flow is likely to be steady separated (SS). However, if the proper combination of  $\theta_1$  and  $\theta_2$  exist and if  $l/D$  falls within the limits described earlier the flow is likely to be metastable (MS) or fully pulsating (FP).
- $\theta_2$  - based upon theoretical considerations (see Section 3.0) if the flare angle is less than the critical angle for shock detachment, the flow is stable. If the flare angle is greater than the critical angle the flow may be unsteady depending upon the combination of  $\theta_1$  and  $l/D$  present.
- $\theta_1$  - apparently if  $\theta_1$  is sufficiently large, the flow is stable regardless of  $l/D$  and  $\theta_2$ . Obviously, if  $\theta_1 = \cot^{-1}(2\frac{l}{D})$  the body is a single cone/cylinder and the flow is steady. Conversely, the flow has increasing tendency to be unsteady if  $\theta_1$  is small and  $l/D$  and  $\theta_2$  fall within the limits mentioned.
- $R_n/D$  - there is a tendency for the stability of the flow to increase with increasing values of  $R_n/D$ . Figures 2-17 and 2-19 illustrate that for Runs 19 and 20 the ability of the flow to remain steady definitely increased when the value of  $R_n/D$  was increased from 0.0 to 05. A possible explanation might be that for small values of  $R_n/D$  the boundary layer and, hence, the shear layer is laminar just after separation, whereas for larger values of  $R_n/D$  the boundary layer and shear layer are turbulent just after separation.

In the former case, transition would occur along the shear layers, resulting in a greater tendency toward unsteadiness<sup>5</sup>.

- $R_f/D$  - the effect of the variable  $R_f/D$  was either weak or negligible for the range of this variable tested. There was no noticeable effect as  $R_f/D$  was varied from 0.0 to 0.20.
- $R_s/D$  - the effect of the variable  $R_s/D$  was also either weak or negligible for the range of this variable tested. There was no noticeable effect as  $R_s/D$  was varied from 0.0 to 0.20.
- $R_e/ft$  - the free stream  $R_e/ft$  was varied from 5 to  $20 \times 10^6$ . At  $R_e/ft = 2.5 \times 10^6$  and at times for  $5.0 \times 10^6$  a steady tunnel flow could not be established. Of particular interest is the series of runs from Run 27 through Run 31. Here the  $R_e/ft$  was continuously reduced holding other variables constant, resulting in an increasing tendency for the flow to become unsteady, Figure 2-20. Figure 2-20a shows a frame taken from Run 27 with  $R_e/ft = 20 \times 10^6$ . The flow is essentially steady separated. Figures 2-20b and 2-20c show two frames taken from Run 28 for which  $R_e/ft = 10 \times 10^6$ ; here the flow is shown to be metastable. Figures 2-20d and 2-20e show two frames taken from Run 30 where  $R_e/ft = 5 \times 10^6$ , resulting in a fully pulsating flow. Comparing two type MS flows in Table 2-3, it can be seen that for Run 28 the flow was type MS at a value of  $l/D = .526$  and  $R_e/ft = 10 \times 10^6$  while for Run 32 the flow was type MS at a value of  $l/D = .367$  at  $R_e/ft = 20 \times 10^6$ . Superficially, this might seem to imply that for geometry considered,

$$\frac{(l/D)_1^{unstable}}{(l/D)_2^{unstable}} = \left\{ \frac{(R_e/ft)_1}{(R_e/ft)_2} \right\}^{-.519} \quad (2-1)$$

However, further inspection of the geometry of Run 32 reveals that  $\sigma_{eff} = \cot^{-1} (2 \frac{l}{D})$ , where  $\sigma_{eff}$  is the effective conical body created by a separation from the tip to the shoulder and is very nearly equal to the critical angle for shock detachment. It was observed that MS type flow was nearly always observed under such a condition. Therefore, for Run 32 the effect of Reynolds number is obscured by this geometric condition, and, therefore, the coefficient shown in equation 2-1 is probably not valid. Therefore, the conclusion is qualitative and indicates that flow stability increases with increasing Reynolds number.



a) Run 27 -  $Re/ft = 20 \times 10^6$



c) Run 28 -  $Re/ft = 10 \times 10^6$



b) Run 28 -  $Re/ft = 10 \times 10^6$



d) Run 30 -  $Re/ft = 5 \times 10^6$



e) Run 30 -  $Re/ft = 5 \times 10^6$

Figure 2 - 20. Effect of Reynolds number  
 $\Theta_1 = 20^\circ$ ,  $\Theta_2 = 70^\circ$ ,  $1/D = .526$

- $\alpha$  - a limited number of angle of attack variations were obtained during Runs 25, 26, 42, and 43; here the angle of attack was variously set at  $0^\circ$ ,  $2.5^\circ$ , and  $5^\circ$ . Due to the limited amount of angle of attack testing, the results are somewhat inconclusive. However, Runs 25 and 26 did seem to indicate a trend towards greater instability as  $\alpha$  increases.

#### 2.6.4 Anomalous Types of Flow Behavior

In the course of observing the high speed movies and still photos taken during this test series several instances of anomalous flow behavior were noted, falling somewhat out of the categories already mentioned.

The metastable type flow has already been discussed in Section 2.6.2.4. Figure 2-21 shows other examples of this type of flow behavior taken from Runs 6 and 38. Owing to the geometry involved, the steady shock pattern is considerably different between the two runs, and Run 38 appears to have a "blended" appearance rather than the two shock structure of Run 6. The other point of interest is that during the oscillation the movement of the strong shock for Run 38 is considerably less than that for Run 6. As will be discussed later, this is apparently correlative to the magnitude of the variation of pressure on the flare face.

The photos shown in Figure 2-22 were taken from Run 24 which exhibited a unique flow behavior. These results indicate that although the flow was essentially of the FP type there were short periods of time when the flow steadied out and appeared as shown in Figure 2-22a. That is, these results are somewhat similar to Run 38 except that the periods of steady flow were short. Note also that when the flow was steady the tip shock was not "blended" as in Run 38 but instead, appears as two distinct shocks. Thus, Run 24 might be also classified as metastable, or perhaps even meta-unstable!

Two other flow anomalies worth mentioning are shown in Figure 2-23. Figure 2-23a shows a photo of Run 7 which was a metastable type flow. Here a disturbance in the shear layer is clearly shown to begin growing. This eventually results in a period of oscillations. Figure 2-23b shows a very interesting shock structure which occurred during a fully pulsating flow, Run 9. Note the abrupt cone-like bulge in the shock structure extending ahead of the main oscillating shock as shown in the lower half of the photo. No explanation has been found for this unusual behavior.





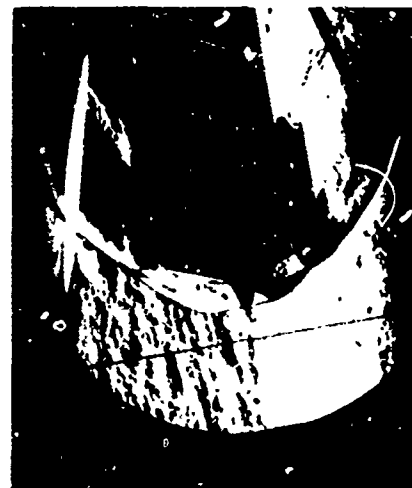
a) Run 6 -  $\phi_1 = 20^\circ$ ,  $\phi_2 = 80^\circ$ ,  $1/D = .674$



b) Run 6 -  $\phi_1 = 20^\circ$ ,  $\phi_2 = 80^\circ$ ,  $1/D = .674$



c) Run 38 -  $\phi_1 = 20^\circ$ ,  $\phi_2 = 70^\circ$ ,  $1/D = .367$



d) Run 38 -  $\phi_1 = 20^\circ$ ,  $\phi_2 = 70^\circ$ ,  $1/D = .367$

Figure 2 - 21. Effect of  $1/D$  and  $\phi_2$  Metastable Flow



a) Nearly Steadies



b) Unsteady

Figure 2 - 22. Nearly Metastable Flow  
Run 24 -  $\phi_1 = 30^\circ$ ,  $\phi_2 = 70^\circ$ ,  $1/D = .341$



a) Run 7 -  $\phi_1 = 20^\circ$ ,  $\phi_2 = 80^\circ$ ,  $1/D = 674$



b) Run 9 -  $\phi_1 = 20^\circ$ ,  $\phi_2 = 80^\circ$ ,  $1/D = .484$

Figure 2 - 23. Unusual Shock Structure

### 2.6.5 Quantitative Results

Two types of quantitative results were available from these tests with respect to analyzing unsteady flow behavior: high frequency pressure data obtained on the face of the flare and accelerometer data relating the net acceleration of the model and sting support system (since the model is not isolated).

Samples of the four basic types of raw pressure and axial accelerometer data are shown in Figure 2-24. The meaning of the exact magnitude of the axial accelerometer data is of little significance since it reflects the system response of the entire model and support system; therefore, no scale is shown. The transverse accelerations are difficult to interpret. The measured approximate maximum, minimum and average values of static pressure measured on the face of the flare are shown in Table 2-4. One interesting point to note is that the maximum and minimum values of pressure for the metastable type flows exhibit greater variation than the fully pulsating flows. It is clear from Figure 2-24 that each type of flow exhibits a unique type of pressure signal. The accelerometer signals are not quite as unique for each type of flow; however, the axial accelerometer obviously indicates when strong oscillations are present.

In addition to the raw signal traces the data were processed to obtain their Power Spectral Densities (PSD). A PSD plot shows the time averaged amplitude squared for each frequency component present in the signal. That is, frequencies containing large amounts of excitation will have the largest values of power spectral density function. Hence, the fundamental frequency and its harmonics are expected to exhibit large values of power spectral density function. Figure 2-25 illustrates, schematically, the nature of the pressure and accelerometer PSD plots as related to the different types of flows observed visually. Here again the pressure PSD plots exhibit characteristic peaks corresponding to the system natural frequency when present, flow field pulsation frequencies.

The actual pressure and accelerometer PSD plots that were computed are shown in Figures 2-26 and 2-27; not all runs are included. All of these PSD plots seem to indicate that the large scale flow oscillations occur at a fundamental frequency of about 1100 cps with harmonics at about 2200 cps and 3300 cps. The fundamental frequency corresponds to a Strouhal number,  $S = vD/V$ , of about 0.20. There exists one interesting exception to the rule, namely, Run 38. During one portion of the run, shown in Figure 2-26.38, a strong peak occurred at

---

\*The pressure and accelerometer oscillograms were generated by A. Galif of the TRW Corporation.

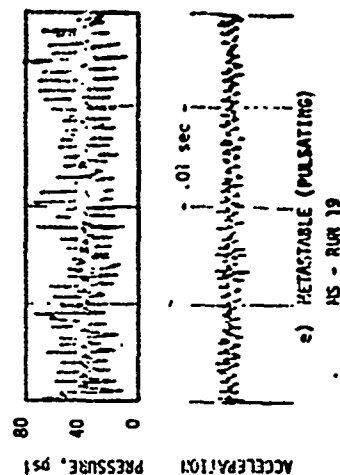
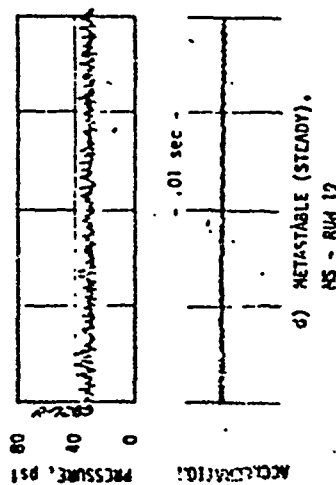
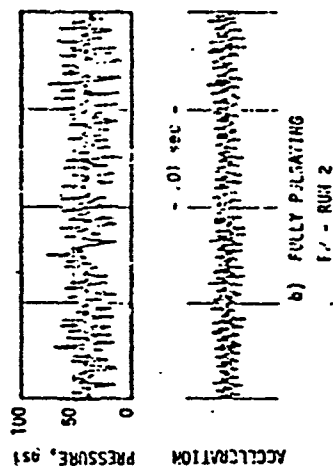
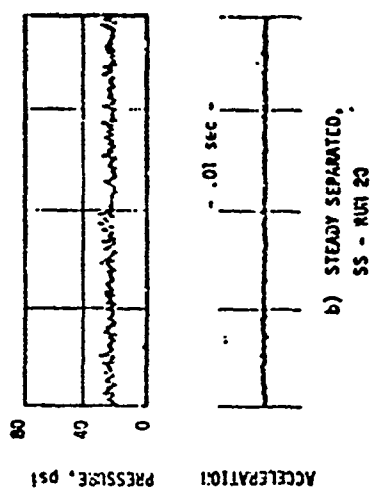


Figure 2-24. Character of K1 Pressure Signal and Axial Accelerometer Signal for Different Types of Flow

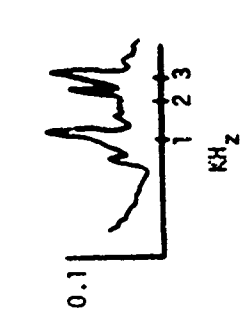
TABLE 2-4  
TABULATION OF HIGH FREQUENCY PRESSURE DATA (K1)

Run	P <sub>avg</sub> psia	P <sub>max</sub> psia	P <sub>min</sub> psia	P <sub>t0</sub> psia	T <sub>t0</sub> °F	C <sub>Davg</sub>	C <sub>Dmax</sub>	C <sub>Dmin</sub>
1	15	28	4	260	245	1.69	3.20	.408
2	38	80	11	575	283	1.94	4.15	.521
4	31	31	31	607	289	1.49	1.49	1.49
5a	50	117	10	607	285	2.43	5.77	.441
5b	20	41	15	607	285	.939	1.99	.690
6a	60	115	15	597	277	2.93	5.67	.703
6b	32	40	30	597	277	1.56	1.97	1.46
8	39	82	7	586	265	1.96	4.17	.304
9	41	77	12	605	284	1.99	3.79	.545
10	44	75	13	614	282	2.11	3.64	.583
11	40	54	31	602	275	1.95	2.65	1.50
12	36	40	34	603	284	1.74	1.95	1.65
13	31	35	26	598	270	1.51	1.71	1.26
14	32	35	29	599	264	1.56	1.71	1.41
15	28	45	21	592	275	1.37	2.24	1.02
16a	26	36	21	609	269	1.23	1.73	.985
16b	26	86	4	609	269	1.23	4.21	.141
17	25	36	21	607	266	1.19	1.74	.989
18	26	36	21	600	263	1.25	1.76	1.00
19a	30	48	24	605	287	1.44	2.34	1.14
19b	30	82	10	605	287	1.44	4.04	.443
20	23	30	18	600	272	1.10	1.45	.850
21	30	30	30	606	292	1.44	1.44	1.44
22	32	48	19	596	277	1.57	2.38	.907
23	35	41	31	603	266	1.70	2.00	1.50
24	31	45	14	580	255	1.56	2.29	.673
25a( $\alpha = 2.5^\circ$ )	22	35	18	608	288	1.04	1.68	.838
25b( $\alpha = 5.0^\circ$ )	21	66	12	608	288	.987	3.22	.540
25c( $\alpha = 0^\circ$ )	30	40	23	600	288	1.43	1.93	1.09
26a( $\alpha = 0^\circ$ )	36	41	31	603	256	1.75	2.00	1.50
26b( $\alpha = 2.5^\circ$ )	32	45	17	603	286	1.55	2.25	.795
26c( $\alpha = 5.0^\circ$ )	28	41	16	603	286	1.35	2.00	.745
27	24	32	20	604	302	1.14	1.54	.944
28	18	40	4	274	288	1.93	4.36	.384
32	34	48	16	606	276	1.64	2.34	.741
33	17	24	12	283	268	1.76	2.51	1.22
35	28	39	24	598	261	1.36	1.91	1.16
36	32	48	19	597	251	1.56	2.37	.905
37	26	42	20	598	292	1.26	2.07	.954
38	42	50	34	607	282	2.03	2.43	1.64

- Notes: (1) Some records not available  
(2) a and b reflect a change in character of the signal

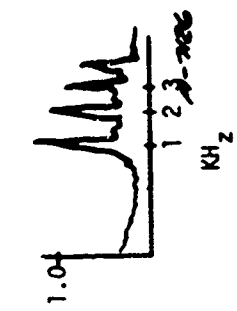
1) FULLY PUI SATING

EX. RUN 2



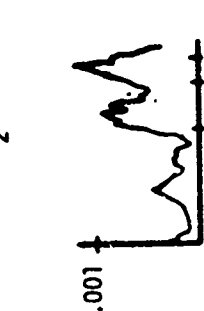
2) STEADY SEPARATED/PULSATING

EX. RUN 19



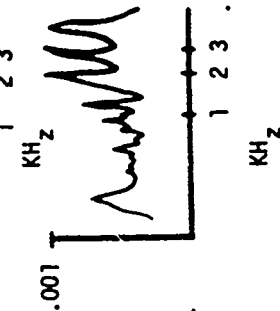
3) STEADY SEPARATED

EX. RUN 20



4) STEADY ATTACHED

EX RUN 47



OR

Figure 2-25. Four Types of Flow Observed

POWER SPECTRAL DENSITY PLOTS



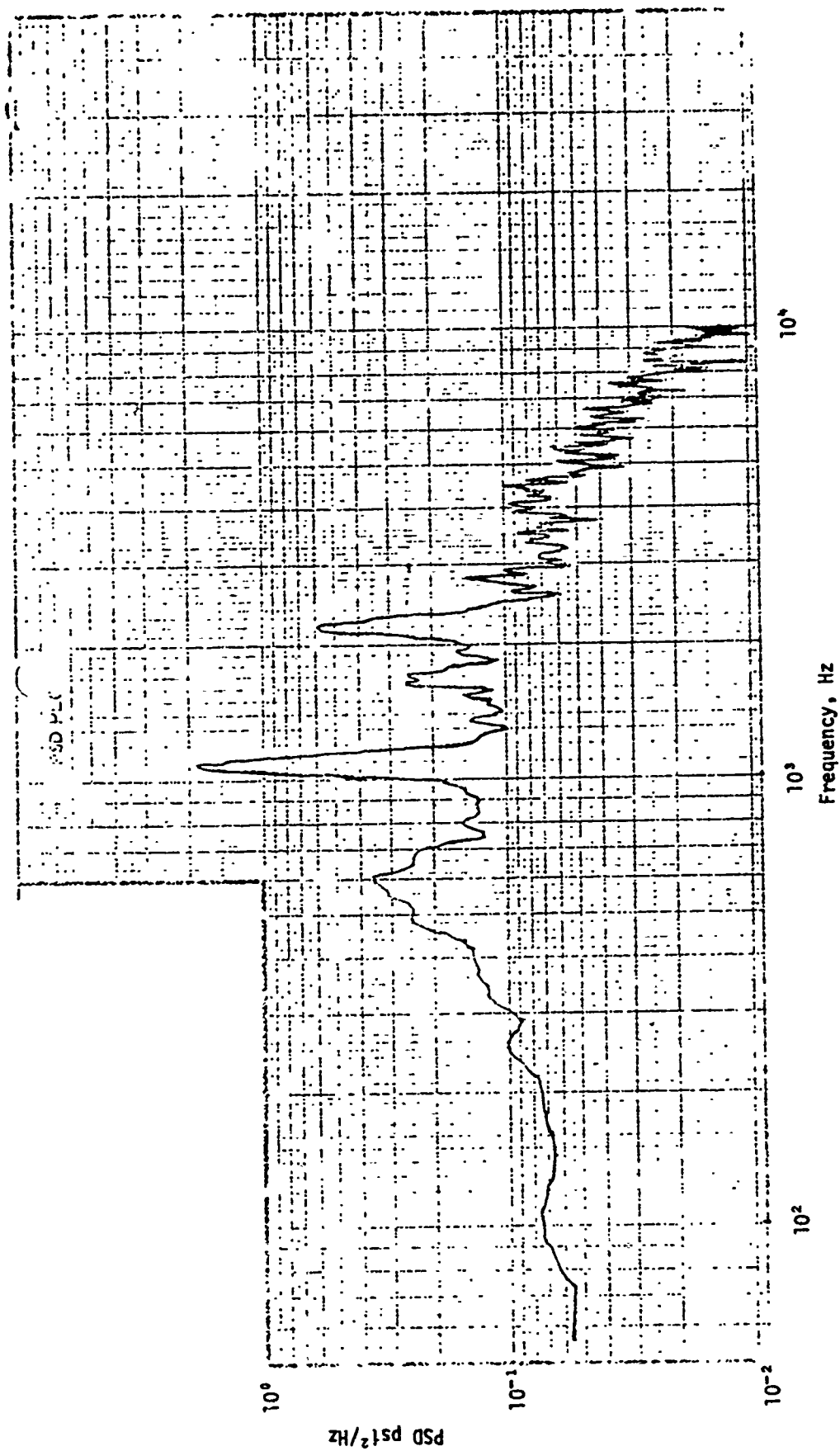


Figure 2-26.01. Pressure PSD for Run 2, Tape Position 19:35:09

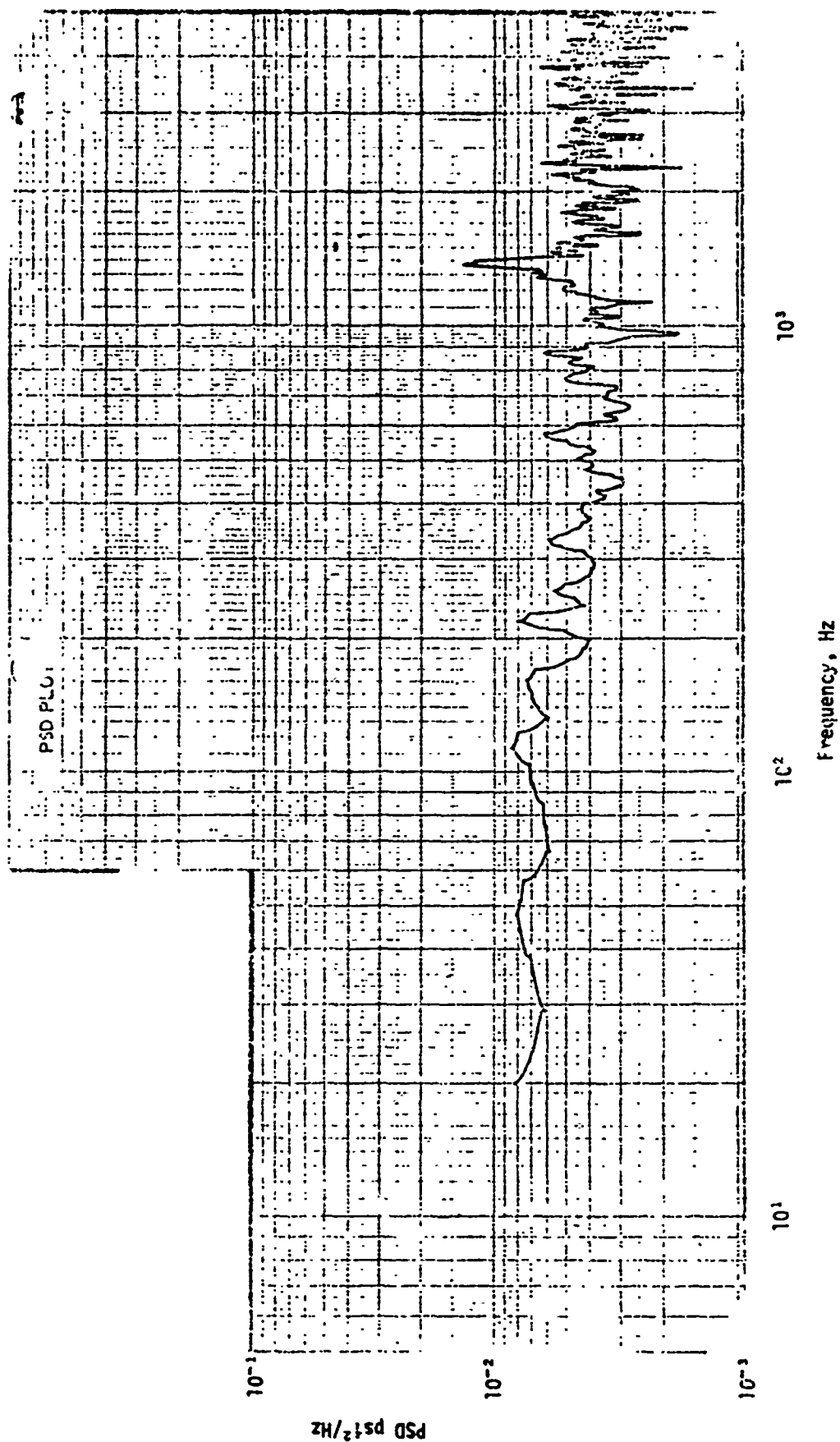


Figure 2-26.02. Pressure PSD for Run 5, Tape Position 01:50:30

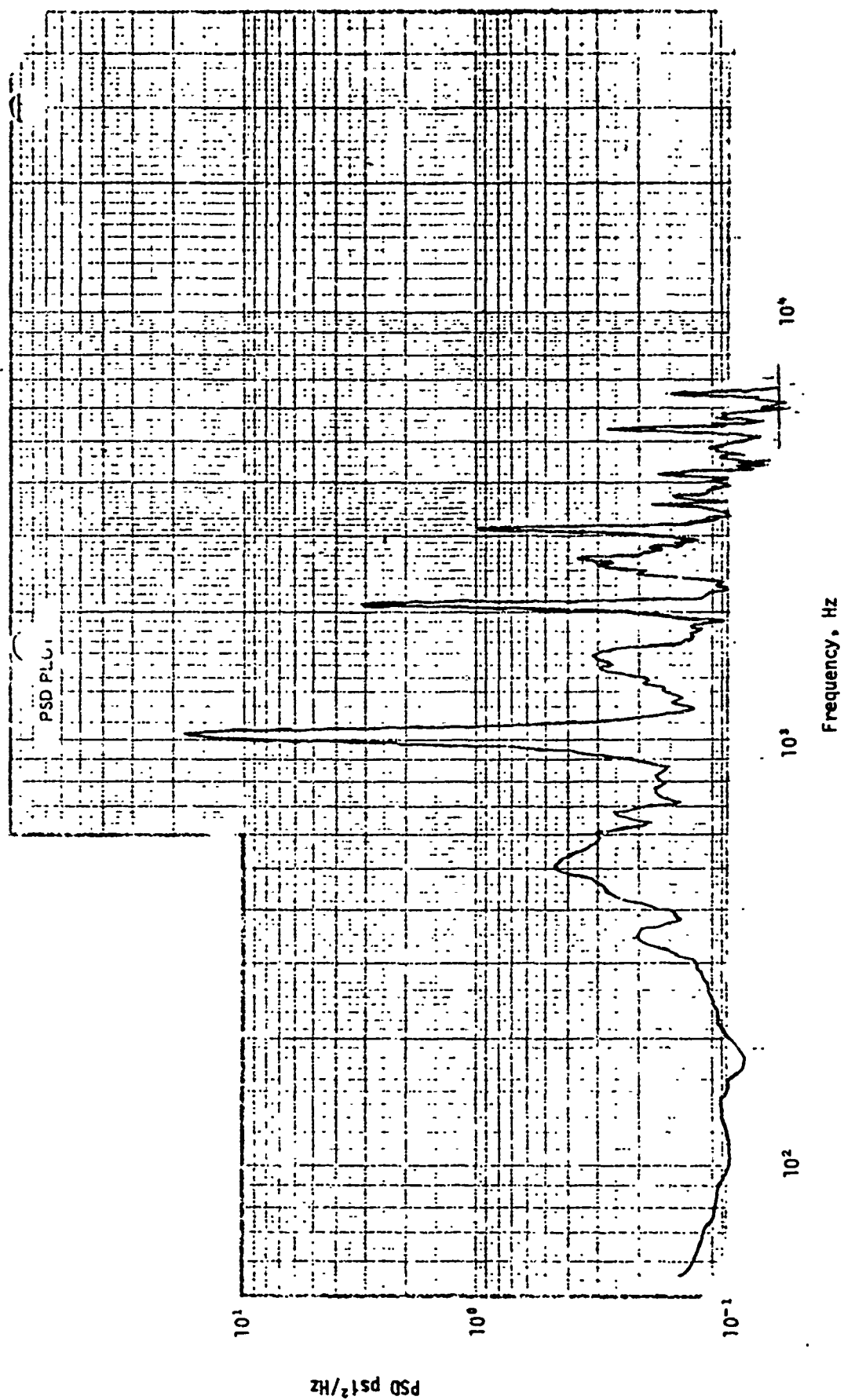


Figure 2-26.03. Pressure PSD for Run 5, Tape Position 01:50:36

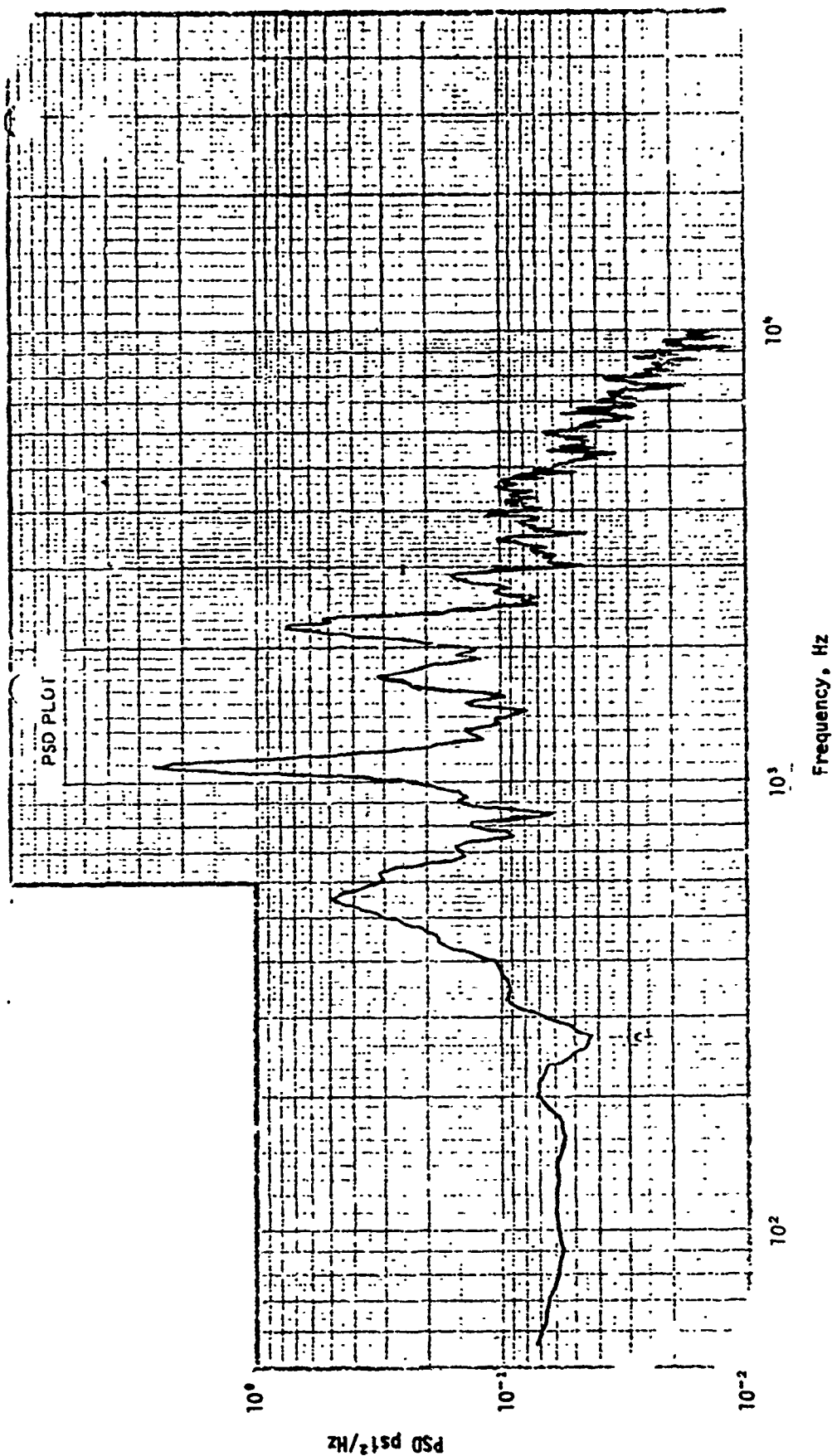


Figure 2-26.04. Pressure PSD for Run 8, Tape Position 06:04:30

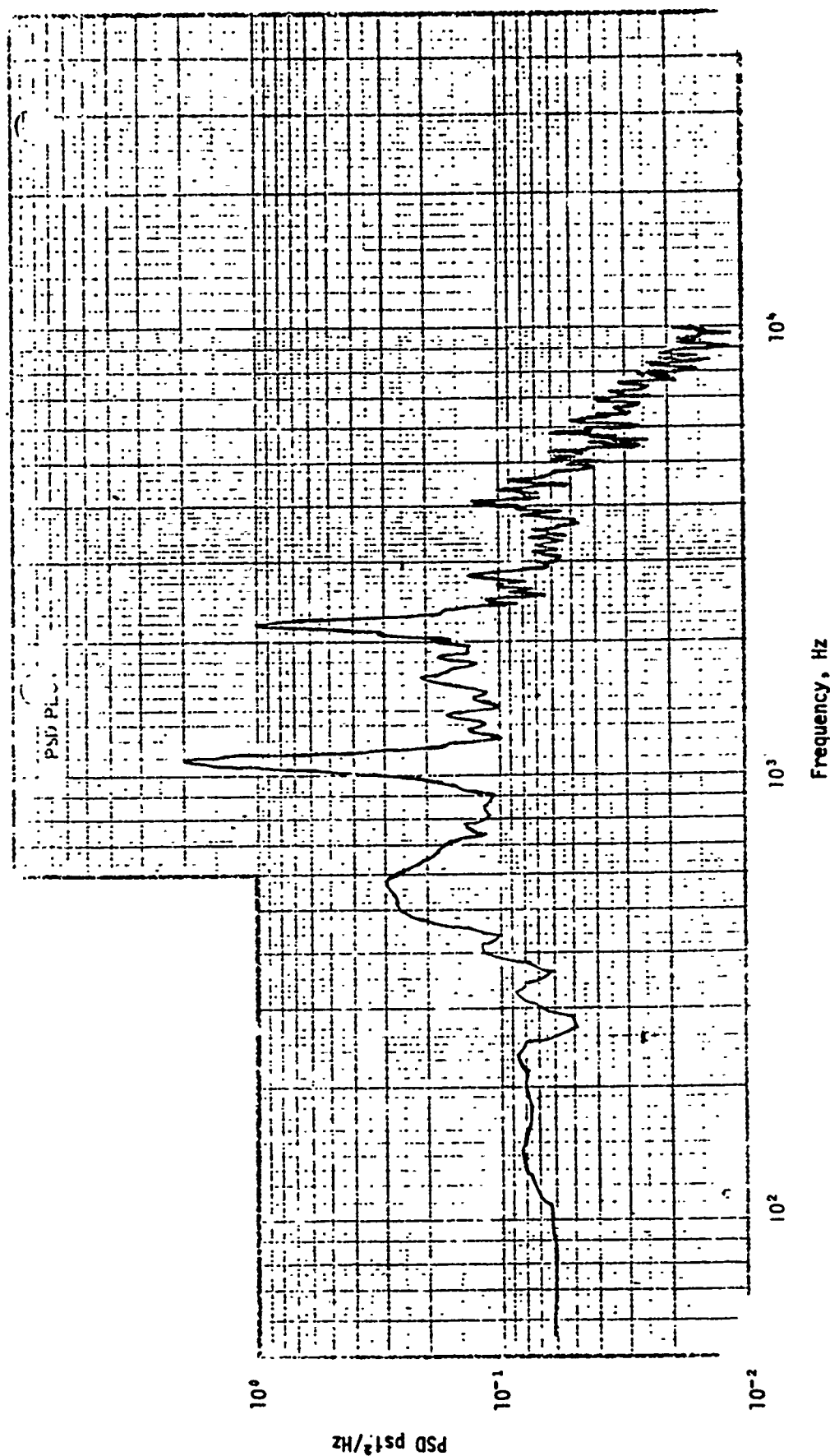


Figure 2-26.05. Pressure PSD for Run 9, Tape Position 01:12:01

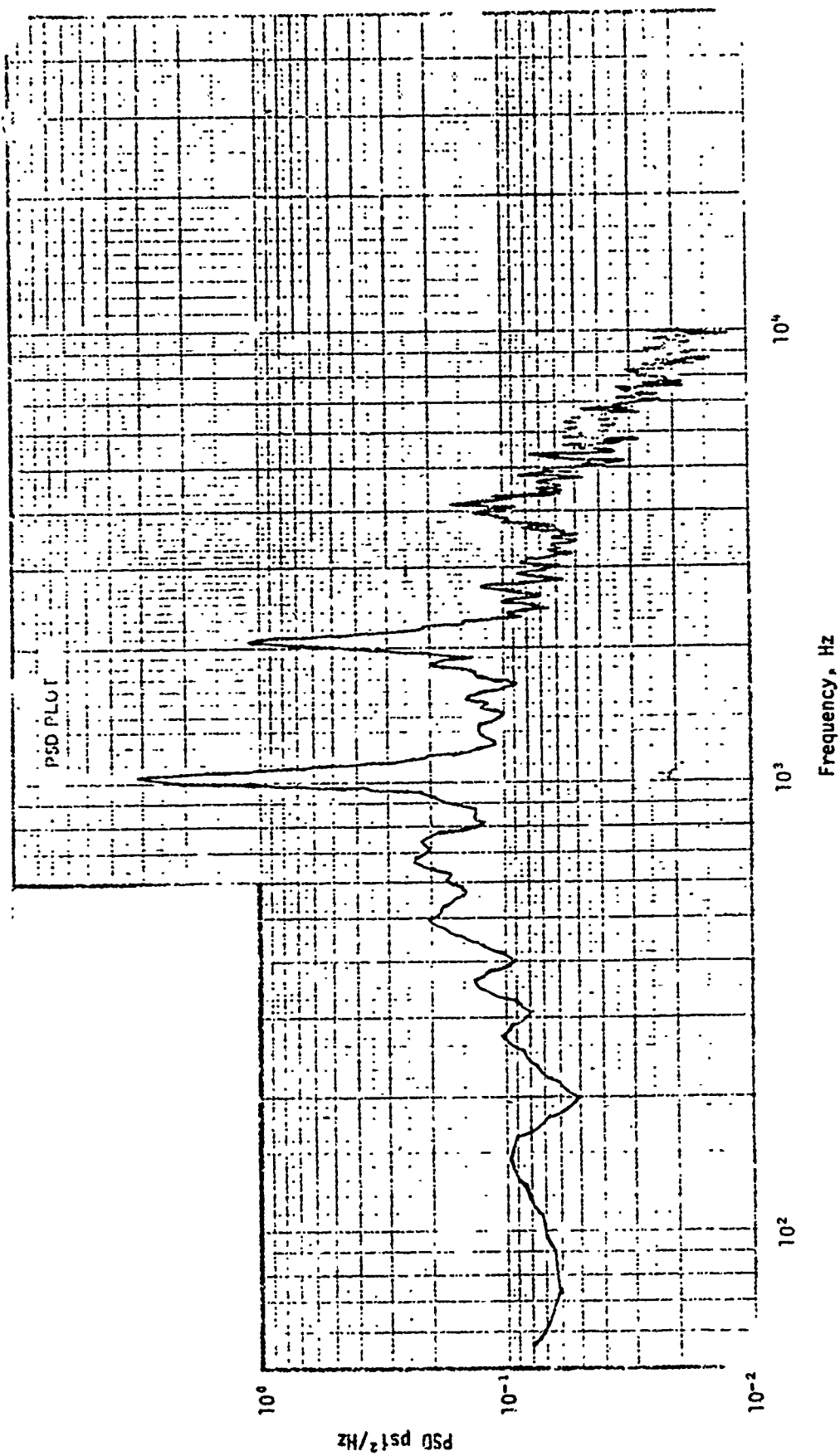


Figure 2-26.06. Pressure PSD for Run 10, Tape Position 01:12:21

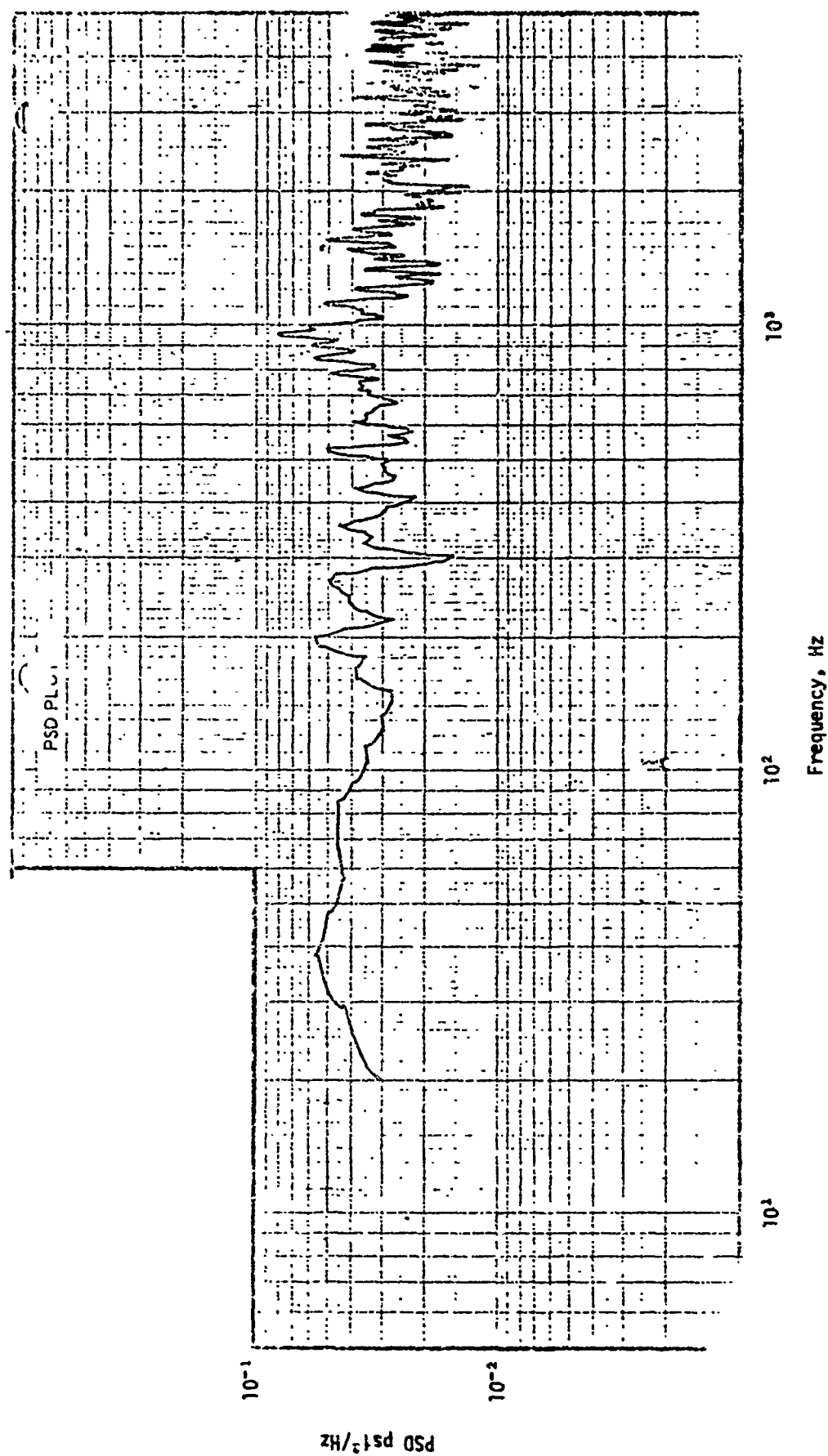


Figure 2-26.0% Pressure PSD for Run 11, Tape Position 01:14:05

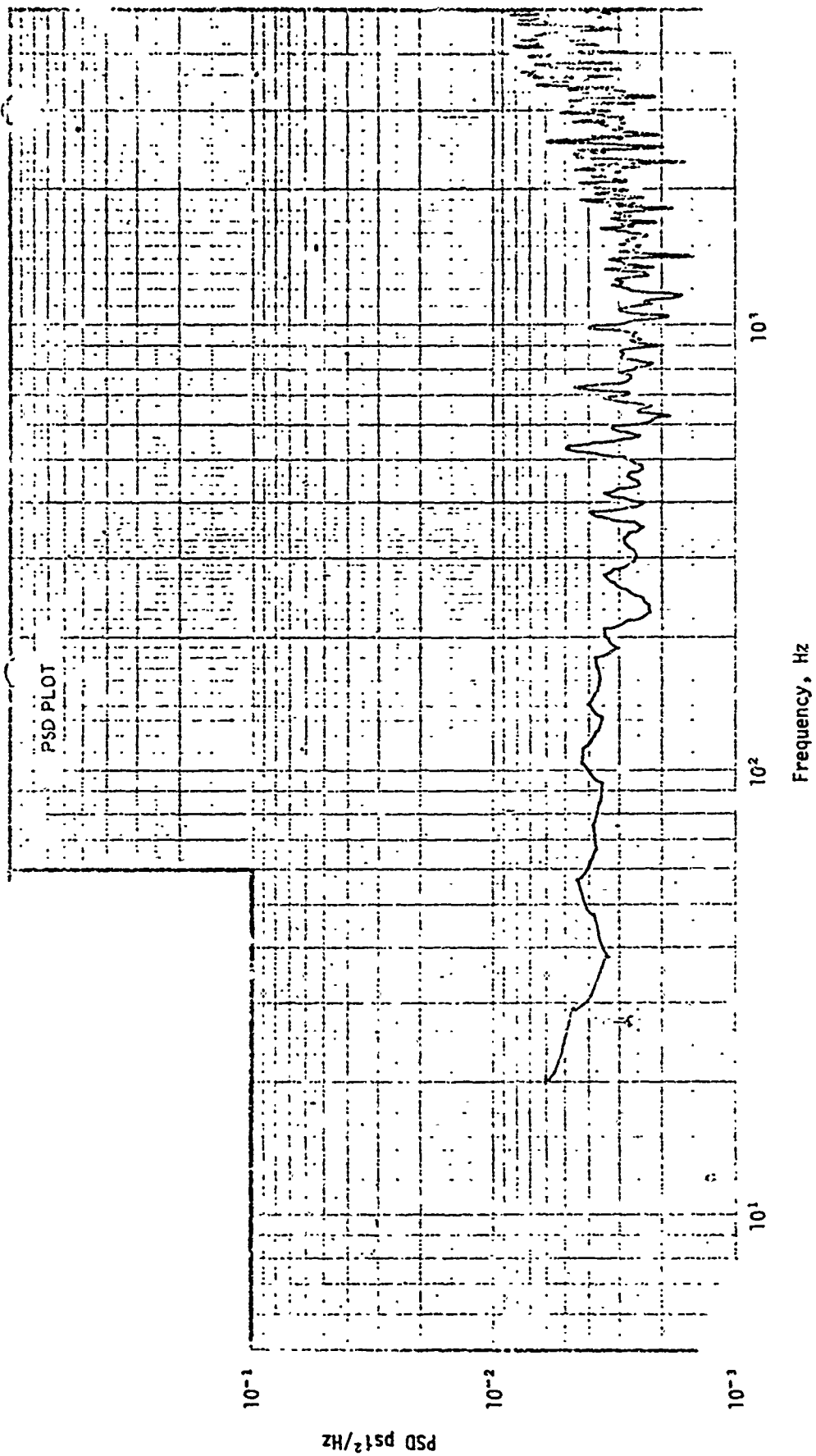


Figure 2-26.08. Pressure PSD for Run 12, Tape Position 01:14:26



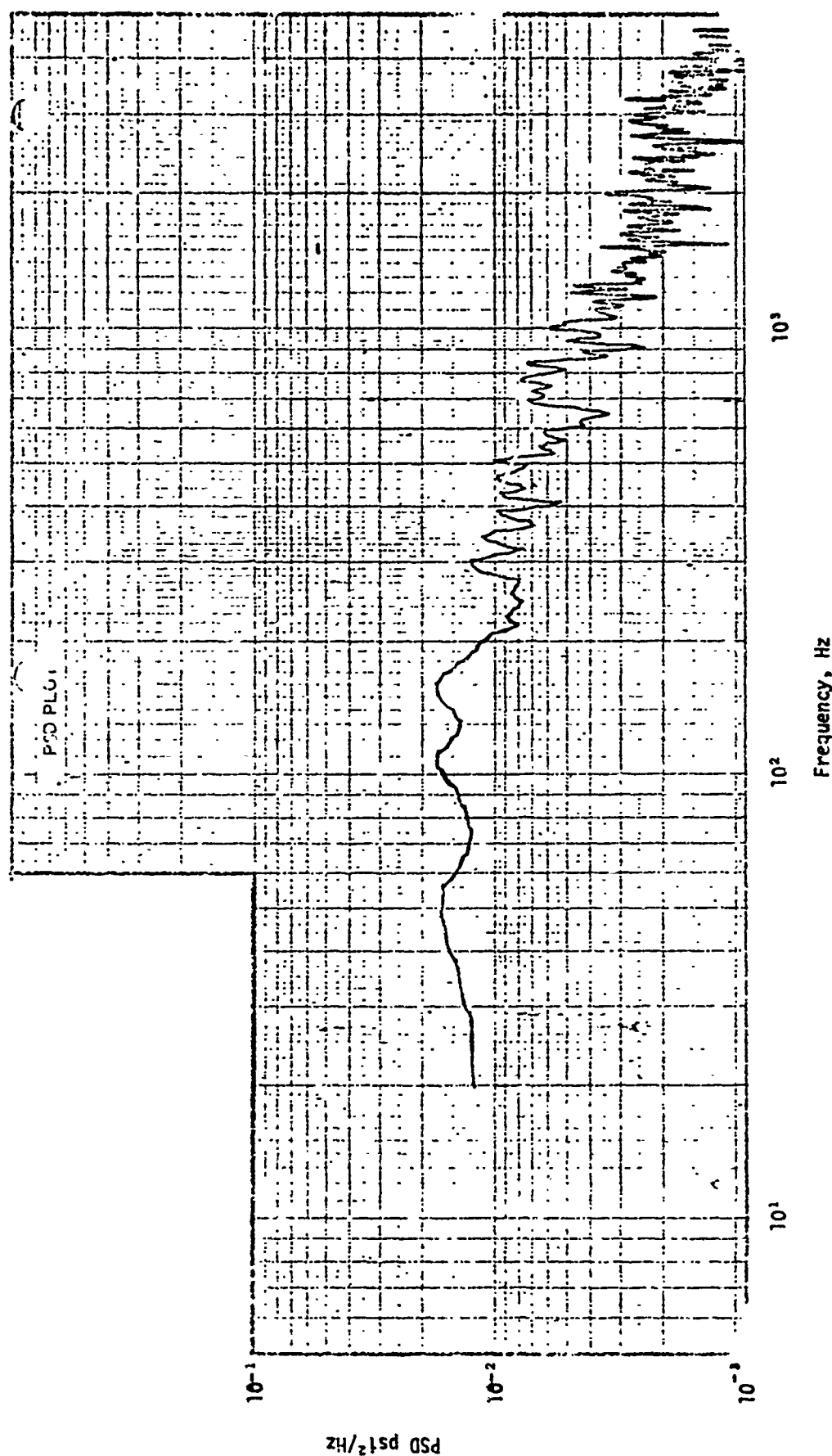


Figure 2-26.09. Pressure PSD for Run 13, Tape Position 01:14:41

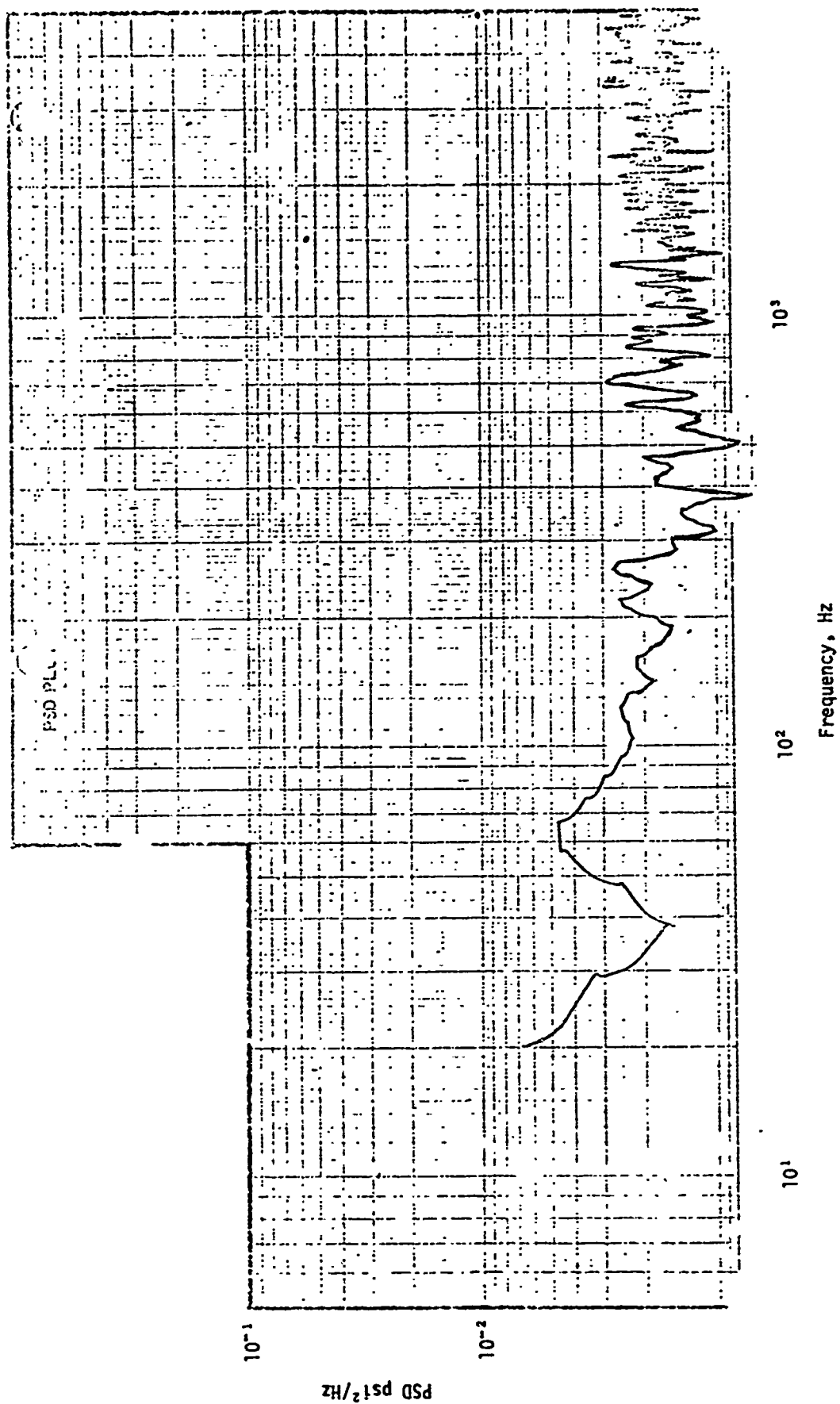


Figure 2-26.10. Pressure PSD for Run 14, Tape Position 01:14:48

Reproduced from  
best available copy.

PSD PLU.

10<sup>-1</sup>

10<sup>-2</sup>

0 2 4 6 8 10

PSD  $\text{g}^2/\text{Hz}$

101

Frequency, Hz  
Figure 2-26.11. Pressure PSD for Run 15, Tape Position 01:18:06

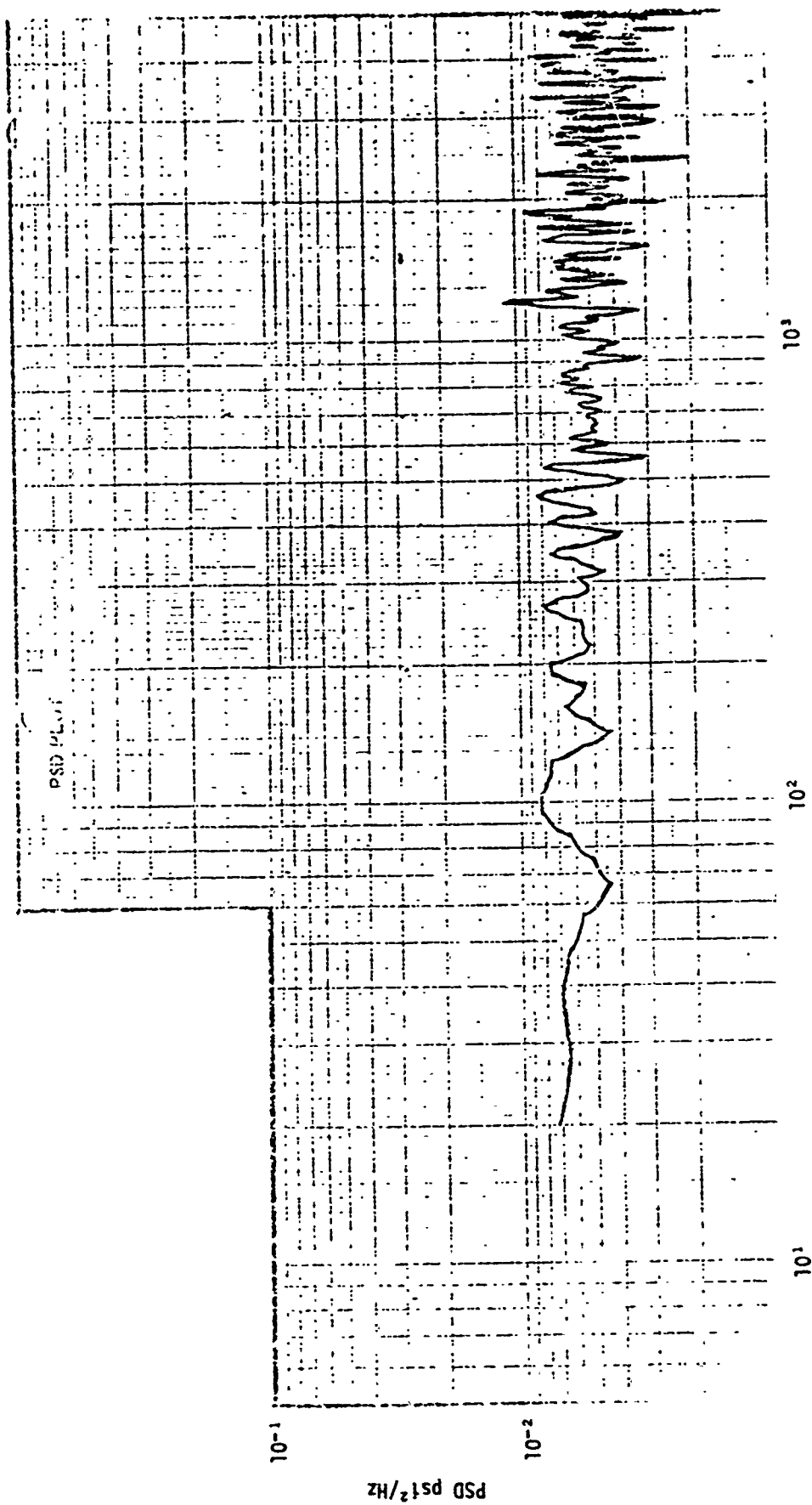


Figure 2-26.12. Pressure PSD for Run 16, Tape Position 01:18:26

Reproduced from  
best available copy.

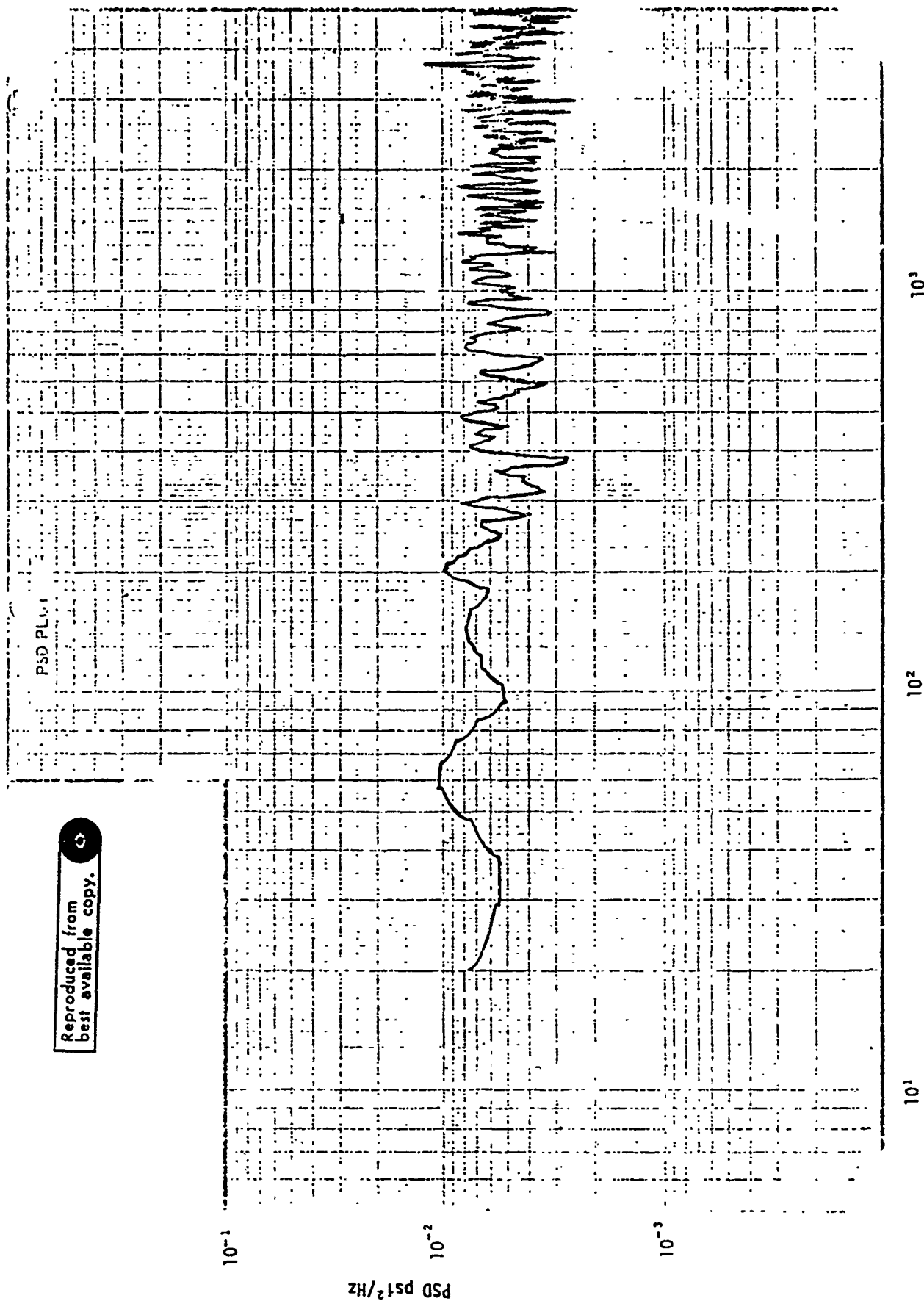


Figure 2-26.13. Pressure PSD for Run 17, Tape Position 01:18:50

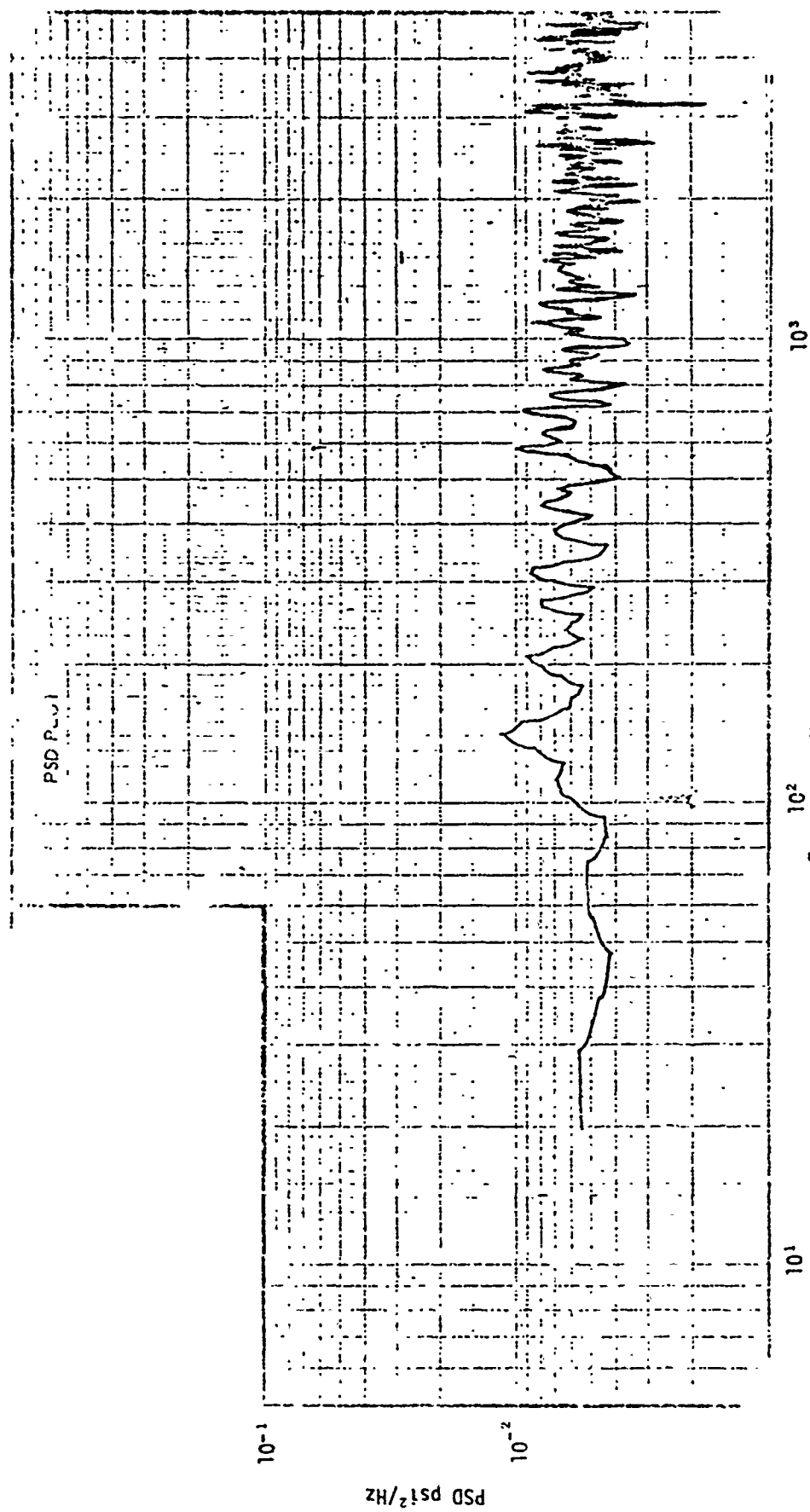


Figure 2-26.14. Pressure PSD for Run 18, Tape Position 01:19:07

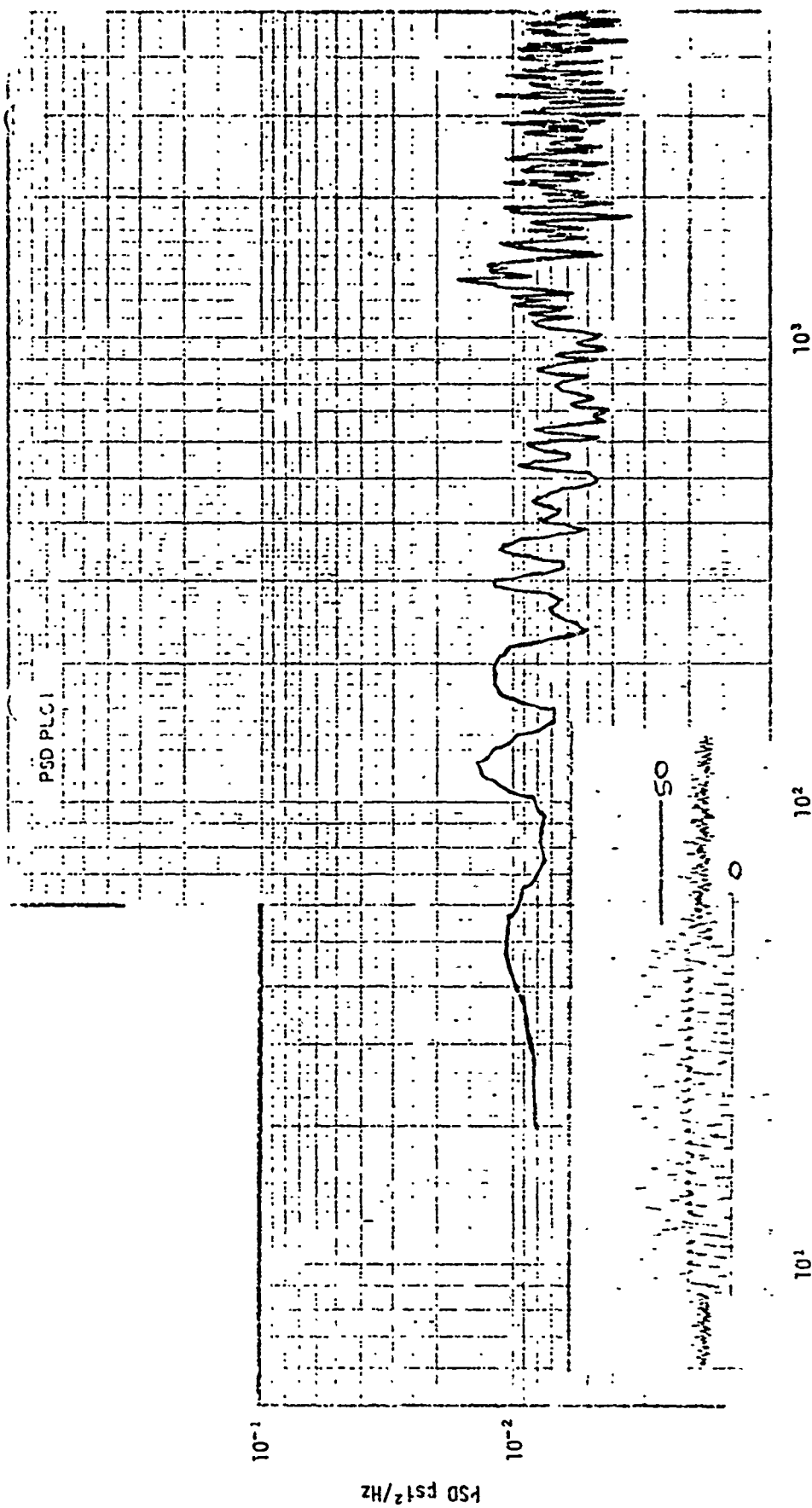


Figure 2-26.15. Pressure PSD for Run 19, Tape Position 01:19:26

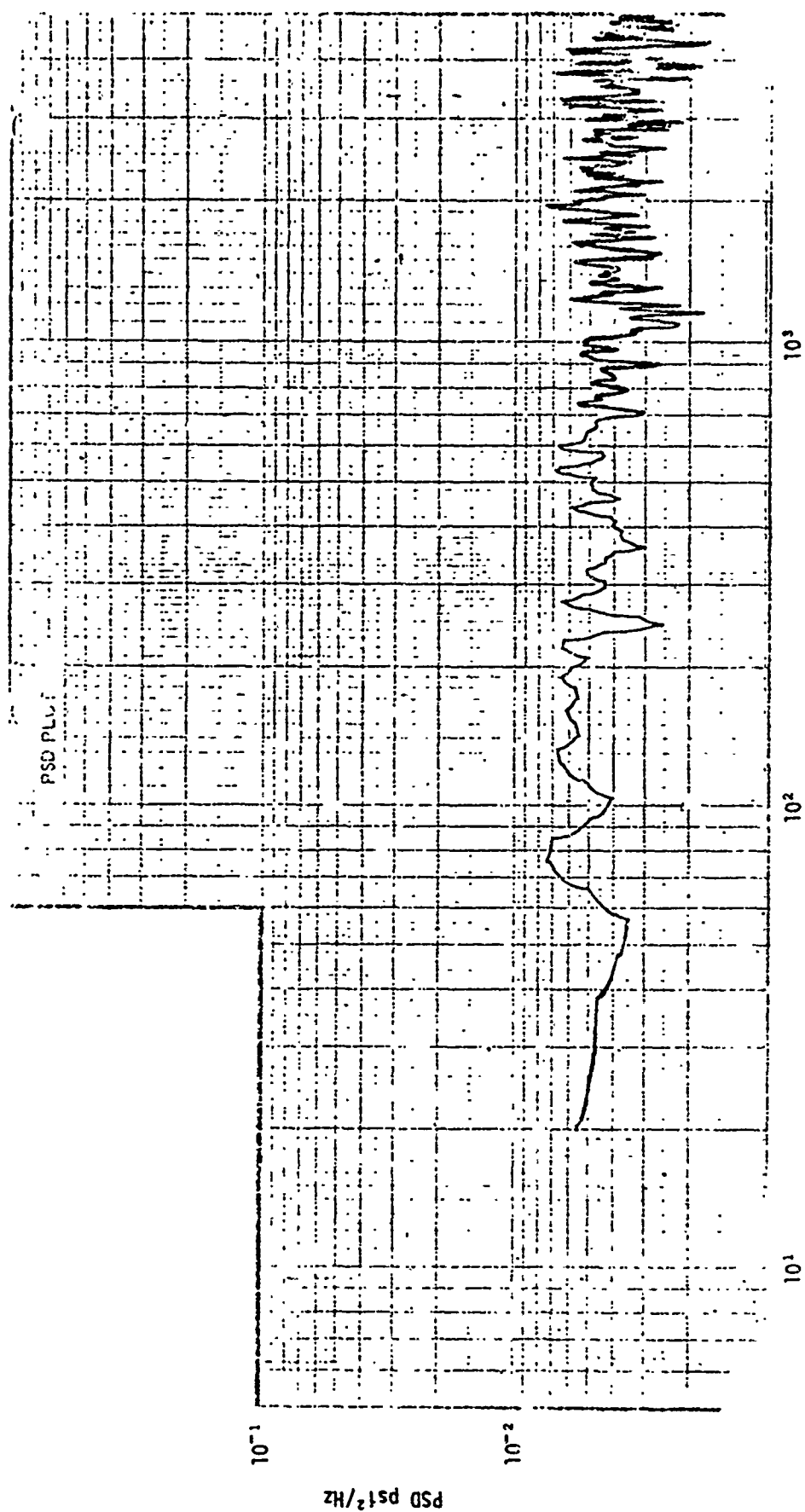


Figure 2-26.16. Pressure PSD for Run 20, Type Position 01:19:45



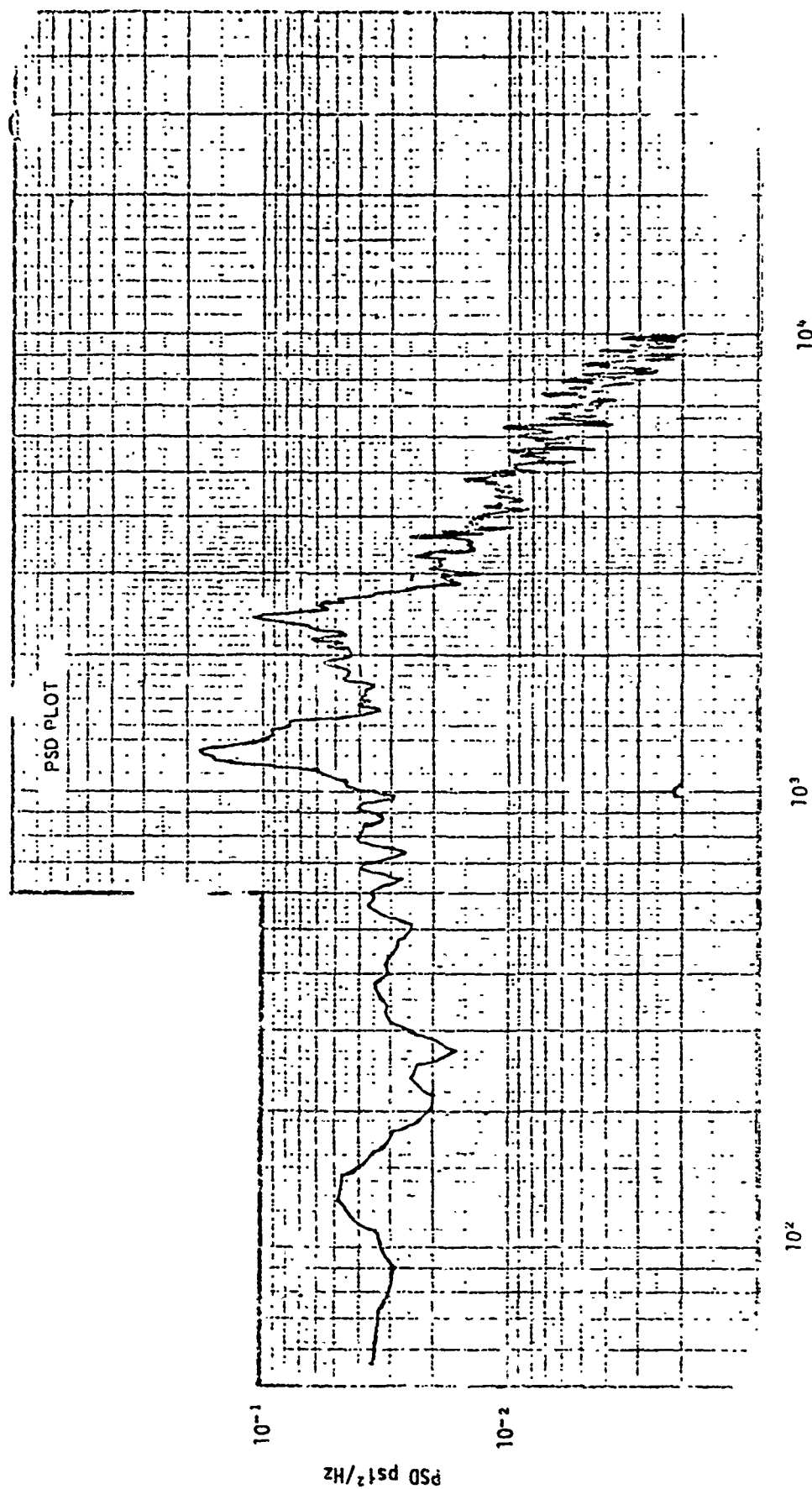


Figure 2-26.17. Pressure PSD for Run 22, Tape Position 01:17:28

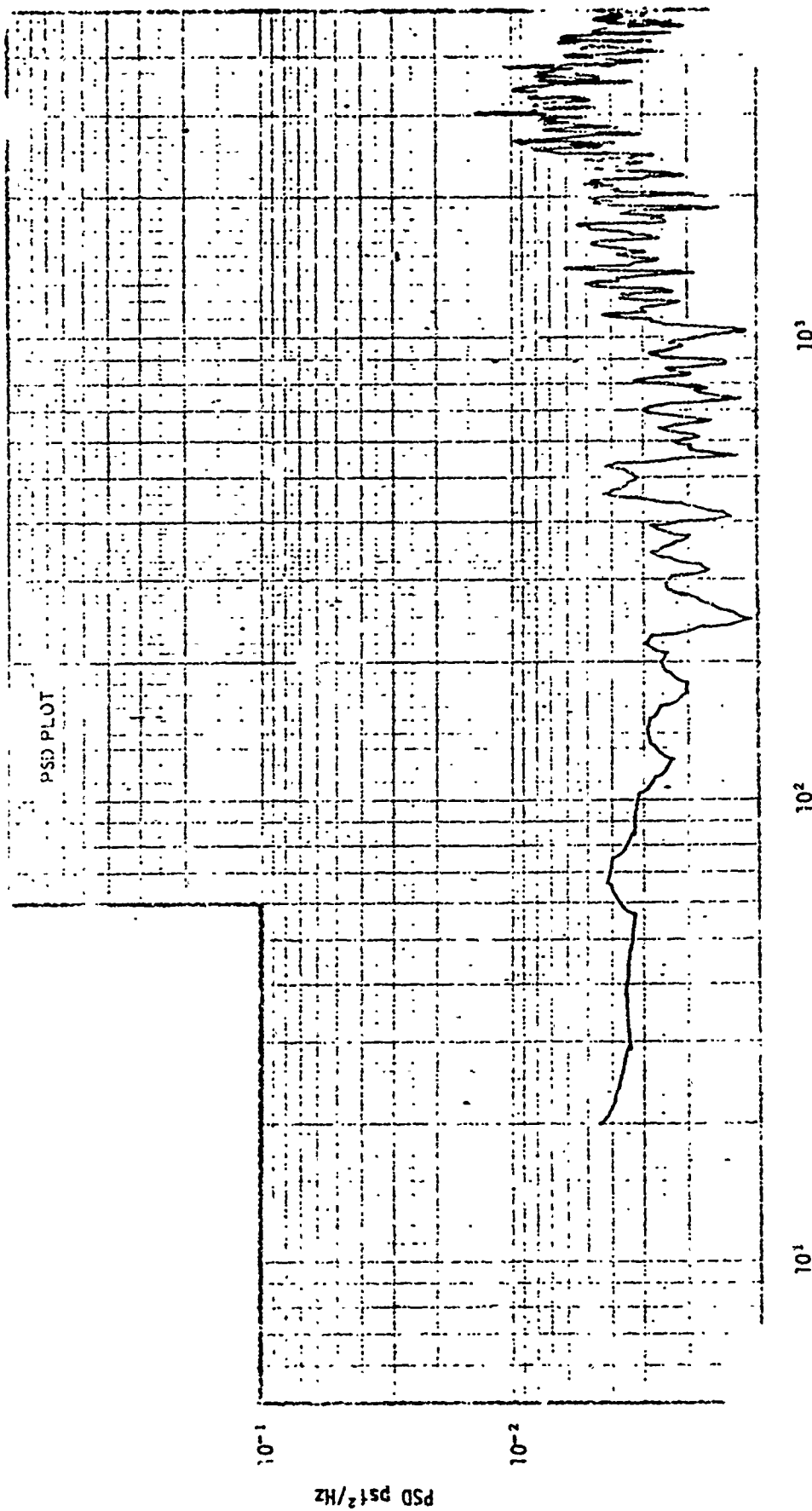


Figure 2-26.18. Pressure PSD for Run 23, Tape Position 01:17:47

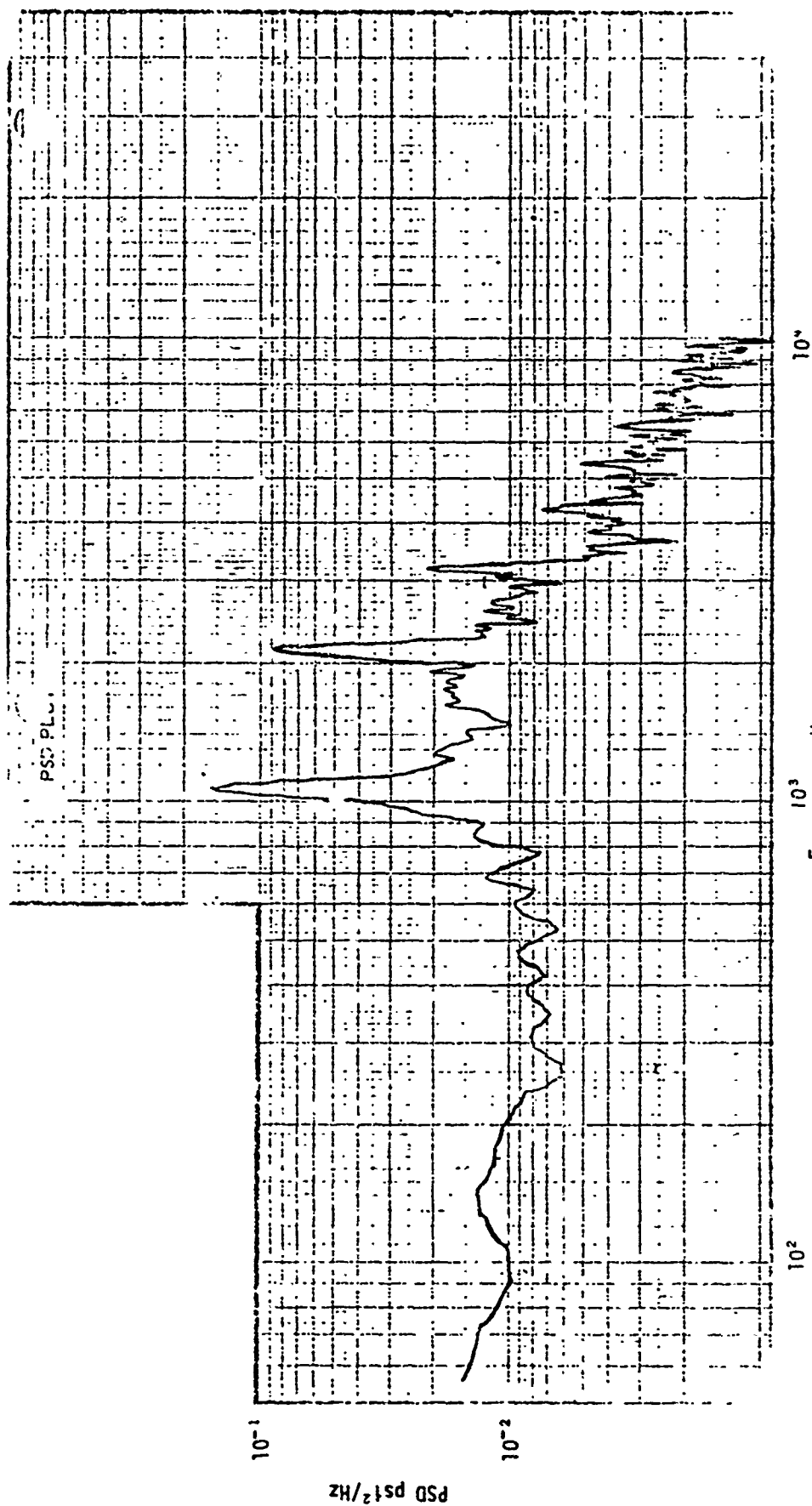


Figure 2-26.19. Pressure PSD for Run 24, Tape Position 01:18:04

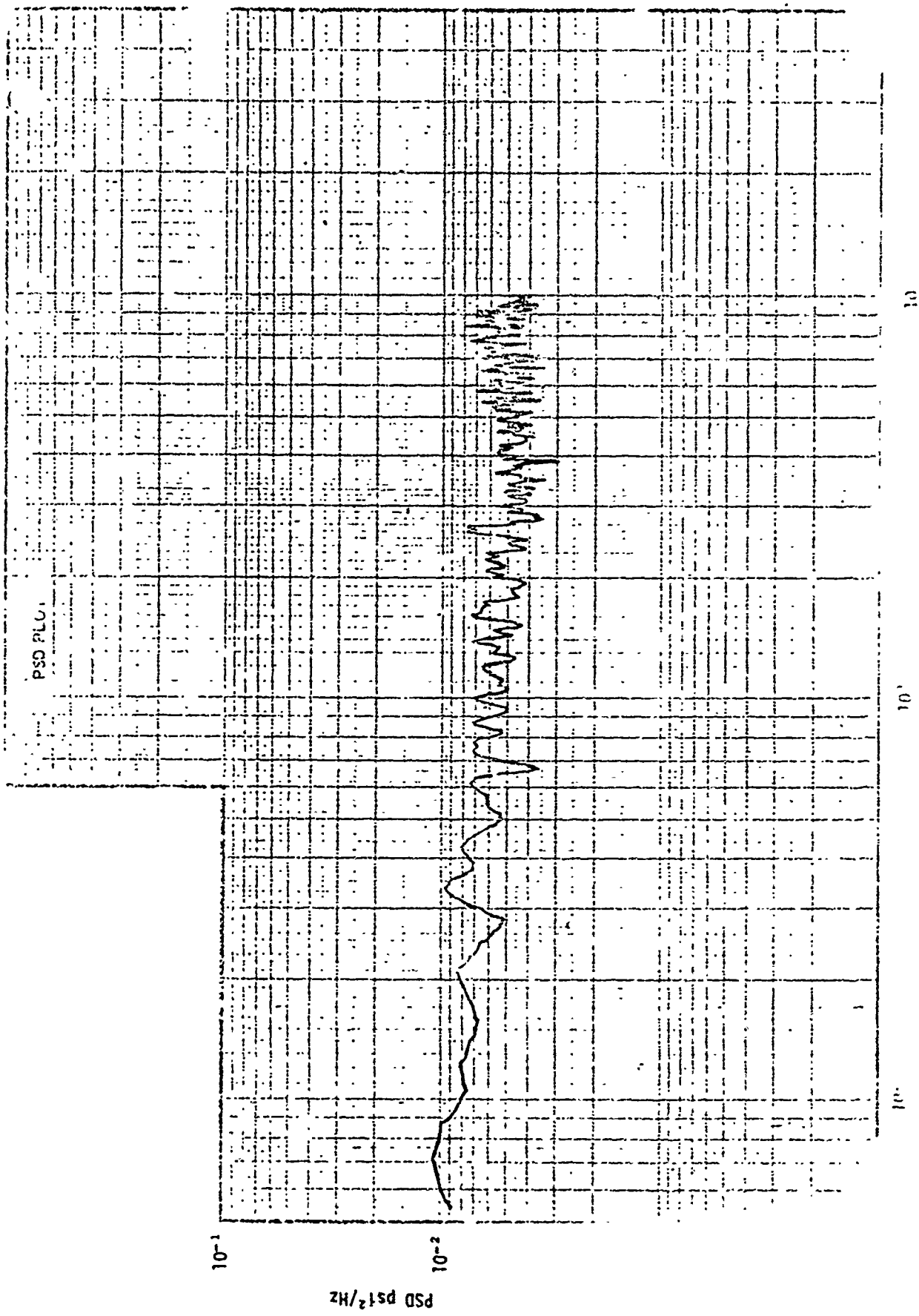


Figure 2. Power Spectral Density

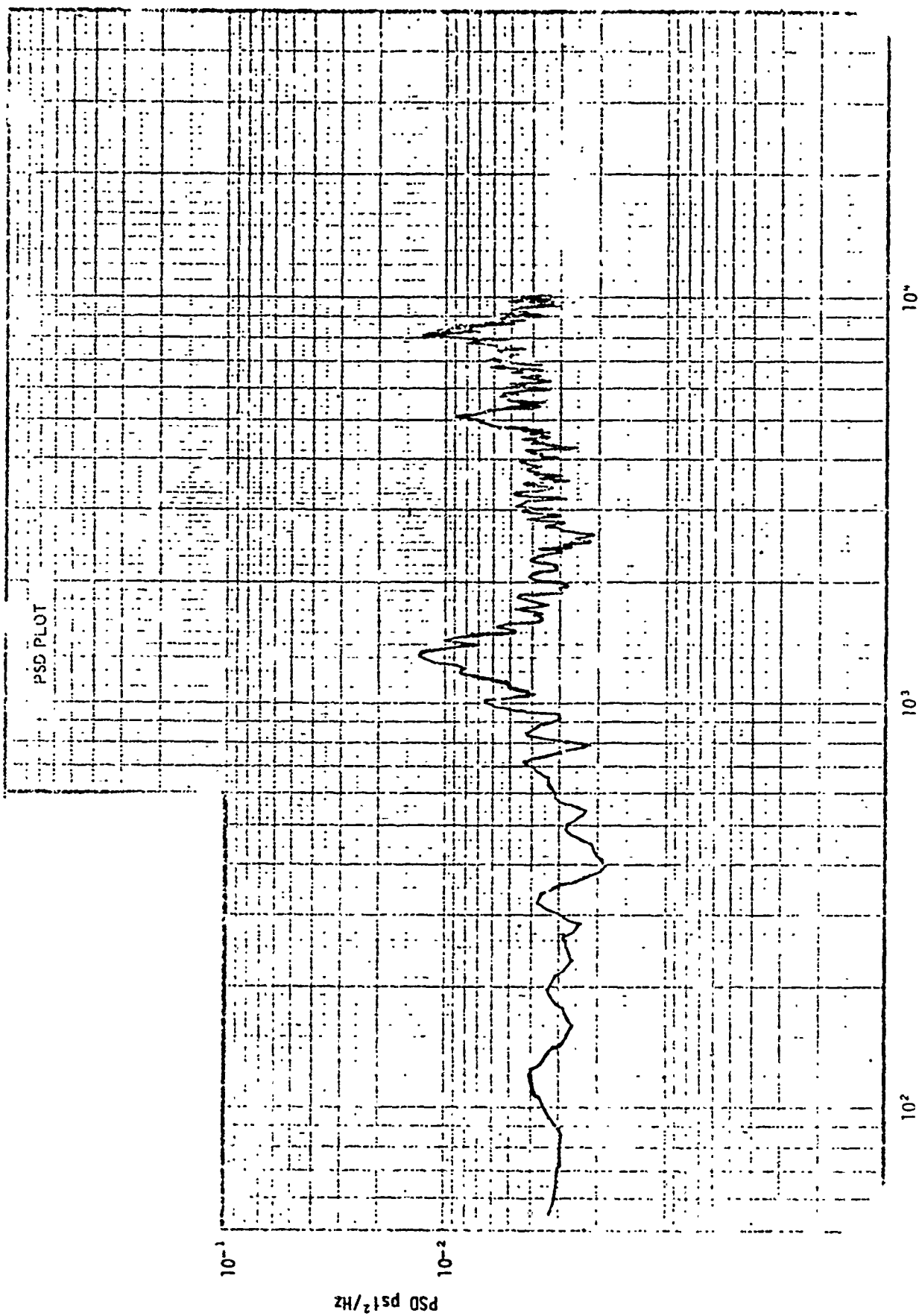


Figure 2-26.21. Pressure PSD for Run 25, Tape Position 11:39:17

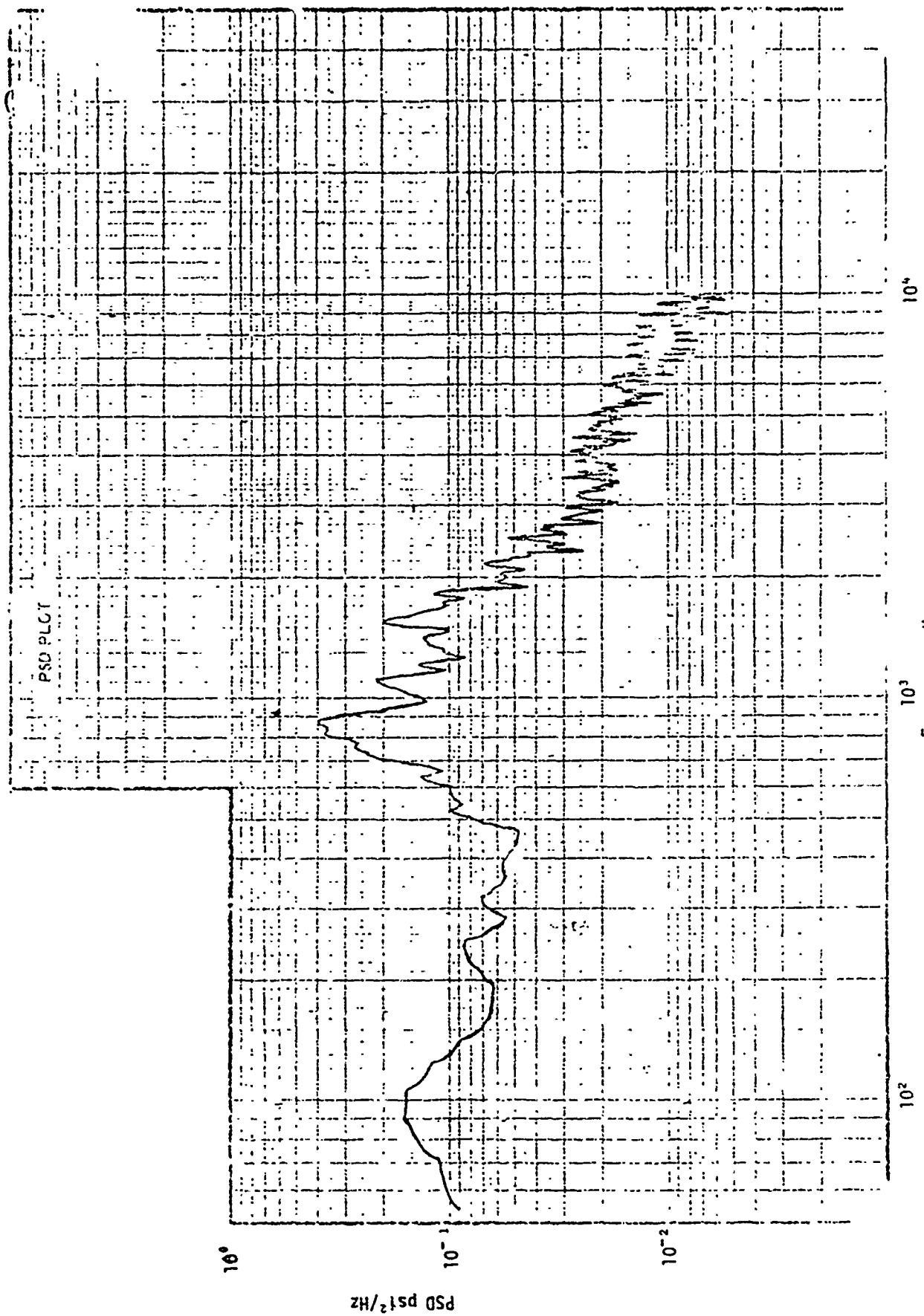


Figure 2-26.22. Pressure PSD for Run 25, Tape Position 11:39:23

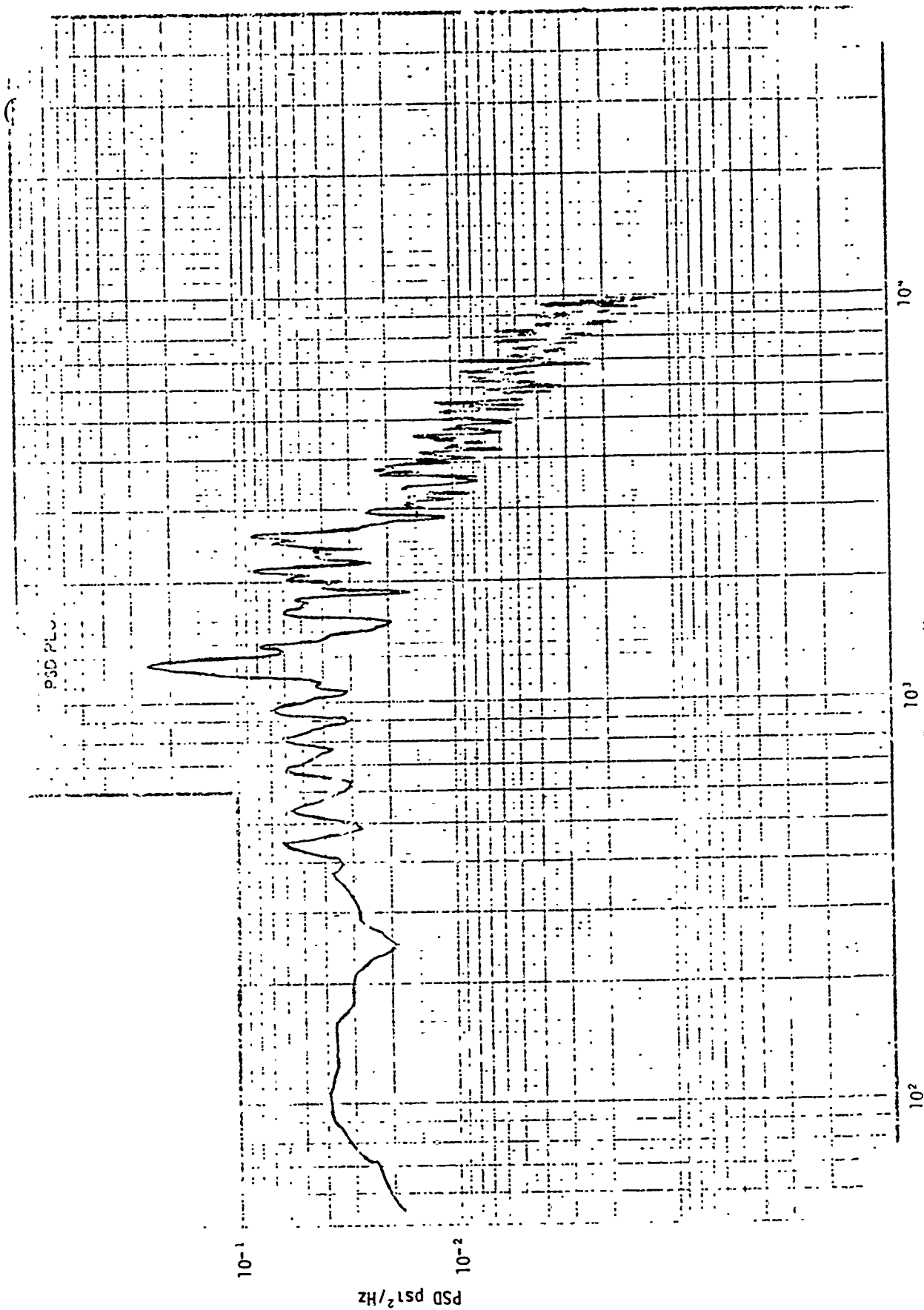


Figure 2-26.23. Pressure PSD for Run 26, Tape Position 11:51:57

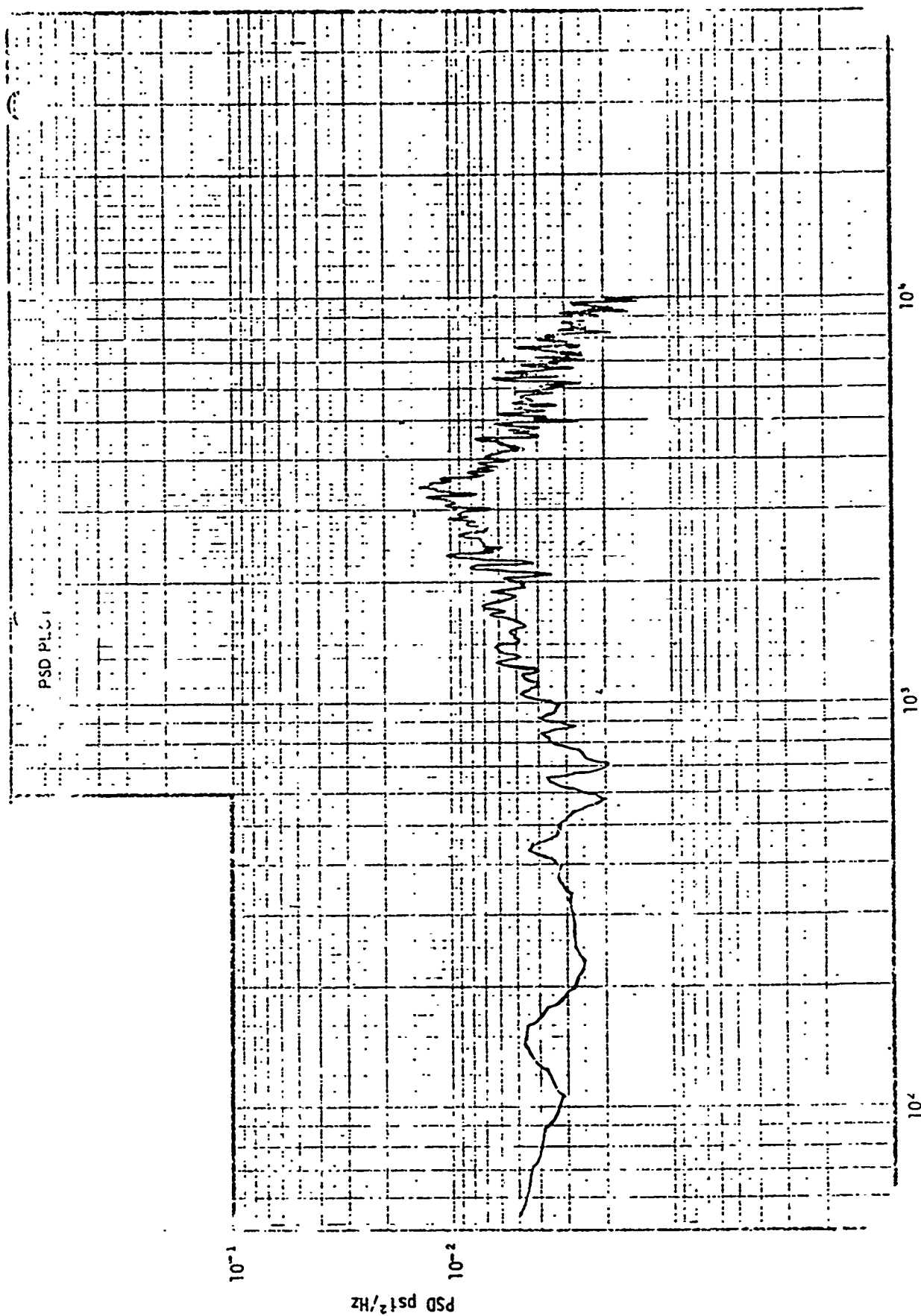


Figure 2-26. 24. Pressure PSD for Run 26, Tape Position 11:51:58



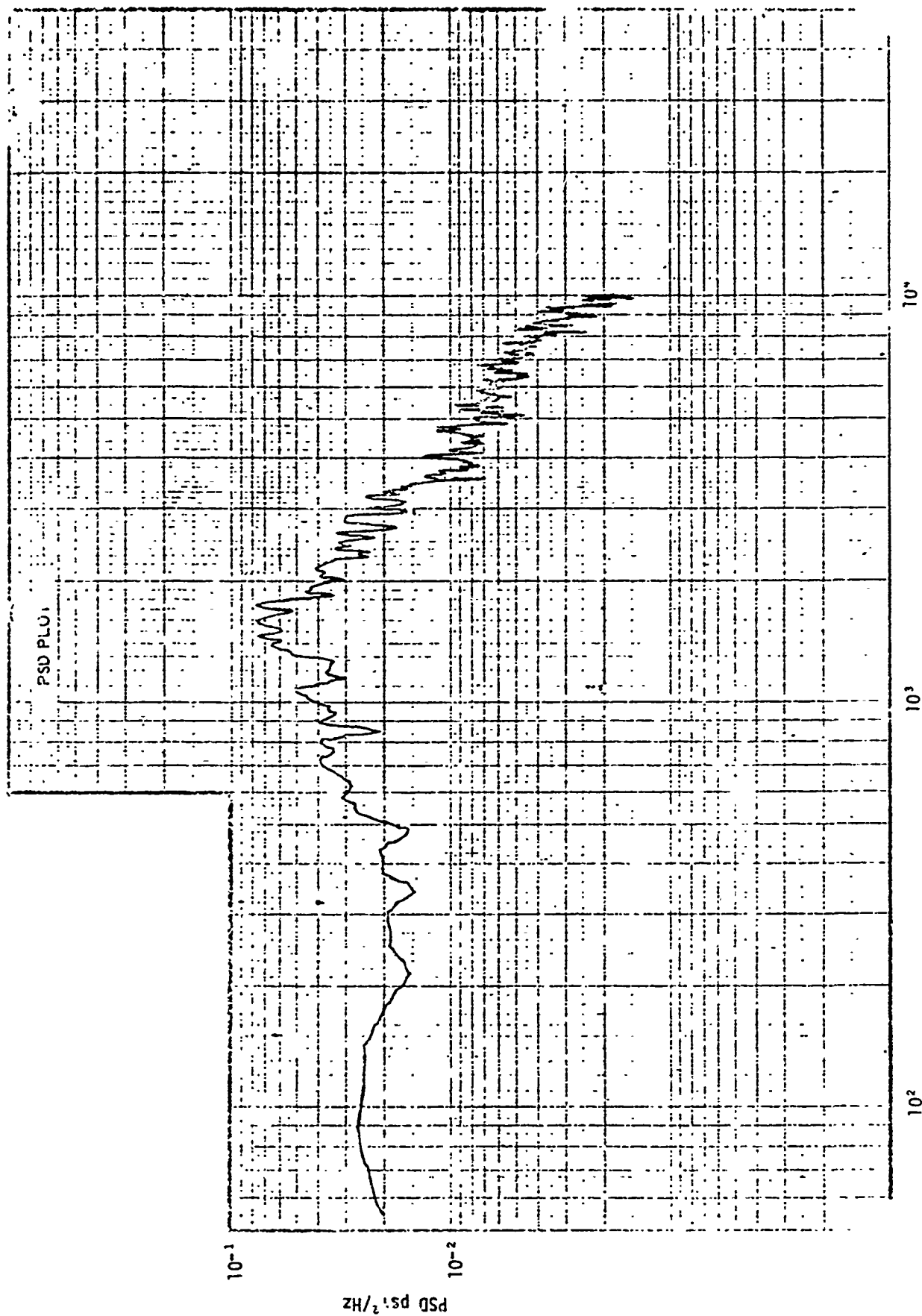


Figure 2-26.25. Pressure PSD for Run 26, Tape Position 11:52:02

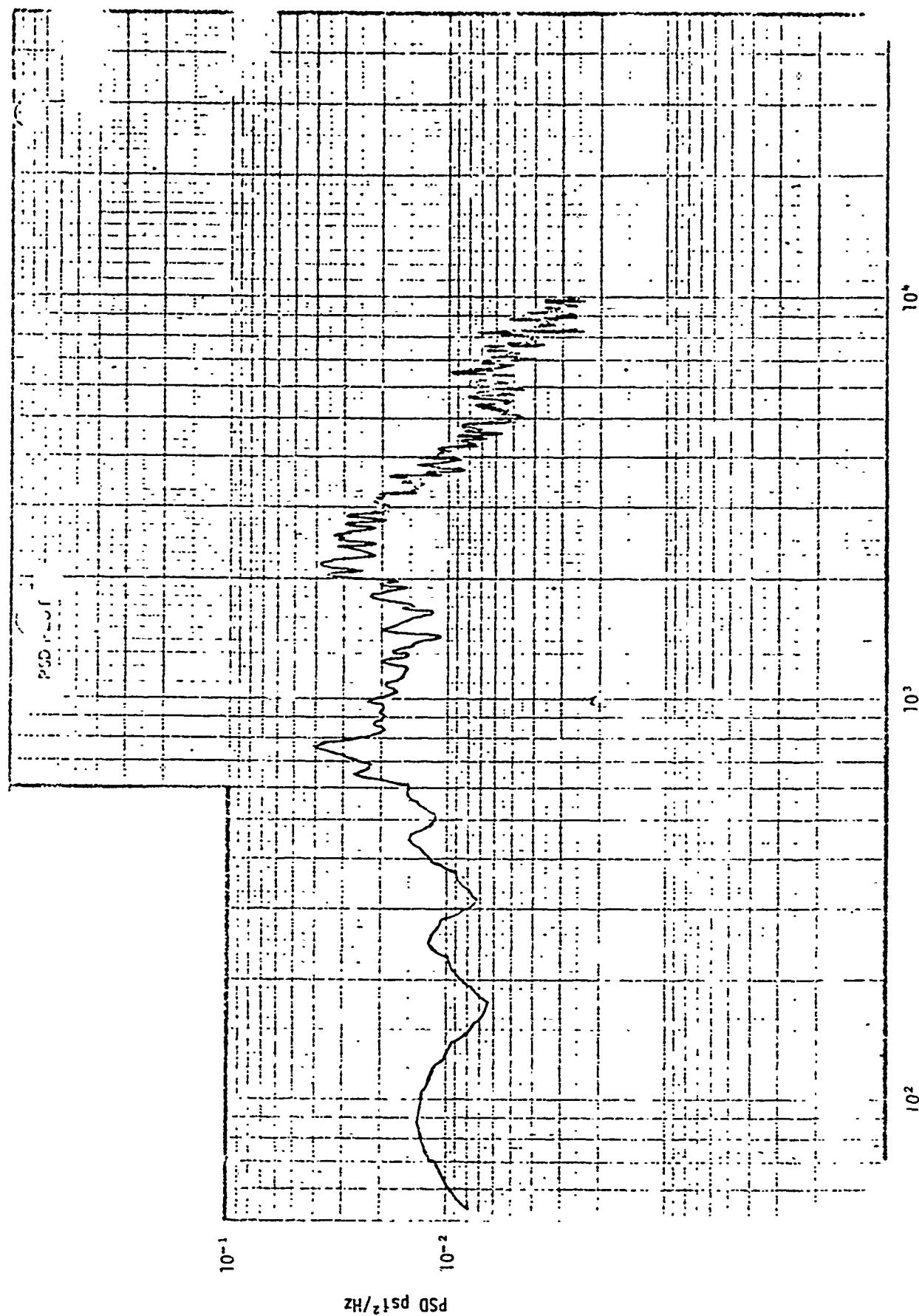


Figure 2-26.26. Pressure PSD for Run 26, Tape Position 11:52:12

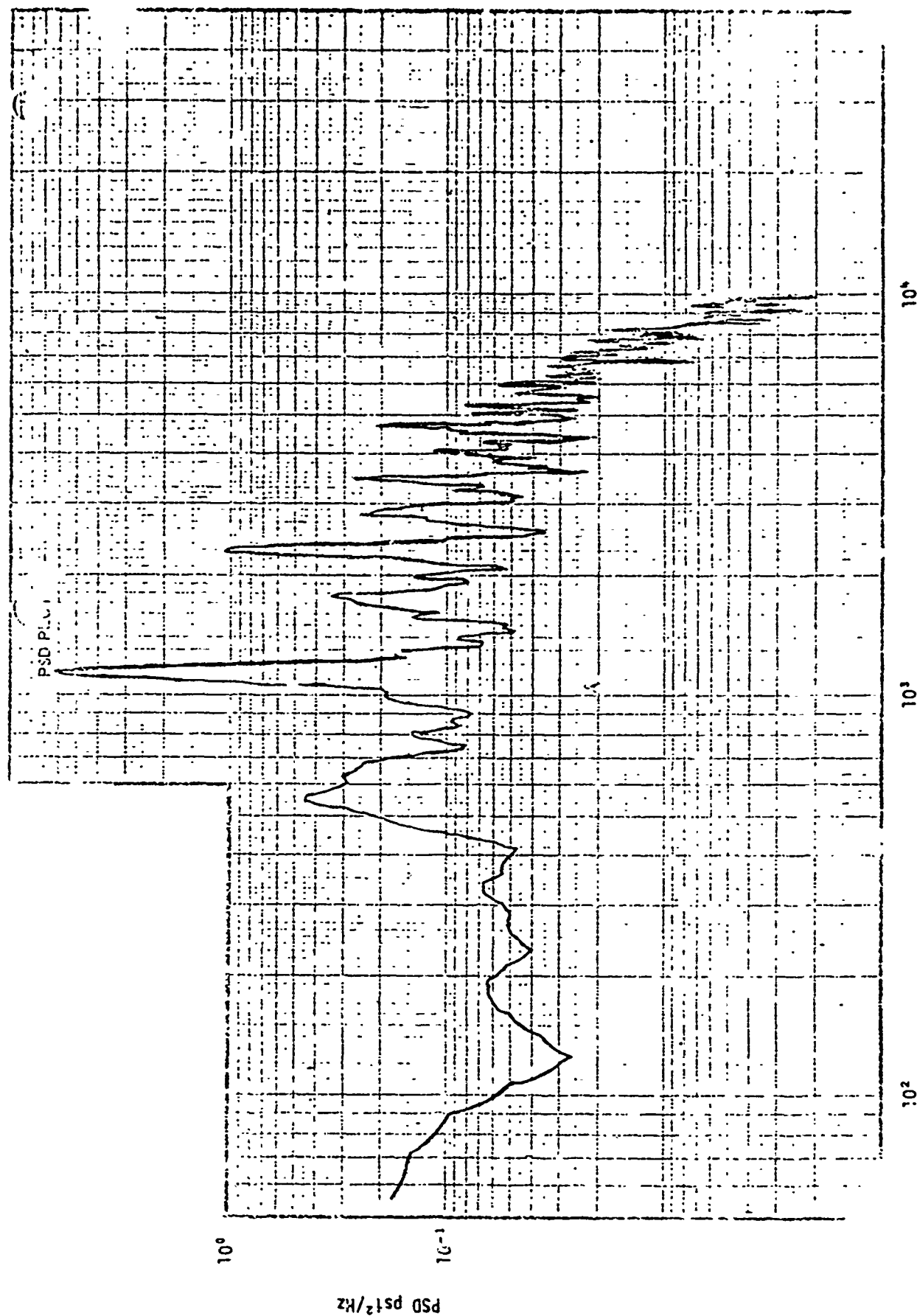


Figure 2-26.27. Pressure PSD for Run 27, Tape Position 14:19:20.5

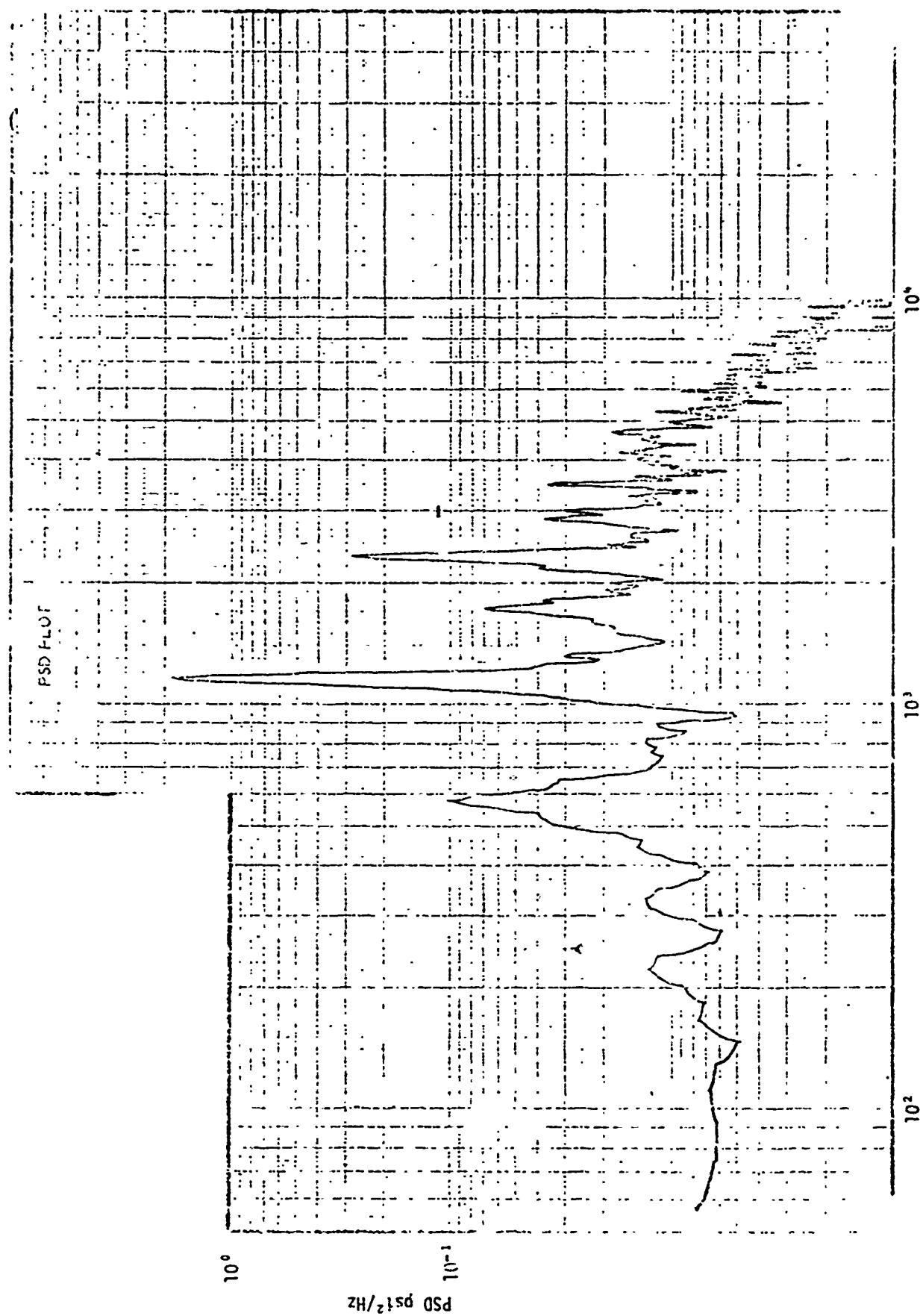


Figure 2-26.28. Pressure PSD for Run 28, Tape Position 14:20:16

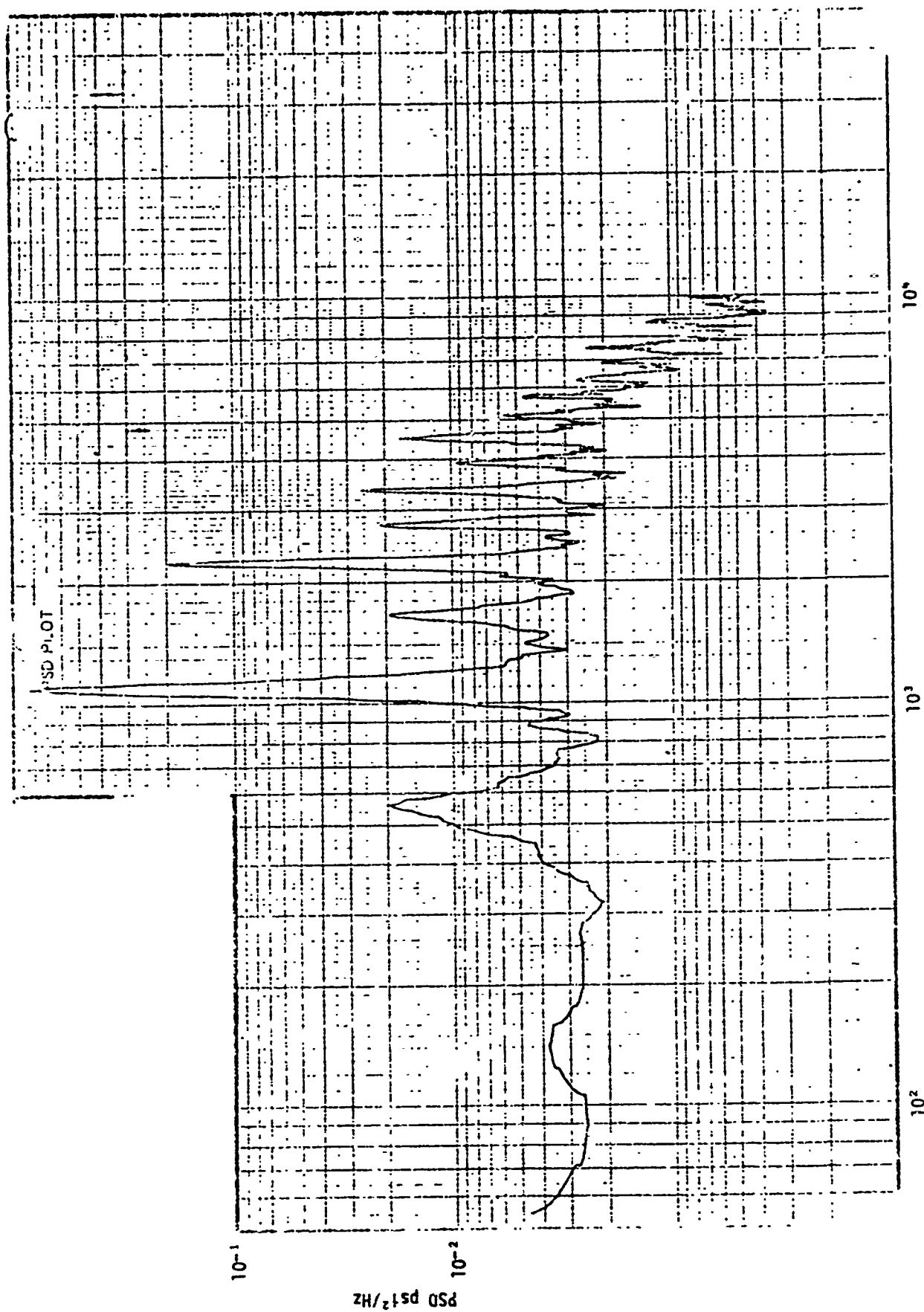


Figure 2-26.29. Pressure PSD for Run 30, Tape Position 14:32:15

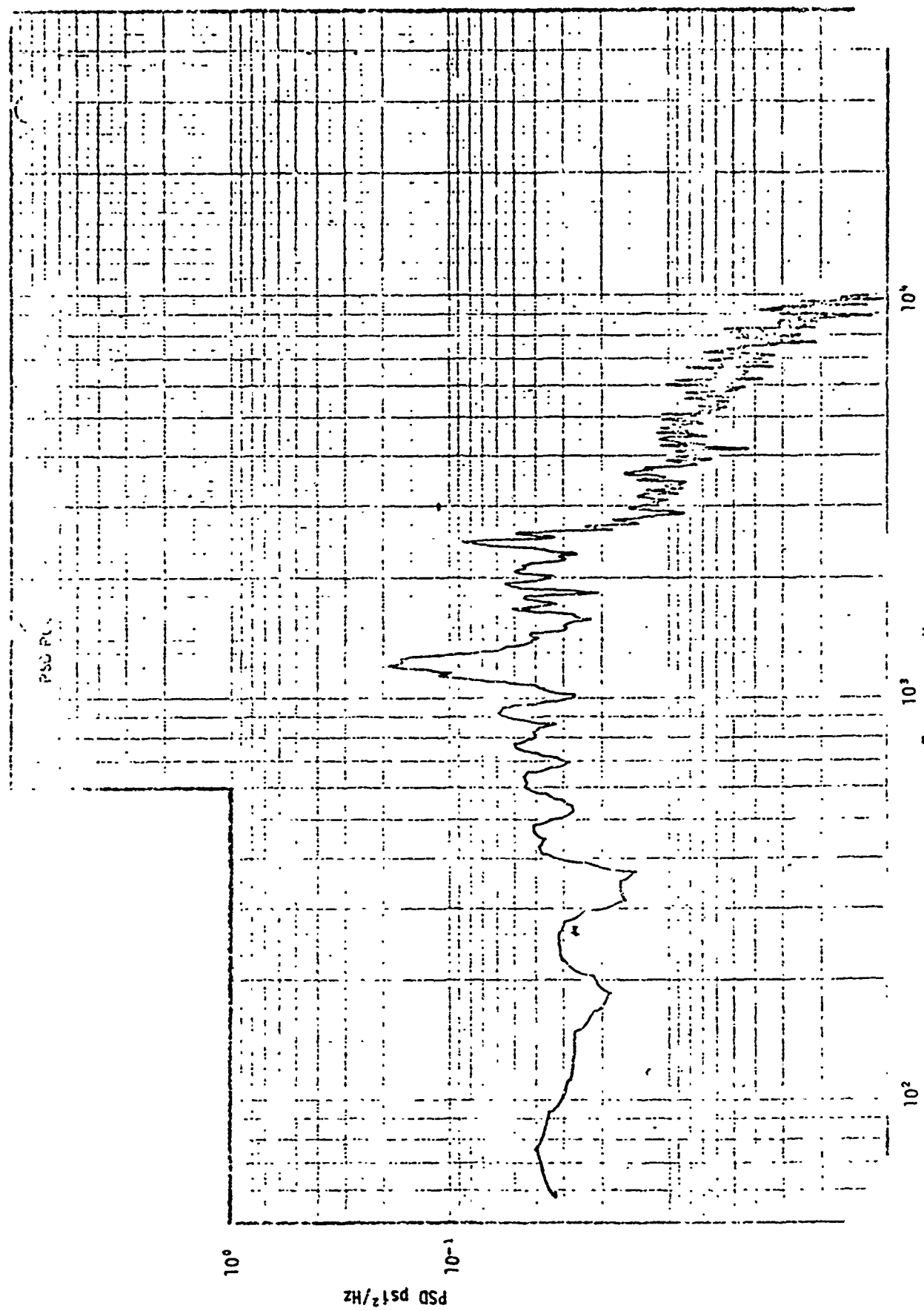


Figure 2-26.30. Pressure PSD for Run 32, Tape Position 15:18:40.2

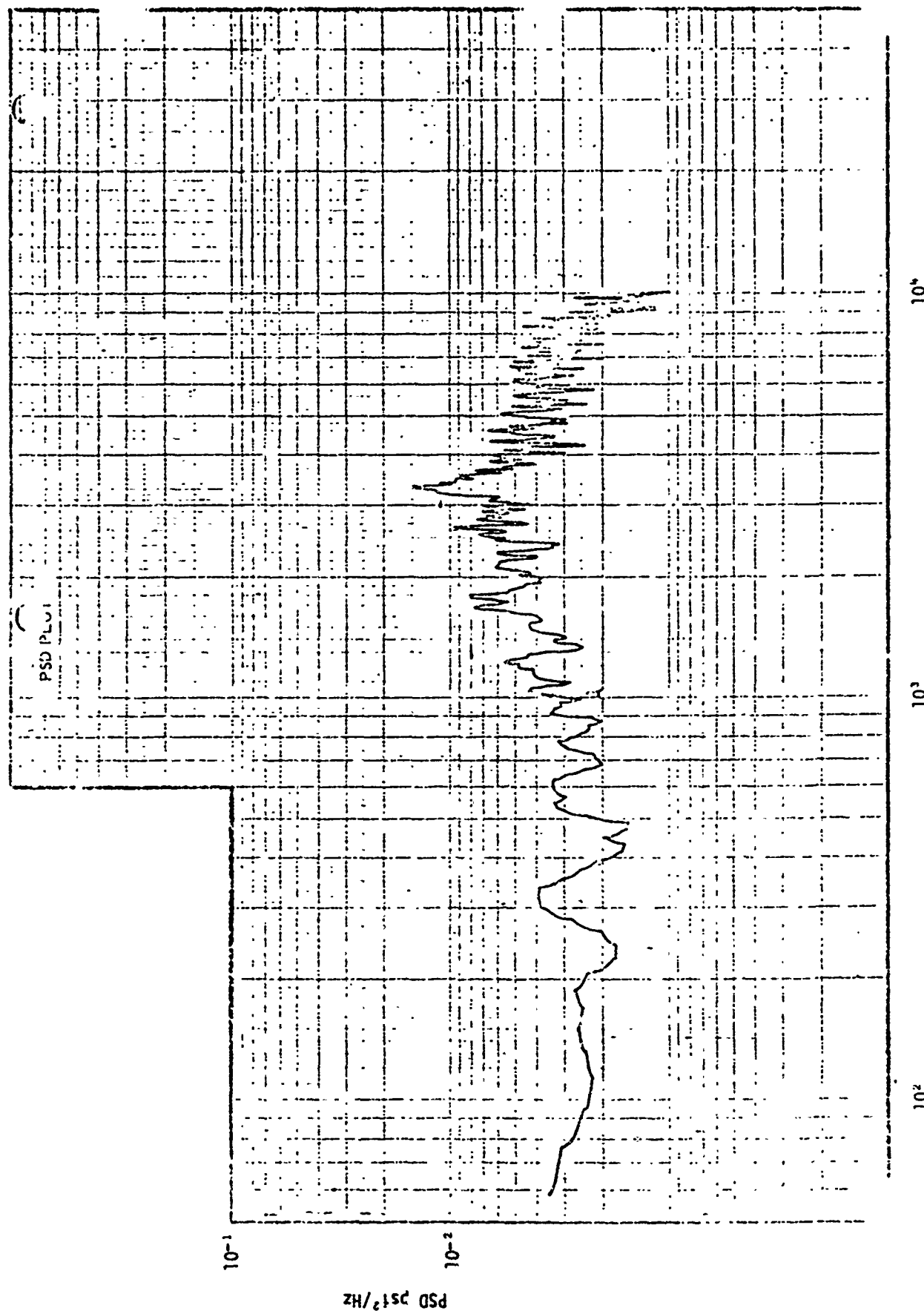


Figure 2-26.31. Pressure PSD for Run 32, Tape Position 15:18:40.6



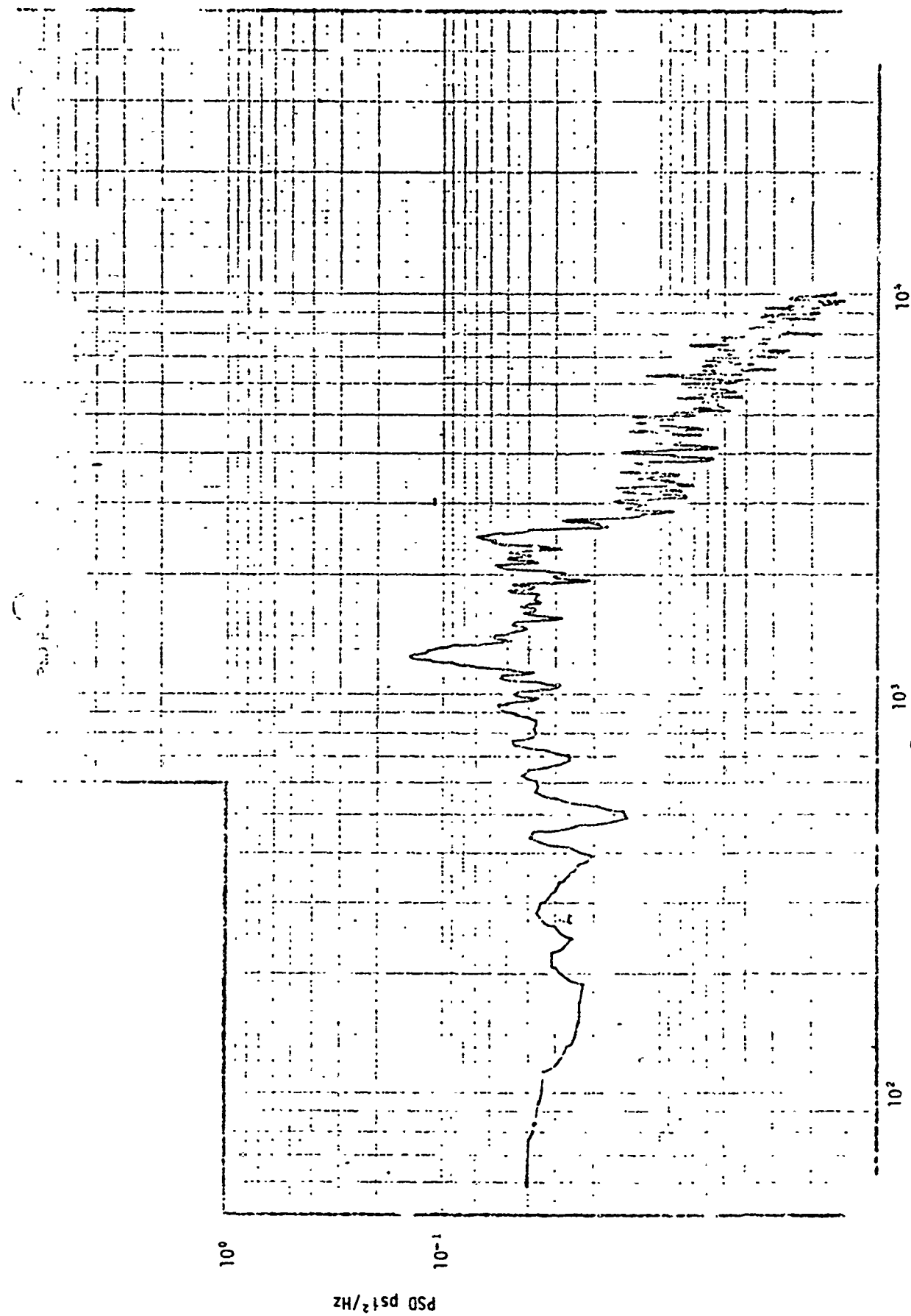


Figure 2-26.32. Pressure PSD for Run 32, Tape Position 15:18:44



Figure 2-26.32. Pressure PSD for Run 32, Tape Position 15:18:44

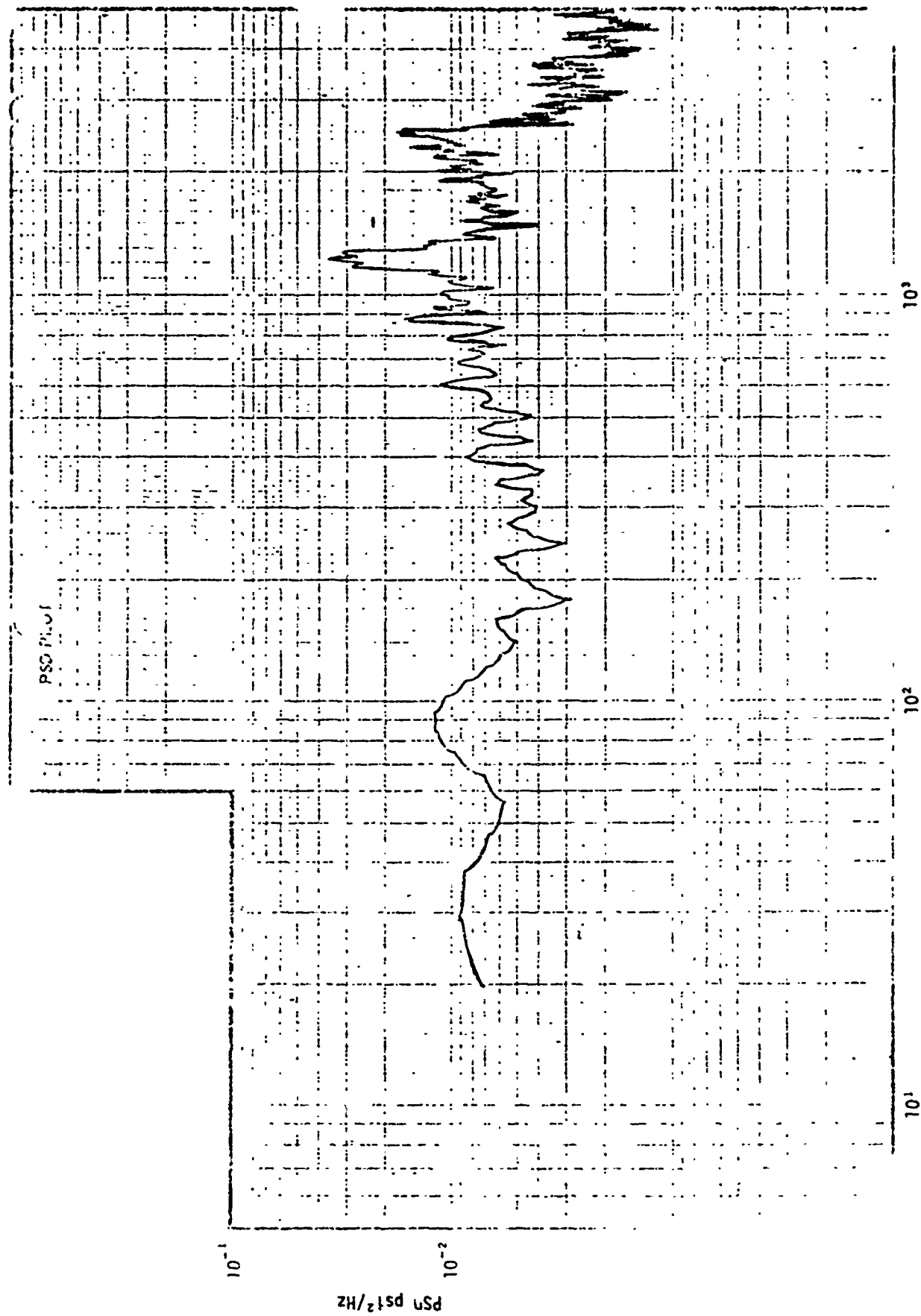


Figure 2-26.33. Pressure PSD for Run 33, Tape Position 15:19:39

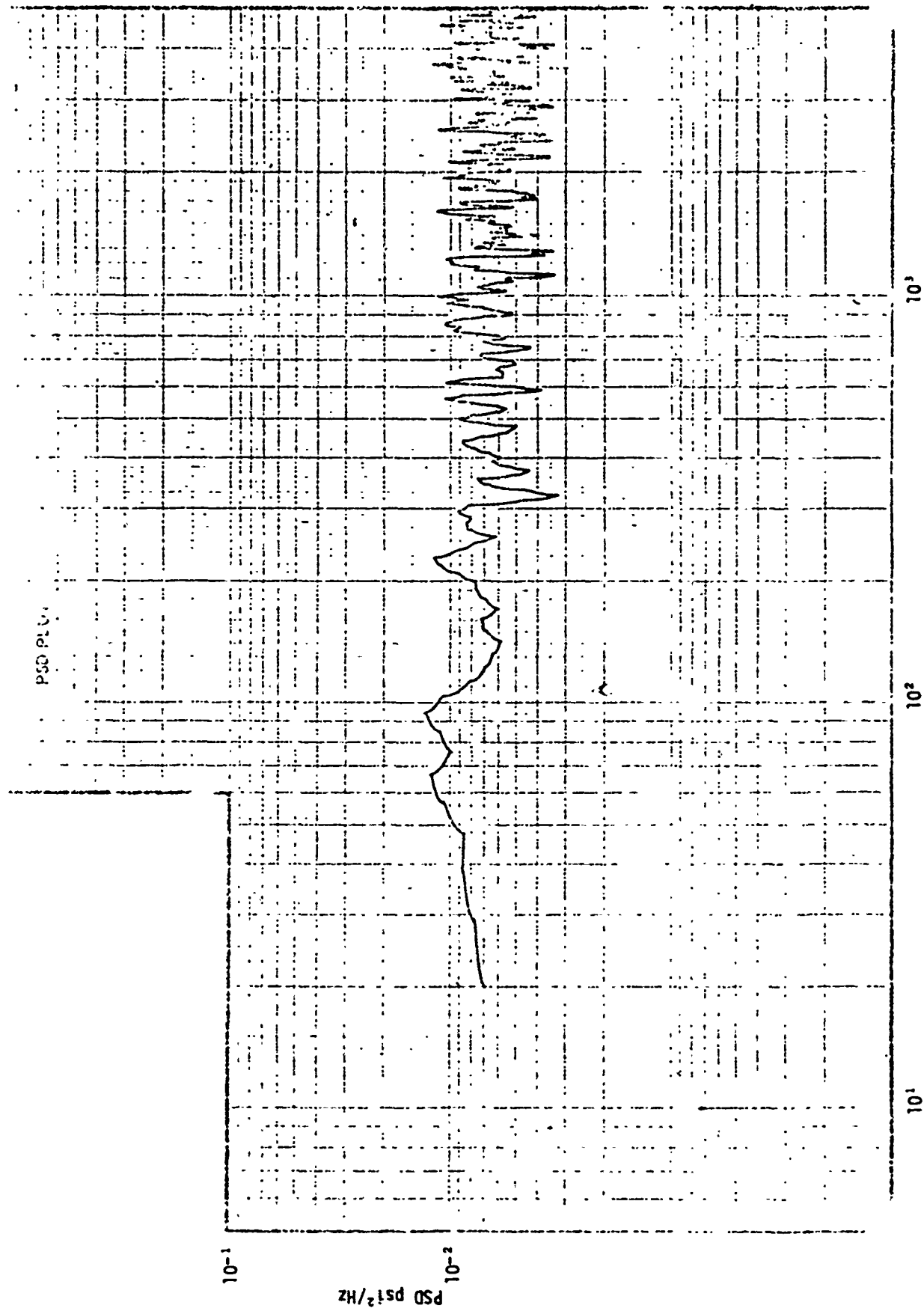


Figure 2-26.34. Pressure PSD for Run 35, Tape Position 16:59:04

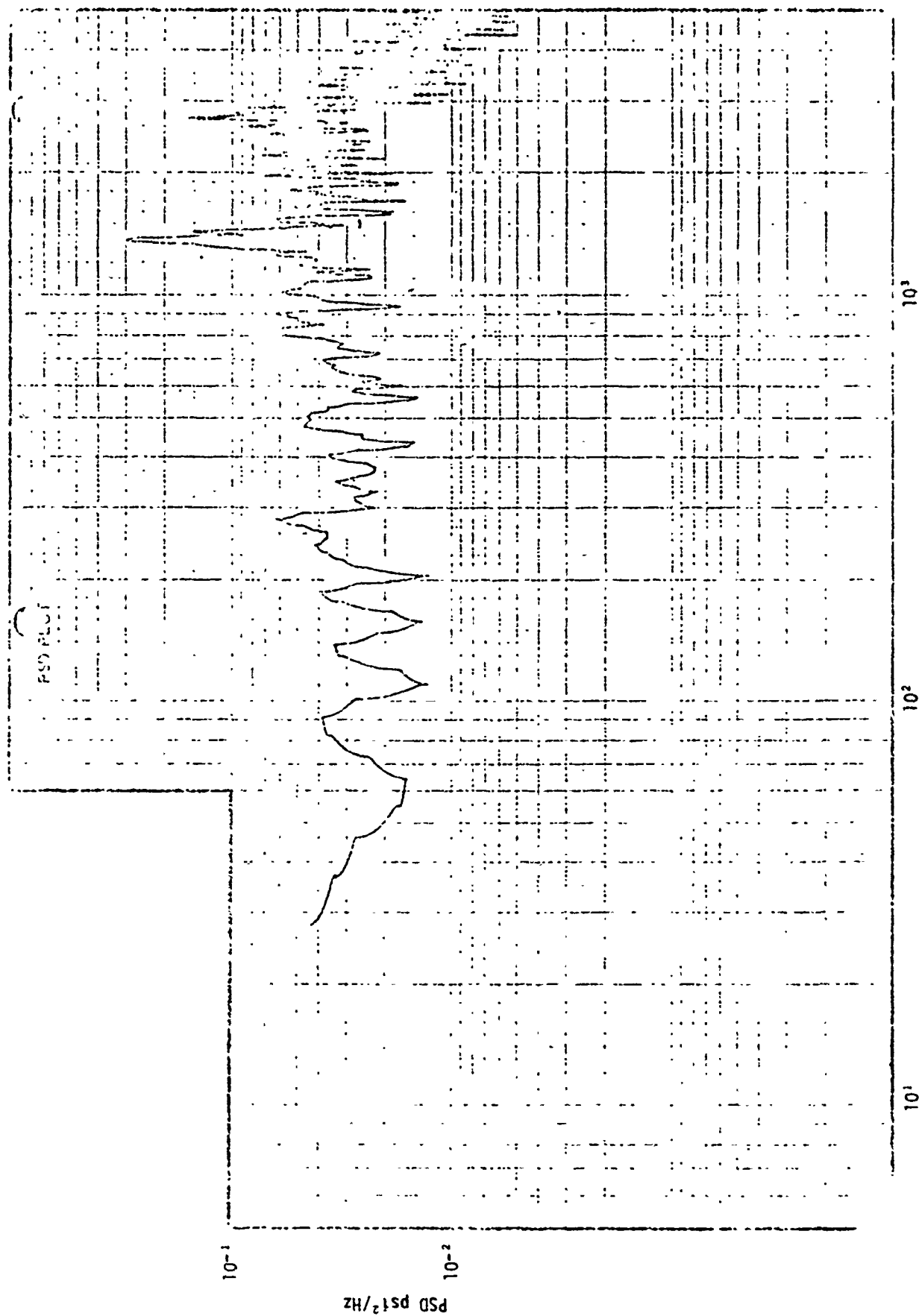


Figure 2-26.35. Pressure PSD for Run 36, Tape Position 17:09:45.25

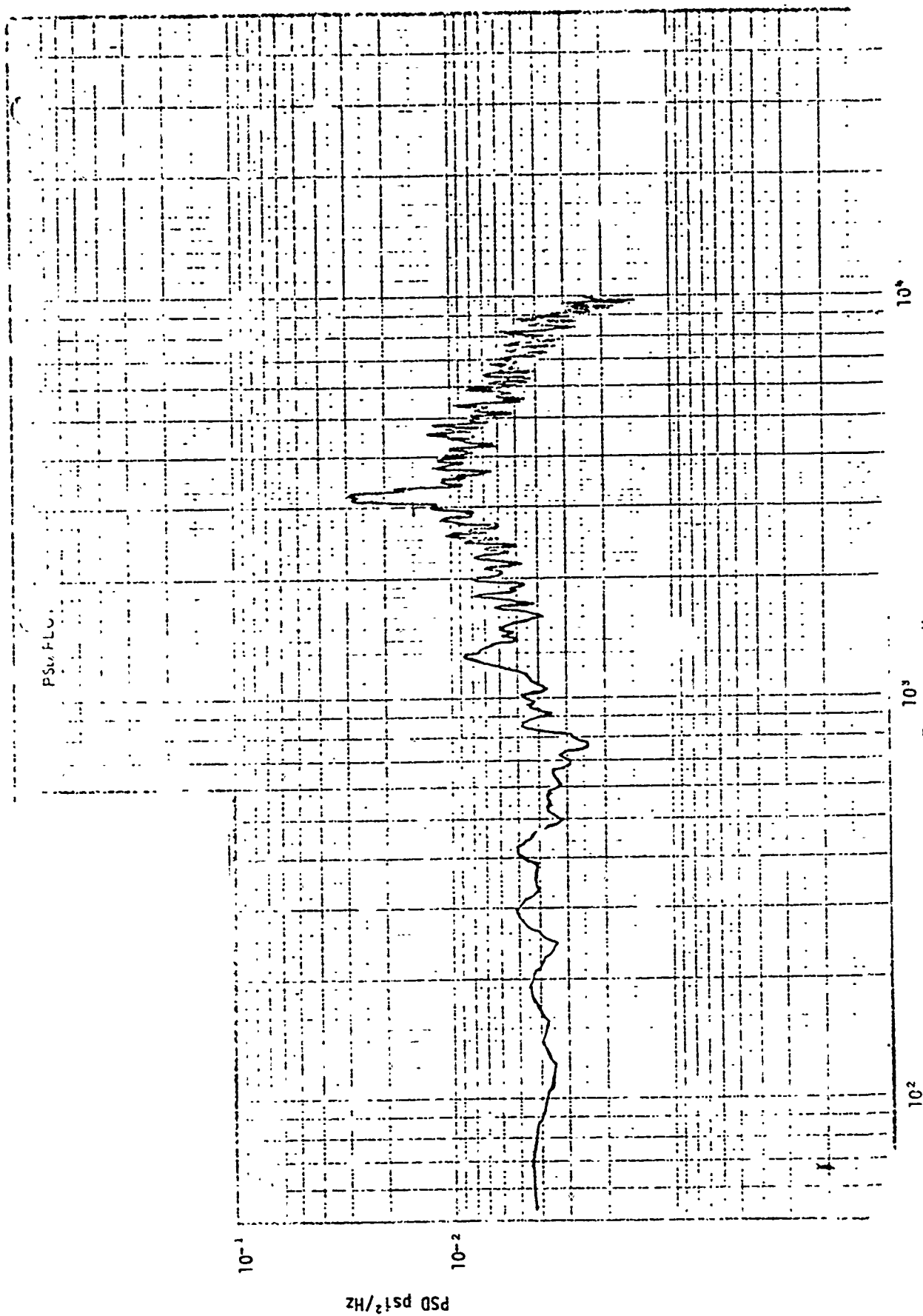


Figure 2-26.36. Pressure PSD for Run 36, Tape Position 17:09:46

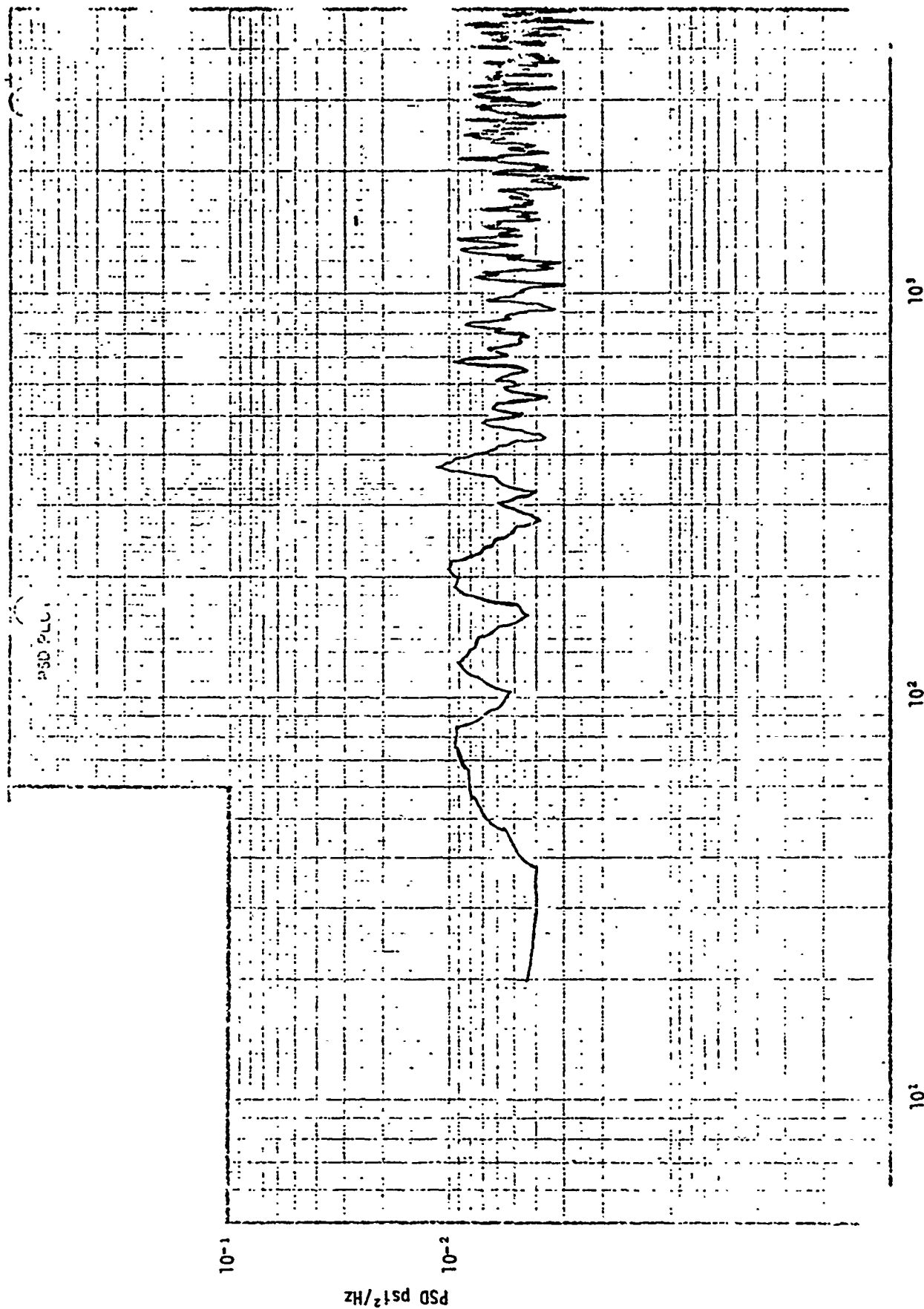


Figure 2-26.37. Pressure PSD for Run 37, Tape Position 08:34:21

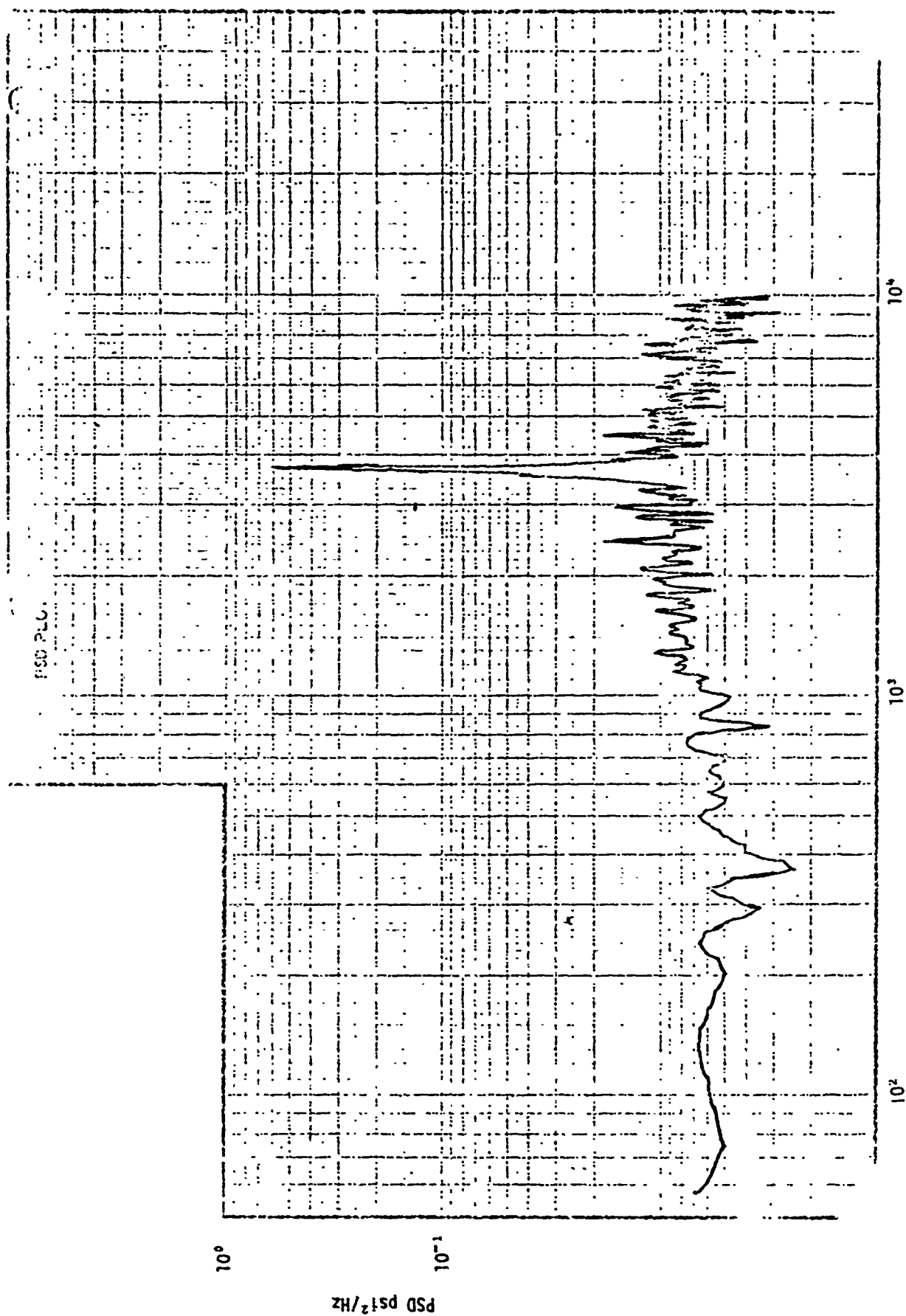


Figure 2-26.38. Pressure PSD for Run 38, Tape Position 08:45:29.4

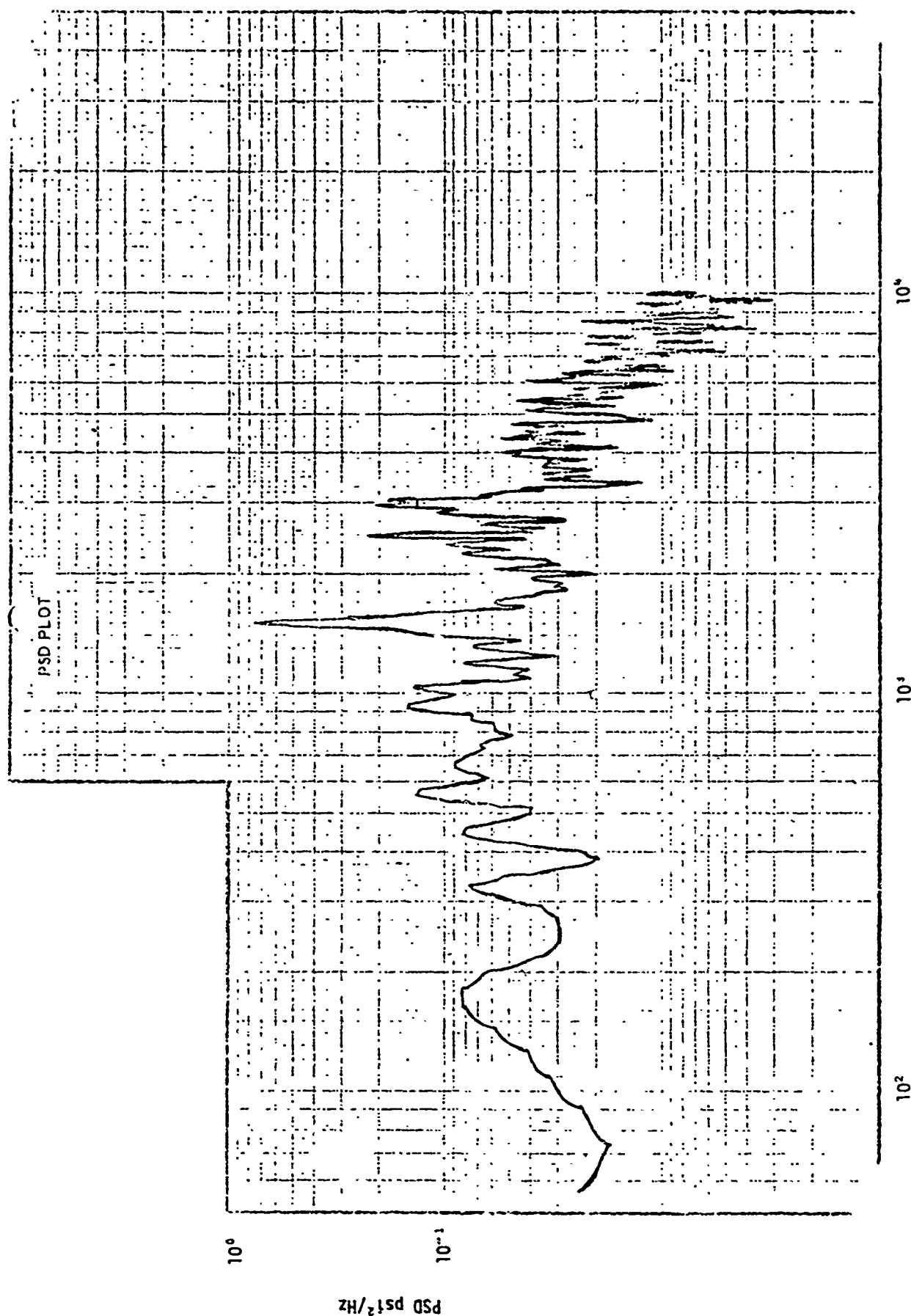


Figure 2-26.39. Pressure PSD for Run 38, Tape Position 08:45:32.3

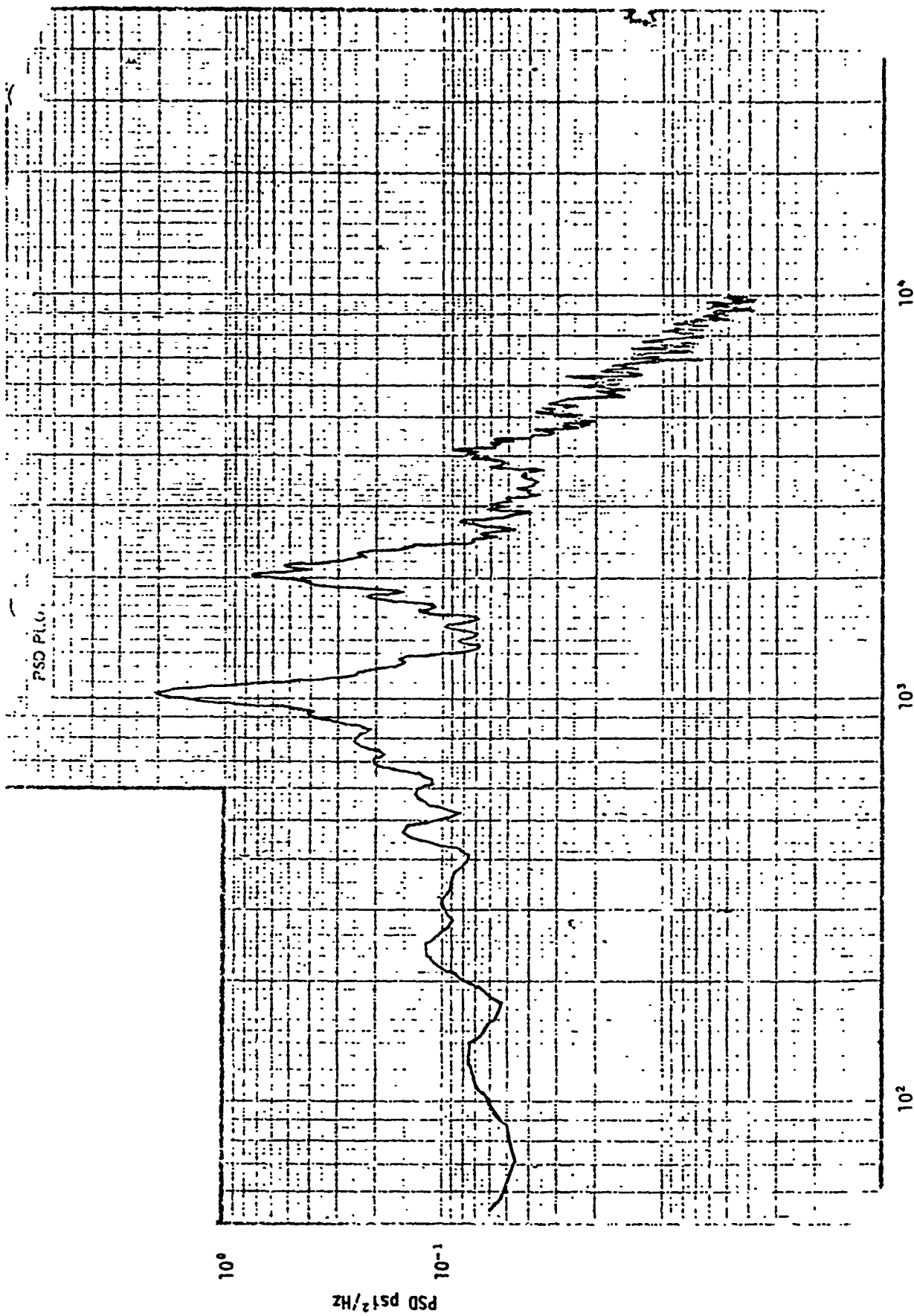


Figure 2-26.40. Pressure PSD for Run 42, Tape Position 11:50:25



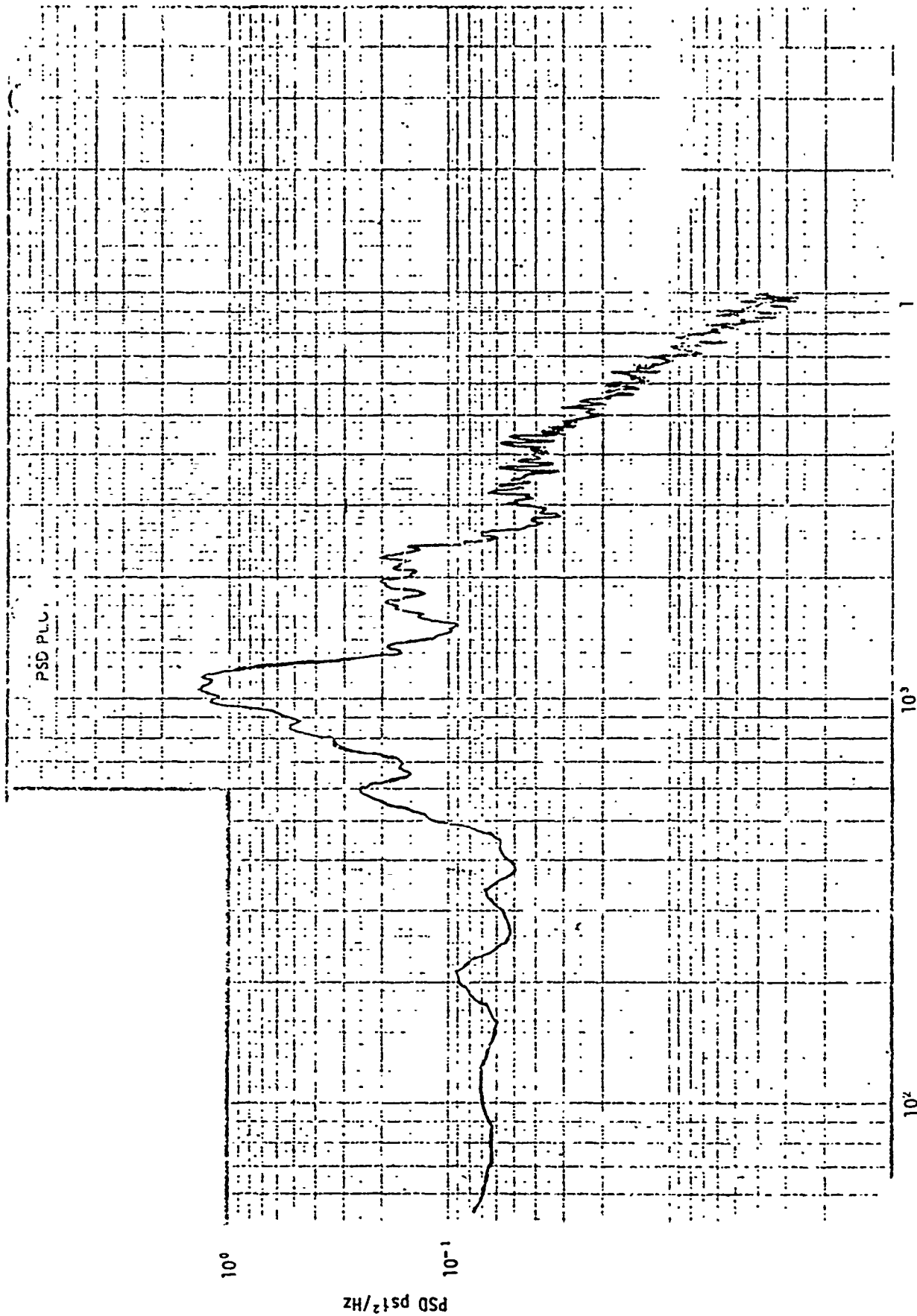


Figure 2-26.41. Pressure PSD for Run 42, Tape Position 11:50:31

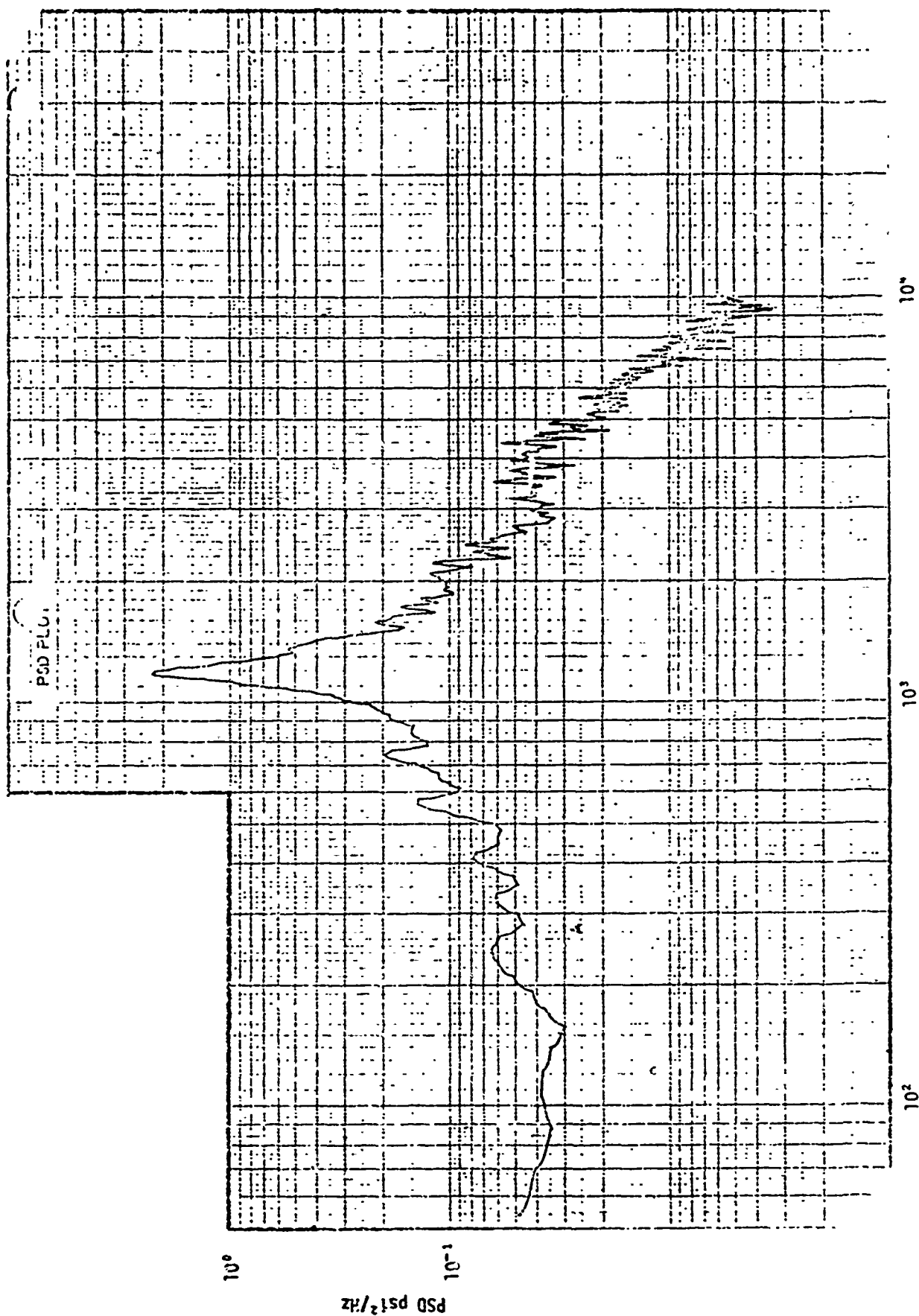


Figure 2-26.42. Pressure PSD for Run 42, Tape Position 11:50:39

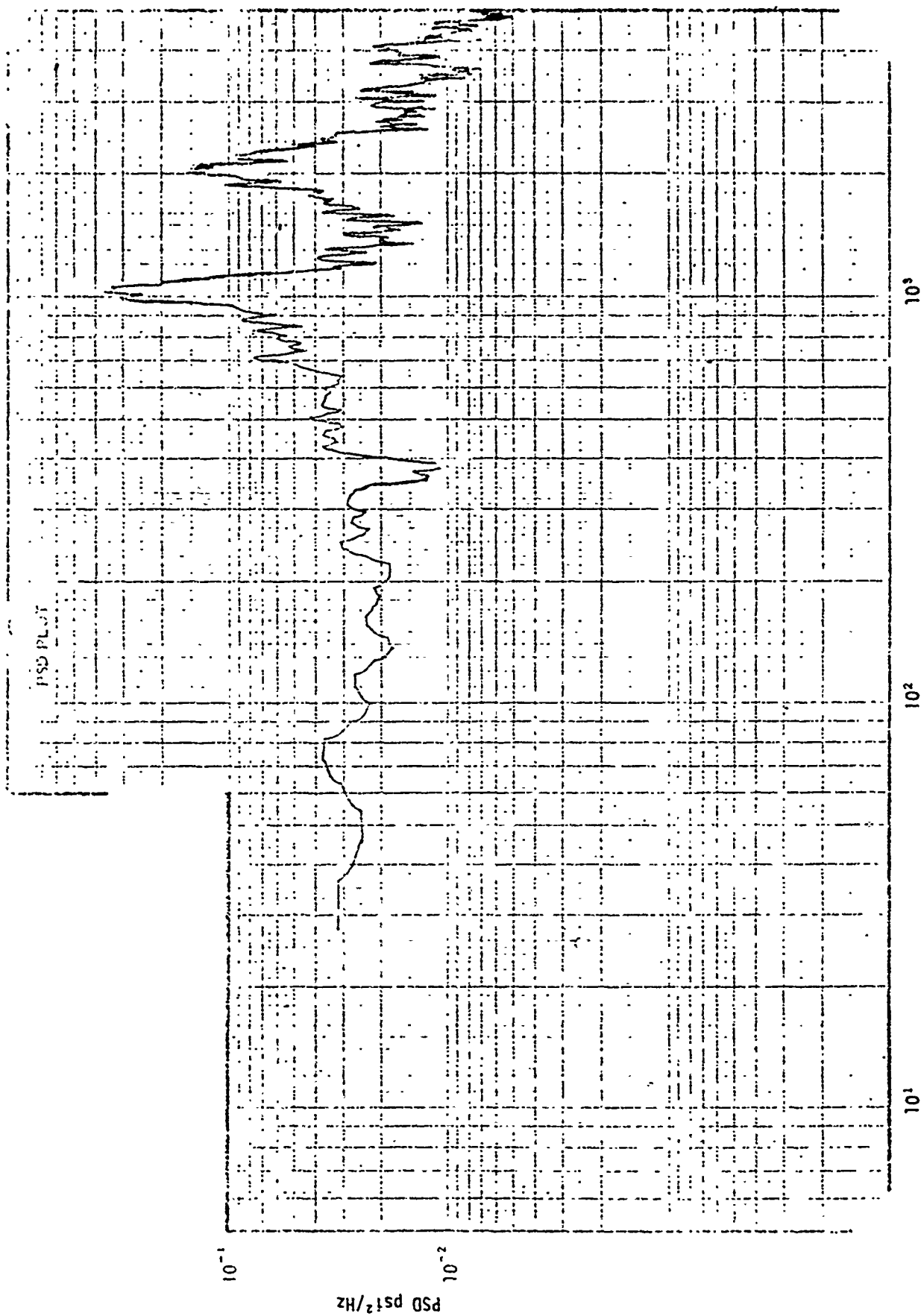


Figure 2-26.43. Pressure PSD for Run 43, Tape Position 11:51:52

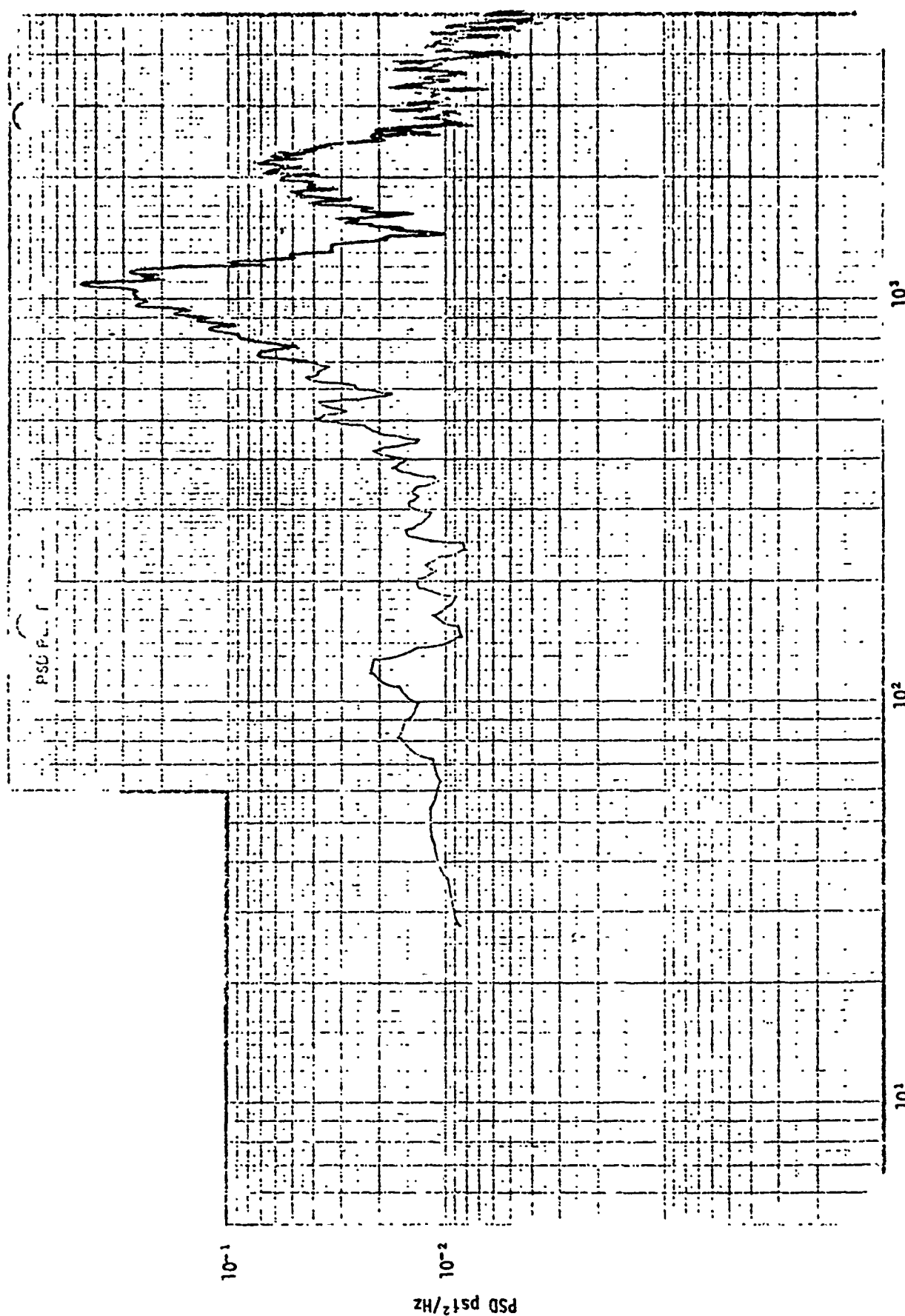


Figure 2-26.44. Pressure PSD for Run 43, Tape Position 11:52:01

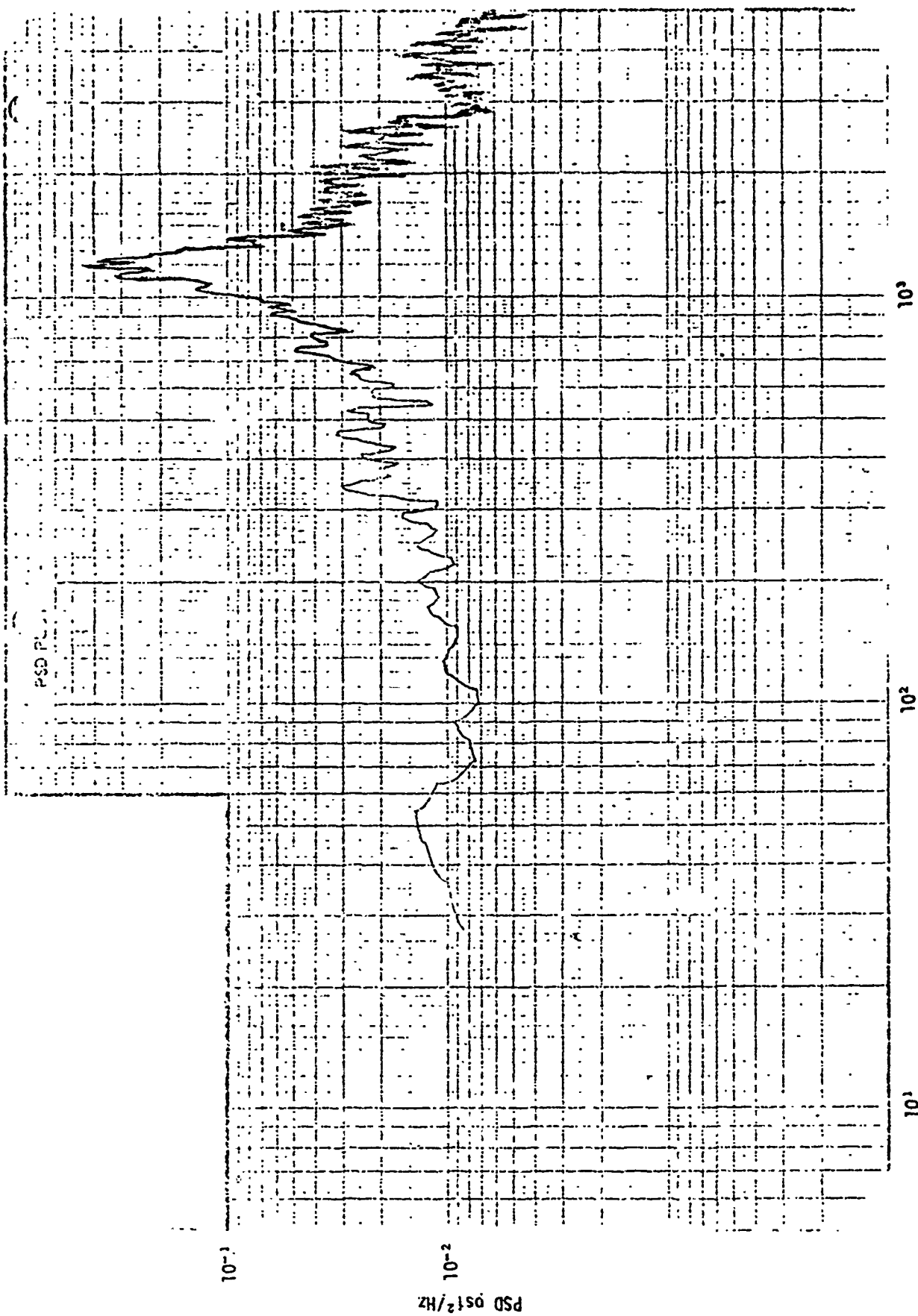


Figure 2-26.45. Pressure PSD for Run 43, Tape Position 11:52:10

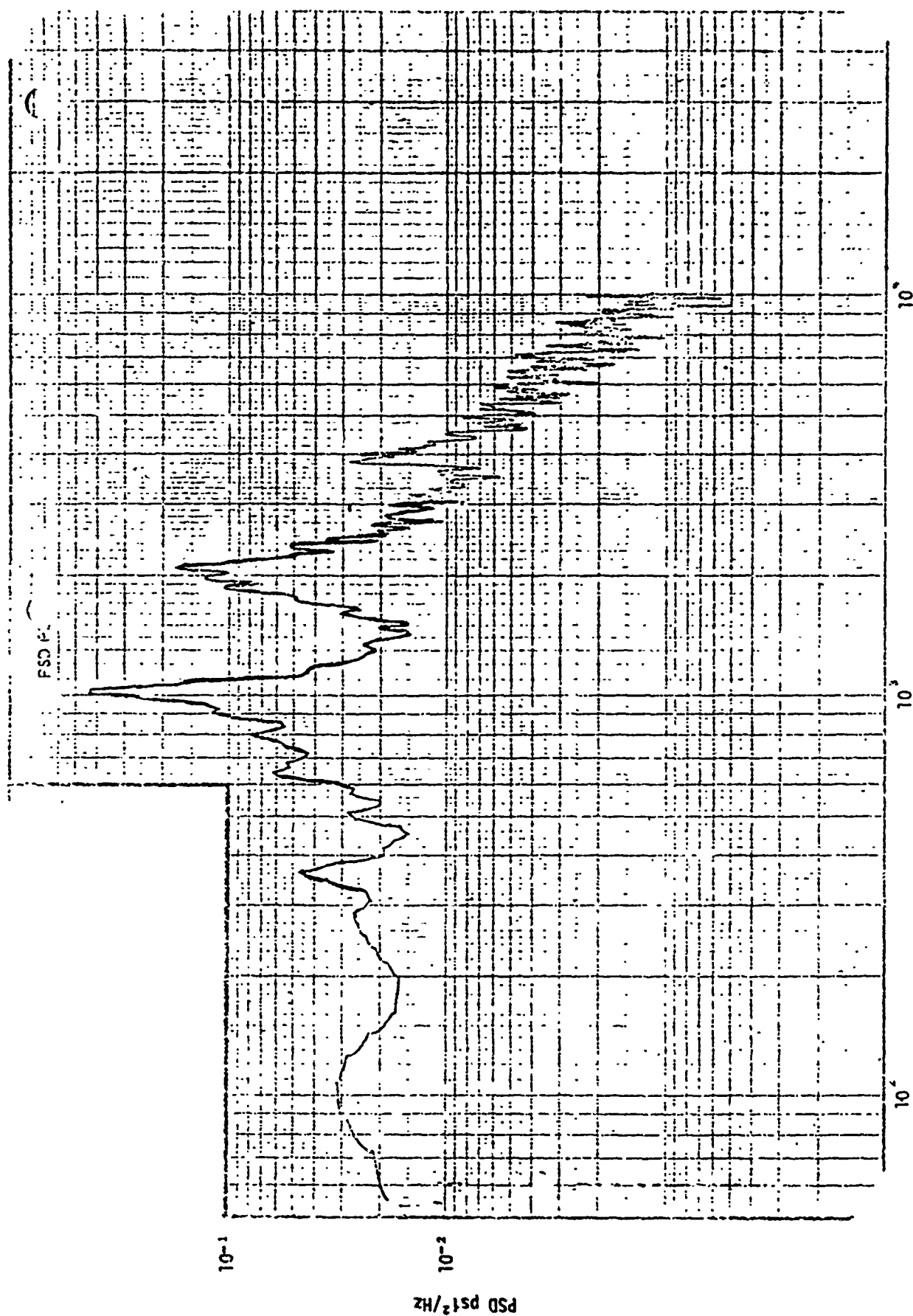


Figure 2-26.46. Pressure PSD for Run 44, Tape Position 12:04:51

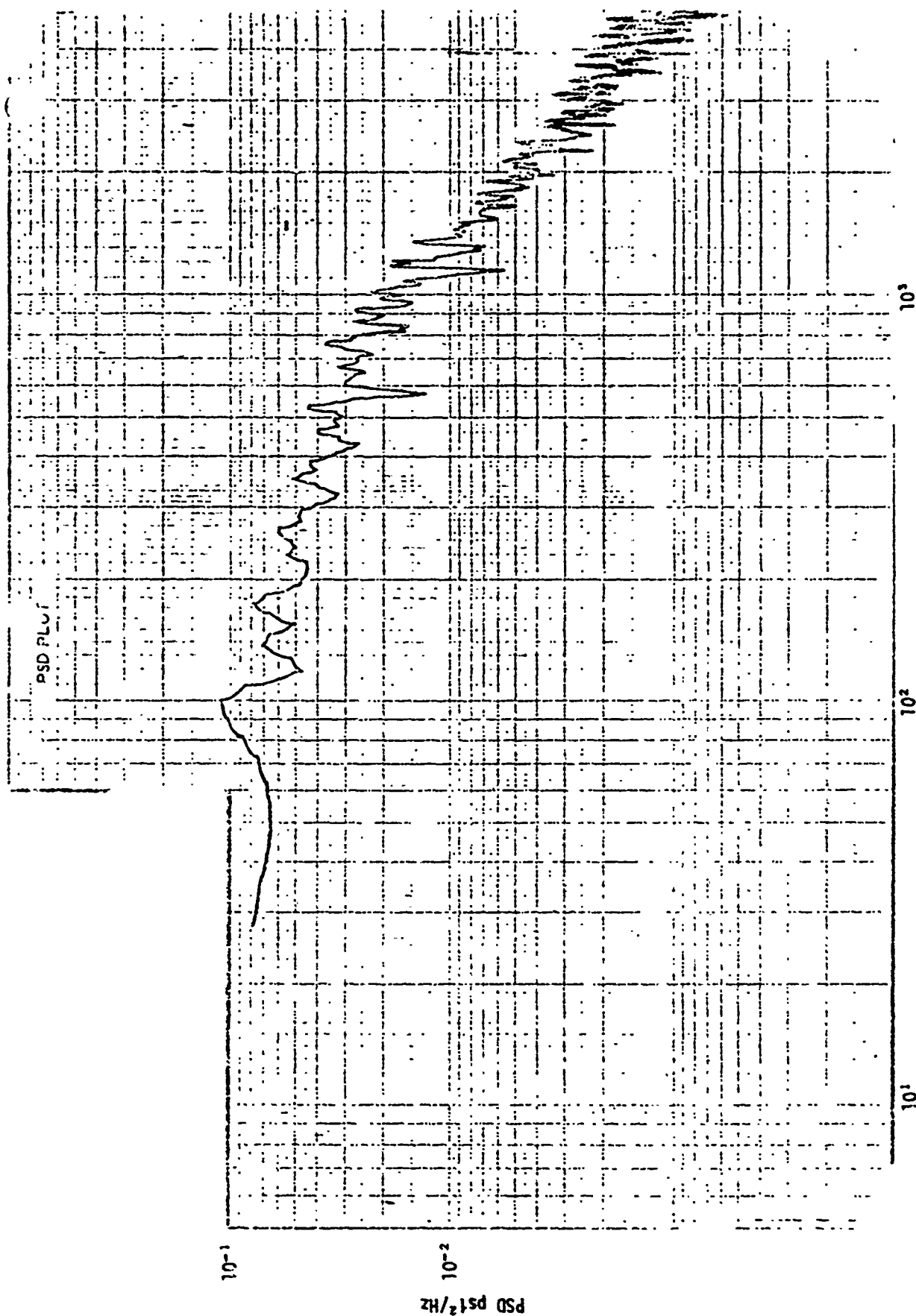


Figure 2-26.47. Pressure PSD for Run 45, Tape Position 12:06:29

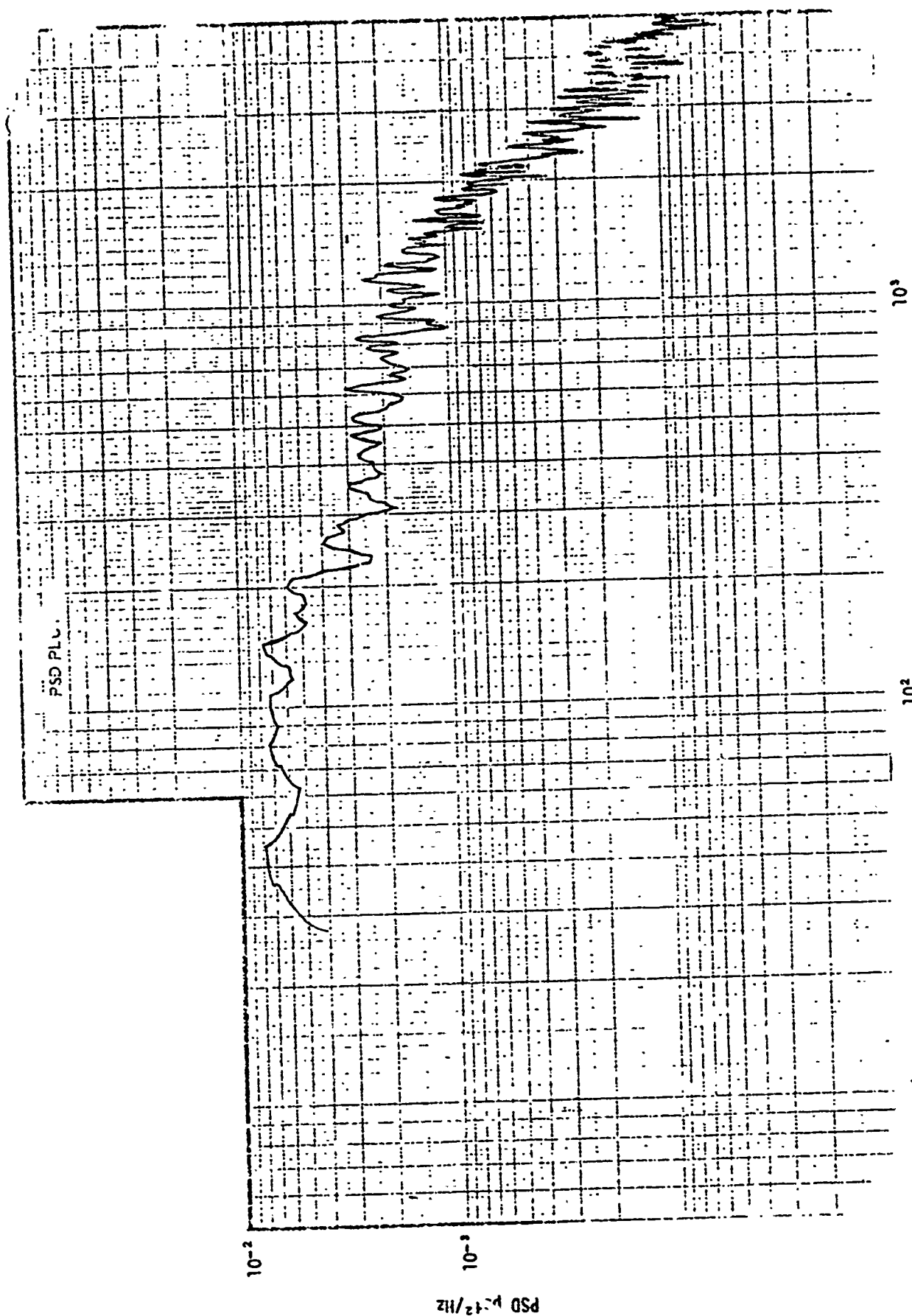


Figure 2-26.48. Pressure PSD for Run 46, Tape Position 15:19:53



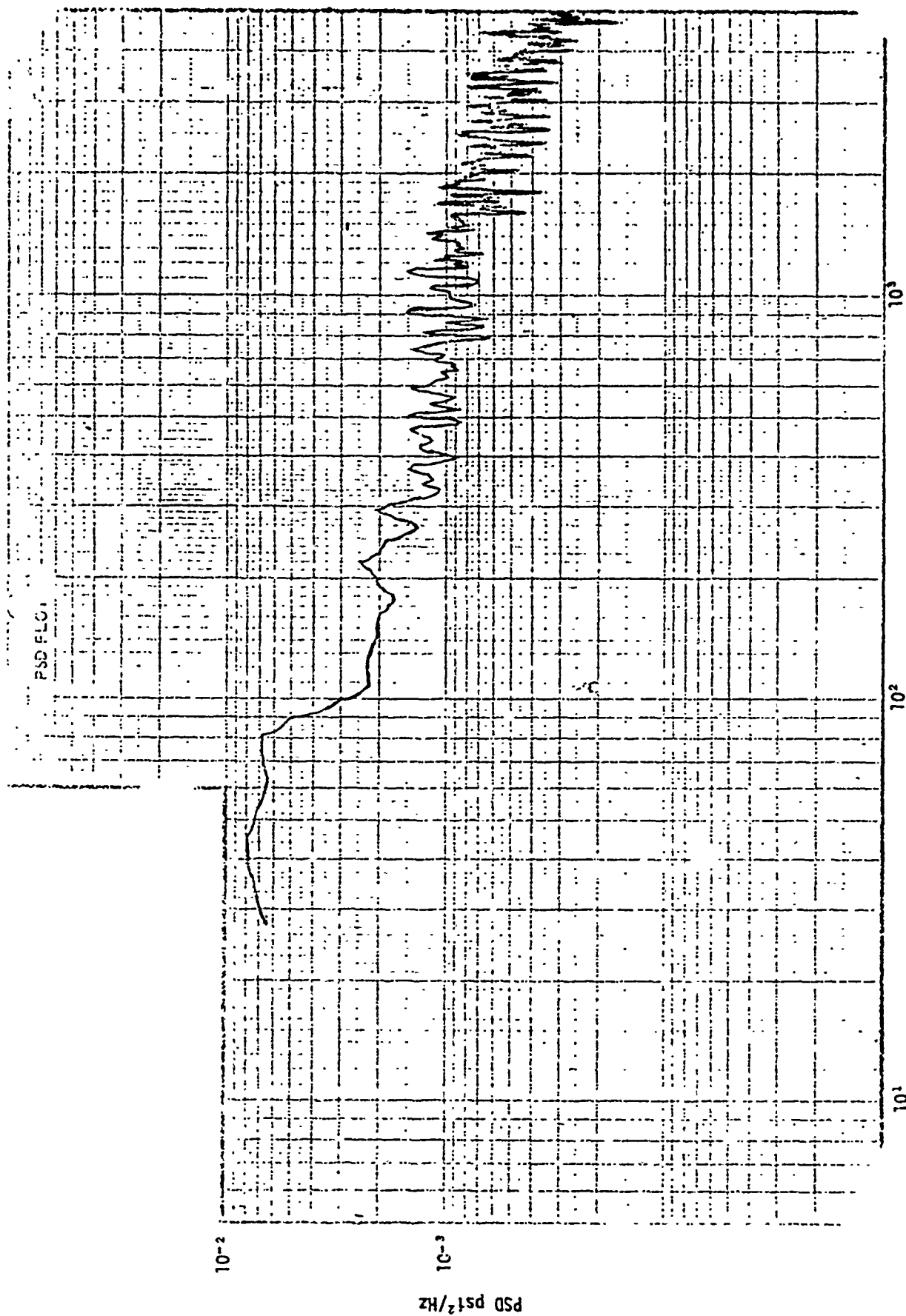


Figure 2-26.49. Pressure PSD for Run 47, Tape Position 16:26:27

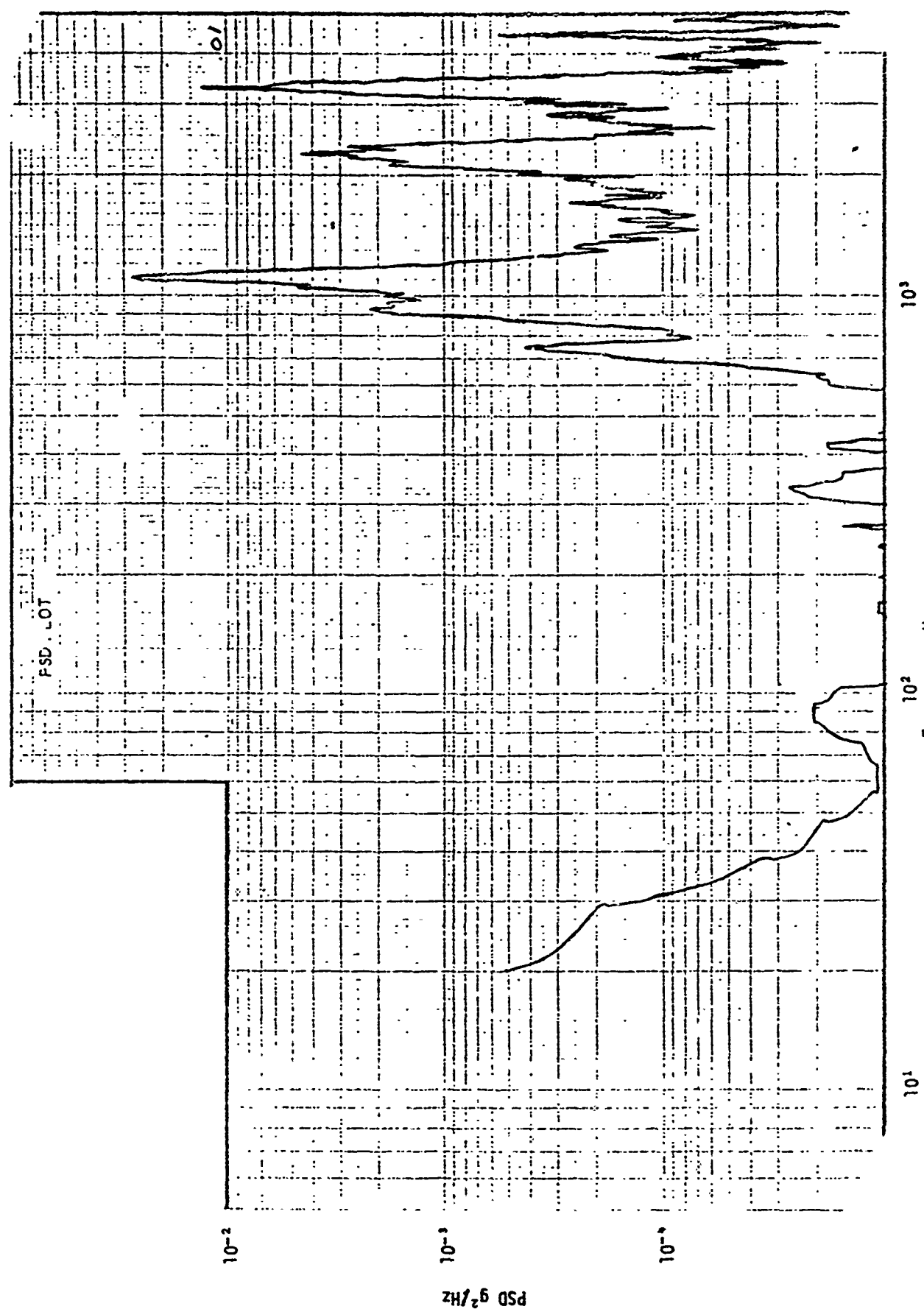


Figure 2-27.01. Accelerometer PSD for Run 2, Tape Position 19:35:07

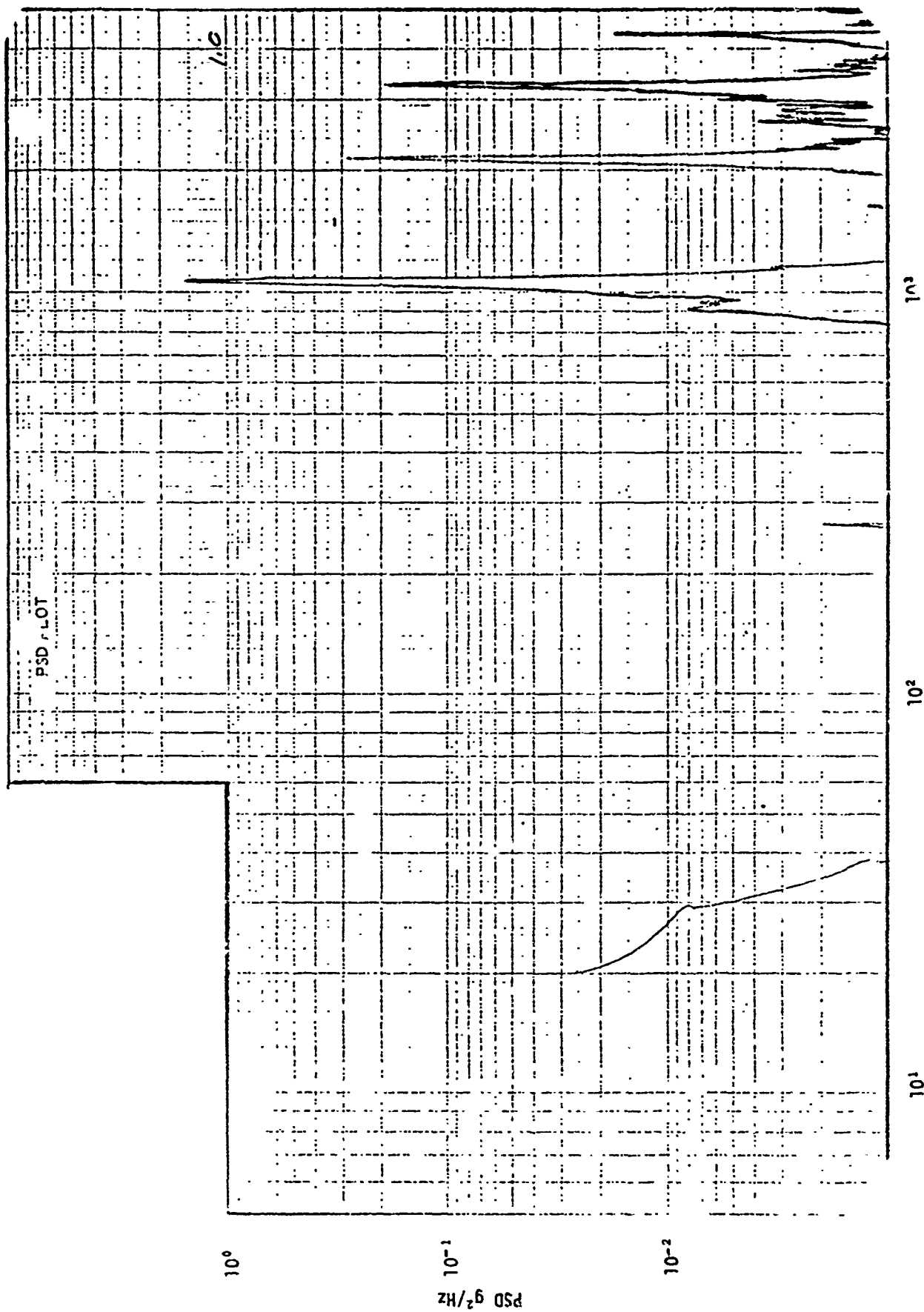


Figure 2-27.02. Accelerometer PSD for Run 5, Tape Position 01:50:36

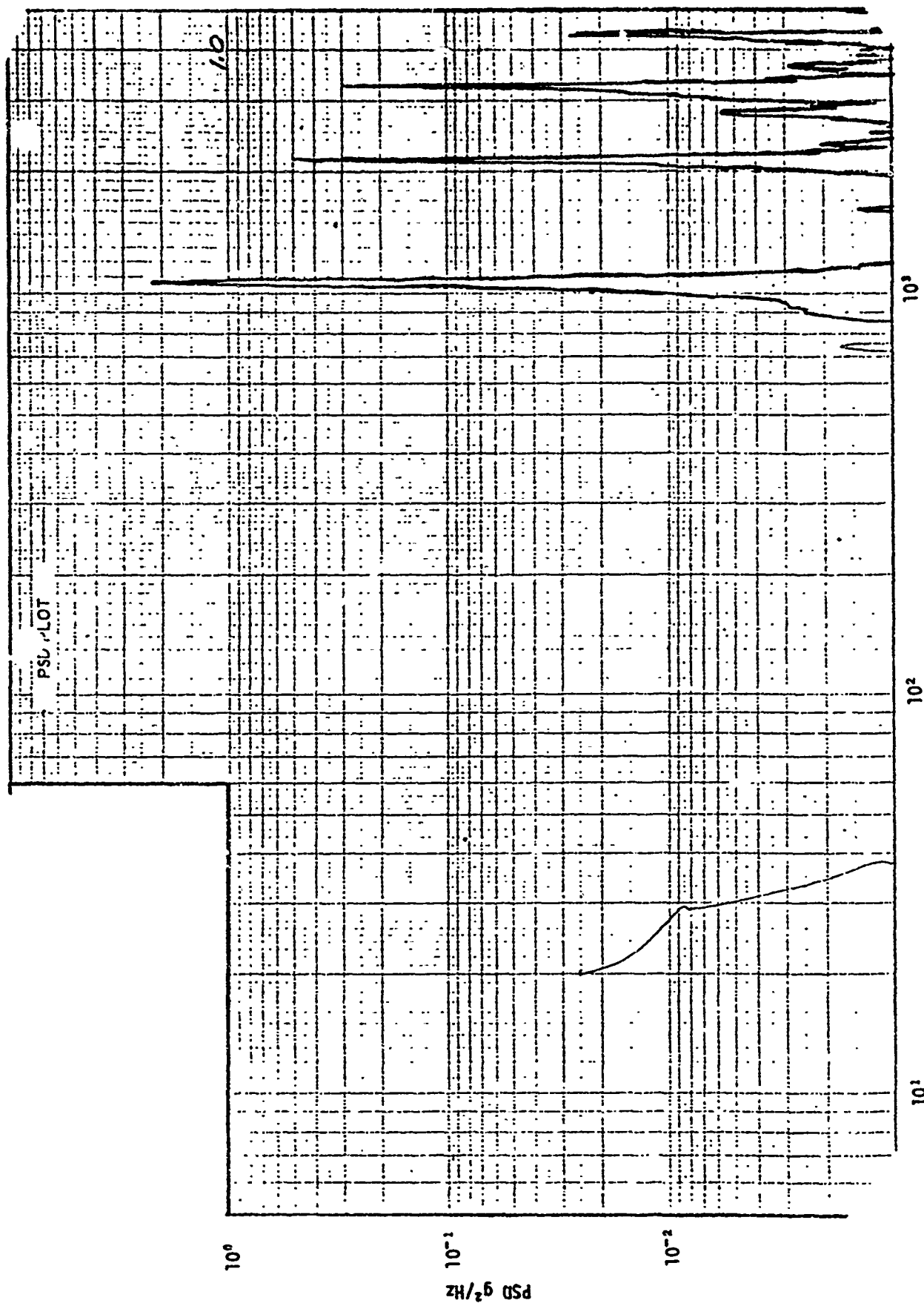


Figure 2-27.03. Accelerometer PSD for Run 6, Tape Position 04:45:55

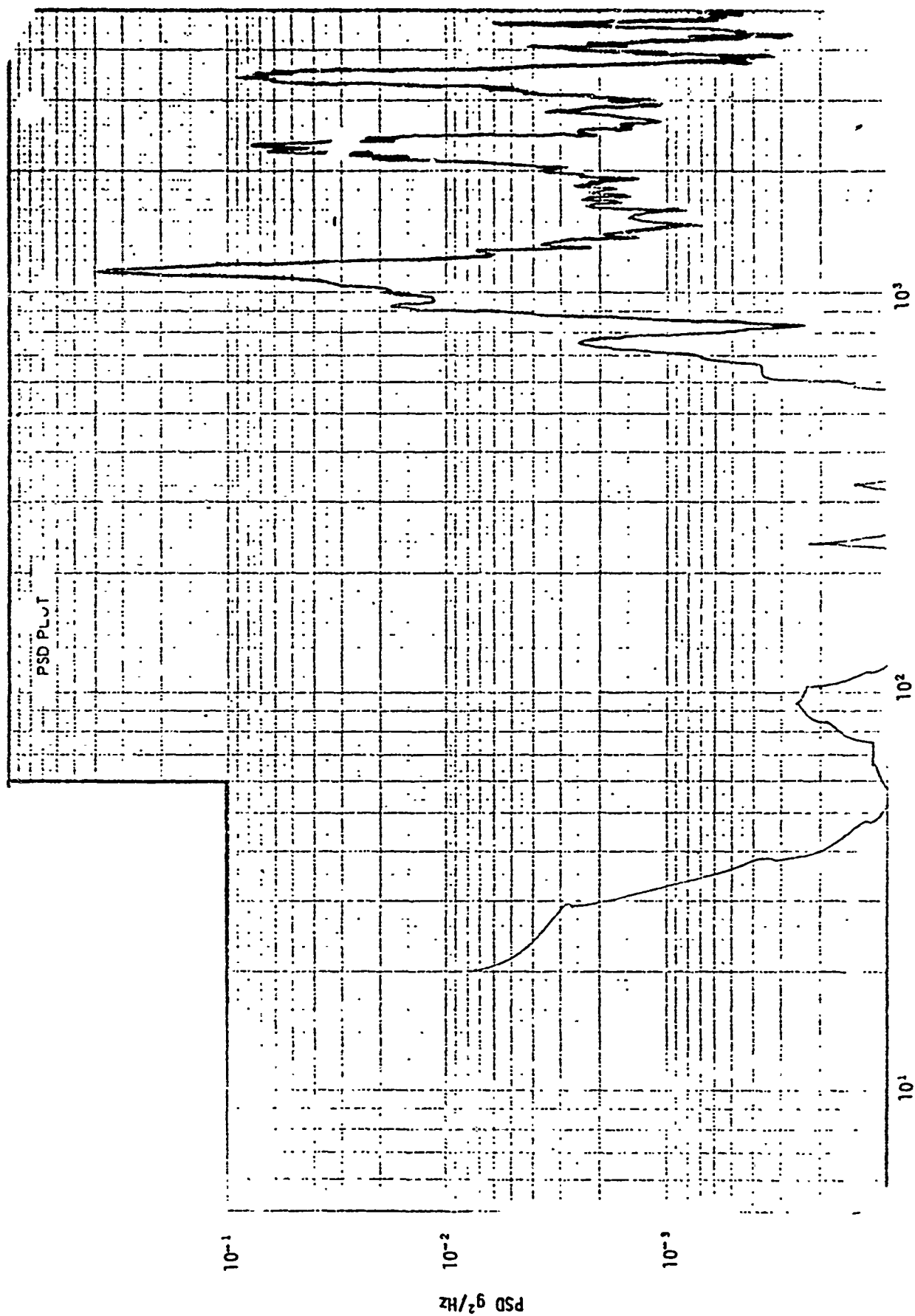


Figure 2-27.04. Accelerometer PSD for Run 8, Tape Position 06:04:30

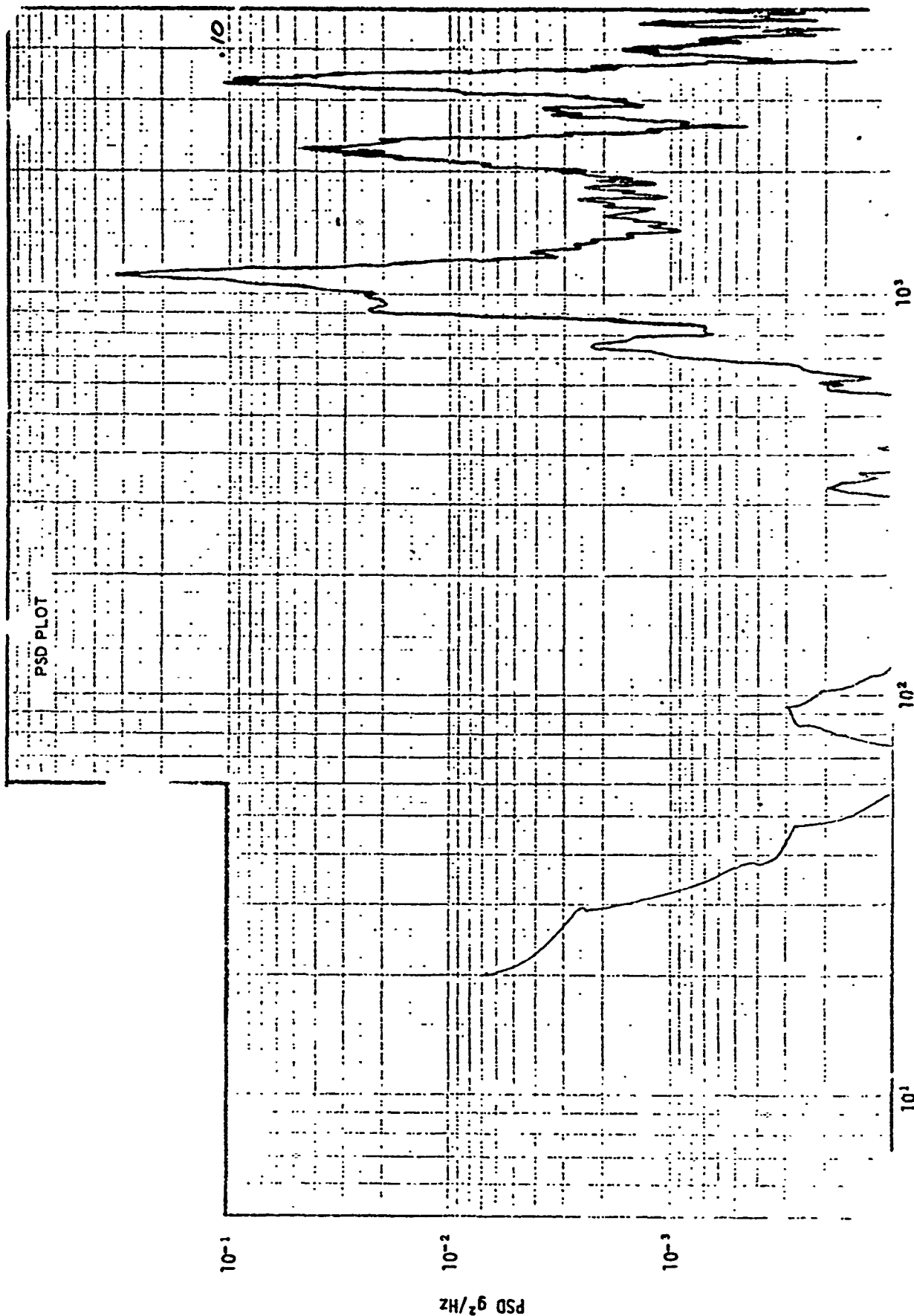


Figure 2-27.05. Accelerometer PSD for Run 9, Tape Position 01:12:01

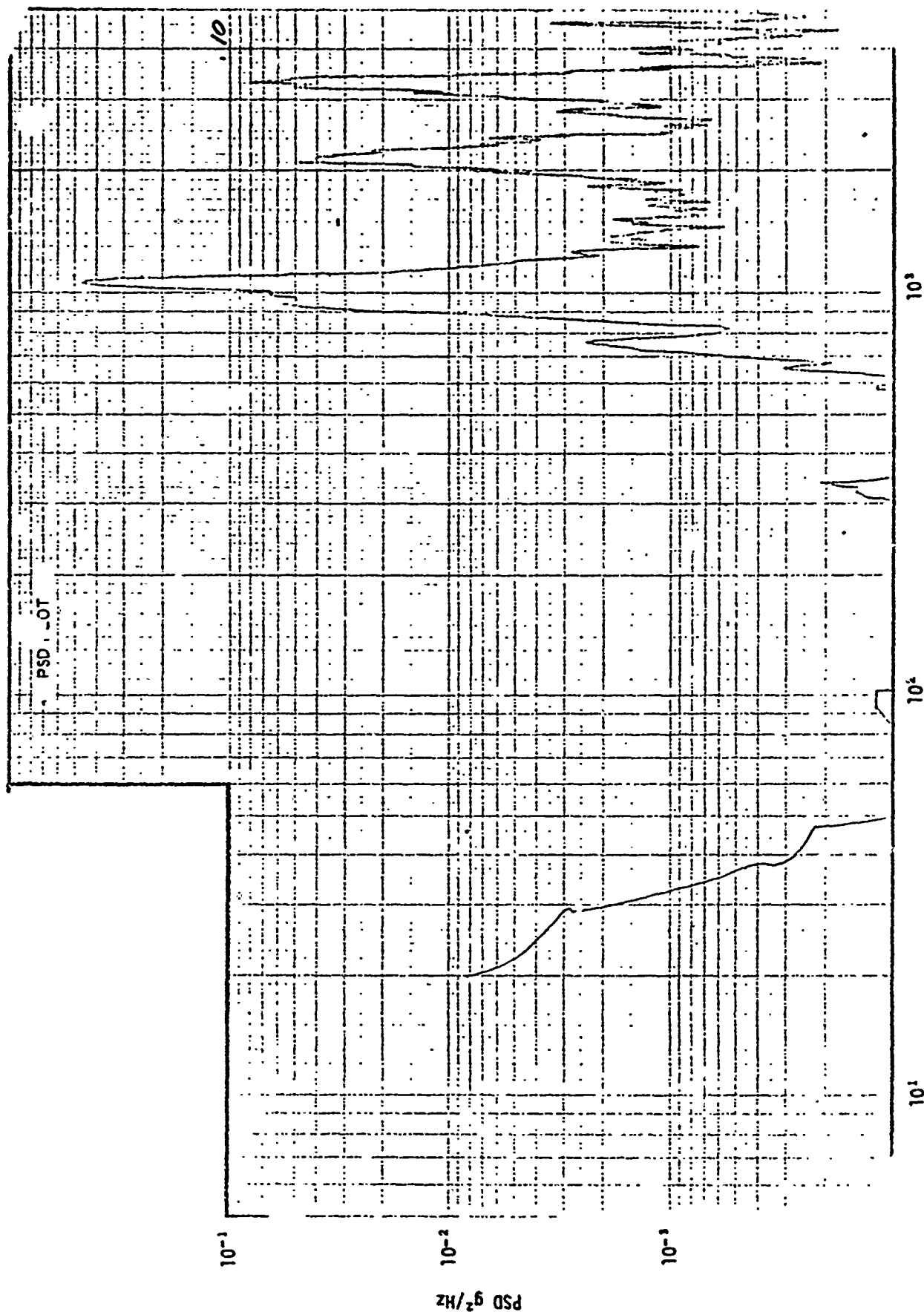


Figure 2-27.06. Accelerometer PSD for Run 10, Tape Position 01:12:21

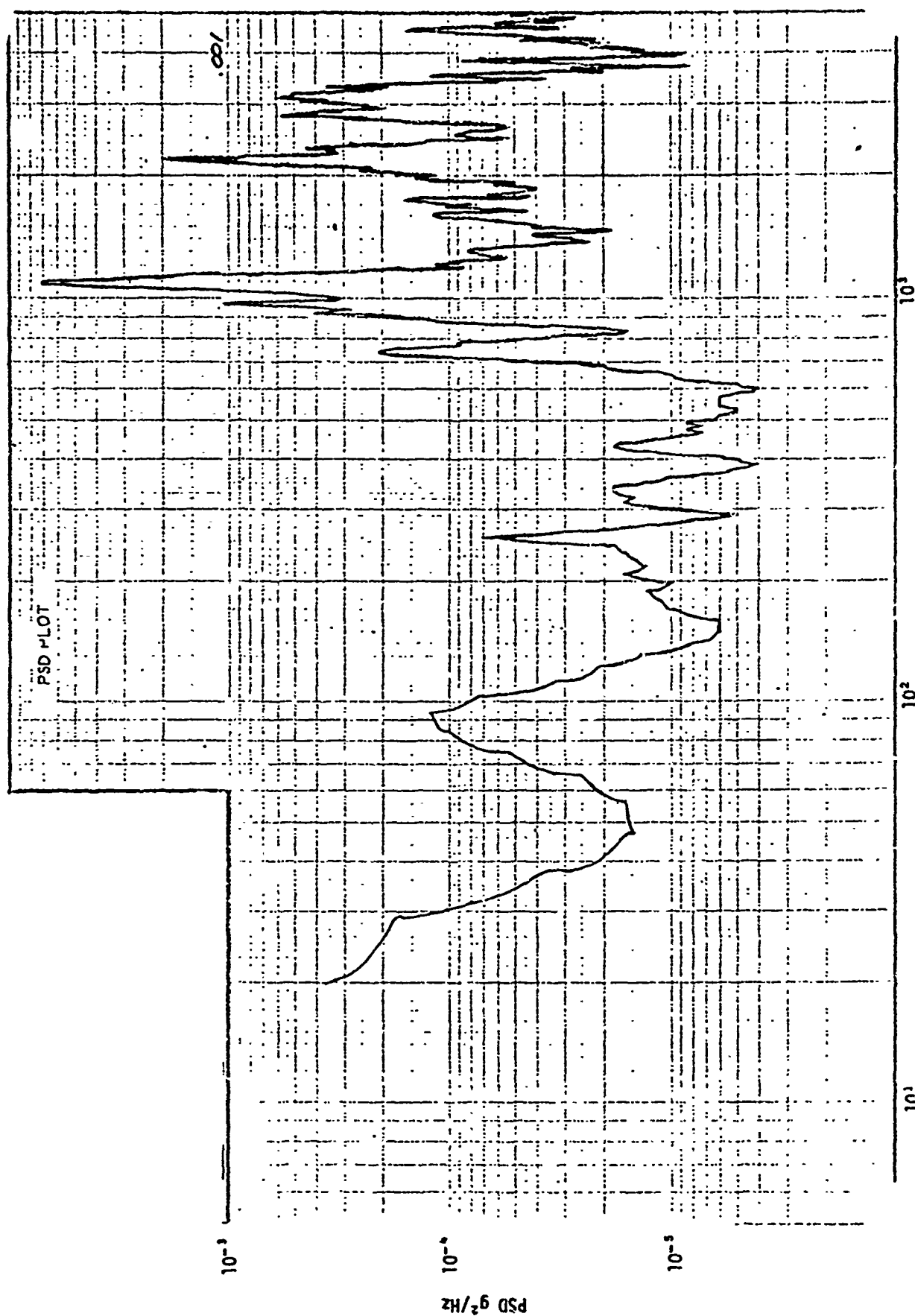


Figure 2-27.07. Accelerometer PSD for Run 24, Tape Position 01:18:04



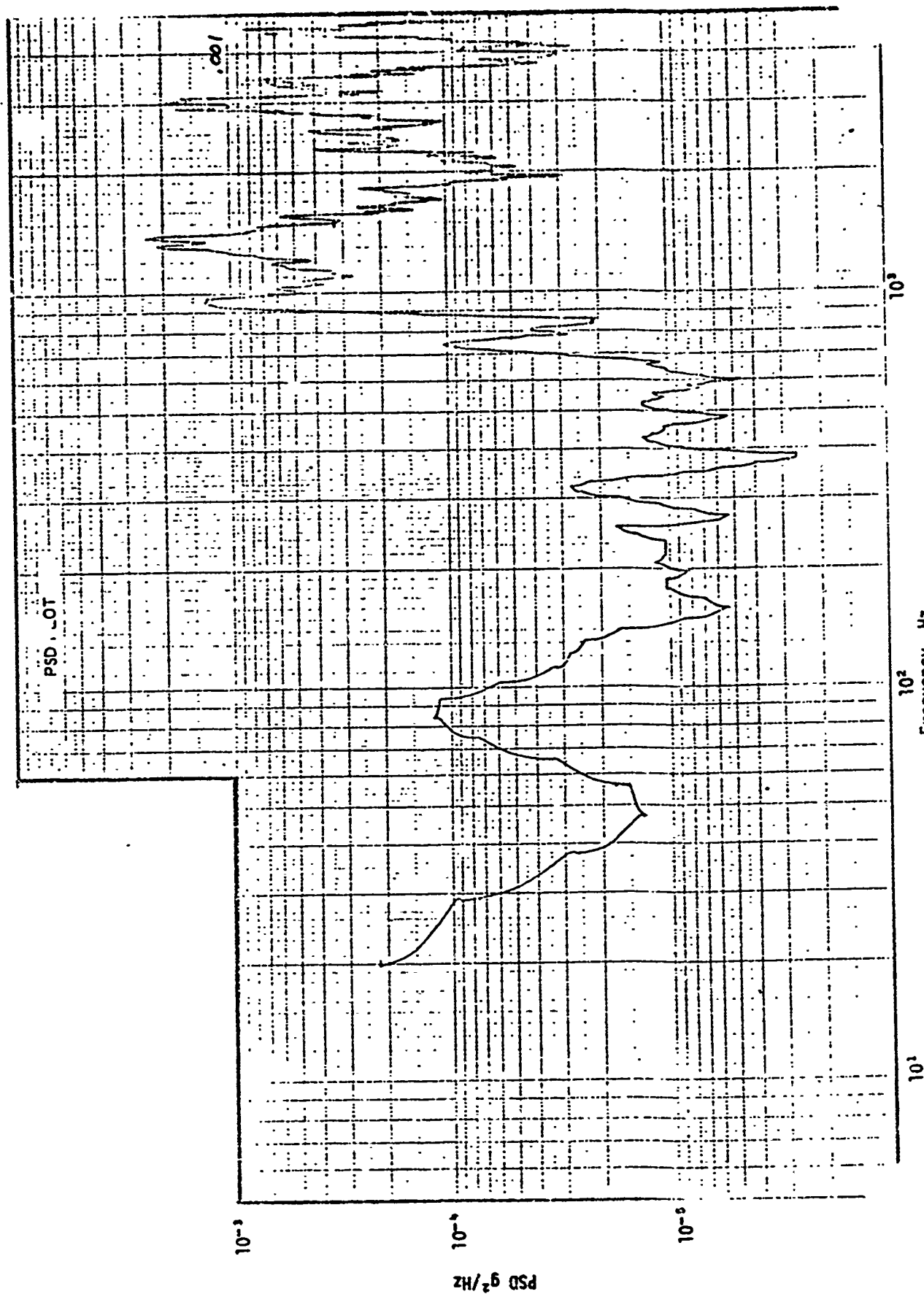


Figure 2-27.08. Accelerometer PSD for Run 25, Tape Position 11:37:17

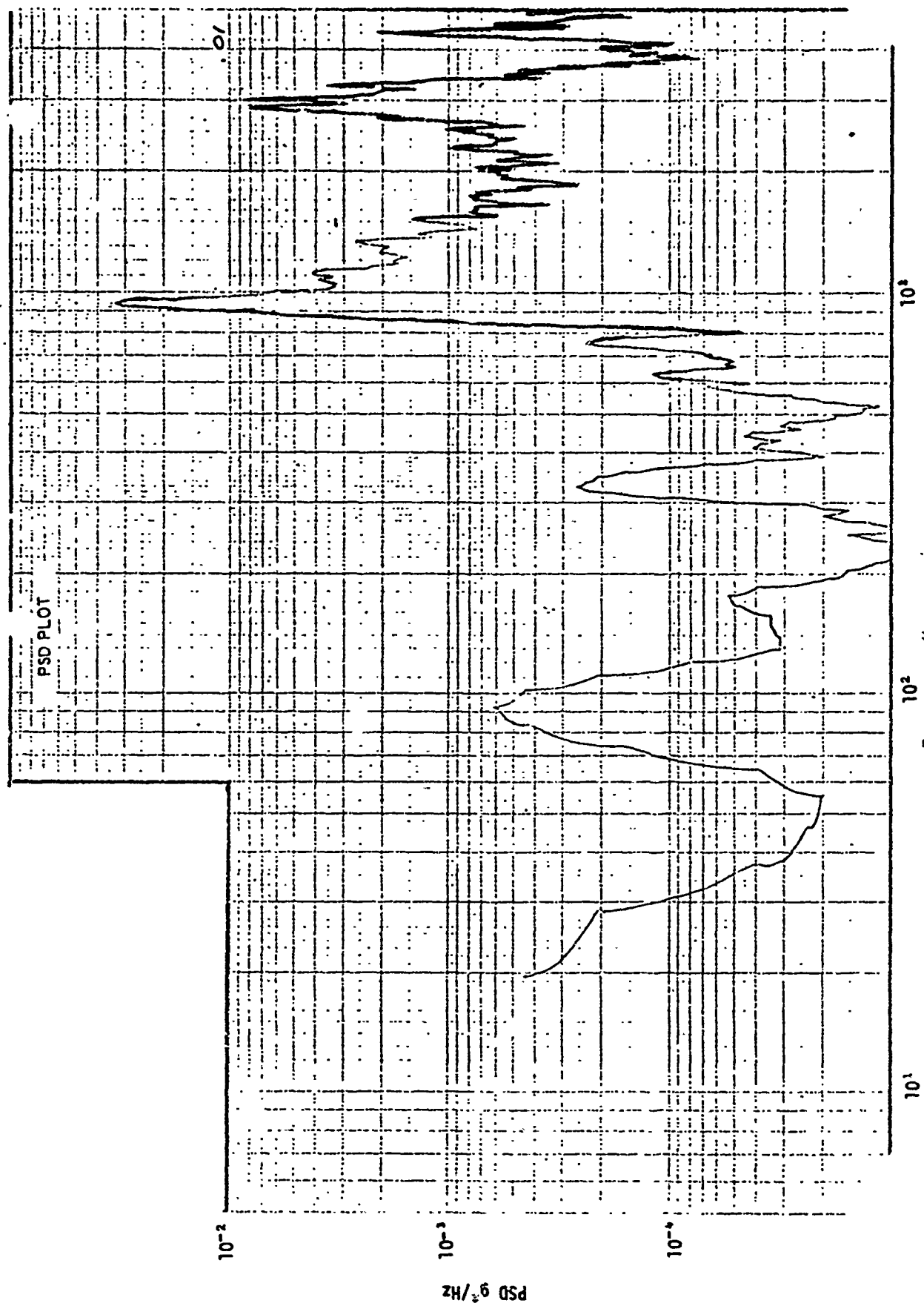


Figure 2-27.09. Accelerometer PSD for Run 25, Tape Position 11:39:23

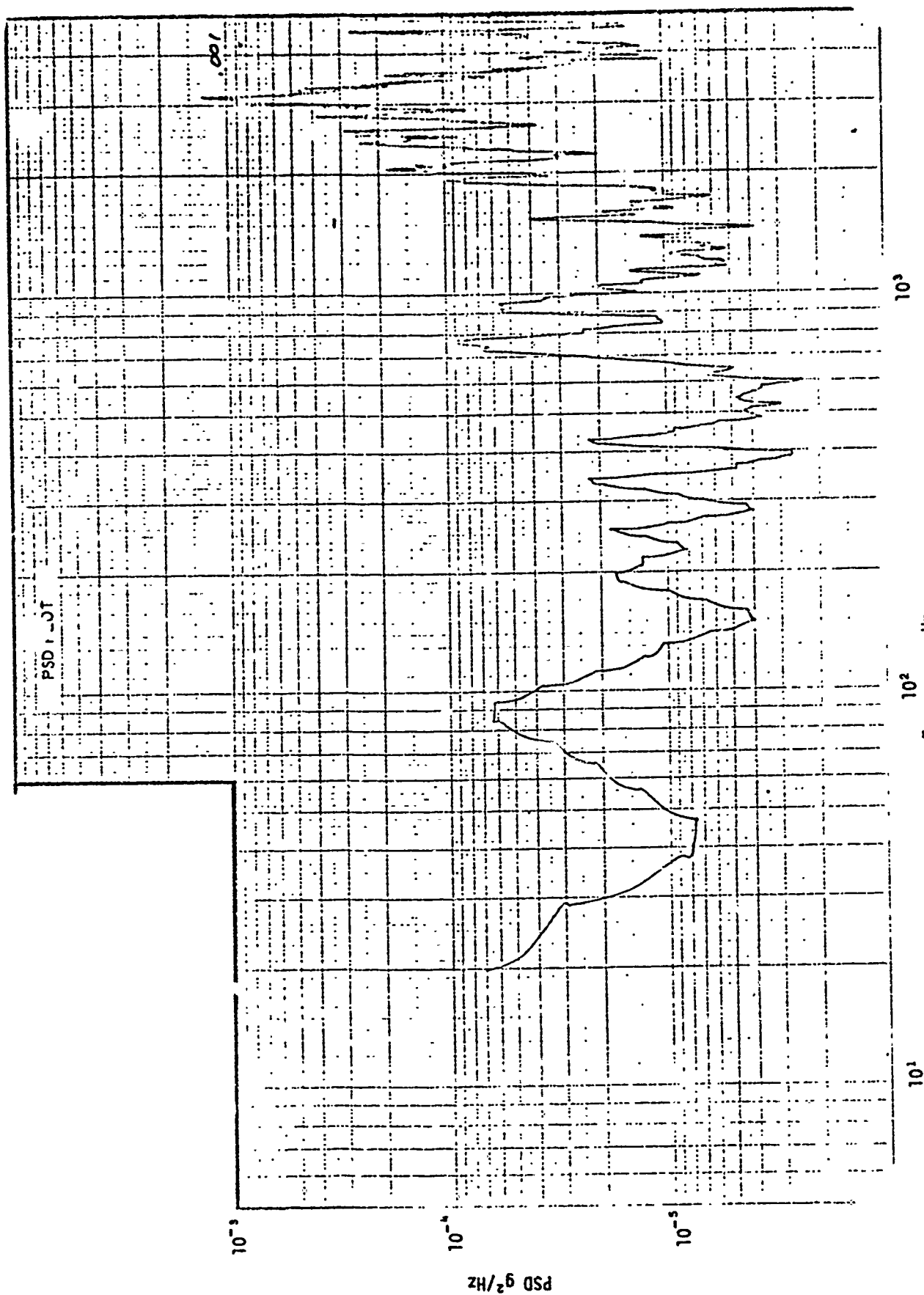


Figure 2-27.10. Accelerometer PSD for Run 25, Tape Position 11:51:58

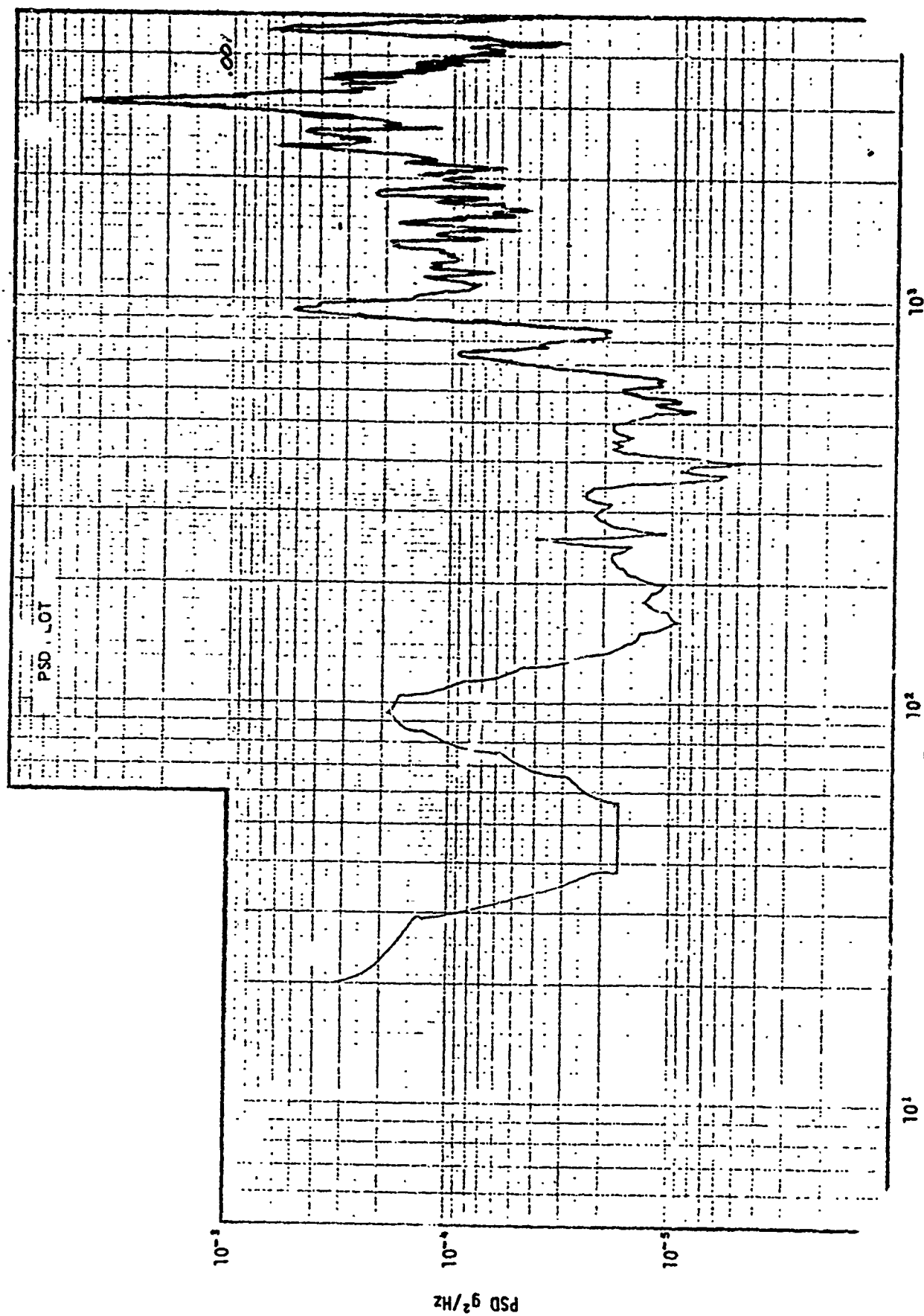


Figure 2-27.11. Accelerometer PSD for Run 26, Tape Position 11:52:02

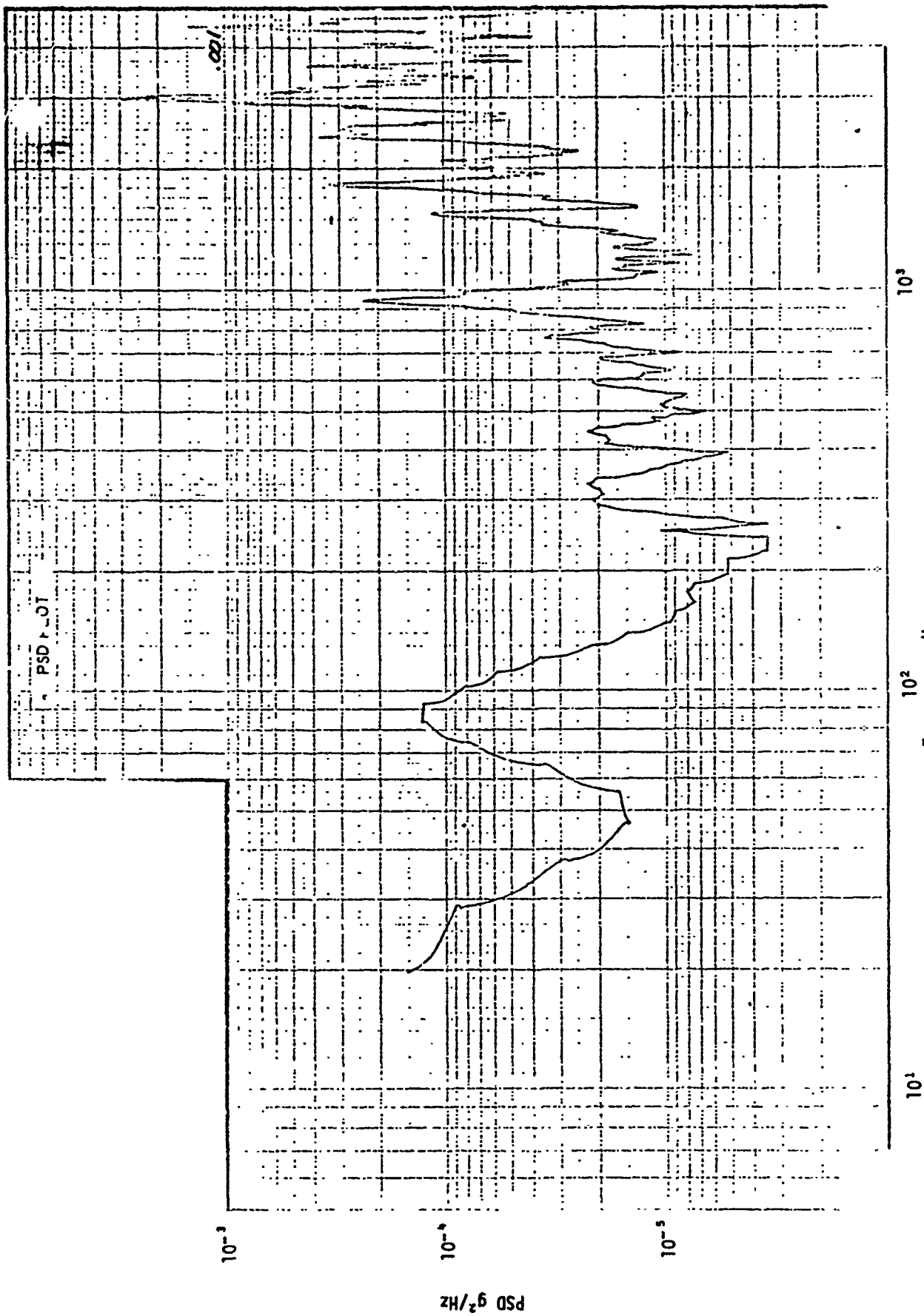


Figure 2-27.12. Accelerometer PSD for Run 26, Tape Position 11:52:12

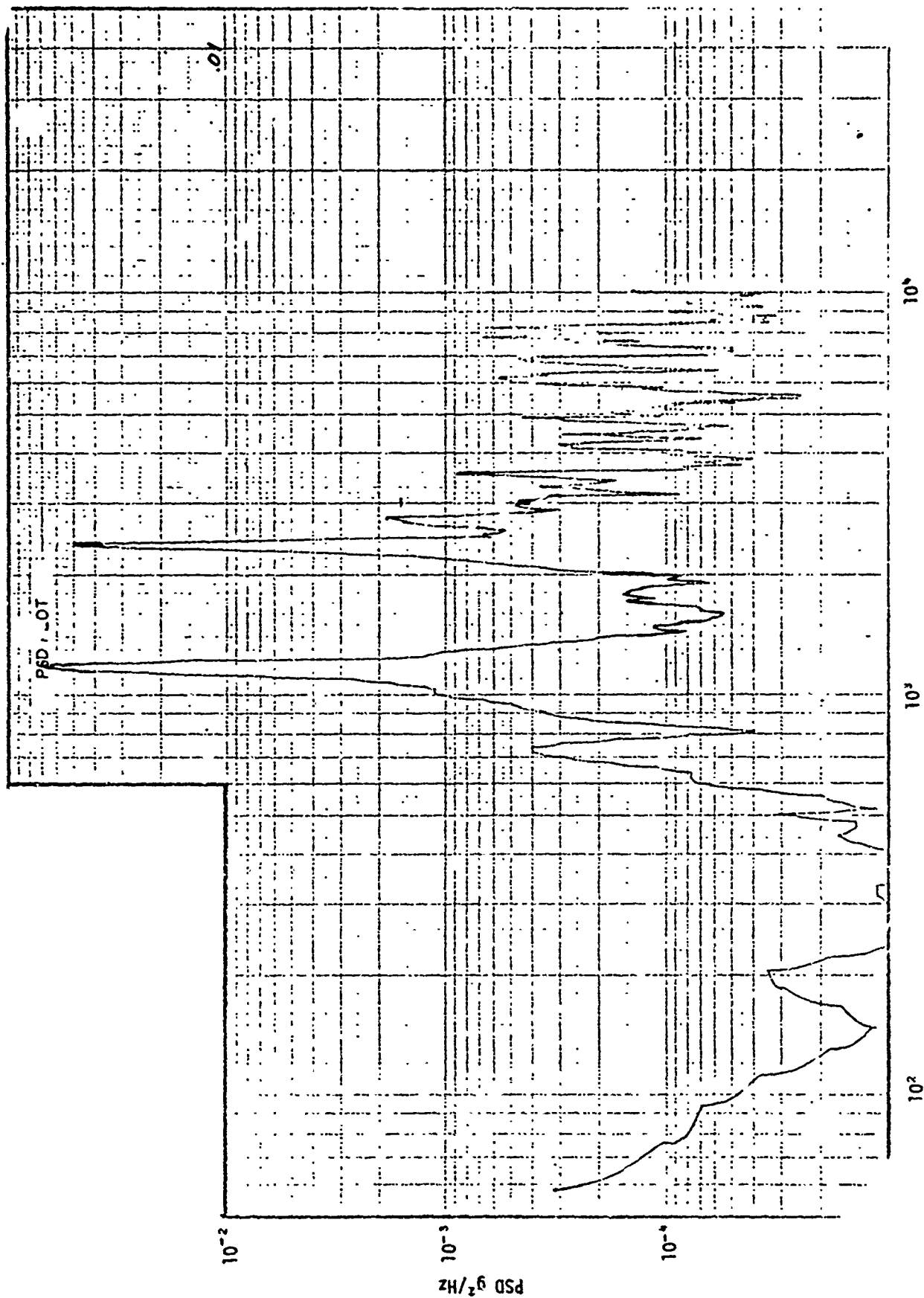


Figure 2-27.13. Accelerometer PSD for Run 28, Tape Position 14:20:16

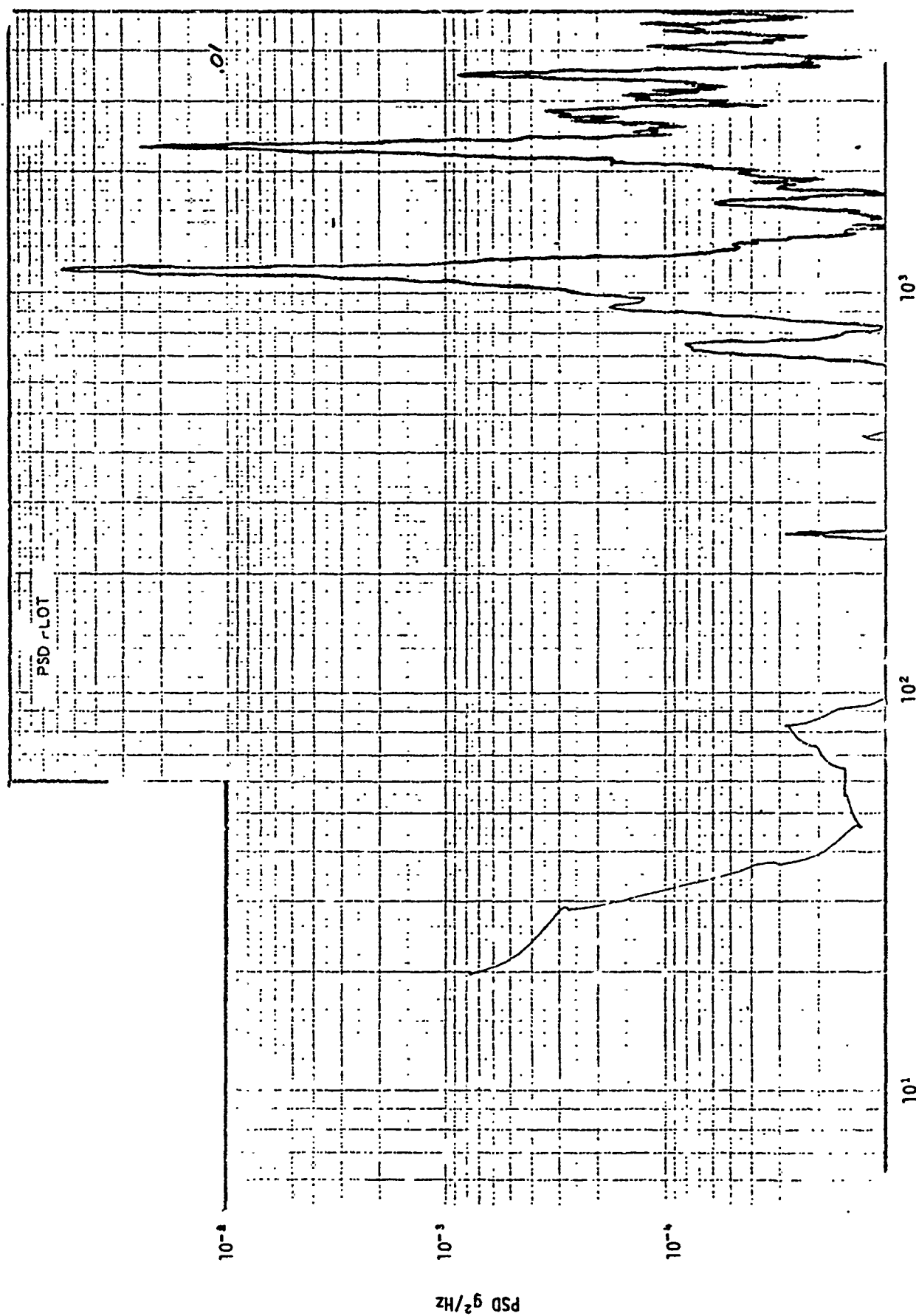


Figure 2-27.14. Accelerometer PSD for Run 30, Tape Position 14:32:15

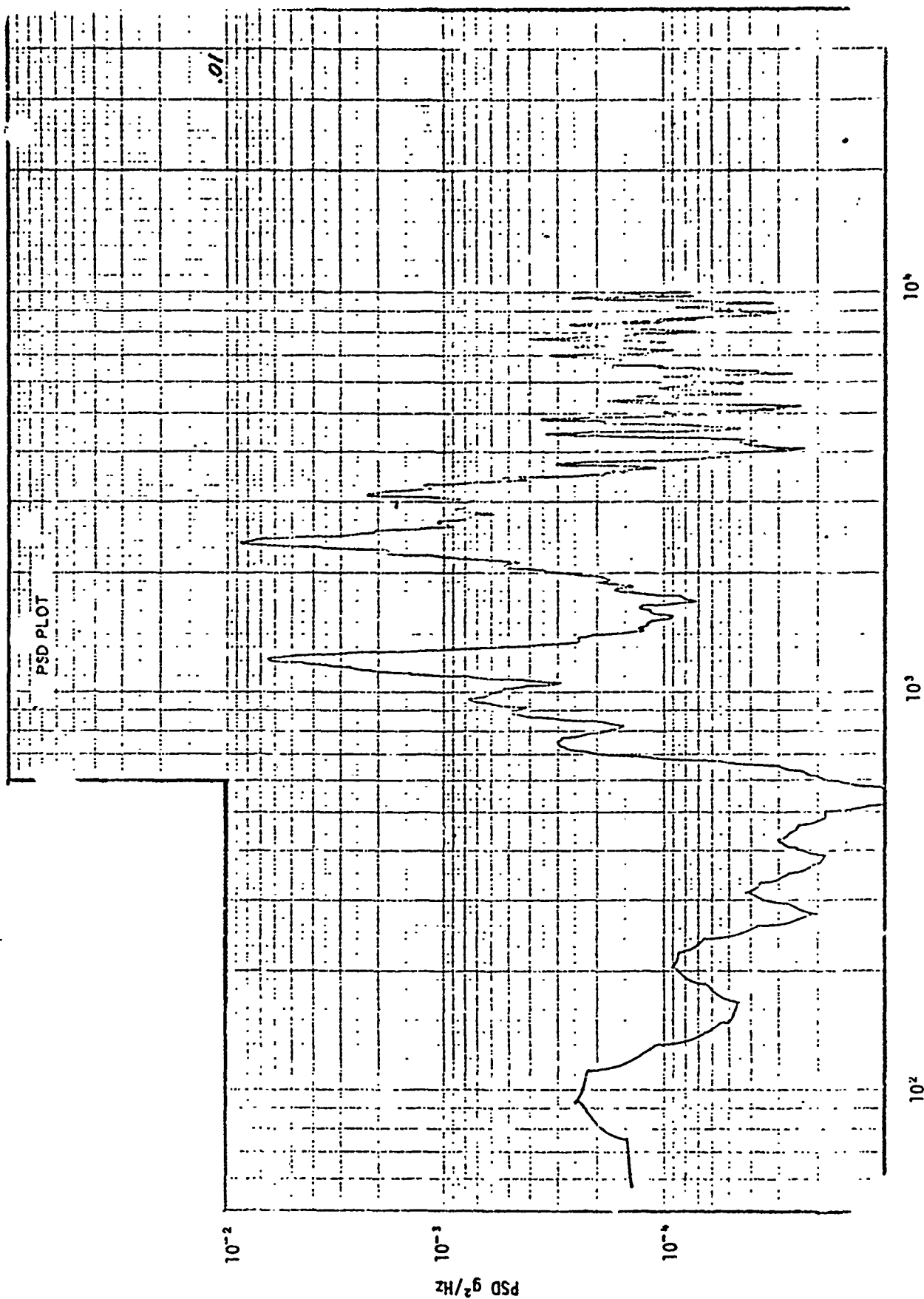


Figure 2-27.15. Accelerometer PSD for Run 32, Tape Position 15:18:40.2



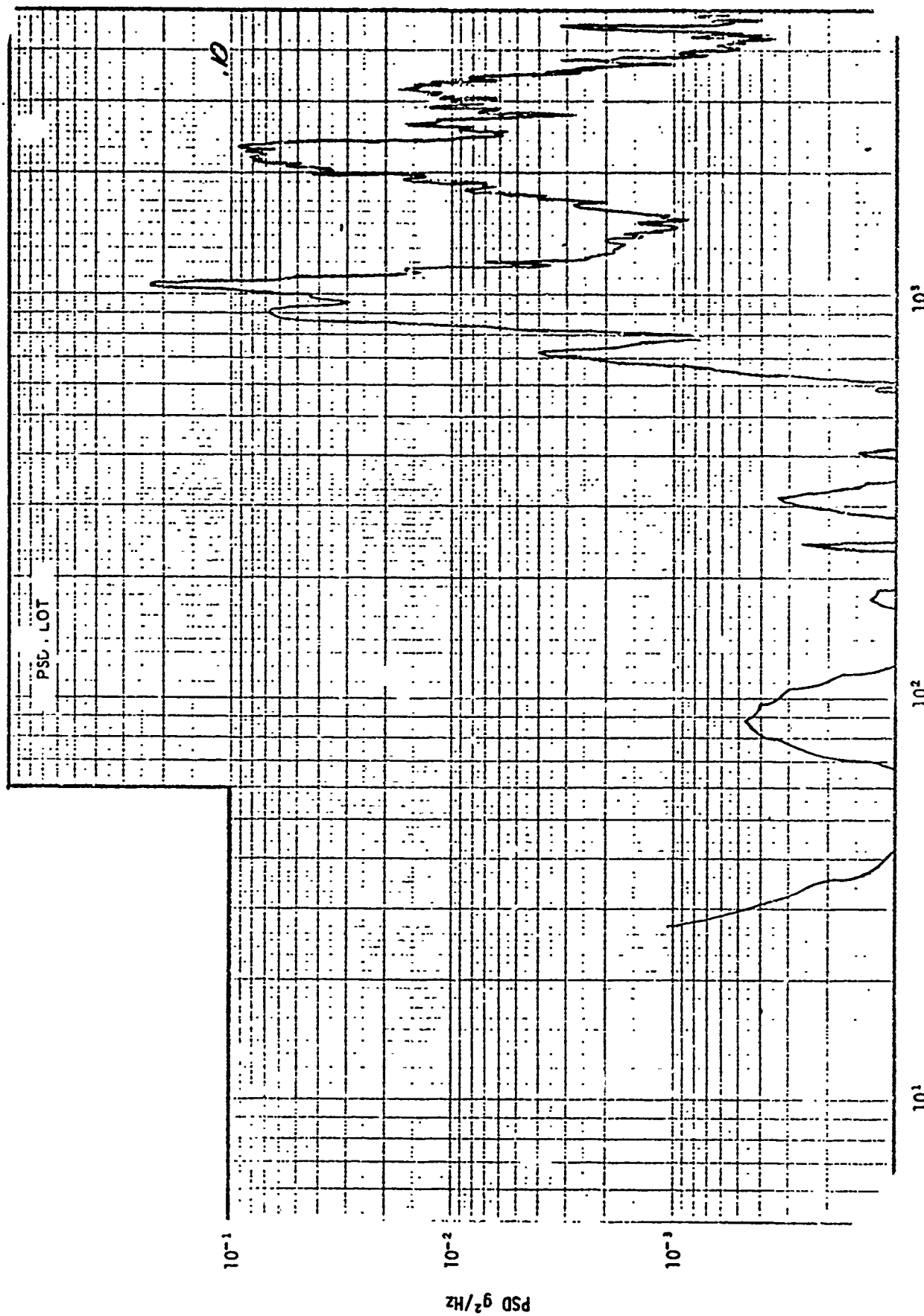


Figure 2-27.16. Accelerometer PSD for Run 42, Tape Position 11:50:25

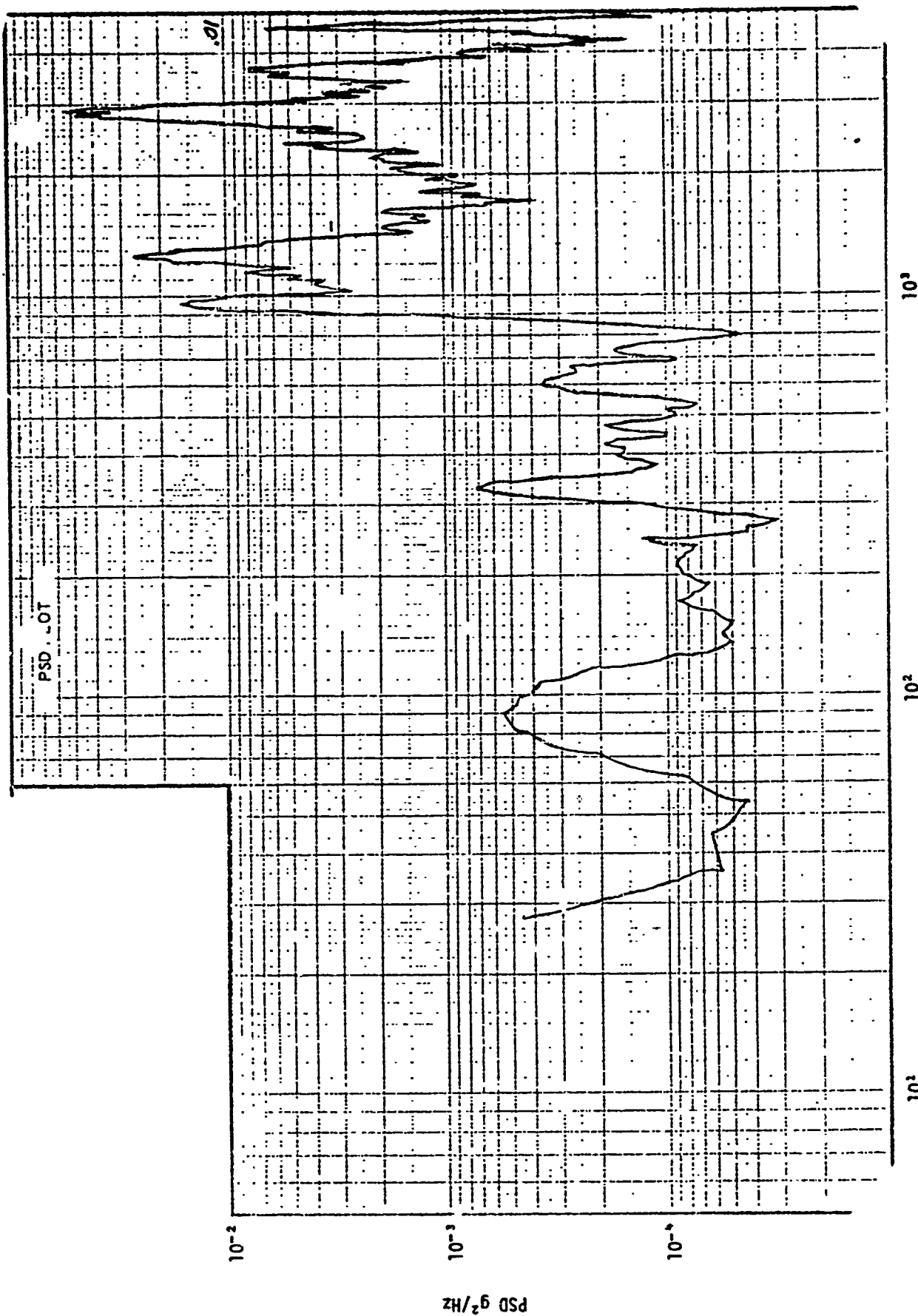


Figure 2-27.17. Accelerometer PSD for Run 42, Tape Position 11:50:39

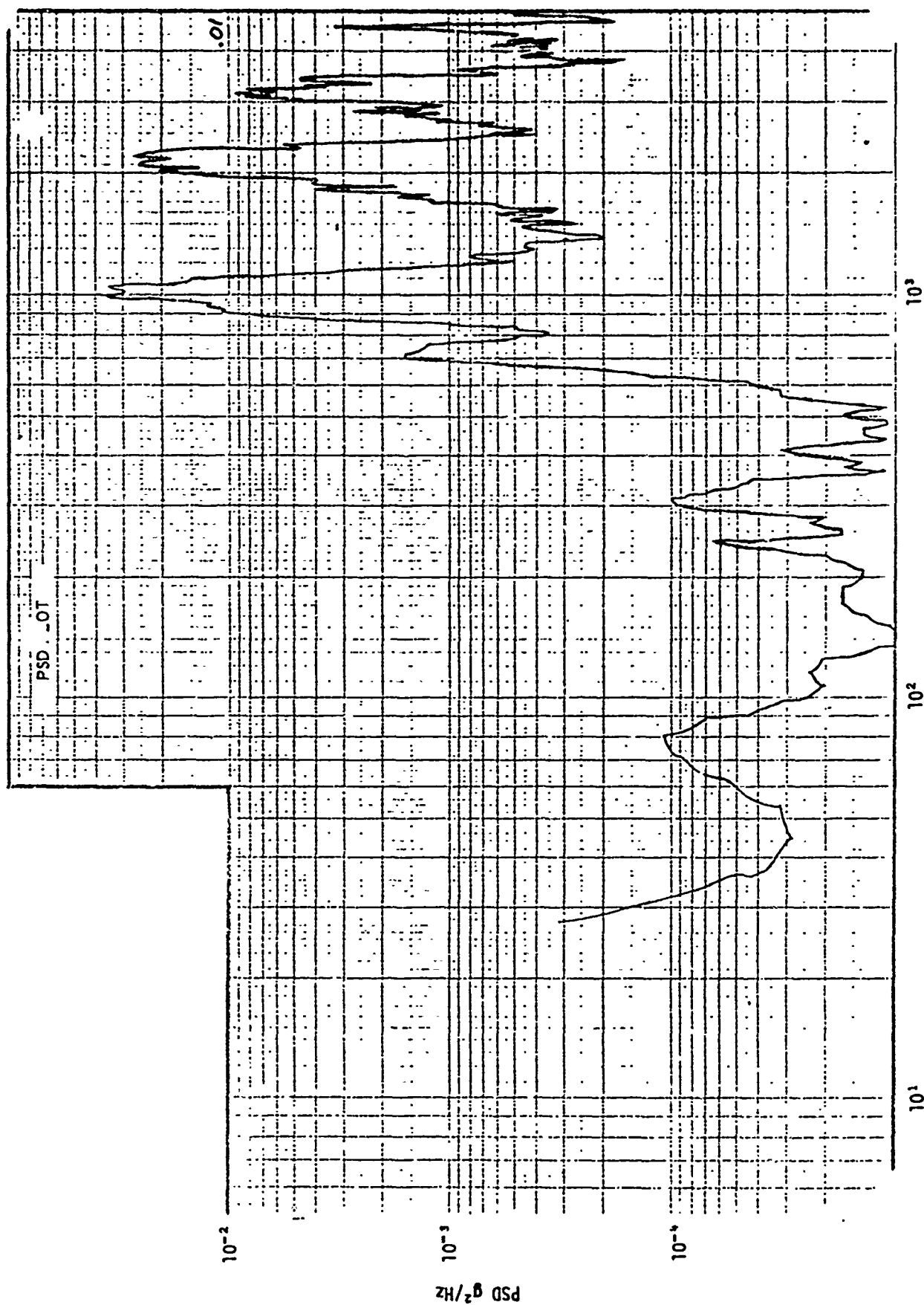


Figure 2-27.18. Accelerometer PSD for Run 43, Tape Position 11:51:52

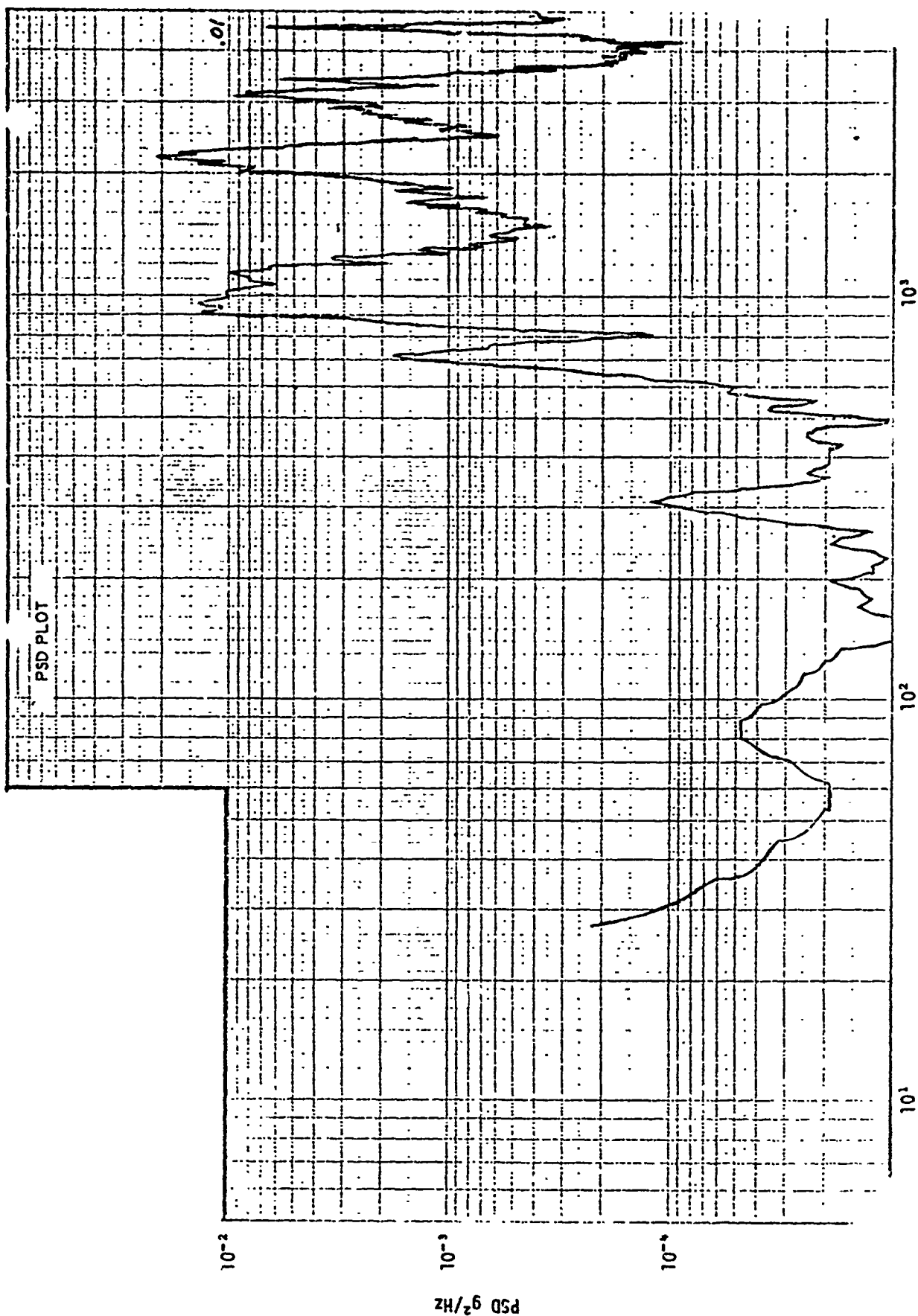


Figure 2-27.19. Accelerometer PSD for Run 43, Tape Position 11:52:01

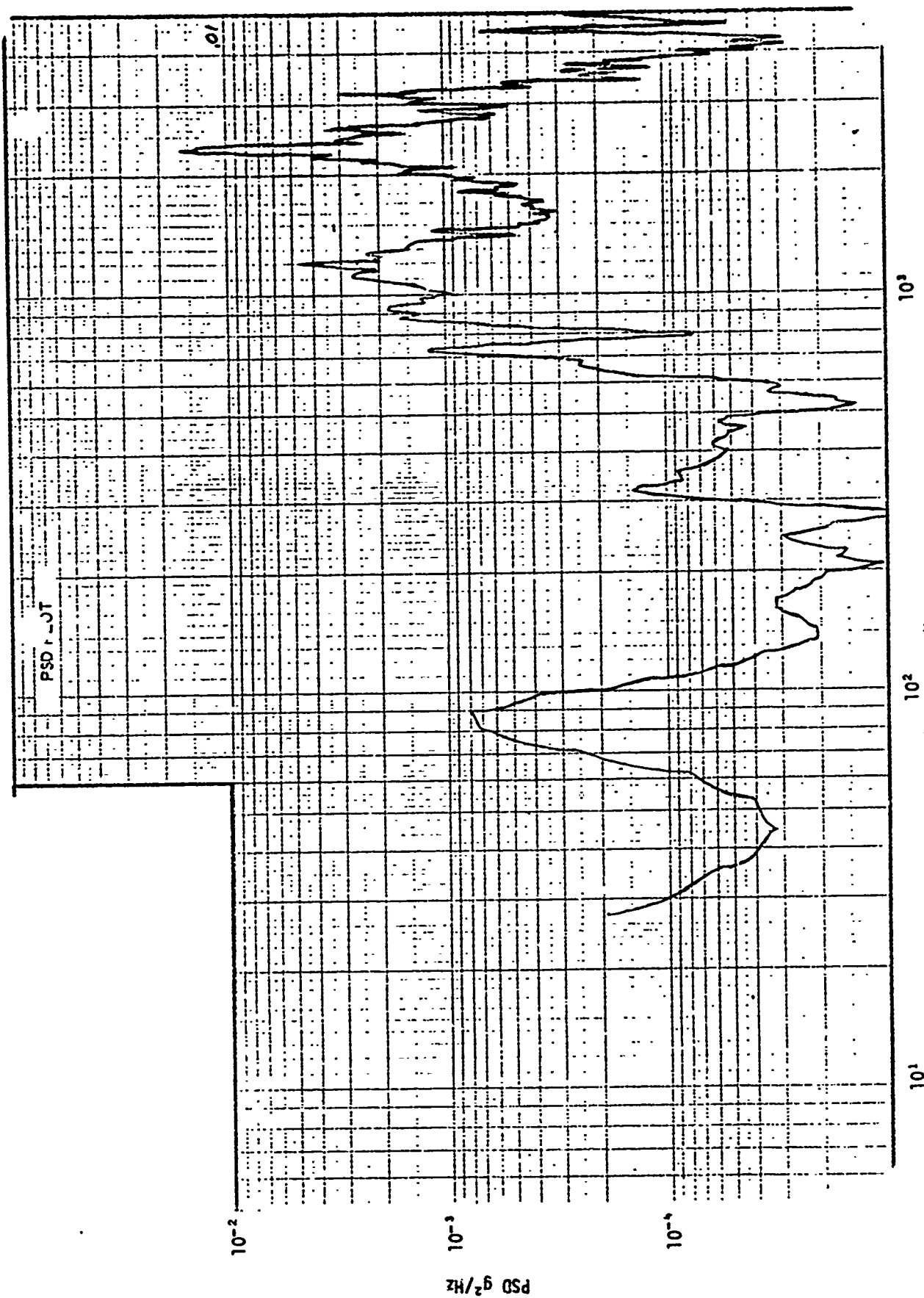


Figure 2-27.20. Accelerometer PSD for Run 43, Tape Position 11:52:10

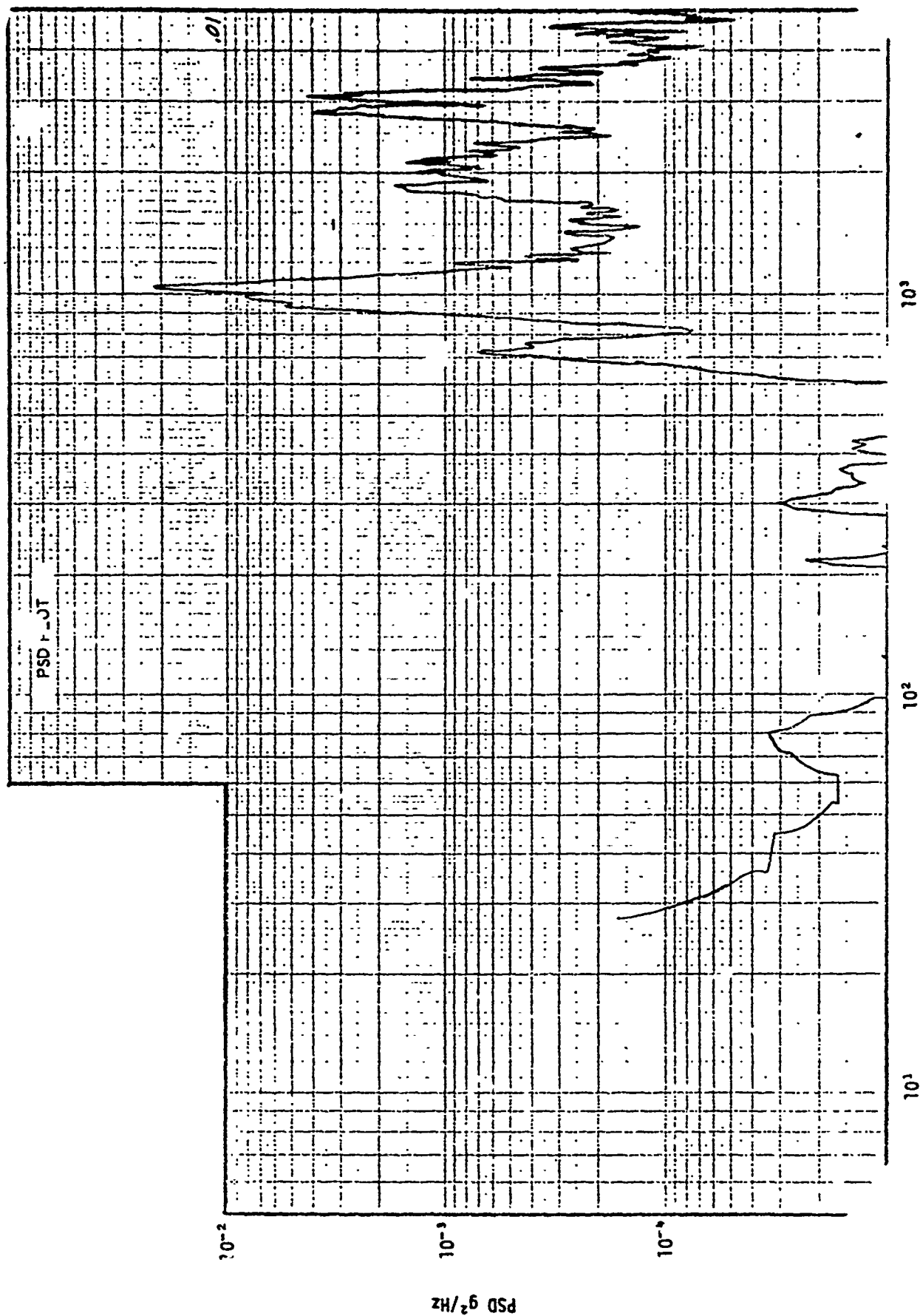


Figure 2-27.21. Accelerometer PSD for Run 44, Tape Position 12:04:46

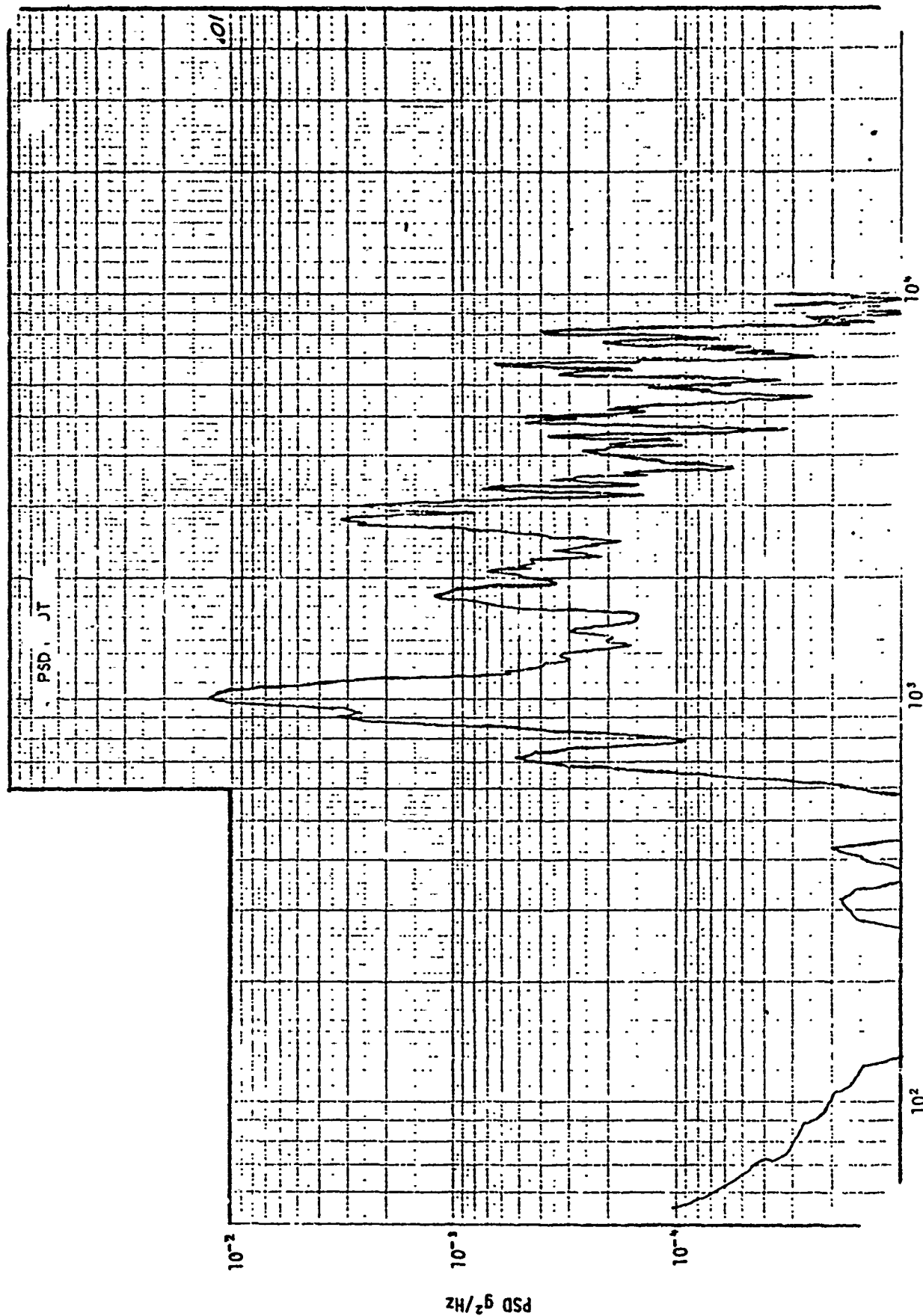


Figure 2-27.22. Accelerometer PSD for Run 44, Tape Position 12:04:51

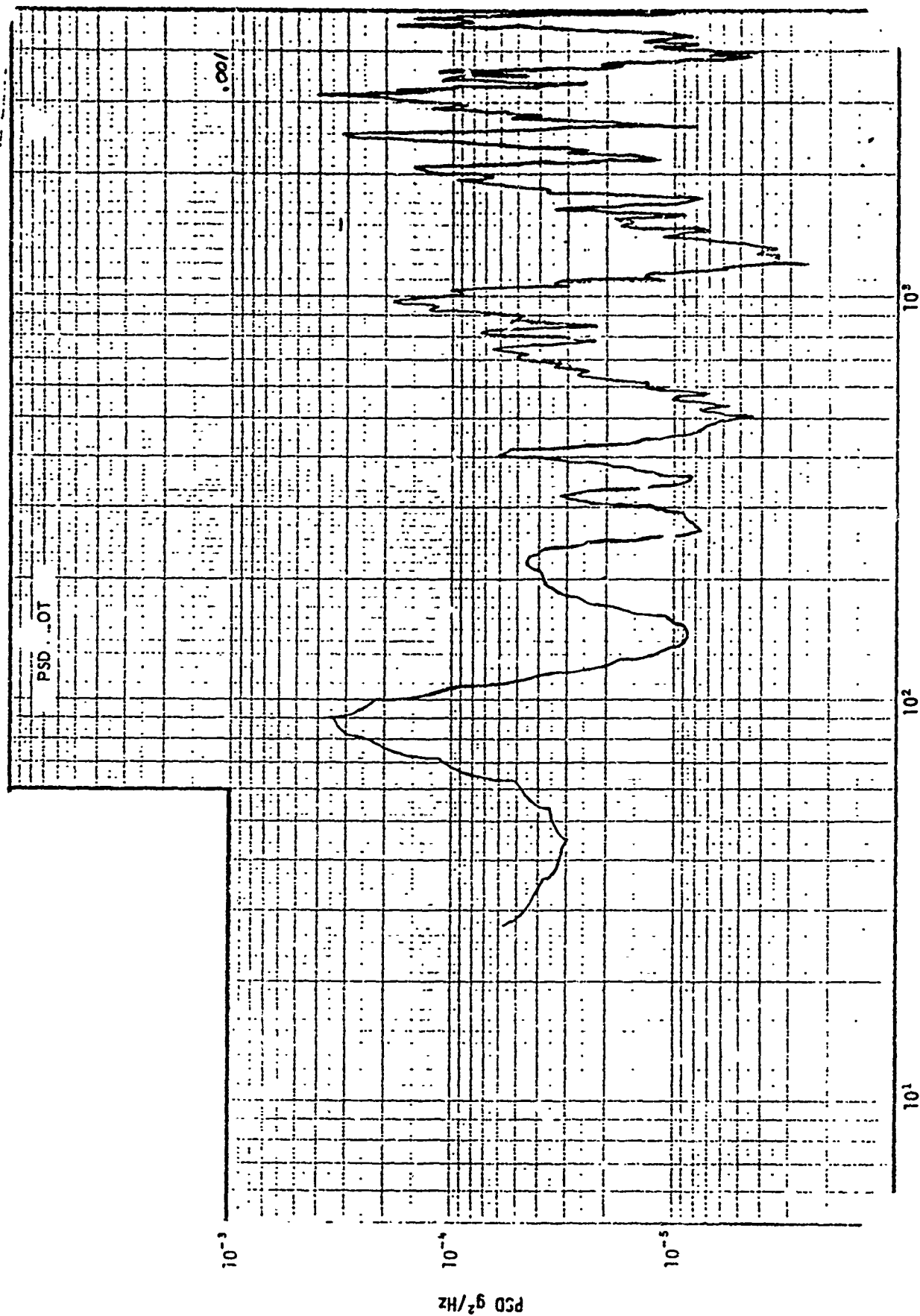


Figure 2-27.23. Accelerometer PSD for Run 46, Tape Position 15:19:55



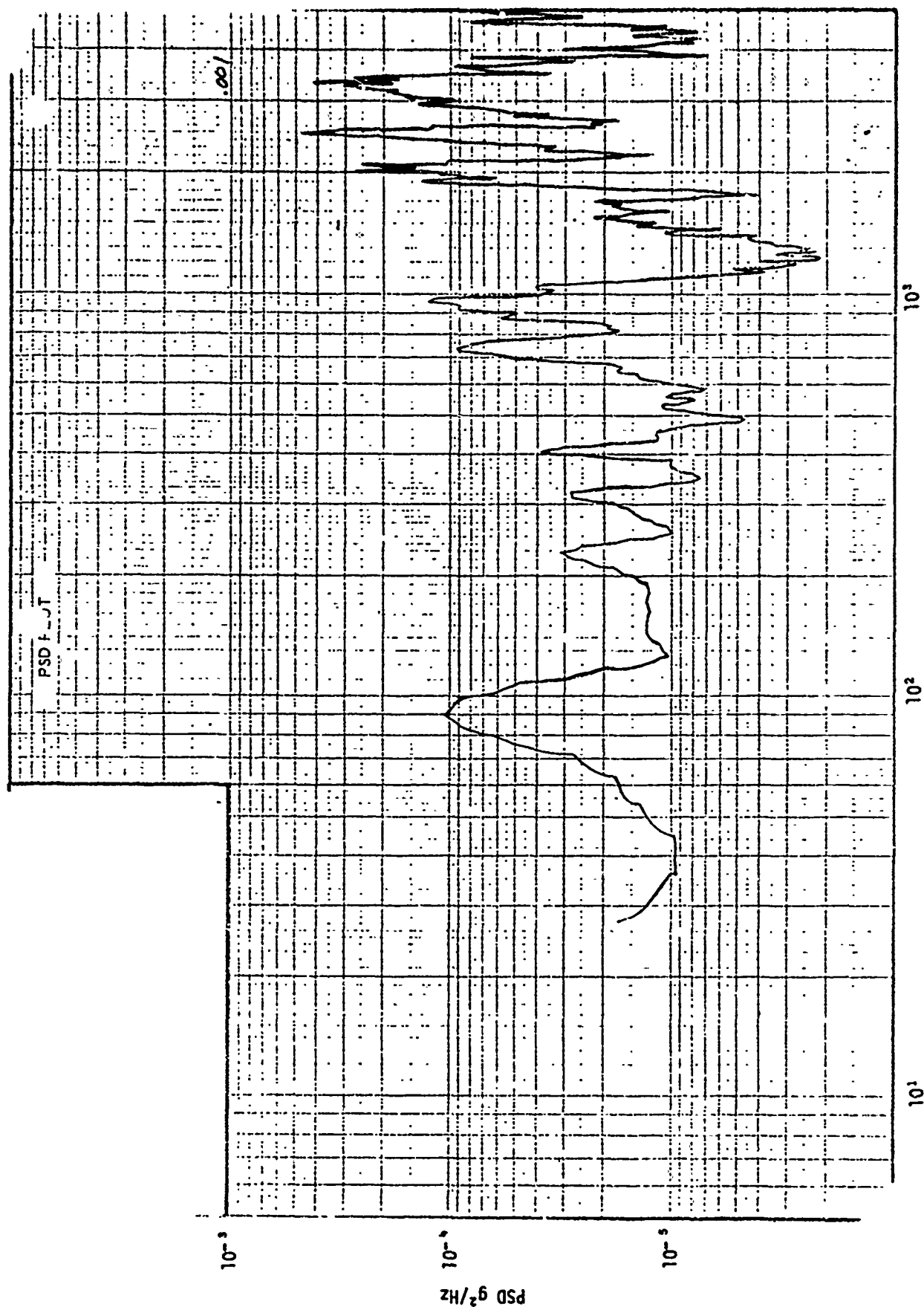


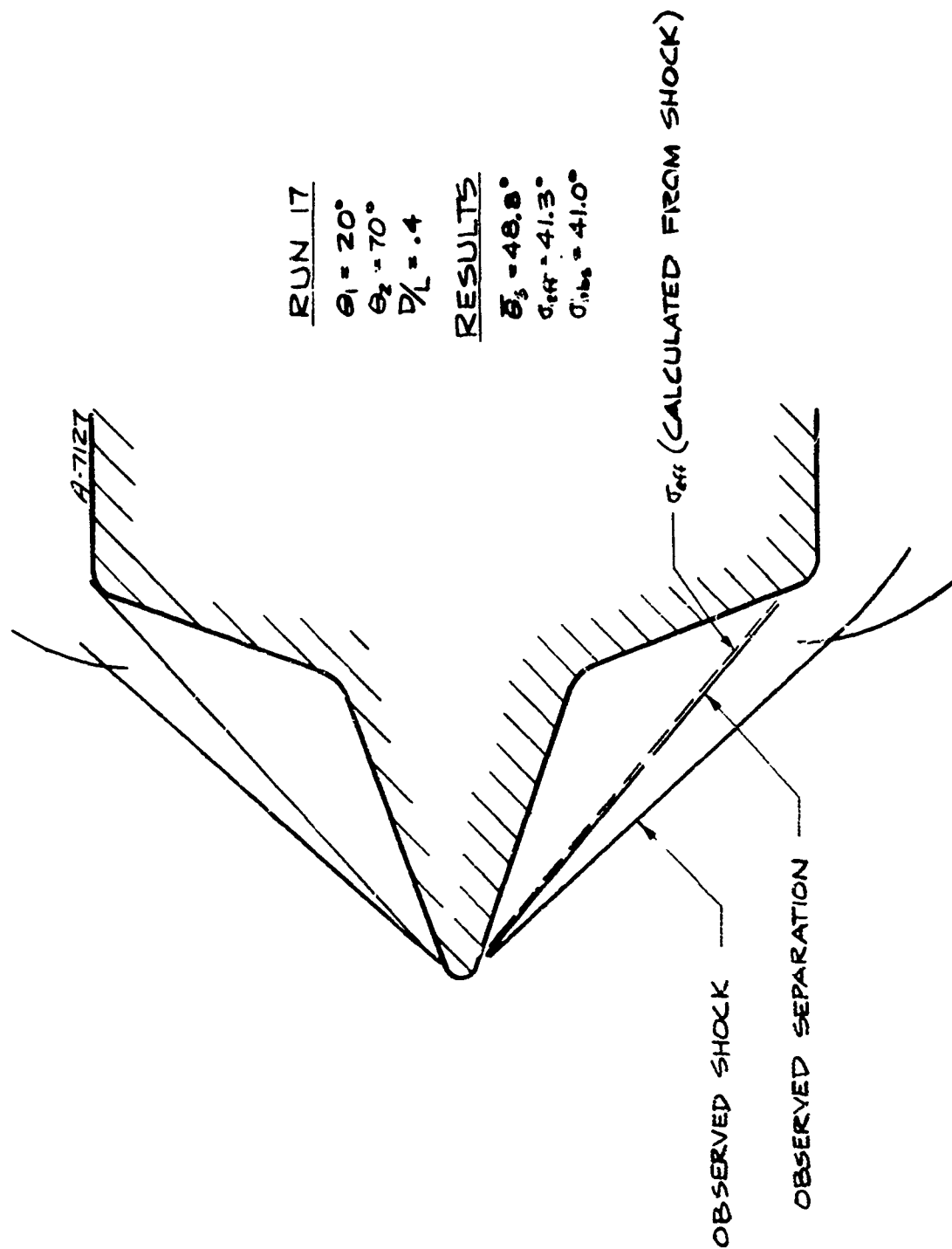
Figure 2-27.24. Accelerometer PSD for Run 47, Tape Position 16:26:27

about 3700 cps. Recall from Figure 2-21' that this behavior is apparently associated with a small amplitude secondary shock motion.

#### 2.6 6 Preliminary Correlation Results

Two basic classes of correlations were attempted: one for steady separated flows and one for establishing the limits for unsteady flows. The correlation for steady separated flows was intended to determine the effective angle of separation. Figure 2-28 shows a sample of this type of calculation. The observed inclination of the tip shock was measured from the 35 mm photos. From the observed shock inclination and the free stream Mach number, the effective conical angle of separation,  $\sigma_{eff}$ , was calculated from conical shock theory. In all cases of steady separated flow the line determined by the effective angle of separation intercepted the body at or near the shoulder as shown. It was also desired to determine how the calculated value of  $\sigma_{eff}$  compared to the observed edge of the separated zone as perceived from the still photos. Figure 2-29 presents a comparison between the calculated value of  $\sigma_{eff}$  and the observed edge of the shear layer. In general the comparison is close, with a general tendency to overestimate the actual angle of separation from the photos.

Figure 2-30 shows the preliminary attempt to correlate the data for stability limits. The method of correlation chosen was similar to that of Wood. For spiked ( $\theta_1 = 0^\circ$ ) cone cylinders, Wood constructed a correlation for stability limits by plotting  $l/D$  (or  $L/D$ ) vs. total turning angle  $\theta_2$ . Wood concluded that the origin of the regime of unsteady flow would be the cone angle,  $\theta_2$ , that corresponds to detachment of a conical shock wave. The data from the current series of tests is shown plotted as a Wood's type correlation in Figure 2-30. It can be seen that the correlation for the limits of stability seem to be fairly distinct. The only anomaly apparent is the data point at  $\theta_2 = 70^\circ$ ,  $l/D = 0.5$ , which is steady separated flow.



RUN 17

$\theta_1 = 20^\circ$

$\theta_2 = 70^\circ$

$D/L = .4$

RESULTS

$\delta_s = 48.8^\circ$

$\sigma_{sh} = 41.3^\circ$

$\sigma_{shs} = 41.0^\circ$

Figure 2-28. Determination of Effective Angle of Steady Separation

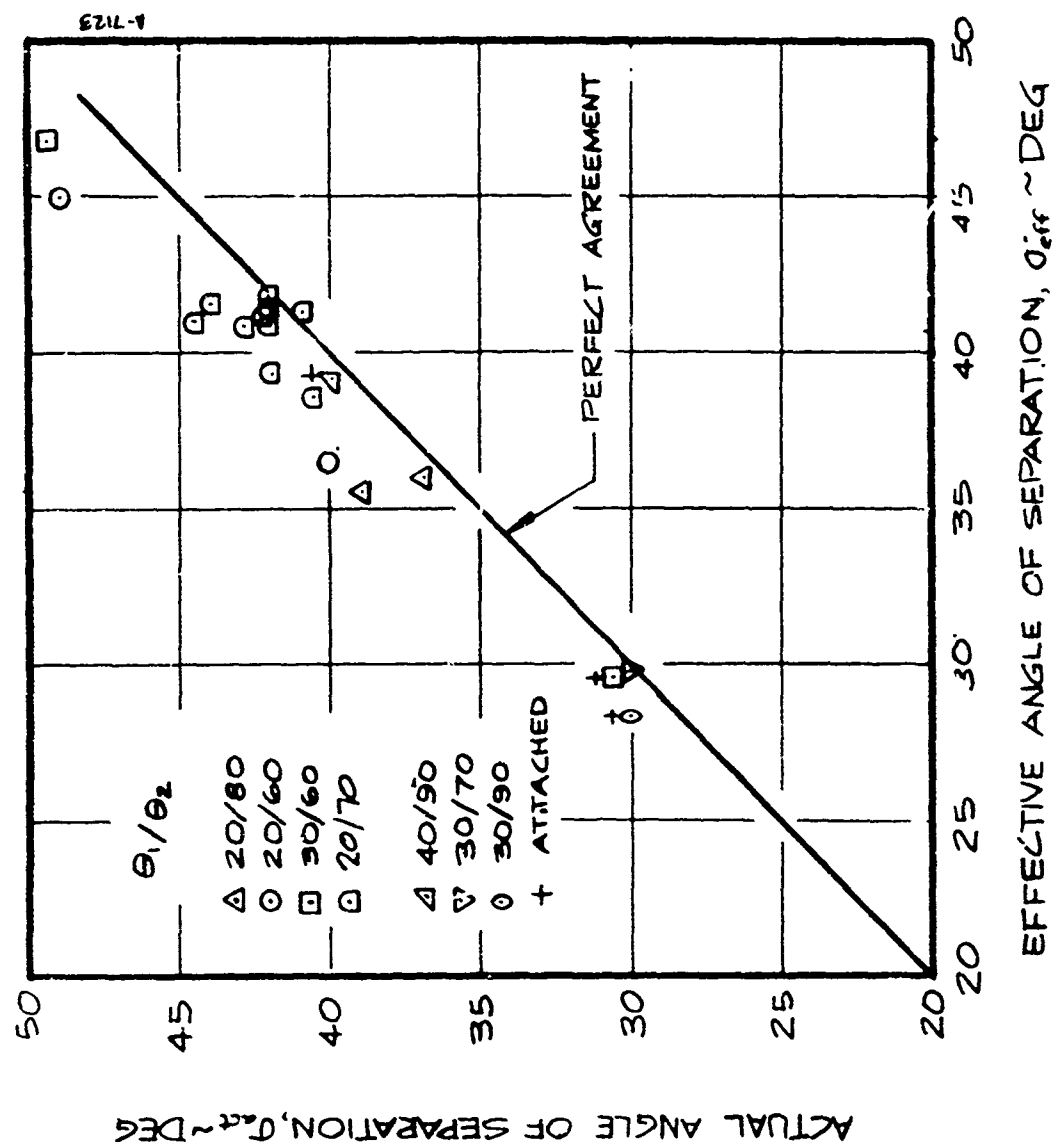


Figure 2-29. Agreement Between Actual and Effective Angles of Separation for Steady Flow Cases

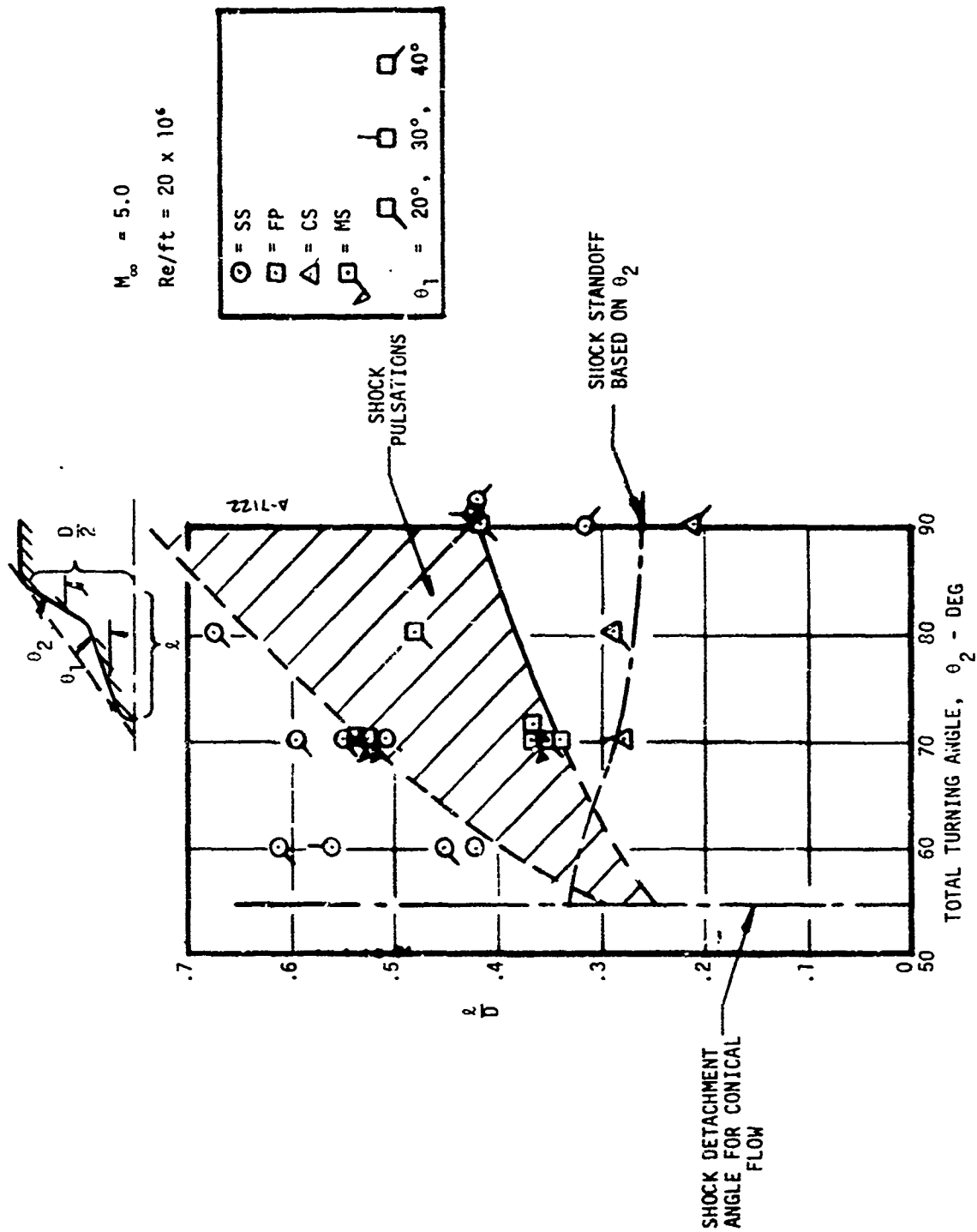


Figure 2-30. Preliminary "Wood Type" Correlation of NOL-8 Series Test Results

### SECTION 3

#### ANALYTICAL PROGRAM

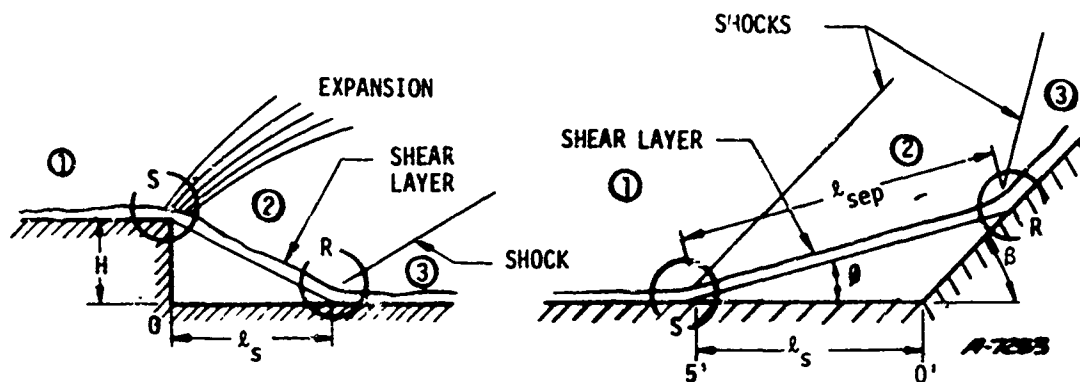
The pulsating flow field is quite complex. Though conceptually feasible, an exact solution of the unsteady equations of motion is not practical for the Reynolds numbers of interest. Even if it were economically feasible to solve the complete equations, current capability to model turbulent transport properties is essentially nonexistent for transient flows of this type. Therefore, analytical efforts in this study have been directed toward developing a simplified model which would aid in understanding the cause of the instability and defining the envelope of instability onset.

The analysis is based on the Korst model of reattaching separated turbulent flows. Korst's model has been used extensively in analyzing many separated turbulent boundary layer flows, particularly base flow, but also including the separation on forward facing ramps and flares.

Korst's model is based upon a reattachment criterion, and it does not include consideration of what causes the separation. Therefore, it must be combined with a model of the separation region before the separated/reattaching flow field problem can be solved in toto. Compare, for a moment, separation over a rearward facing step with that over a forward facing ramp (Figure 3-1). As noted above, Korst's model relates the flow in regions 2 and 3, using simplifying assumptions about the details of the reattachment process (R in Figure 3-1). For the rearward facing step, the flow external to the shear layer in region 2 and the reattachment point R are unique functions of the approach Mach number and turning angle at the corner. The separation length is uniquely determined by the angular geometry set by the separation/reattachment process and the step height, H. For the forward facing ramp, if there is sufficient running length ahead of the corner, the edge conditions in region 2 are again uniquely determined by the flow in region 1 and the shock induced turning angle between regions 1 and 2. In such a case the turning from region 1 to 2 is governed by a free interaction process.\* There is no corner imposing the separation point, and there is no length scale in Korst's analysis with which to select the

---

\* See below for a discussion of free vs. forced interaction.



a) Rearward Facing Step

b) Forward Facing Ramp

Figure 3-1. Schematic of Separation over a Rearward Facing Step and a Forward Facing Ramp

separation length,  $l_s$ . Thus, it is necessary to include a correlation for separation length to solve the free interaction problem of the forward facing ramp.

There is another aspect in which the forward facing ramp differs from the rearward facing step. In the latter case the flow definitely separates at the corner and reattaches on the recompression surface. But for the forward facing ramp, the flow may not separate at all, or it may not be fully separated. Thus, the Korst type analysis is applicable when the flow is fully separated in the sense that the velocity profile in the shear layer has reached a developed shape and remains unchanged in shape, that is, the velocity profiles are similar.

As with many flow models which are relatively simple physically, details of Korst type analyses of reattaching flow are somewhat complex. Details of the present analyses are included in the Appendix.

To this point the discussion has been about steady flow, and a Korst type analysis in its basic form provides no information about the transient in an unsteady flow process. On the other hand, one may anticipate that such an analysis may approximately model physical interactions which define boundaries between different flow regimes. That is, the Korst type analyses are, in a sense, analyses of limiting cases which may provide insight into the nature of the boundaries between different flow regimes.

We now set aside the rearward facing step problem and concentrate on the question of the forward facing ramp. With regard to separation, the question arises as to what occurs when the body surface extends upstream a distance less than the length,  $l_g$ , defined by the free interaction geometry. This corresponds to the condition where the separation occurs at or near the leading edge of the body. In such a case, common plateau pressure criteria for establishing the angle of separation,  $\phi$ , are inapplicable since there is not an established boundary layer approaching the point of separation. This, therefore, indicates that no longer can the angular geometry at the separation point be set by the local conditions at the point of separation, this being the definition of a free interaction, but instead is set by a downstream reattachment criteria. The latter type of separation is termed a forced interaction as opposed to a free interaction.

Recall that the Korst reattachment model provides no information about the separation process. For free interaction at separation, the plateau pressure coefficient for region 2 can be correlated approximately with the relationship

$$C_{p12} = \frac{8}{1 + 10 M_1} \quad (3-1)$$

This correlation reflects the fact that for fully turbulent separations, the plateau pressure rise is largely independent of the Reynolds number. Thus, for given  $M_1$ , the pressure in region 2 can be obtained from the Equation (3-1). The separation angle  $\theta$  and all edge conditions in region 2 can then be calculated from oblique shock relations. Then the Korst analysis can be applied to determine the unique ramp angle which satisfies that reattachment criterion.

To illustrate some of these points further, the sequence of events defining the transition from a free interaction to a forced interaction is schematized in Figure 3-2. Figure 3-2a illustrates a Type I free interaction in which the separation has not reached its full extent. In this case the ramp angle,  $\beta$ , is less than the critical angle for reattachment computed from Korst's theory. That is,  $\beta_{crit}$  represents the ramp angle associated with a large separated region in which the shear layer has become fully developed. (If the separated region is very small, then free interaction may not exist because the separation and reattachment processes may directly affect each other.) For the Type I free interaction, there is sufficient body length so that a fully developed boundary layer is established ahead of the point of separation, and the angular geometry at the separation point is determined independent of the reattachment process, and, for example, a plateau pressure



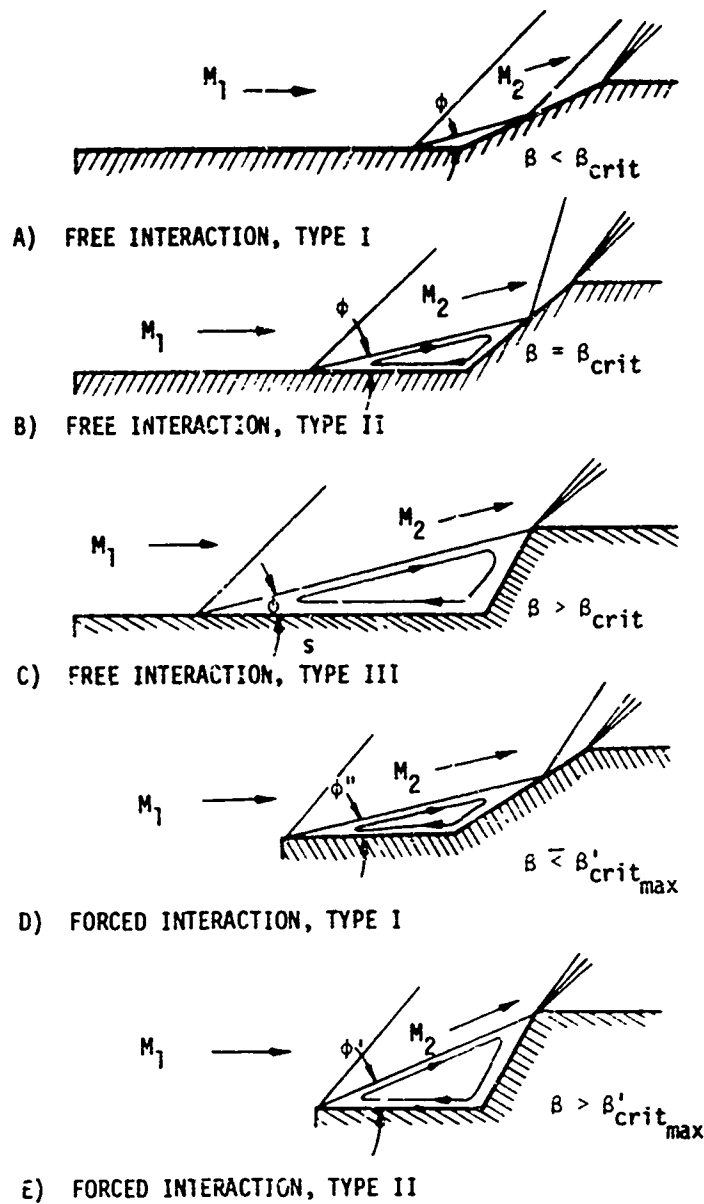


Figure 3-2. Sequence of Free and Forced Interactions for Forward Facing Ramp

correlation such as that represented by Equation 3-1 is appropriate. The length of the separated region is governed by the height of the approaching boundary layer and the ramp angle. Because the shear layer has not become fully developed, the Korst theory of reattachment is not applicable.

Figure 3-2b illustrates the second type of free interaction separation. In this instance the ramp angle is increased to a value equal to that which yields a fully separated region having a fully developed shear layer. The Korst reattachment model is applicable; hence, the critical ramp angle,  $\theta_{crit}$ , corresponds to the minimum angle for which the shear layer is fully developed. Again since an established boundary layer precedes the point of separation, the geometry at the point of separation is governed primarily by the approach Mach number and the height of the approaching boundary layer. The turning at reattachment is governed by the Korst reattachment model and oblique shock relations. This type of flow separation/reattachment can be fully analyzed within the context of the theory developed herein.

Now suppose that the ramp angle is increased further to some angle,  $\theta$ , greater than  $\theta_{crit}$ , as shown in Figure 3-2c. This represents the third type of free interaction. In this case, since the shear layer has already reached its fully developed shape, and since the ramp angle is greater than that governed by the Korst reattachment model, reattachment on the ramp face is not possible. Hence, the separation point is forced to move upstream so that reattachment occurs at the shoulder of the ramp. Since the approach Mach number dominates the angular geometry at separation (e.f. the plateau pressure coefficient correlation, Equation 3-1), the length of the separation zone is no longer dependent upon the height of the approaching boundary layer but, instead, upon the height of the ramp. Zukoski<sup>7</sup> shows this to be the case for various forward facing steps; that is, the flow geometry now behaves as though the separation occurred over a forward facing step.

The three situations depicted in Figures 3-2a-c have one thing in common, the incident boundary layer develops over a long length and there are no geometrical considerations restricting the separation point. That is, the separation location and geometry are free to adjust themselves according to local flow field interactions. Obviously, separation could be forced to occur at some point s downstream of a free interaction separation point simply by removing all of the wetted surface upstream of s. Two such forced separation situations are of interest in this study, differing in the nature of the flow at reattachment.

In the first such forced separation case, the separated shear layer reattaches on the ramp surface upstream of the shoulder, Figure 3-2d. Therefore, Korst's model is applicable to the reattachment process, and the theory for this type of forced interaction predicts the angle of separation in addition to the total amount of turning possible. Hence, there is a continuous variation of Type I forced interactions possible up to a maximum value of ramp angle,  $\beta'_{crit, max}$ . Also as the flare angle,  $\beta$ , decreases, there is an obvious lower limit for the Type I forced interaction result, that being when  $\beta = \beta_{crit'}$ , the free interaction value corresponding to the Korst limiting case. When  $\beta < \beta_{crit}$  the flow no longer separates from the leading edge but returns to one of the free interaction models shown in Figures 3-2a, b.

In the second type of forced interaction, the reattachment point is also determined by geometrical conditions rather than local flow field interactions. We designate  $\beta'_{crit, max}$  as the minimum value of  $\beta$  for which the separated shear layer reattaches at the shoulder, Figure 3-2e. Certainly an upper bound on  $\beta'_{crit, max}$  is the ramp angle corresponding to sonic flow behind the reattachment shock. The separated shear layer geometry for the Type II forced interaction is set by an equivalent ramp drawn from the leading edge to the aft shoulder.

In order to validate the hypothesis that there exists a limiting ramp angle for a free interaction reattachment, a study was initiated utilizing existing separation data. A detailed investigation of this study is presented in the Appendix. In summary, the ratio of separation length to approach boundary layer height was computed as a function of ramp angle. The experimental data is generally presented in the form of static pressure ratio distributions. By taking the plateau pressure ratio and assuming that the separated region acts essentially as an equivalent ramp surface, a separation angle was computed using oblique shock relations. Then by measuring the distance,  $l_s$ , from the ramp corner to the point of separation and applying appropriate trigonometric relationships, the length of the separated shear layer,  $l_{sep}$ , Figure 3-1, was calculated. According to the preceding discussion for a free interaction reattachment on the ramp face, Type II, there should exist a limiting ramp angle,  $\beta_{crit'}$ , such that the ratio  $l_{sep}/\delta_0$  approaches this limit. Figure 3-3 illustrates the expected behavior of the data. Actual data are not as well behaved as illustrated in Figure 3-3. However, examination of the results shown in the Appendix illustrates that the general concept shown in Figure 3-3 is likely to be valid. Naturally, owing to the indirect means in which the separation data were obtained from the pressure distributions, considering that the approaching boundary layer is affected by the presence of boundary layer trips, and, in

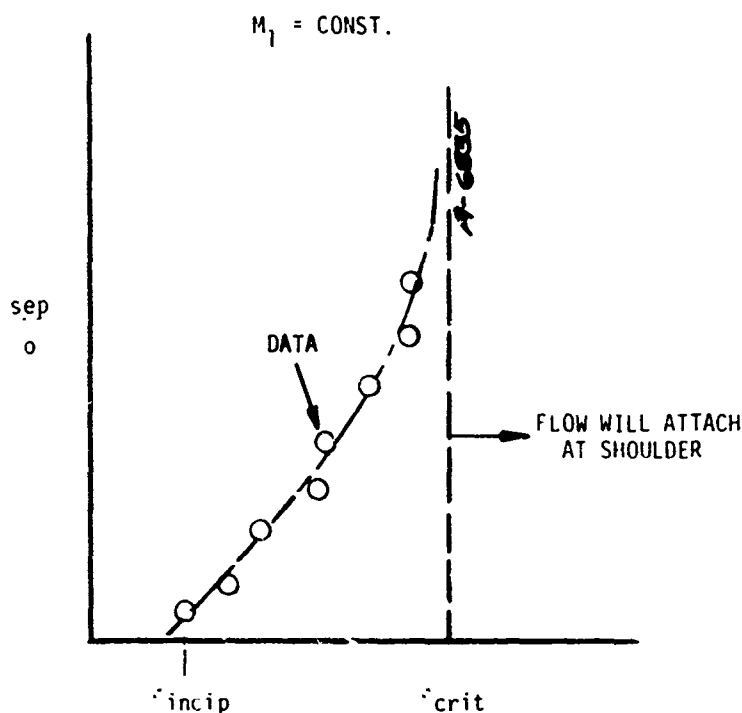


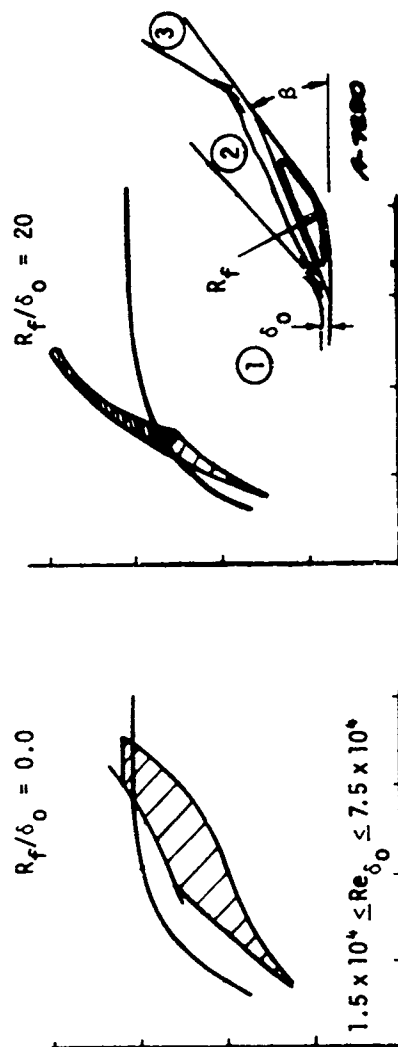
Figure 3-3. Schematic of Hypothesized limit of Separation Length

addition, allowing for a certain amount of inexactness in the data, the scatter in the results obtained is not unexpected.

The preceding discussion pertaining to the character of separated flows applies to the hypothesized theoretical model proposed herein. Portions of this theory are taken from observed experimental evidence. This is not to say that the theory is all encompassing. For instance the theory cannot predict when separation occurs; on the other hand, the question may be asked as to whether the theory can be used to predict the onset of flow instabilities for separated flows. For the case of free interaction type separations, experimental evidence indicates that, if  $\beta_{crit}$  is exceeded at a given free stream condition, the flow may become unstable.

Figure 3-4 illustrates this point more fully by comparing the present theory for predicting  $\beta_{crit}$  for a two-dimensional free interaction with experimental data gathered by Kuehn<sup>(5)</sup> et al<sup>(6)</sup>. This data indicate that, for a free interaction type separation, some type of flow anomaly is likely to result if

— SEPARATION FROM PLATEAU PRESS CORRELATION, REATTACHMENT FROM KORST



DATA OF KUEHN ET. AL.

ONE OR MORE OF  
HYSTERISIS  
UNSTEADY  
JUMP FROM ATTACHED TO SEPARATED

Figure 3-4. Theory Compared with Observed Flow Behavior on Two - Dimensional Ramps

the ramp angle exceeds  $\beta_{crit}$  as predicted by Korst's theory. These anomalies, as observed by Kuehn, et. al., may take one of three forms:

- i) The flow may be grossly unsteady with large scale oscillations
- ii) If the flow is not separated, a hysteresis in the pressure distribution may be exhibited with increasing and decreasing Mach number variation, and
- iii) If the ramp angle exceeds the critical value,  $\beta_{crit}$ , the flow may jump from an attached flow to a fully separated flow.

These behavior patterns indicate that the boundary defined by  $\beta_{crit}$  is significant in predicting the nature of the stability of the flow separation.

The question now arises as to how the Korst theory can be used to gain insight into the nature of flow separations occurring on the nosetip shapes of interest and how this information can be related to the prediction of the limits of flow instability on these shapes. For shapes of interest, if  $\theta_2$  falls within the limits of allowable reattached solutions, then the method can be used to predict the free or forced interactions which exist, and the flow should be steady (Figures 3-2b, c, d). The results of the analysis for forced interaction (Figure A6-4 of the Appendix) indicate that the values of  $\theta_2$  tested in this program exceed the value of  $\beta_{crit_{max}}$  so that the reattachment should be forced to the shoulder. Also, the tip lengths tested are considerably less than lengths consistent with free interaction at separation for such large values of  $\theta_2$ ; therefore, it is concluded that in these tests the separated flows should be Type II forced interaction flows, Figure 3-2e. In fact this was observed to be the case for all steady separated flows in the test program.

The next question that is posed is how the Korst model can be used to predict the limits of flow stability, if at all. Consider the shapes of interest shown in Figure 3-5. Figure 3-5a depicts the case discussed in the previous paragraph relating to the steady forced interaction which results in the flow reattaching at or near the shoulder. However, if the geometry is such that the tip protrudes through the bow shock that would exist if the tip were not present, and if, in addition, the ratio of  $l/D$  as shown in the sketch is such that an attached conical oblique shock could not be realized, then it is expected that the flow will be unstable, Figure 3-5b. That is to say, if the effective conical body angle,  $\sigma_{eff}$ , created by the separation exceeds the maximum value for the occurrence of an attached oblique shock then flow instability will occur. The cause is illustrated in Figure 3-5c and 3-5d. If the separation were to occur from the tip to the shoulder, a strong shock would have to appear as shown in Figure 3-5c (assuming the flow is steady). However, this steady state can not persist because the large separation bubble required

cannot be sustained by the subsonic flow behind the strong shock. The bubble must collapse, as shown in Figure 3-5d. However the flow/geometry conditions are incompatible with the limited separation region (Figure 3-5d), and the separation point moves back toward the tip, leading to the observed oscillatory flow. This does not preclude, however, the existence of steady flow with a completely attached boundary layer and a shock structure similar to that in Figure 3-5d.

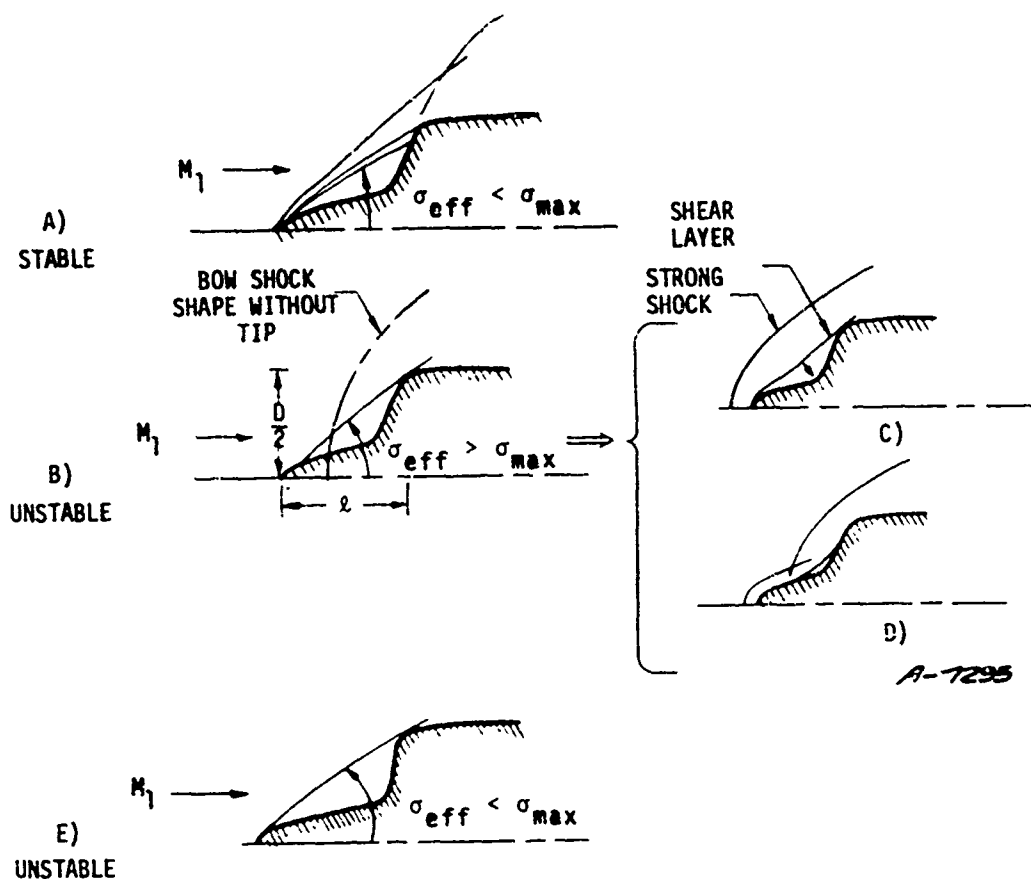


Figure 3-5. Limits of Instability as Predicted from Theory

In the current experiments it was shown that when the flow is separated and  $\sigma_{eff}$  exceeds the maximum value for an attached shock, flow instabilities did occur. This seems to be the extent to which the current theory can be used to predict the occurrence of flow instability. That is, it was observed in the current test series that a range of strong instabilities exists for instances where the  $l/D$  did not indicate that  $\sigma_{max}$  would be exceeded. The cause of this

type of instability is not fully understood and, therefore, illustrates the importance of determining these limits experimentally.



## SECTION 4

### STABILITY CORRELATION CONSIDERATIONS

A comparison of the current correlation technique was made with the data taken by Wood at Mach 10 as shown in Figure 4-1. It is expected that above  $M = 5$  there will not exist a strong Mach number dependency upon stability limits. This is based upon the fact that the conical shock detachment angle does not vary greatly with Mach number above  $M = 5$ .<sup>8</sup> Secondly, as previously mentioned, the upper limit of the stability regime is associated with separated flow attaching at the shoulder, and for  $M \geq 5$  the shock structure is relatively insensitive to changes in Mach number. The comparison of the regimes of unsteady flow for the current tests and Wood's data illustrates a drastic difference in the extent of the limits, Figure 4-1. In addition the data point shown for an AVCO/VKI test indicates that according to Wood's data the flow should have been unsteady, but in fact the flow was steady.\* The Series E data points, which were both unsteady are also shown in Figure 4-1.

The one obvious difference between Wood's models and the present series of models is the difference in the tip angle; that is, Wood only tested models with spike-like protrusions,  $\theta_1 = 0^\circ$ , and in the present series of tests the tip angle varied from  $20^\circ$  to  $40^\circ$ . It seems clear that the tip angle probably has a strong influence upon the stability limits. One reason for this postulation is that, as mentioned previously, as the tip angle increases and approaches the line tangent from the nose to the shoulder then the body becomes a plain cone cylinder and is obviously steady. At the other extreme when  $\theta_1$  is small, that is, when the tip approaches a spike configuration, then for a forced separation the separation bubble volume is large. Hence, a stability condition can be hypothesized as follows. If a forced separation exists and the bubble is large, assume that the dividing streamline is perturbed from being straight and instead assumes a disturbed sinusoidal condition. The question arises as to whether or not this disturbance will amplify and cause a flow instability to exist. In a very general sense the forces which will tend to nullify the disturbance are the momentum in the shear layer and the restoring force of the

\*Private communication from B. E. Richards.

# REGIONS OF PULSATIONS

AVCO MODEL (VKI) WOOD'S RESULTS

SERIES E (LONG TIP)  
 $M_\infty = 10^1$   
 $Re/\delta^* = 8.1 \times 10^6$

SERIES E (SHORT TIP)  
 $M_\infty = 10^1$   
 $Re/\delta^* = 8.1 \times 10^6$

NOL-8 SERIES  
 $M_\infty = 5$   
 $Re/\delta^* = 20 \times 10^6$

VKI TEST:  
 $M = 15.6$   
 $Re/\delta^* = 5.7 \times 10^6$

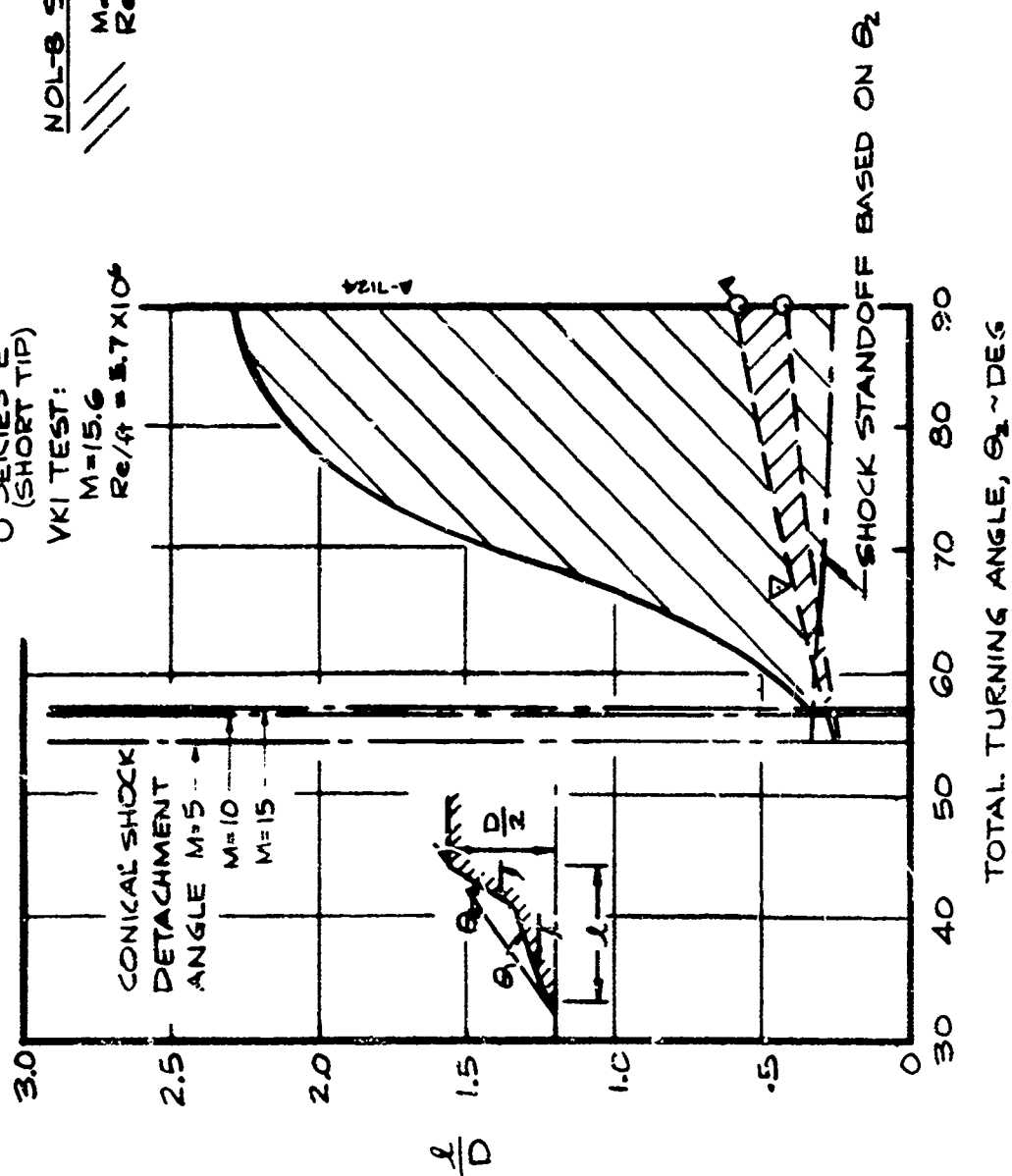


Figure 4-1. Comparison of Wood's and NOL-8 Series Test Results - Preliminary Correlation

bubble. Viscous effects in the shear layer will tend to retard shear layer momentum. The restoring force of the bubble is inversely proportional to the size of the bubble; hence, one would expect that for small  $\theta_1$  the flow is more likely to become unsteady. This is a broad brush treatment of a very difficult problem; however, the basic precepts seem very reasonable.

It was, therefore, concluded that  $\theta_1$  must play a significant role in creating the potential for unsteady flow. The body of data from the current test series was replotted along with Wood's data in a new correlation format in Figure 4-2. Here another dimension has been added to the correlation, namely, planes of constant  $\theta_1$ . In place of  $\theta_2$  used by Wood, it seems appropriate to use  $\Delta \theta = \theta_2 - \theta_1$  which leaves Wood's data unchanged since  $\theta_1 = 0^\circ$ . In addition the left hand boundary which was previously based upon the critical angle for shock detachment,  $\theta_{2\max}$ , for Wood's data was extended to correspond to the maximum combination of angles  $\theta_{\max} = [(\theta_1 + \Delta \theta)]_{\max}$  to yield shock detachment via a conical shock plus a two dimensional shock. This left hand limit was established for  $M = 5$  but should not change significantly for higher Mach numbers.

The result of this correlation is a volume of instability; that is, any points falling inside the volume should be unstable. One of the particularly satisfying aspects of this correlation is that the previously mentioned AVCO/VKI data point falls outside of the volume of instability and explains why the flow was steady in that test. The volume shown in Figure 4-2 also makes it apparent that there is a significant increase in the limits of the unstable flow regime as  $\theta_1$  decreases.



## SECTION 5

### CONCLUDING REMARKS

The fluid mechanical interactions associated with the flow fields of interest in this study are quite complex. It is certainly within existing technical capability to develop computer codes to obtain exact solutions of the full Navier-Stokes equations of motion (though the problems associated with accurately representing the transient shock structure are formidable). Such an approach would enable us to study the detailed interactions which lead to instability onset and to parametrically vary key shape and flight configurations to determine the dependence of instability onset. Each such calculation would, in itself, require an exorbitant amount of computer time, making such an approach economically unacceptable. In addition, we have very little understanding of how to model turbulent transport properties for transient flow, and the regimes of interest in flight are for transitional and fully turbulent boundary layers. Therefore, this program is oriented toward a semi-empirical approach to solve the problem of pulsating flow on ablated shapes.

The result is a collection of experimental data and empirical, semi-empirical and approximate analytical models which are patched together to form a "solution" to the problem. As is often the case, the simpler, engineering approach is more piecemeal than an exact numerical solution would be, because the engineering solution is a synthesis of many fragments. In such a situation it is easy to focus on the parts and to lose sight of the whole of the model. Therefore, we conclude with a synopsis of the major conclusions of this study.

The overall objective is to define the envelope of instability onset for ablated shapes of interest in flight environments. There is no data to define shapes associated with flight to the required precision for our needs. The flow field/model shape interaction is qualitatively the same for wind tunnel conditions as it is for flight, and Mach number effects are relatively weak and can be adequately accounted for with approximate analyses. Therefore, the solution is based on ground test data of low temperature ablator shape change experiments.

The highlights of the study are:

- Realistic ablated shapes are represented by a simplified but adequate model which has been described by two angles, three radii, and a length.
- The three parameters most important to instability onset are the two angles,  $\theta_1$  and  $\theta_2$ , and the length to diameter ratio,  $l/D$ .
- The flare and shoulder radii,  $R_f$  and  $R_s$ , are of secondary importance for the range of shapes likely to be encountered in realistic trajectories.
- The nose radius appears to be of intermediate, but closer to secondary than primary, importance. The phenomenology of the nose radius effect is unclear.
- As long as the flow is fully turbulent, Reynolds number variations have a weak effect.
- For  $M \geq 5$ , Mach number effects should be relatively small and predictable.
- For shapes and conditions of interest, separation of the boundary layer (when it separates) is of the forced type and the shear layer reattaches at or very near the shoulder. Therefore, free interaction theory results cannot be used directly to predict the separated flow.
- As noted by Maull and Wood, the inviscid, conical detachment angle for the recompression cone ( $\theta_2$ ) is important in determining the envelope of instability onset.
- Wood's envelope of instability onset was modified and extended to realistic ablated nosetip shapes. The forecone angle,  $\theta_1$ , is a strong parameter in this correlation, and as  $\theta_1$  increases, the range of  $\theta_2$  and  $l/D$  for which the flow field pulsates decreases rapidly.

#### REFERENCES

1. Maull, D. J., "Hypersonic Flow over Axially Symmetric Spiked Bodies," J. of Fluid Mechanics, Vol. 8, Part 4. Aug. 1960.
2. Wood, C. J., "Hypersonic Flow over Spiked Cones" J. of Fluid Mechanics, Vol. 12, Part 4. April 1962.
3. Anderson, A. D., "Analysis of PANT Series A Rough Wall Calorimeter Data --Part II: Surface Roughness Effects on Boundary Layer Transition," Aerotherm Report 78-81
4. Baltakis, F. D., "Performance Capability of the NOL Hypersonic Tunnel," NOLTR 68-187, October 1968.
5. Kuehn, D. M., "Experimental Investigation of the Pressure Rise Required for the Incipient Separation of Turbulent Boundary Layers in Two Dimensional Supersonic Flow," NASA Memo 1-21-59A, Feb. 1959.
6. Chapman, D. R., Kuehn, D. M., and Larson, H. K., "Investigation of Separated Flows in Supersonic and Subsonic Streams with Emphasis on the Effect of Transition," NACA TN 3869, Mar. 1957.
7. Zukoski, E. E., "Turbulent Boundary-Layer Separation in Front of a Forward-Facing Step," AIAA Journal, Vol. 5, No. 10. Oct. 1967.
8. NACA 1135, "Equations, Tables, and Charts for Compressible Flow," Ames Research Staff, 1953.

APPENDIX A

ANALYSIS OF STABILITY OF FLOW SEPARATIONS ON  
EICONIC SURFACES

Larry Cooper  
Thomas J. Dahm



# LIST OF SYMBOLS FOR APPENDIX A

$C_2$	Crocco number at edge of shear layer
$C_p$	pressure rise coefficient
erf	error function
$G_{ib}$	dimensionless bleed rate
$I_1, I_2$	integral properties of the shear layer
$l_{sep}, l$	length of shear layer
$M$	Mach number
$\dot{m}_{ib}$	bleed flow per unit width
$P$	static pressure
$P_t$	total pressure
$T$	static temperature
$T_t$	total temperature
$u$	velocity in direction of reference coordinates
$v$	velocity transverse to reference coordinates
$x, y$	intrinsic coordinates
$X, Y$	reference coordinates
$\alpha_R$	angle between reference axis and reattachment streamline

# LIST OF SYMBOLS FOR APPENDIX A (Continued)

$\alpha_{SEP}$	angle separation makes with flow in Region 1
$\beta$	ramp or total turning angle
$\beta_{CRIT}$	ramp angle for fully developed shear layer
$\beta_{INCIP}$	ramp angle for which separation just begins
$\beta_{max}$	maximum ramp angle for forced separation
$\delta_o$	height of approaching boundary layer
$\delta_{12}$	inviscid flow turn from 1 to 2
$\delta_{23}$	inviscid flow turn from 2 to 3
$\Delta x$	distance from corner to point of separation
$\Delta$	equal to $y_m$ in magnitude
$\eta$	dimensionless coordinate
$\sigma$	turbulent mixing parameter
$\rho$	density
$\epsilon$	eddy viscosity
$\theta_1$	angle of tip surface
$\theta_{12}$	shock angle off tip
$\theta_{23}$	shock angle off flare or ramp
$\gamma$	ratio of specific heats
$\tau$	static temperature ratio, $T/T_2$

LIST OF SYMBOLS FOR APPENDIX A (Concluded)

$\lambda$  total temperature ratio,  $T_t/T_{t2}$

$\phi$  velocity ratio,  $u/u_2$

Subscripts

j dividing streamline for  $G_{ib} = 0$

s dividing streamline for  $G_{ib} \neq 0$

1,2,3,4 separated flow regions

M signifies distance between intrinsic and reference coordinate systems

R point near edge of shear layer

## SECTION A1

### INTRODUCTION

The possibility of encountering unsteady flow oscillations about biconic and spiked bodies has been noted in the literature. Several experimenters such as Wood<sup>(A1)</sup>, Maull<sup>(A2)</sup>, and Mair<sup>(A3)</sup> observed these oscillations on wind tunnel models and, to a limited extent, correlated the bounds of steady and oscillatory flow based upon the geometry of the body. Few attempts were made to model the mechanism which triggers the unsteady condition. Maull suggested that the instabilities are triggered by separations which lead to strong family reattachment shocks. He suggested that this would lead to a growth and collapse of the separated zone. The present paper offers a proposed model which is intended to predict the separation characteristics about a biconic shape and indicate when oscillatory flow is likely to occur.

## SECTION A2

### APPROACH

The approach to the problem of studying the onset of flow instabilities was to first look at the possible causes for unsteadiness rather than to attempt a full model of the oscillatory process itself. From a design standpoint the critical question is when the oscillations occur and how they can be avoided.

At present the general consensus is that the flow oscillations are related to changes in the effective geometry of the body due to growth of the separation bubble. (A1) (A2) (A3) The bubble is thought to grow to some critical state at which time further growth cannot be sustained and the bubble suffers a collapse due to outflow near the shoulder. The exact mechanism of bubble growth and collapse is a matter of speculation at this point.

The approach taken in the present study was to examine the separation and reattachment mechanisms for the steady flow case and to observe when these steady flow mechanisms become violated. It is hypothesized that when these critical steady separated conditions are violated that a readjustment in the flow relating to either steady or quasi-pulsating reattachment at the shoulder will occur or the flow will become completely oscillatory.

The present flow model consists of a mechanisms for flow separation, either free-interaction or forced separation, a free shear flow analysis of the separated zone based upon the theory of Kozik, and reattachment turning conditions relating to oblique shock theory.

## SECTION A3

### A3.1 BOUNDARY LAYER SEPARATION

There are several references in the literature which discuss, in detail, what is known about the mechanism of turbulent flow separation induced by steps and ramps in supersonic flow. Suffice it to say that the separation is caused by the fact that the momentum of the boundary layer flow cannot negotiate a rapid rise in pressure associated with the compression at a corner.

Figure A3-1 illustrates the salient features of the type of flow separation considered. At a given value of approach Mach number,  $M_1$ , there will exist some critical ramp angle,  $\beta_{\text{INCIP}}$ , which corresponds to the appearance of an inflection point in the static pressure rise as measured at the wall surface (Figure A3-1a). As the angle  $\beta$  is increased to values greater than  $\beta_{\text{INCIP}}$ , holding  $M_1$  fixed, the extent of the separated zone continues to grow. Figure A3-1b illustrates a typical pressure distribution for a fully separated region. The pressure rises from its initial value up to a so-called plateau level. Experiments have shown that the rise to the plateau level is mainly Mach number dependent and that the plateau level agrees well with the inviscid pressure in Region 2. During this phase of separation the length of the separated region,  $l_{\text{sep}}$ , correlates well with the height of the approaching boundary layer,  $\delta_o$ , and the plateau pressure coefficient,  $C_{p1,2}$ . However, it is well known that, for a forward facing step with sufficient running length ahead of the step, the separated flow will always attach at the shoulder (A4). In this case the length of the separated region no longer is dependent upon the height of the approaching boundary layer but instead upon the height of the step and the plateau pressure coefficient. The question then arises whether there exists some critical ramp angle,  $\beta_{\text{crit}}$ , Figure A3-2, that corresponds to an asymptotic limit for  $l_{\text{SEP}}/\delta_o$ . It is supposed that at this value of  $\beta$  the separated shear layer reaches a similar profile and achieves the maximum allowable reattachment pressure on the face of the ramp. A further increase in  $\beta$  will then drive the reattachment toward the shoulder while the shear layer separation angle and the plateau pressure coefficient are unchanged. Existing data have been analyzed to verify this hypothesis. The results are summarized in Section A3.2.

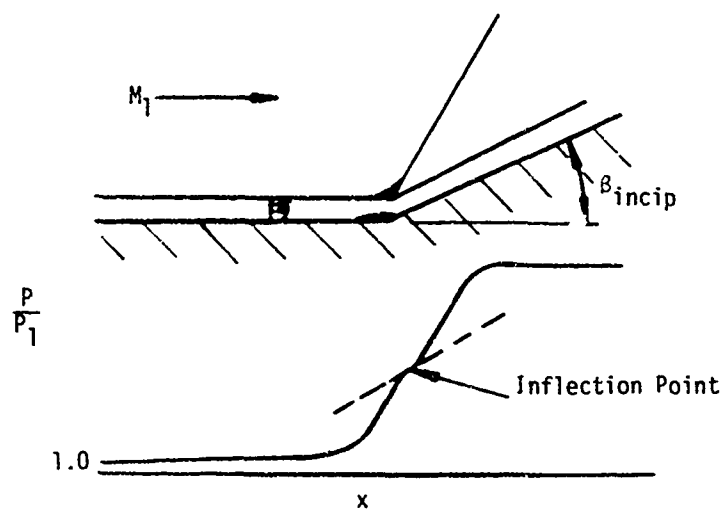


Figure A3-1a. Incipient Separation

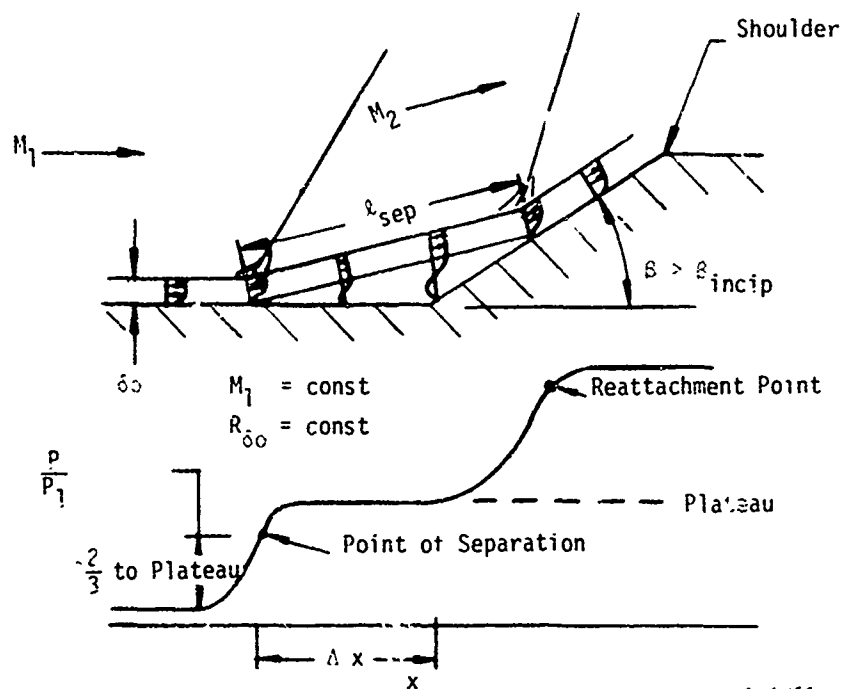


Figure A3-1b. Fully Separated Flow

Figure A3-1. Schematic of Ramp/Flare Separation

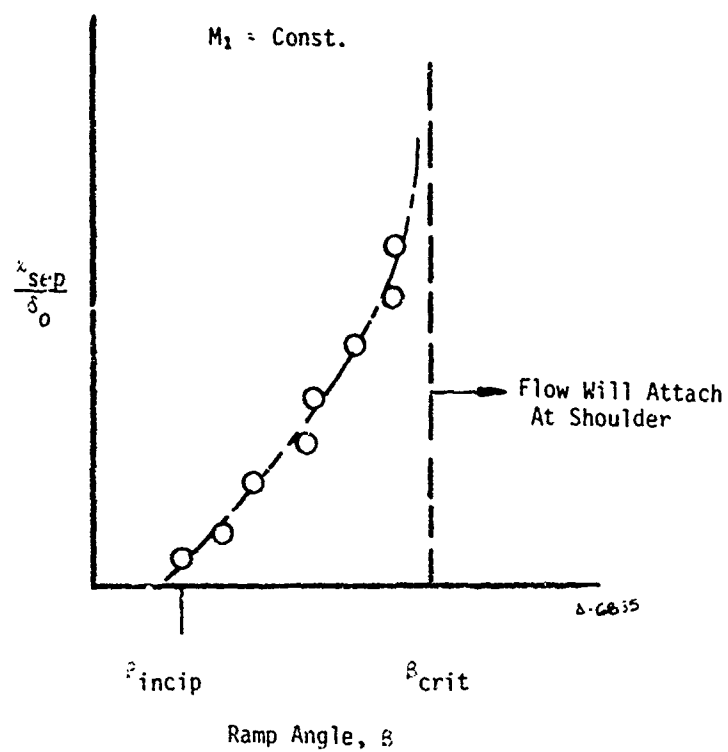


Figure A3-2. Schematic of Hypothesized Limit of Separation Length



### A3.2 EXTENT OF SEPARATION LENGTHS FOR COMPRESSION CORNERS

The literature contains a limited number of attempts to correlate separation lengths. None of these attempts to correlate  $l_{SEP}$  is wholly extensive or successful. The available data consists mainly of two-dimensional and nearly two-dimensional (flared surfaces far from the axis) pressure distributions. Therefore, little or no data is available which considers a strong radial effect. In addition the literature is nearly void of consideration of flow separations such that the required turning at reattachment exceeds the critical turning angle for an attached oblique shock. The small amount of data that is available indicates that the flow may be unstable if this condition is exceeded. A third type of data that is lacking is that which considers separations at the leading edge in which the free interaction would no longer allow reattachment at the ramp shoulder; this would be termed a forced separation.

To correlate turbulent separation lengths at supersonic Mach numbers for ramp-induced separation, we define the point of separation as shown in Figure A3-1b. If the plateau pressure level is not clearly definable, an empirical plateau coefficient such as

$$C_P = \frac{3.2}{8 + (M_0 - 1)^2} \text{ (Reference A5)}$$

is used to define the plateau level. Given the plateau level either by inspection of the experimental pressure distribution or from the above expression, the angle of separation can be determined from the two-dimensional oblique shock relations.

$$\delta_{12} = \delta_{12} \left\{ M_1, \frac{P_2}{P_1} \right\}$$

With the angle of separation,  $\delta_{12}$ , and the measured value of  $\Delta X$ , the separation length,  $l_{SEP}$ , can be determined from geometric considerations.

$$l_{SEP} = l_{SEP} \left\{ \Delta X, \alpha_{SEP}, \beta \right\}$$

This procedure defines a uniform method of reducing the pressure distribution data into the desired form. The data sources, References A6 - A14, are shown in Figure A3.3. The data is shown plotted in Figures A3-4 to A3-8. Also shown is the two-dimensional free-interaction critical angle for reattachment. That is, the ramp angle that produces a separation which extends sufficiently so that the velocity profile in the shear layer has become similar (see Section 3.0 in body of report).

Source No.	Source Name	Symbol	Ref
1	Settles	○	A6
2	Kuehn	□	A7
3	Law	◇	A8
4	Roshko	△	A9
5	Chapman	▵	A10
6	Sterrett	▷	A11
7	Todisco	◻	A12
8	Spaid	◊	A13
9	Kuehn	◡	A14

Figure A3-3. Sources of Separation Data

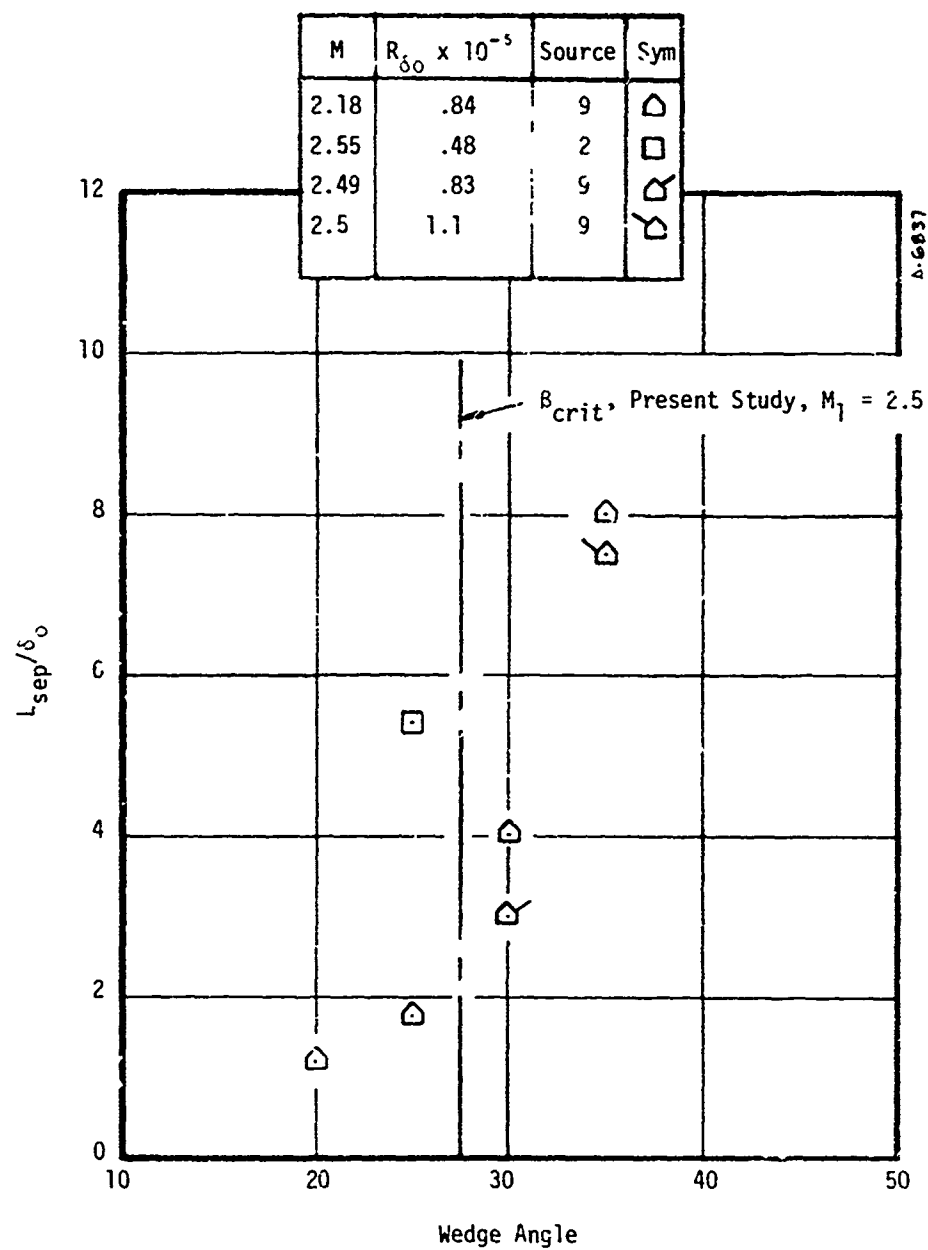


Figure A3-4. Separation Lengths,  $M_1 = 2.0 - 2.5$

Note that all points to the right are from source 9.

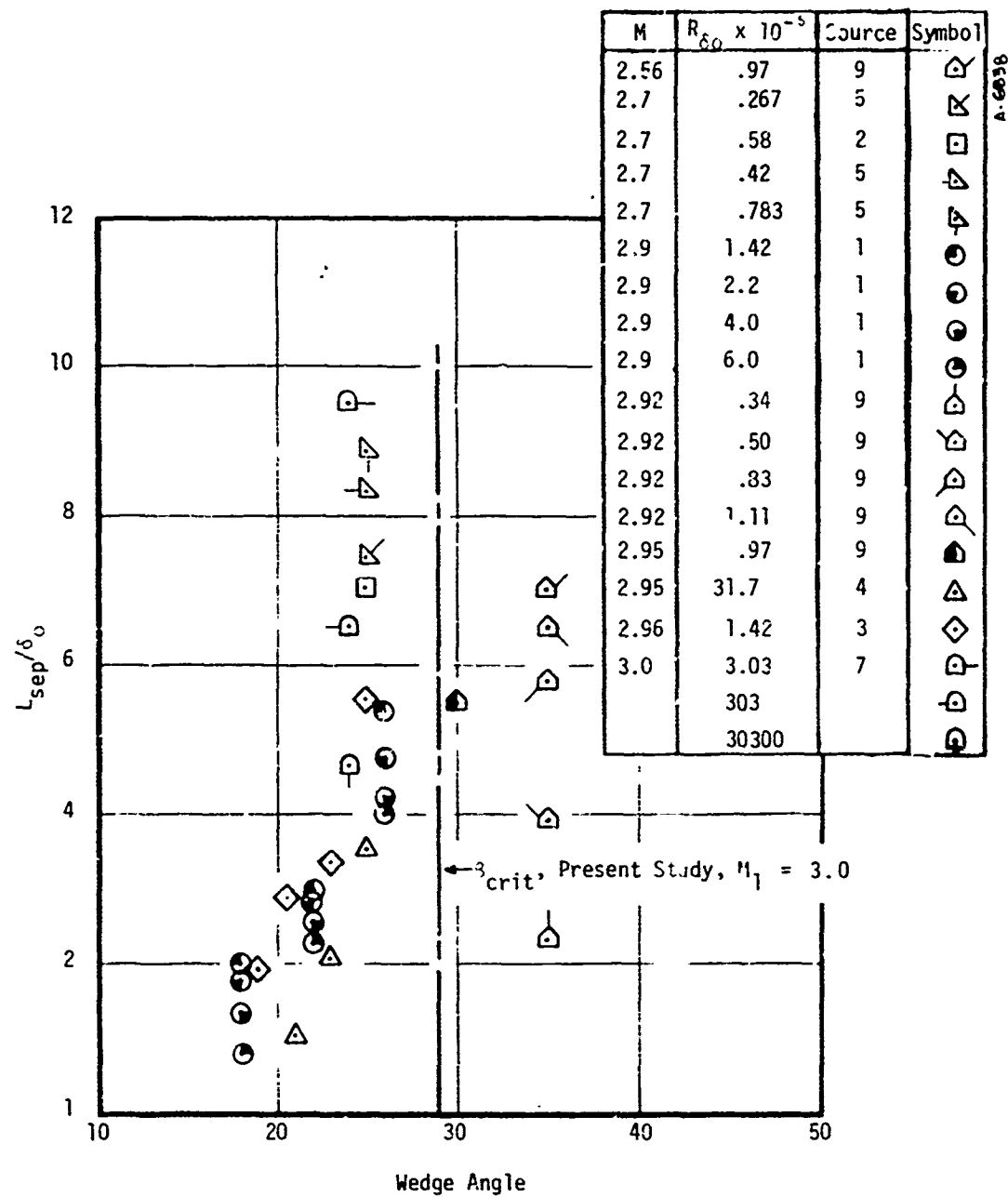


Figure A3-5. Separation Lengths,  $M_1 = 2.5 - 3.0$

Note that all points to the right are from source 9.

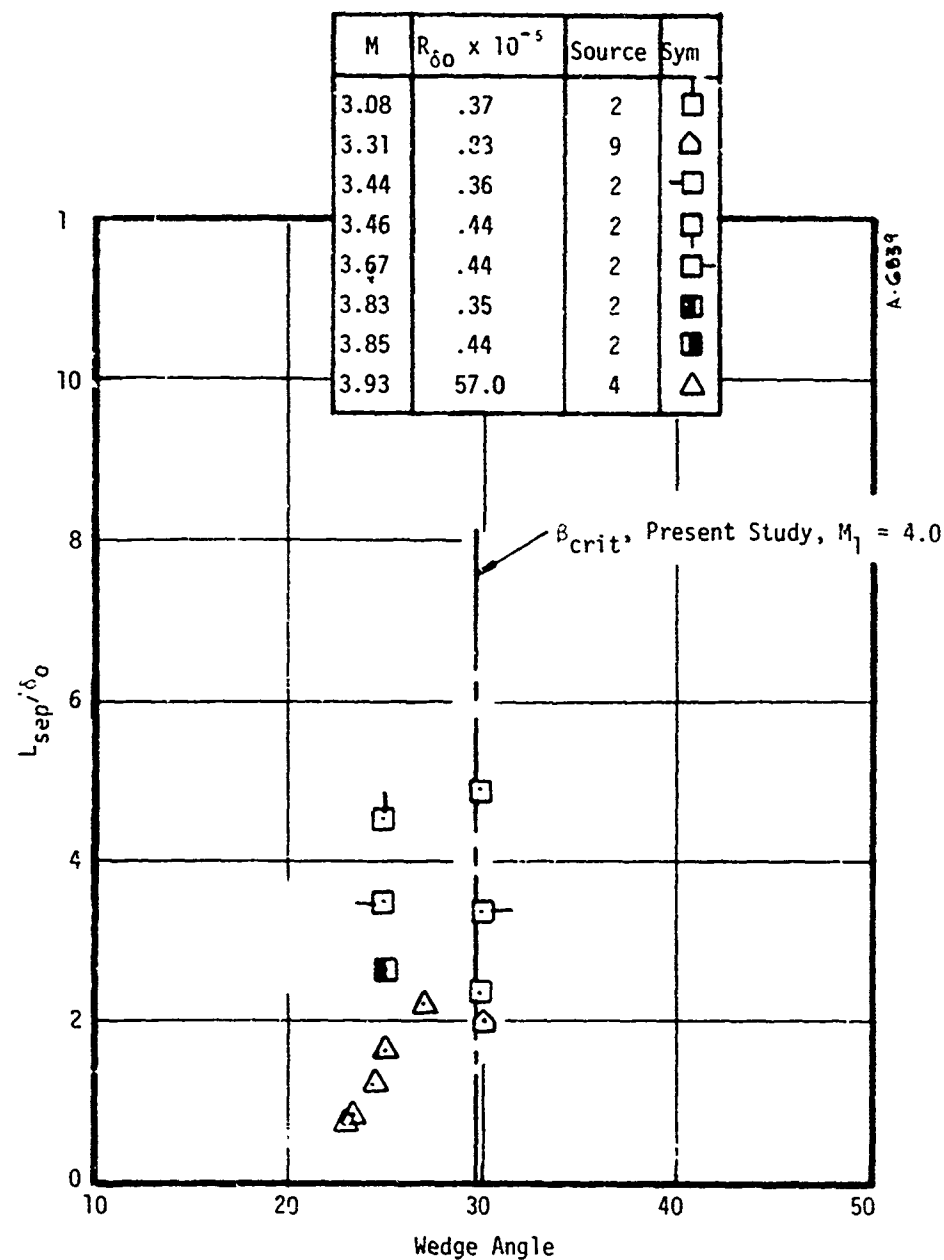


Figure A3-6. Separation Lengths,  $M_1 = 3.0 - 4.0$

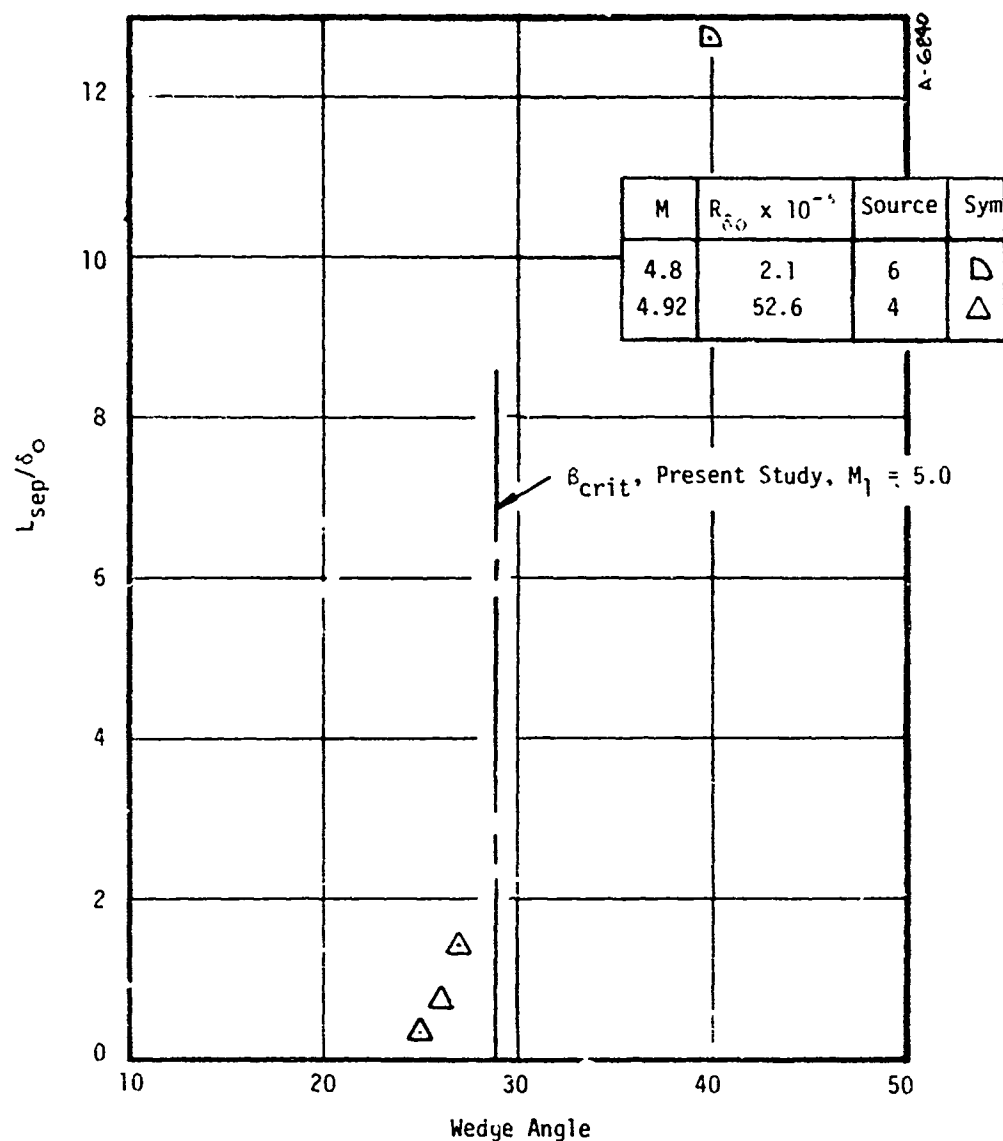


Figure A3-7. Separation Lengths,  $M_1 = 4.0 - 5.0$

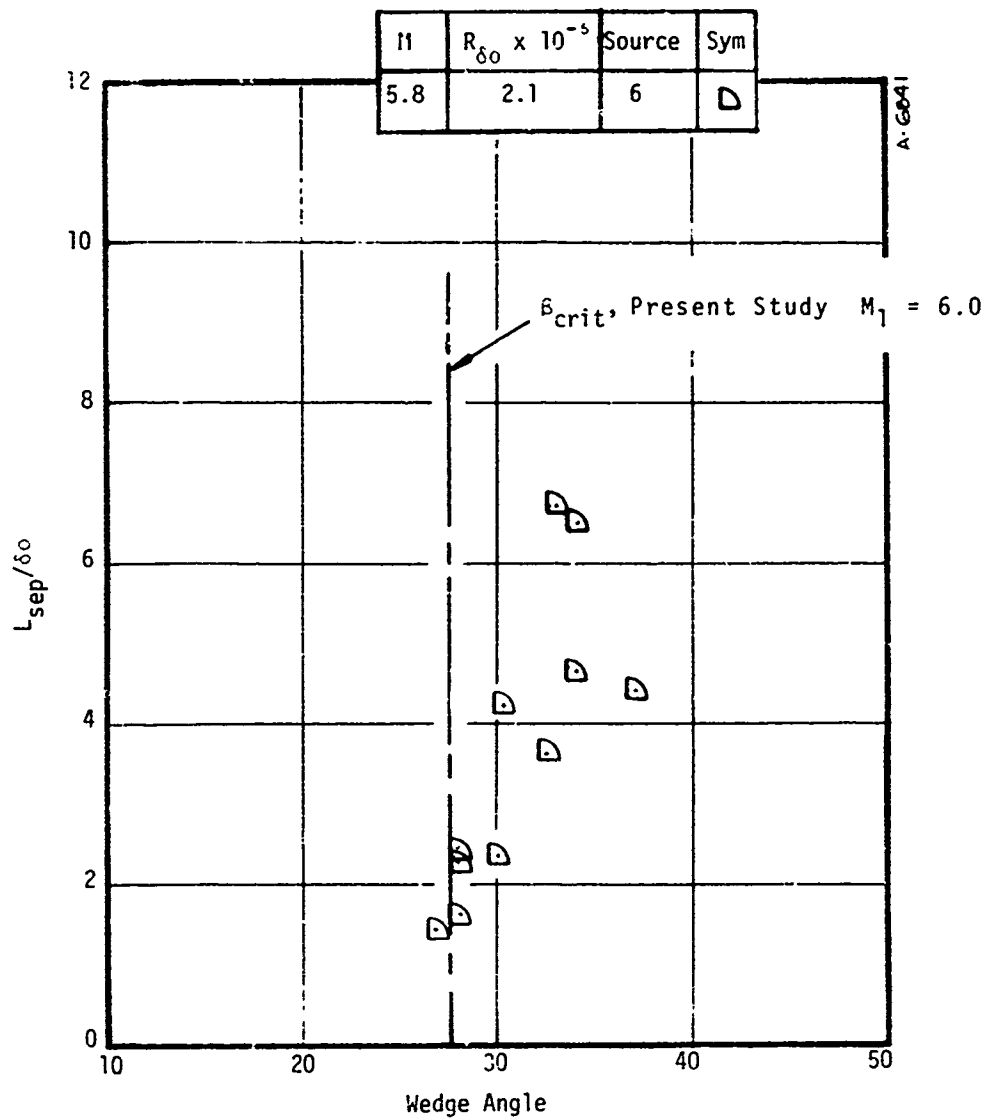


Figure A3-8. Separation Lengths,  $M_1 = 5.0 - 6.0$

## SECTION A4

### TURBULENT MIXING ANALYSIS FOR NON - ISOENERGETIC SEPARATED FLOWS

#### A4.1 APPROACH AND ASSUMPTIONS

In order to establish a criterion for reattachment of the separated shear layer, a defining set of conditions must be imposed upon continuity, momentum, and energy considerations in the shear layer itself and at the reattachment point. The separation bubble behind a backward facing step has been analyzed by Korst (A15) and Page (A16). Their approach for the base pressure problem has been extended in the present case to consider the reattachment of a separated shear layer produced by a forward facing compression surface. The essential ingredients to such an analysis are:

- Continuity considerations
- Momentum considerations
- Energy considerations
- A turning criterion at reattachment based upon oblique shock theory.

The mixing theory contains the following assumptions:

- The mixing region is at a state of constant pressure
- The length of the mixing zone is sufficiently long so that the velocity profiles in the mixing layer have become similar
- The fluid velocities in the separation bubble are small compared to velocities in the mixing zone
- The boundary layer approaching the point of separation is thin
- The fluid is an ideal gas (i.e., it obeys Boyle's and Gay-Lussac's laws).



#### A4.2 MODEL FORMULATION

The geometric aspects of the flow separation model are depicted in Figure A4.1. Here the boundary layer approaching the separation point,  $a$ , is considered either thin or nonexistent, as in the case of a leading edge separation. After separation occurs by whatever mechanism has produced it, a free-shear layer will develop between the external inviscid flow in Region 2 and the low velocity flow in Region 4. The mixing process can be considered to occur at constant pressure by virtue of a quasi-boundary layer assumption of zero normal and axial pressure gradient. As shown, the abrupt turn of an approaching supersonic flow caused by the separation induces a separation shock to form emanating from point,  $a$ , and will cause the flow to turn an amount  $\delta_{12}$ .

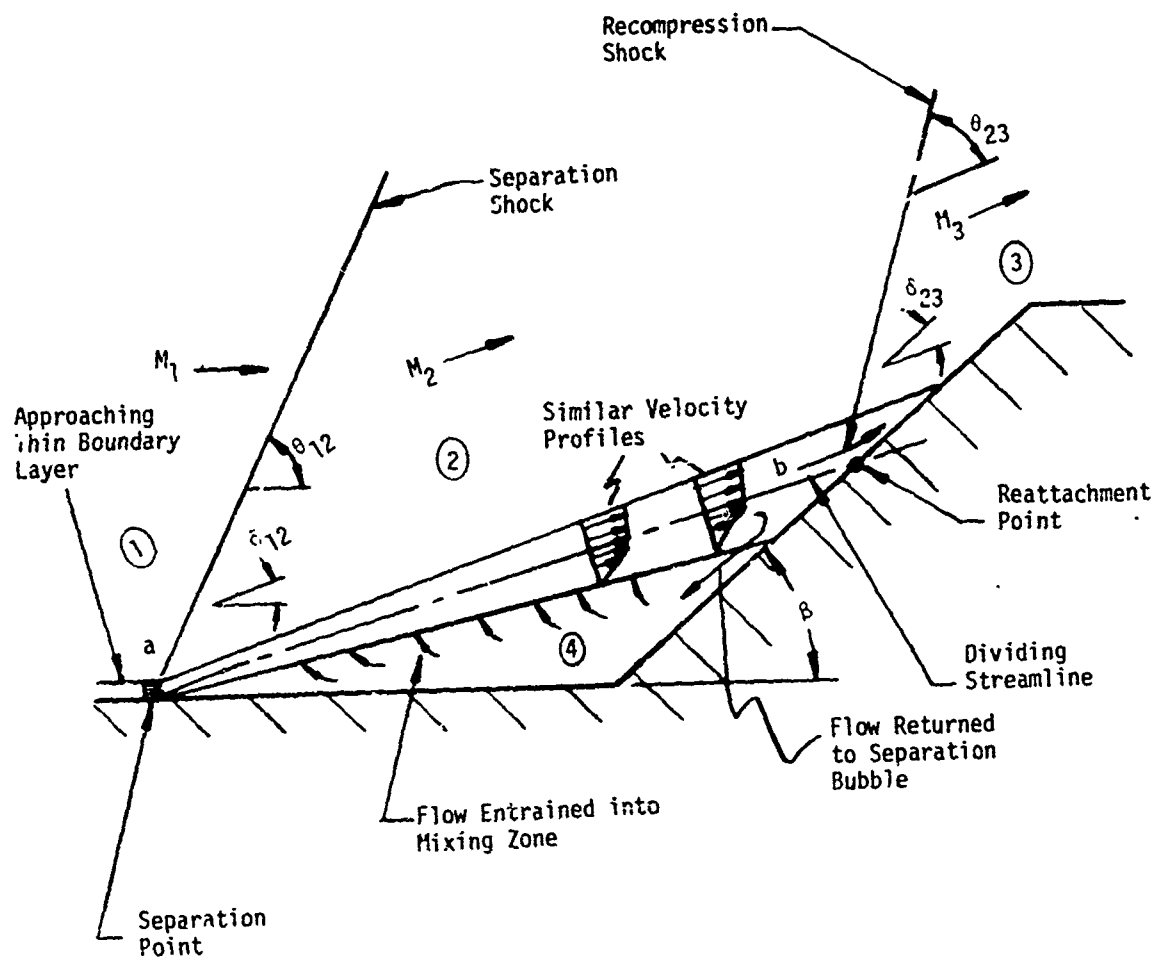
At some distance downstream of the separation point (on the order of several approach boundary layer thicknesses), the velocity profiles in the shear layer become similar. The point of reattachment is determined by a so-called escape criterion. That is, the point of reattachment acts as essentially a stagnation point below which the flow in the shear layer must return to the separation bubble, Region 4. In order for a steady separation to exist, the amount of flow returned to the separation bubble must be exactly equal to the amount of fluid entrained from the bubble by the shear layer. This condition also establishes the existence of the dividing streamline within the shear layer. That is, all flow below the dividing streamline is trapped within the separation bubble and, conversely, all flow outside of the dividing streamline never enters the separation bubble. It is assumed here, as is the usual case, that the dividing streamline is straight between points  $a$  and  $b$ .

Upon reattachment of the dividing streamline to the ramp surface, the flow must undergo a second abrupt change in flow direction,  $\delta_{23}$ . This turning of the flow in Region 2 at Mach number,  $M_2$ , produces a recompression shock as shown. Hence, the total amount of turning produced by the separation and reattachment shocks must equal the final flow direction,  $\beta$ . Hence

$$\beta = \delta_{12} + \delta_{23} \quad (\text{A4-1})$$

#### A4.3 INTRINSIC AND REFERENCE COORDINATE SYSTEMS

Because the mixing equations are solved subject to a given simple set of boundary conditions independent of geometric considerations at the point of reattachment and that determination of dividing streamline position is based upon integral considerations of continuity and momentum, there exists the need to establish two sets of coordinate systems. These two coordinate systems will



A-6045

Figure A4-1. Separation Model Geometry

be termed the  $X, Y$ , or reference system and the  $x, y$ , or intrinsic system. The exact reasons for establishing two systems and relating them will become apparent in the paragraphs which follow.

Figure A4.2 points out some of the considerations which establish the need for a two coordinate system approach. Figure A4.2a defines the intrinsic system,  $x, y$ , from which the velocity profile is defined based upon the edge conditions in regions 2 and 4. The profile independent variable is defined as,  $\eta = \sigma y/x$ , in the intrinsic system where  $\sigma$  is the turbulent mixing parameter. The extent of jet spreading is defined by lines a and e in Figure A4-2b. Figure A4.2b shows the relation of the reference system and the intrinsic system. The reference system is orthogonal and aligned with the  $u_2$  direction. Introduction of the profile defined in the intrinsic system shown as line d is required since the profile is described in terms of the variable,  $\eta$ . It is necessary, therefore, to define the displacement of the  $Y$  and  $y$  coordinates, namely,  $y_m$ . It will be shown that this displacement between the  $u_2$  direction (line b, reference system) and the intrinsic direction (line d) can be determined from the integral relations defining the location of the dividing streamline, c. Hence, the two coordinate systems coincide at  $x = X = 0$  and elsewhere are related by

$$X \cong x \quad (A4-2a)$$

$$Y = y - y_m \quad (A4-2b)$$

#### A4.4 VELOCITY AND TOTAL TEMPERATURE PROFILES

The turbulent equations of motion and energy in two-dimensional space are given by,

$$\rho u \frac{\partial u}{\partial x} + \rho v \frac{\partial u}{\partial y} = \frac{\partial}{\partial y} \left( \epsilon_0 \frac{\partial u}{\partial y} \right) \quad (A4-3)$$

$$\rho u \frac{\partial T_t}{\partial x} + \rho v \frac{\partial T_t}{\partial y} = \frac{\partial}{\partial y} \left( \epsilon_0 \frac{\partial T_t}{\partial y} \right) \quad (A4-4)$$

Equation (A4-4) is derived based on the assumption of unity Prandtl number. Hence, it can be seen that Equations (A4-3) and (A4-4) are analogous if the boundary conditions are made compatible. Equation (A4-3) can be further simplified by a linearization scheme described in Reference A17 and reduced to the following form.

$$\frac{\partial u}{\partial x} = \frac{\epsilon}{u_2} \frac{\partial^2 u}{\partial y^2} \quad (A4-5)$$

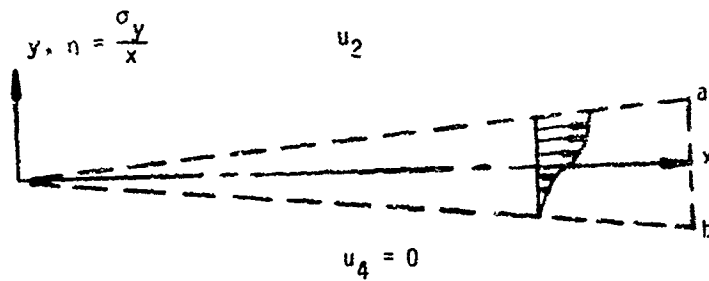


Figure A4-2a. Intrinsic Coordination System

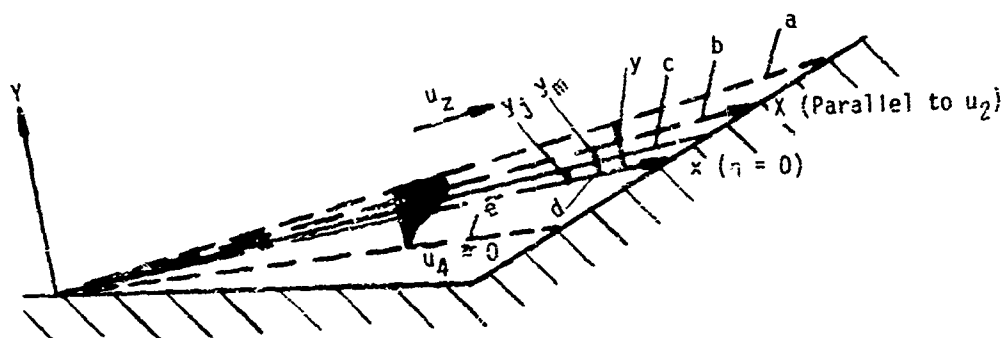


Figure A4-2b. Combined Reference Systems

A-6845

A transformed set of coordinates is introduced as described in Reference 15A to yield an equation similar to the heat conduction equation. The final solution to this equation is given by

$$\phi = \frac{u}{u_2} = \frac{1}{2} (1 + \operatorname{erf} \eta) \quad (\text{A4-6})$$

where

$$\eta = \frac{cy}{x} \quad (\text{A4-7})$$

$\sigma$  = turbulent mixing parameter = 12  
(typical turbulent value)

and

$$\operatorname{erf}(\eta) = \frac{2}{\sqrt{\pi}} \int_0^{\eta} e^{-w^2} dw \quad (\text{A4-8})$$

The energy equation may be treated in a similar manner and, since Equations (A4-3) and (A4-4) are analogous, the result is

$$\frac{T_t - T_{t4}}{T_{t2} - T_{t4}} = \phi \quad (\text{A4-9})$$

or

$$\lambda \equiv \frac{T_t}{T_{t2}} = \frac{T_{t4}}{T_{t2}} + \left(1 - \frac{T_{t4}}{T_{t2}}\right) \phi \quad (\text{A4-10})$$

The static temperature ratio will be given by

$$\frac{T}{T_2} = \frac{T}{T_t} \frac{T_t}{T_{t2}} \frac{T_{t2}}{T_2} = \left(1 + \frac{\gamma-1}{2} M_2^2\right) \frac{T_t}{T_{t2}} \frac{T_{t2}}{T_2} \quad (\text{A4-11})$$

$$= \left(1 - \frac{C_2^2 \phi^2}{\lambda}\right) \left(\lambda\right) \left(\frac{1}{1 - C_2^2}\right) \quad (\text{A4-12})$$

$$\tau \equiv \frac{T}{T_2} = \frac{\lambda - C_2^2 \phi^2}{1 - C_2^2} \quad (\text{A4-13})$$

where the Crocco number in Region 2 is defined by

$$C_2 = \frac{u_2}{u_{\max}} = \frac{M_2^2}{2/(\gamma - 1) + M_2^2} \quad (\text{A4-14})$$

and temperature ratios are defined by isoenergetic expansion from the local stagnation conditions.

#### A4.5 INTEGRAL MOMENTUM AND CONTINUITY CONSIDERATIONS

Figure A4-3 illustrates the two control volumes of interest, CV1 and CV2.

##### A4.5.1 Momentum Considerations

Since the mixing process occurs at constant pressure and since no other external forces act on CV1 in Figure A4-3a, conservation of momentum is defined by the fact that the stream momentum remains constant.

$$\int_0^{Y_R} \rho u^2 dy \Big|_{(1)} = \int_{-\infty}^{Y_R} \rho u^2 dy \Big|_{(2)} \quad (\text{A4-15})$$

Neglecting any momentum deficiency in the thin approaching boundary layer and noting that

$$\text{at (1)} \quad |Y_R| = |Y| \quad (\text{A4-16})$$

$$\therefore \eta = \frac{\sigma Y}{X} = \frac{\sigma Y}{X} \quad (\text{A4-17})$$

$$\text{at (2)} \quad Y = y - y_m \quad (\text{A4-18})$$

$$\therefore dY = dy \quad (\text{A4-19})$$

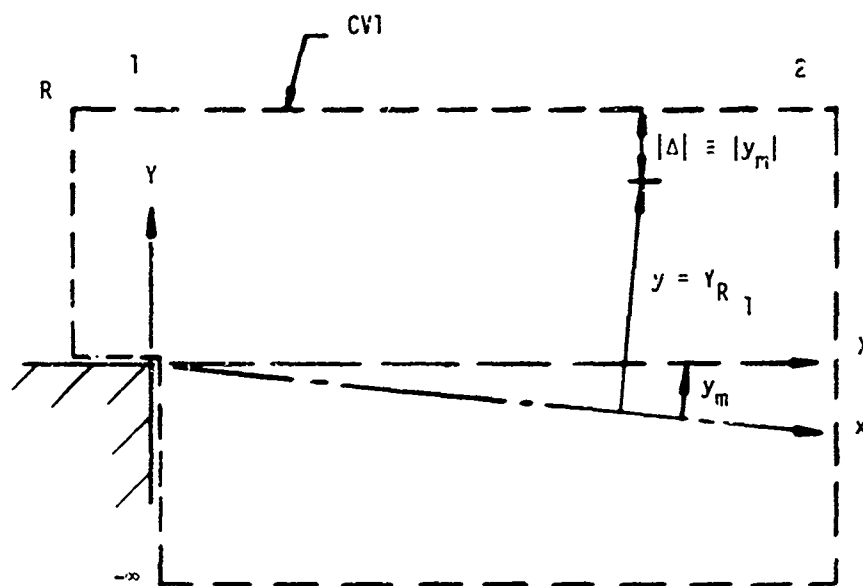
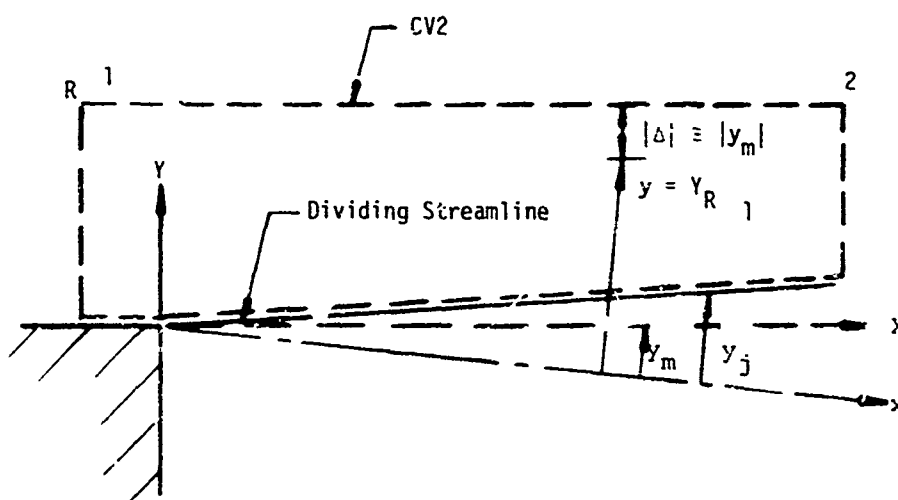


Figure A4-3a. Momentum Control Volume



A-6647

Figure A4-3b. Continuity Control Volume

Then, at (1)

$$\int_0^{y_R} \rho u^2 dy = \rho_2 u_2^2 \int_0^{y_R} dy = \rho_2 u_2^2 y_R \quad (A4-20)$$

and at (2)

$$\int_{-\infty}^{y_R} \rho u^2 dy = \int_{-\infty}^{y_R + \Delta} \rho u^2 dy = \int_{-\infty}^{y_R} \rho u^2 dy + \rho_2 u_2^2 y_m \quad (A4-21)$$

since

$$\int_{\Delta} \rho u^2 dy = \rho_2 u_2^2 \Delta = \rho_2 u_2^2 y_m \quad (A4-22)$$

Hence

$$\rho_2 u_2^2 y_p = \int_{-\infty}^{y_R} \rho u^2 dy + \rho_2 u_2^2 y_m \quad (A4-23)$$

or

$$\eta_R = \int_{-\infty}^{\eta_R} \frac{\rho}{\rho_2} \phi^2 dy + \eta_m \quad (A4-24)$$

Now, also for constant pressure mixing of an ideal gas

$$\frac{\rho}{\rho_2} = \frac{T_2}{T} = \frac{1 - C_2^2}{\lambda - C_2^2 \phi^2} \quad (A4-25)$$

so that

$$\eta_m = \eta_R - I_2(\eta_R) \quad (A4-26)$$

where

$$I_2(\eta) = (1 - C_2^2) \int_{-\infty}^{\eta} \frac{\phi^2 d\eta}{\lambda - C_2^2 \phi^2} \quad (A4-27)$$

Hence, the distance between the intrinsic and reference coordinate systems is given by Equation (A4-26).



#### A4.5.2 Continuity Considerations

The escape criterion described previously to define the dividing streamline is used to determine the location of the dividing streamline with respect to the intrinsic coordinate system. Figure A4-3b illustrates the control volume, CV2, above the dividing streamline. Hence,

$$\int_0^{Y_R} \rho u dy \Big|_1 = \int_{Y_j}^{Y_R} \rho u dy \Big|_2 \quad (\text{A4-28})$$

$$= \int_{Y_j}^{|Y_R|=|Y_R|} \rho u dy \Big|_2 + \rho_2 u_2 \Delta \quad (\text{A4-29})$$

$$\int_0^{Y_R} \rho u dy \Big|_1 = \int_{Y_j}^{Y_R} \rho u dy \Big|_2 + \rho_2 u_2 Y_m \quad (\text{A4-30})$$

In dimensionless form eliminating the density ratio and neglecting the massflow deficiency in the approaching boundary layer, we have

$$\eta_R = \int_{\eta_j}^{\eta_R} \frac{\phi}{\lambda - C_2^2 \phi^2} d\eta + \eta_m \quad (\text{A4-31})$$

Substituting Equation (A4-26) and noting that

$$\int_{\eta_j}^{\eta_R} \frac{\phi}{\lambda - C_2^2 \phi^2} d\eta = \int_{-\infty}^{\eta_R} \frac{\phi}{\lambda - C_2^2 \phi^2} d\eta - \int_{-\infty}^{\eta_j} \frac{\phi}{\lambda - C_2^2 \phi^2} d\eta \quad (\text{A4-32})$$

yields

$$I_1(\eta_j) = I_1(\eta_R) - I_2(\eta_R) \quad (\text{A4-33})$$

where

$$I_1(\eta_j) = \int_{-\infty}^{\eta_j} \frac{\phi}{\lambda - C_2^2 \phi^2} d\eta \quad (A4-34)$$

and

$$I_1(\eta_R) = \int_{-\infty}^{\eta_R} \frac{\phi}{\lambda - C_2^2 \phi^2} d\eta \quad (A4-35)$$

Therefore, if  $I_1$  and  $I_2$  are evaluated up to the limit of the inviscid boundary (say  $\eta_R = 3$ ) then the position of the dividing streamline in terms of  $\eta_j$  can be deduced from the value of  $I_1(\eta_j)$ .

#### A4.6 MASS ADDITION

If mass is added or subtracted from the separated zone as depicted in Figure A4-4 in order to retain continuity an equal amount of fluid would have to leave or be added to the separated zone if the separation were to remain stable. That is, the fluid being added would ultimately have to escape through the plane of reattachment. This would, therefore, cause the point of reattachment to shift from the  $j$  streamline to a new streamline defined as the  $S$  streamline. This then becomes simply a displacement of the attaching streamline by an amount which allows the injected flow to escape.

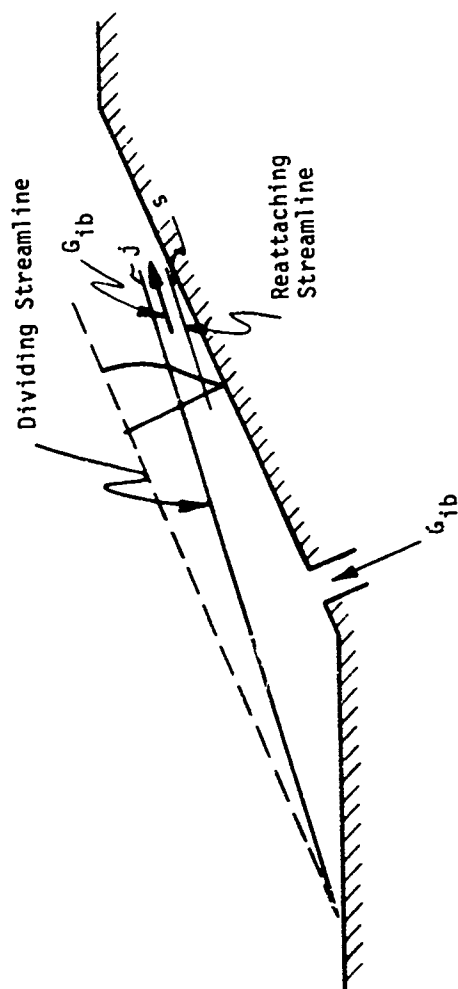
$$I_1(\eta_S) = I_1(\eta_j) - G_{ib} \quad (A4-36)$$

where

$$G_{ib} = \frac{\dot{m}_{ib} c}{\ell \rho_2 u_2} \quad (A4-37)$$

Here  $G_{ib}$  is the dimensionless blowing ( $G_{ib} > 0$ ) or bleed ( $G_{ib} < 0$ ) rate from the separated zone,  $\dot{m}_{ib}$  is the corresponding massflow per unit width, and  $\ell$  is the length of the separation.

Inspection of Equation (A4-36) shows that if flow is added or subtracted from the separated zone the velocity at reattachment will be smaller or greater respectively, than the  $j$  streamline velocity. The following paragraph will detail how this will affect the allowable turning at reattachment. It will be



A-6848

Figure A4-4. Effect of Injection

shown in Section A6.2 how in the case of the reattachment condition being violated, it may be possible to relate the rate of bubble growth to the parameter,  $G_{ib}$ . In this instance the parameter  $G_{ib}$  is to be thought of as the driving potential for bubble growth.

#### REATTACHMENT CONDITIONS

The Mach number on the reattaching streamline would be given by  
: for  $G_{ib} = 0$

$$M_j = M_2 \frac{M_j}{M_2} = M_2 \frac{\frac{u_j}{u_2}}{\sqrt{\frac{T_j}{T_2}}} = M_2 \frac{\phi_j}{\sqrt{\tau_j}} \quad (A4-36)$$

: and for  $G_{ib} \neq 0$

$$M_s = M_2 \frac{\phi_s}{\sqrt{\tau_s}} \quad (A4-37)$$

In order to determine the conditions after reattachment the following approach was taken. If the Mach number on the reattaching streamline is subsonic then just before reattachment

$$\frac{P_{t_{2r}}}{P_2} = \left( 1 + \frac{\gamma - 1}{2} M_r^2 \right)^{\frac{\gamma}{\gamma - 1}} \dots (M_r < 1) \quad (A4-38)$$

where  $r = j$  or  $s$

and since the reattachment point is considered essentially a stagnation point then

$$P_{3r} = P_{t_{3r}} = P_{t_{2r}} \text{ (at reattachment)}. \quad (A4-39)$$

If, on the other hand, the reattachment Mach number is greater than 1.0 then the recompression shock which forms within the shear layer must bend nearly normal to the approaching flow. Then the stagnation pressure behind the recompression shock and at the stagnation point will be given by the Rayleigh pitot formula.

$$\frac{P_{t_{3r}}}{P_2} = \left( \frac{\gamma + 1}{2} M_r^2 \right)^{\frac{\gamma}{\gamma-1}} \left[ \frac{\gamma + 1}{2\gamma M_r^2 - (\gamma - 1)} \right]^{\frac{1}{\gamma-1}} \dots (M_r > 1) \quad (A4-40)$$

$$P_{3r} = P_{t_{3r}} \quad (\text{at reattachment}) \quad (A4-41)$$

In both instances the static pressure level behind the reattachment shock is assumed to be equal to the reattachment pressure. This technique was used with success by Korst <sup>(A15)</sup>

The allowable turning at reattachment is then determined by the oblique shock relations at recompression. The recompression shock angle,  $\theta_{23}$ , with respect to the flow direction in region 2 is given by,

$$\theta_{23} = \sin^{-1} \left\{ \frac{1}{M_2^2} + \frac{\gamma + 1}{4} C_{P_{23}} \right\}^{1/2} \quad (A4-42)$$

where

$$C_{P_{23}} = \frac{\frac{P_3}{P_2} - 1}{\frac{\gamma M_2^2}{2}} \quad (A4-43)$$

and the flow is turned an amount,  $\delta_{23}$ , given by

$$\delta_{23} = \cot^{-1} \left\{ \tan \theta \left[ \frac{\frac{\gamma + 1}{2} M_2^2}{M_2^2 \sin^2 \theta} - 1 \right] \right\} \quad (A4-44)$$

The flow on the reattachment streamline will turn an amount

$$\delta_r = \delta_{23} + \alpha_r \dots (r = j \text{ or } s) \quad (A4-45)$$

where

$$\alpha_r = \tan^{-1} \left( \frac{\eta_m - \eta_r}{\sigma} \right) \quad (A4-46)$$

Hence, it can be seen that the Mach number on the reattaching streamline sets the allowable amount of turning at recompression. The turning criteria developed here along with appropriate turning criteria at separation,  $\delta_{12}$ , will define the total amount of sustainable steady reattachment provided the separation is large enough to allow for similar velocity profiles.

## SECTION A5

### FLOW SEPARATION INTERACTIONS

#### A5.1 FREE AND FORCED INTERACTIONS

Two types of turbulent boundary layer separations may be defined as those which are free interactions and those which are forced interactions. A free interaction may be defined as one in which the separation geometry is not dependent upon any downstream effects or what produced the separation. Figure A5-1a illustrates some of the salient features of the free interaction. The flow approaching the point of separation has a well defined turbulent boundary layer. The flow deflection,  $\delta_{12}$ , at separation and the rise to plateau pressure level are defined by a delicate balance of pressure and momentum forces at the point of separation. Therefore, the cause of the separation, whether it be a ramp, curved surface or forward facing step, is of no consequence in determining the angular geometry at separation.

Suppose, however, the distance from the corner to the leading edge is significantly less than the typical length associated with a free-interaction, or suppose that the separation is forced to occur at or near the leading edge, as shown in Figure A5-1b. It will no longer be true that the geometry of separation,  $\delta_{12}$ , will be independent of downstream influences. In fact the angle,  $\delta_{12}$ , may be totally dependent upon the downstream reattachment condition.

#### A5.2 FREE INTERACTION MODEL

In the instance of a free interaction separation the geometry at separation was deduced from the empirical plateau pressure rise coefficient found in Reference A13.

$$C_{P12} = \frac{8}{1 + 10 M_1} \quad (A5-1)$$

This correlation reflects the fact that for fully turbulent separations the plateau pressure rise coefficient is largely independent of Reynolds number. The separation angle with respect to the approaching flow was determined using the locally two-dimensional oblique shock relations given by equations similar to A4-42 and A4-44. The Mach number in region 2 is given by

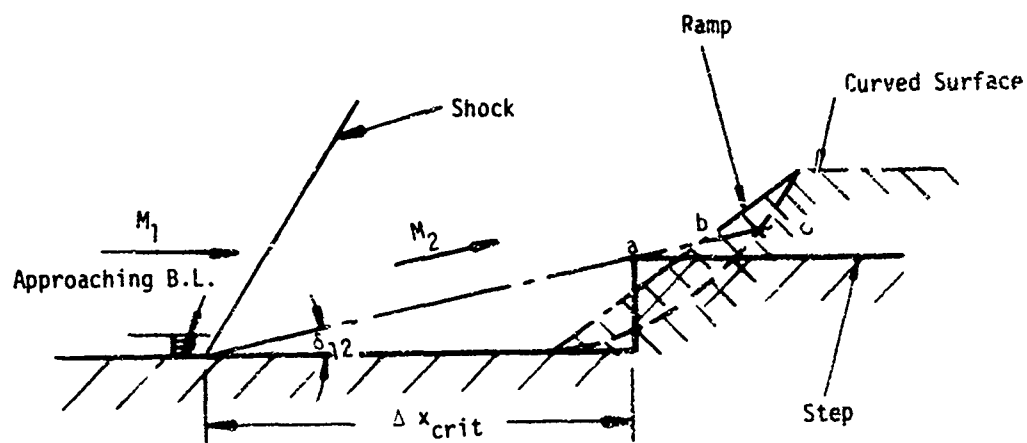
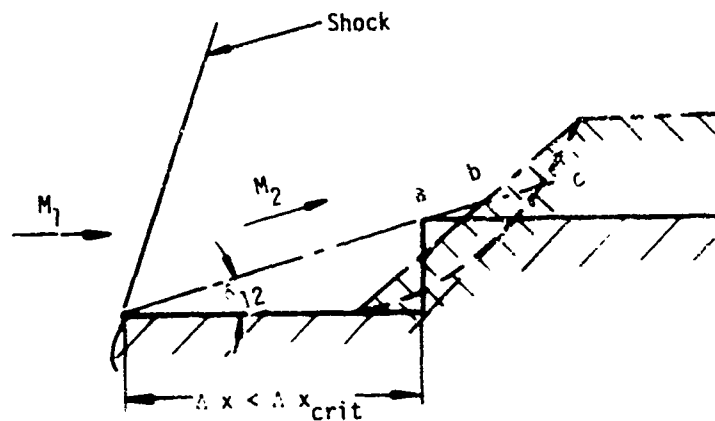


Figure A5-1a. Free Interaction



A-6819

Figure A5-1b. Forced Interaction



$$M_2 = \left\{ \frac{(\gamma + 1)^2 M_1^4 \sin^2 \theta_{12} - 4(M_1^2 \sin^2 \theta_{12} - 1)(\gamma M_1^2 \sin^2 \theta_{12} + 1)}{[2\gamma M_1^2 \sin^2 \theta_{12} - (\gamma - 1)][(\gamma - 1)M_1^2 \sin^2 \theta_{12} + 2]} \right\}^{1/2} \quad (A5-2)$$

Hence, the free interaction plateau pressure coefficient is sufficient to specify all required conditions to proceed with the reattachment analysis. The total amount of turning sustainable by an asymptotic free interaction is given by

$$\beta = \delta_{12} + \delta_{23} \quad (A5-3)$$

where  $\delta$  is obtained from Figure A5-2 and  $\delta_{23}$  is obtained by the methods detailed in Section A4.

### A5.3 FORCED INTERACTION MODEL

The forced interaction model is similar in concept to a model applied to forced laminar separations occurring right at the leading edge found in Reference A19. In the present instance the separation is not forced to the leading edge but instead to the vicinity of the tangent point between the sphere-like nose and the first conical surface. The calculation proceeds as follows:

- At a fixed freestream Mach number,  $M_\infty = M_1$ , approaching the point of separation the flow is allowed to sustain some specified amount of initial turning,  $\delta_{12}$ , caused by the forced separation.
- The conditions in region 2 are obtained by either two-dimensional oblique shock theory or conical shock theory ignoring the entropy gradient due to the rounded nose.
- The reattachment conditions are determined by the methods outlined in Section A4 to obtain the turning at reattachment,  $\delta_{23}$ .
- The maximum second flare angle  $\beta$  for reattachment on the face of the second flare, is then

$$\beta_{\max} = \delta_{12} + \delta_{23} \quad (A5-4)$$

The conical shock theory used is discussed in Reference A20. The two dimensional reattachment criteria developed in Section A4 should be nearly correct for most important axisymmetric cases considered in the context of this study if one accepts the error function profile as being nearly correct. The reason for this is that at the reattachment point for large values of  $\beta$  there is only a small percentage radial change from the innermost to outermost edges of

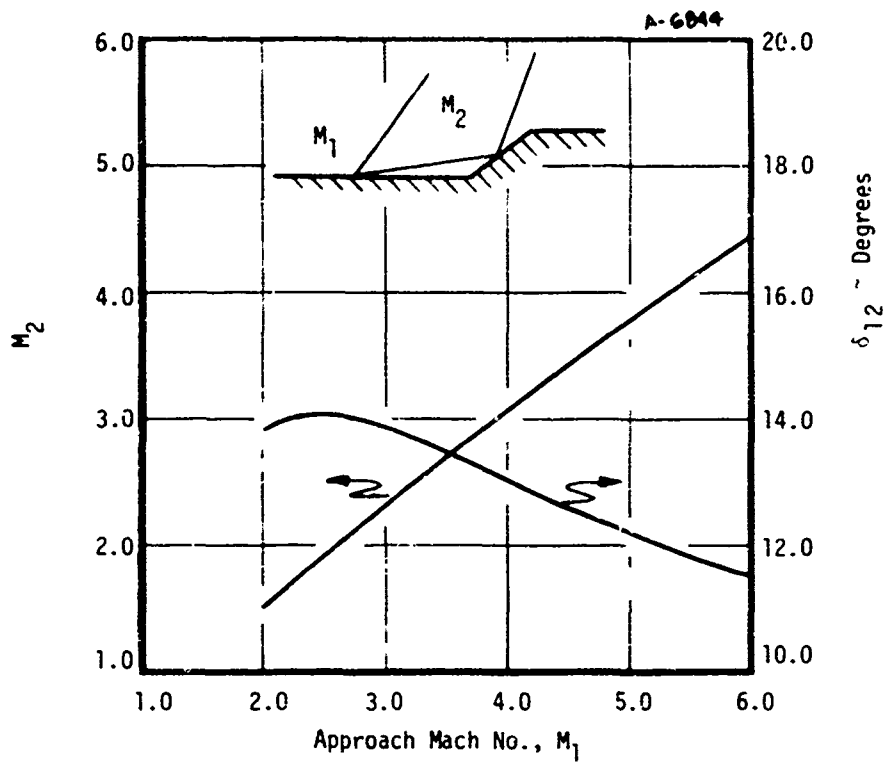


Figure A5-2. Turbulent Flow Free Interaction  
Based upon 2-D Separation and

$$C_{p_{12}} = \frac{8}{1 + 10M_1} \quad (\text{Ref. A18}), \gamma = 1.4$$

the shear layer. Hence, a radial integration of the pertinent integrals will not be significantly different than the two dimensional integrals. In the case of axisymmetric base flows the reattachment is close to the centerline and the radial effect may be important as discussed in Reference A21.

Note that for the configurations considered in this study there is no effect of the physical surface angle  $\theta_1$  in the forced interaction model. In terms of the free interaction model if the separation occurs downstream of the leading edge then  $\theta_1$  enters the calculation by virtue of relating the freestream Mach number,  $M_\infty$ , to the Mach number ahead of the point of separation as shown in Figure A5-3a. As will be discussed in Section A6 it is concluded that for the configurations considered in this study that all separations are of the forced type. The questions posed serve to define the following procedures:

- Determine for the particular configuration of interest ( $\theta_1, \delta$ ) whether an asymptotic attached solution is possible.
- If the free-interaction solution is not possible then determine if a forced interaction solution is possible.
- If neither is possible then the separation may try either to attach near the shoulder or force the flow to become unstable.

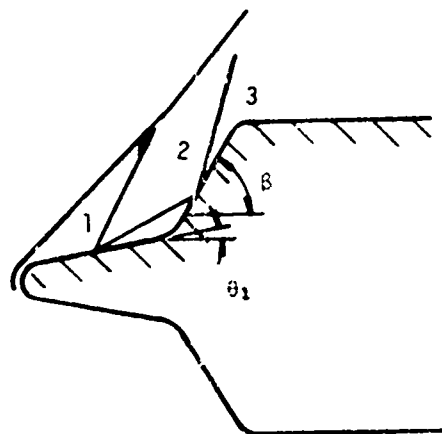


Figure A5-3a. Free Interaction

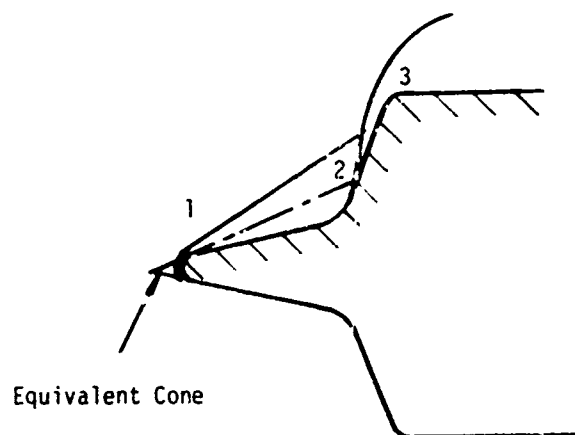


Figure A5-3b. Forced Interaction

A- 6850

## SECTION A6

### RESULTS

#### A6.1 EFFECT OF NON-ISOENERGETIC FLOW

The relations described in Sections A4 and A5 were coded in Fortran IV and programmed on an UNIVAC 1108 digital computer. In order to determine if the effects of heat transfer to the separated region represented a significant effect upon the asymptotic reattachment model a set of sample calculations was performed. Figure A6-1 presents the results of this investigation for a 2-D free-interaction. Clearly, relatively large differences in total temperature do not alter the amount of turning at reattachment, significantly. Therefore, the effects of non-iscenergetic flow was not considered further.

#### A6.2 EFFECT OF BLEED FLOW

Figure A6-2 represents a study of the effect of bleeding flow from the separated region of a 2-D free-interaction. Clearly, a significant increase in the total amount of turning can be realized if flow is removed from the separation zone. Since, in the present application no flow removal can be realized one may ask what significance can be placed upon this study. The following interpretation is offered. If the separation cannot remain stable as either a free interaction or as a forced interaction an unsteady growth of the bubble will occur. The collapsed bubble will begin to grow from the corner. As an example of how  $G_{ib}$  may be used to estimate the rate of bubble growth consider the following. Say the approach Mach number at the beginning of bubble growth is  $M_1 = 4.0$ , and say  $\beta \approx 42^\circ$ . Examination of Figure A6-2 shows that if  $G_{ib} = -.20$ , that is, if that quantity of flow is removed the separation will be steady and stable. However, if the outflow valve is shut off so to speak then instantaneously the bubble will accumulate that amount of flow which is not removed by bleed. Hence, the rate of a non-dimensional bubble growth is  $G_{ib} = .20$ . If on the other hand  $\beta$  exceeds the allowable limiting value at  $M_1 = 4.0$  namely  $\beta_{max} = 47.5^\circ$  then the rate of bubble growth is interpreted as  $G_{ib} \approx .36$ .

#### A6.3 FREE AND FORCED INTERACTION RESULTS

Two sets of forced interaction results were generated and are shown in Figures A6-3 and A6-4. The results shown in Figure A6-3 are for a two-dimensional

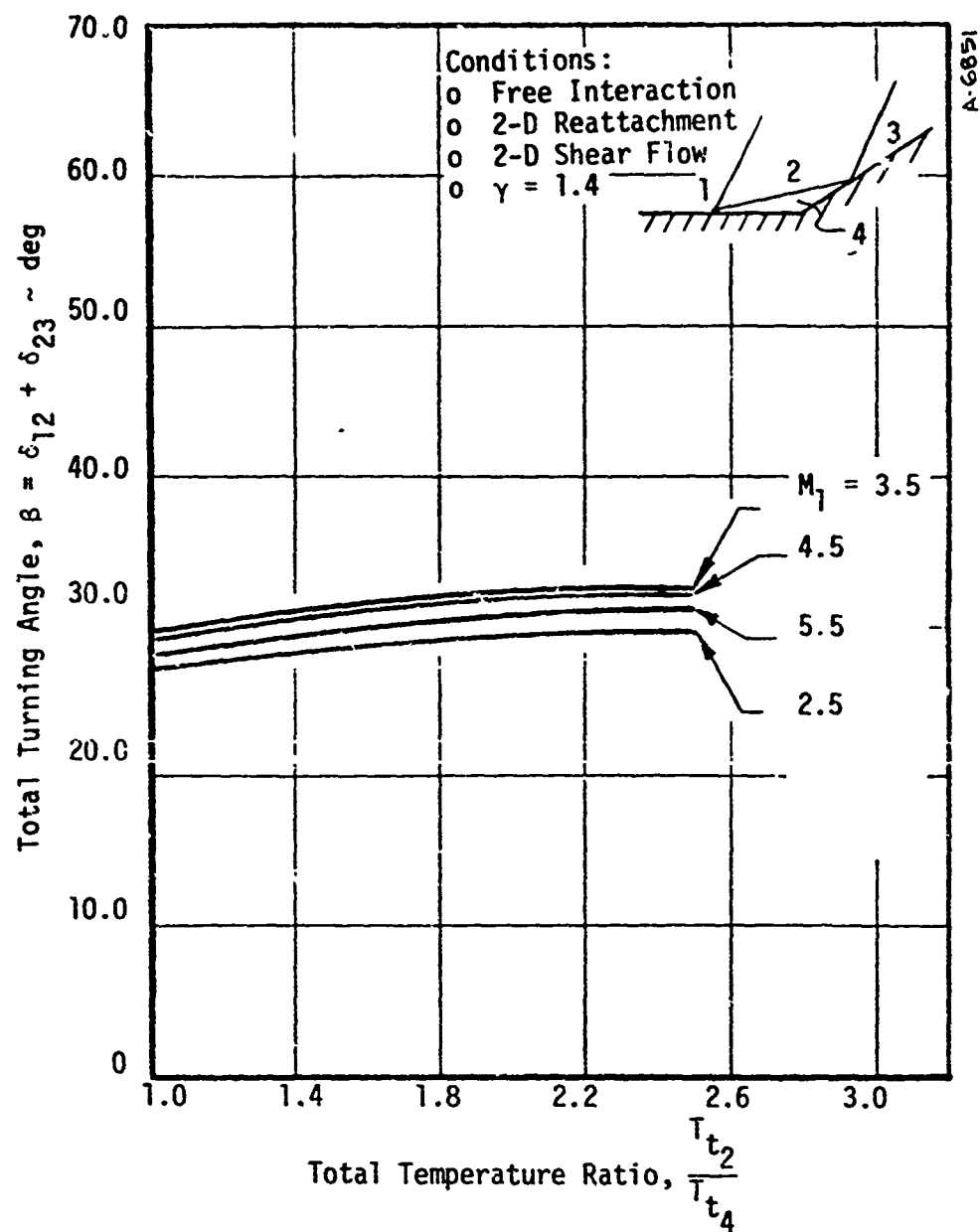


Figure A6-1. Effect of Total Temperature Ratio,  $\frac{T_{t2}}{T_{t4}}$

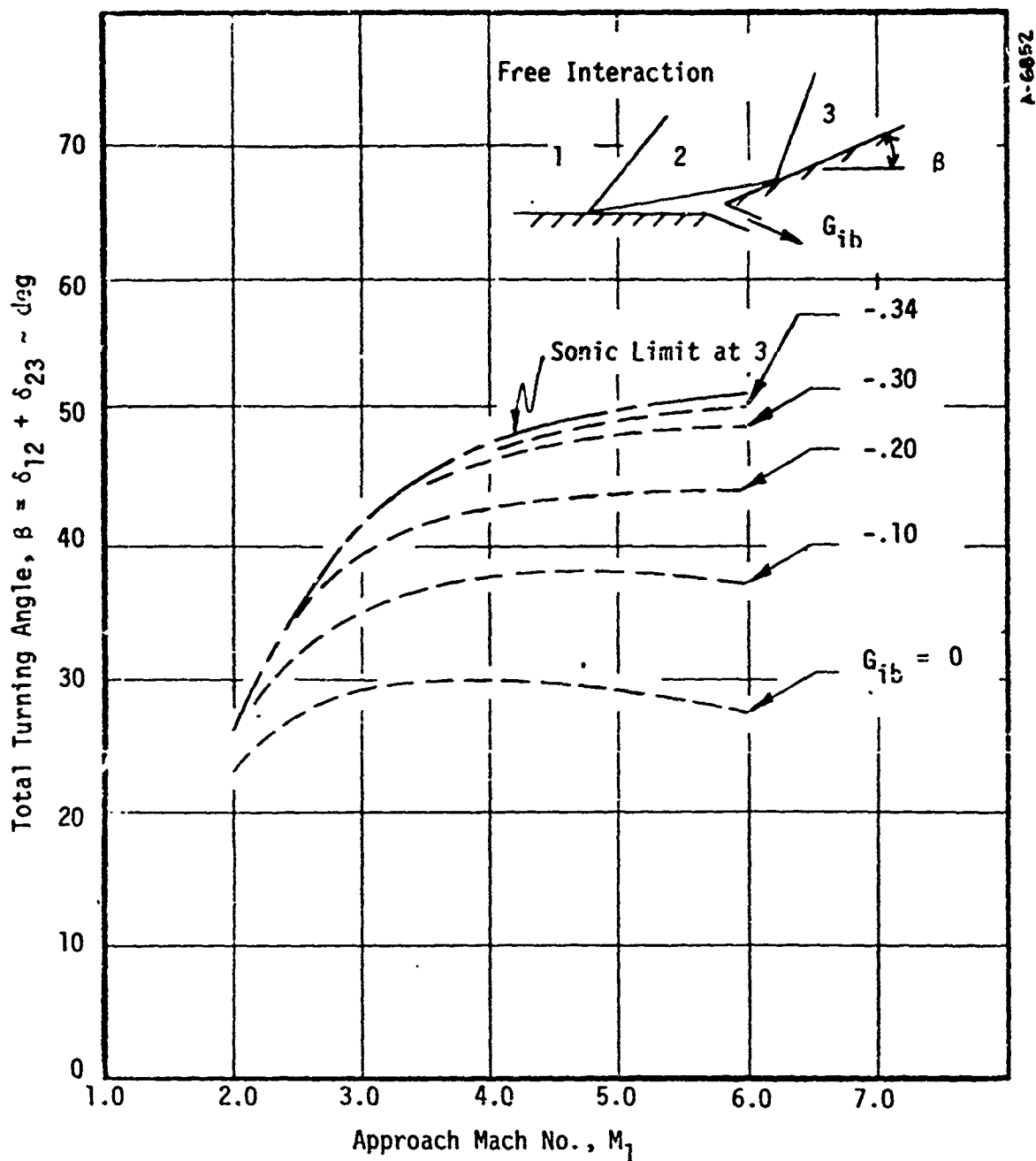


Figure A6-2. Total Turning Angle Based Upon Korst Reattachment with Bleed

- 2-D Separation
- 2-D Shear Flow
- $\gamma = 1.4$

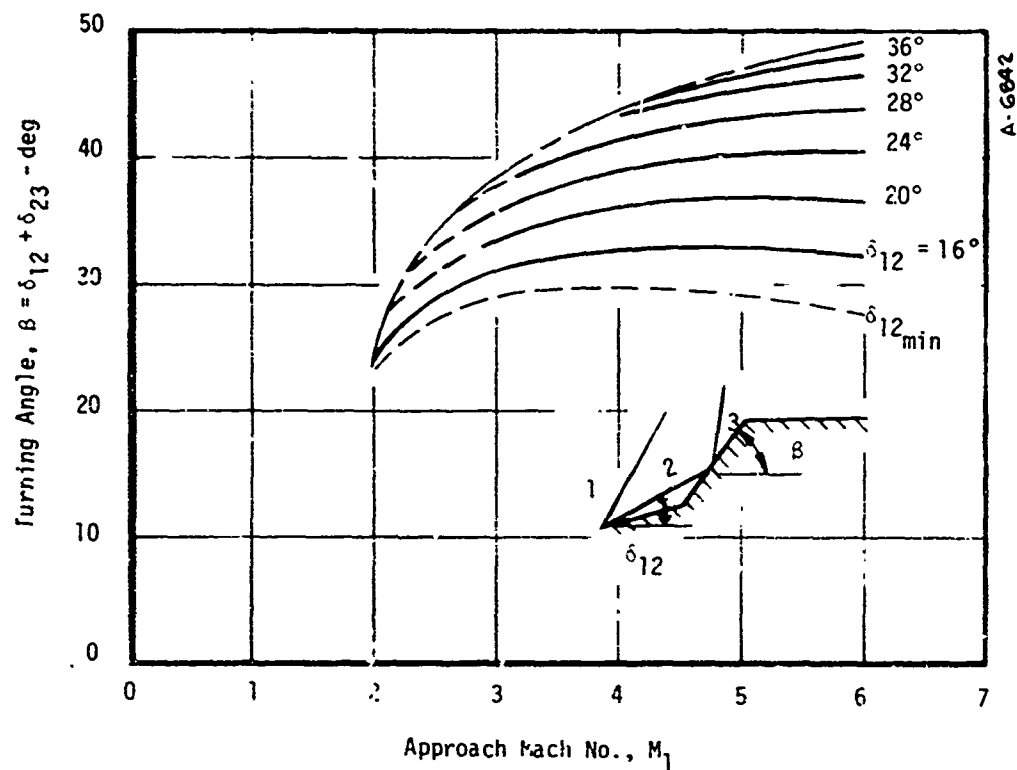


Figure A6-3. Forced Leading Edge Interaction Results .

- 2-D Separation
- 2-D Shear Flow
- $\gamma = 1.4$



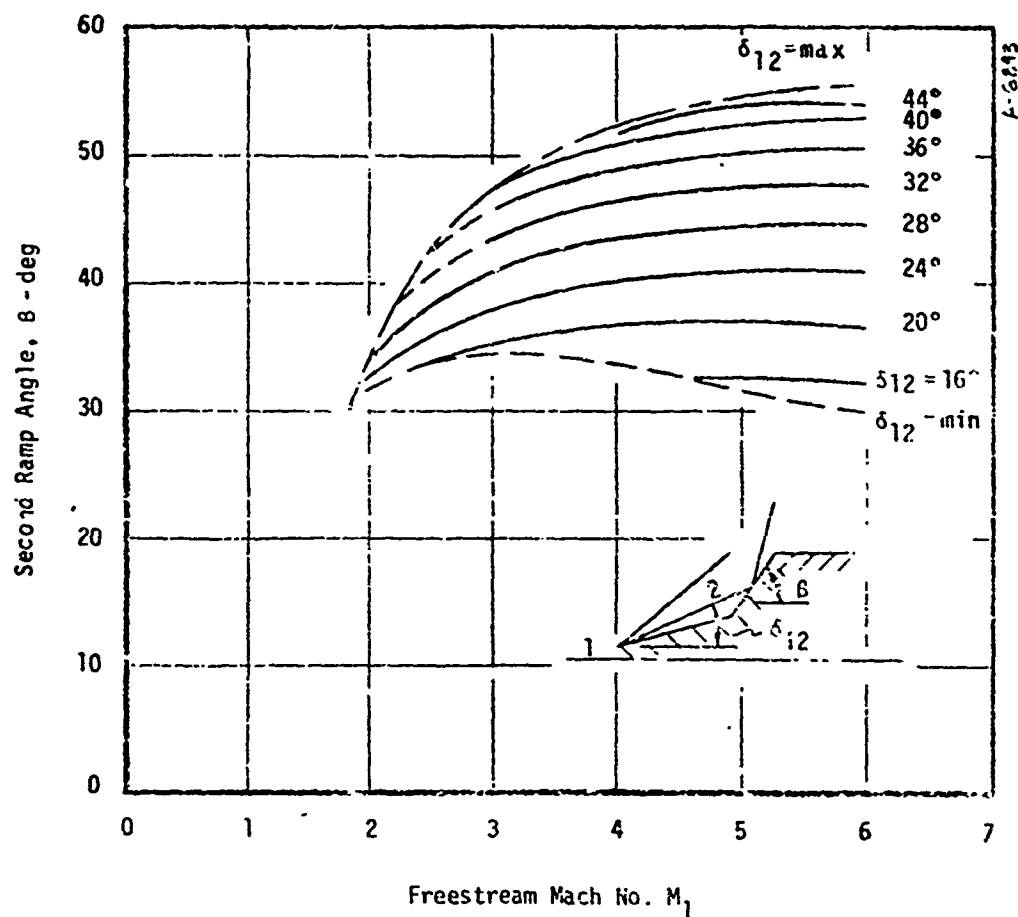


Figure A6-4. Forced Leading Edge Interaction Result

- Conical Separation
- 2-D Shear Flow
- $\gamma = 1.4$

forced interaction. The curved labeled  $\delta_{12 \text{ min}}$  represents the free-interaction solution. The results shown in Figure A6-4 are for a forced separation initiated with a conical shock. The results of Figures A6-3 and A6-4 do not differ greatly although the allowable amount of turning is somewhat greater for the axisymmetric case. As mentioned previously the reattachment results for Figure A6-4 were performed using the two-dimensional model; however, the radial effect at reattachment should be small for the larger values of  $\beta$

## SECTION A7

### CONCLUSIONS

A supersonic asymptotic separation and reattachment model has been formulated to predict whether the flow separation on a biconic surface will be stable or unstable. The model is formulated on the basis of the initial separation being either a free interaction or a forced interaction. The reattachment is based on a free-shear flow analysis. If the separation is a forced interaction the criteria for maximum allowable turning is independent of the first cone angle. The effects of heat transfer to the separated zone are small in relation to the allowable turning angle. The effect of bleed flow has been related to the growth rate of the separation bubble for the unstable cases. The forced separation cases illustrate that the maximum amount of turning can be significantly greater than for the free-interaction. The results of the present study indicate that the maximum allowable turning for a conical reattachment is about  $55^\circ$  at Mach 5.

It seems clear that the weakness of the model lies in its inability to predict occurrences after the sonic limit has been reached. Once the flow becomes locally sonic a closer coupling to the inviscid flow would be necessary to predict the reattachment criteria. This is clearly beyond the scope of the model presented herein.

## REFERENCES

### FOR APPENDIX A

- A1. Wood, C. J., "Hypersonic Flow over Spiked Cones" J. of Fluid Mechanics, Vol. 12, Part 4 April 1962.
- A2. Maull, D. J., "Hypersonic Flow over Axially Symmetric Spiked Bodies", J. of Fluid Mechanics, Vol. 8, Part 4. Aug. 1960.
- A3. Mair, W. A. Phil. Mag. 1952, 43, 695.
- A4. Zukoski, E. E., "Turbulent Boundary-Layer Separation in Front of a Forward-Facing Step" AIAA Journal, Vol. 5, No. 10, Oct. 1967.
- A5. Love, E. S., "Pressure Rise Associated with Shock-Induced Boundary-Layer Separation", NACA TN 3601, Dec 1955.
- A6. Settles, G. S., and Bogdonoff, S. M., "Separation of a Supersonic Turbulent Boundary Layer at Moderate to High Reynolds Numbers." AIAA Paper 73-666, July 1973.
- A7. Kuehn, D. M., "Experimental Investigation of the Pressure Rise Required for the Incipient Separation of Turbulent Boundary Layers in Two Dimensional Supersonic Flow" NASA Memo 1-21-59A, Feb. 1959.
- A8. Law, C. H., "Supersonic, Turbulent Boundary-Layer Separation Measurements at Reynolds Numbers of  $10^7$  to  $10^8$ ", AIAA Paper 73-665, July 1973.
- A9. Roshko, A., and Thomke, G. J., "Supersonic, Turbulent Boundary-Layer Interaction with a Compression Corner at Very High Reynolds Number".
- A10. Chapman, D. R., Kuehn, D. M., and Larson, H. K., "Investigation of Separated Flows in Supersonic and Subsonic Streams with Emphasis on the Effect of Transition", NACA TN 3869, Mar. 1957.
- A11. Sterrett, J. R., and Emery, J. C., "Experimental Separation Studies for Two-Dimensional Wedges and Curved Surfaces at Mach Numbers of 4.8 to 6.2," NASA TND-1014 Feb. 1962.
- A12. Tadisco, A., and Reeves, B. L., "Turbulent Boundary Layer Separation and Reattachment at Supersonic Speeds".
- A13. Spaid, F. W., "Cooled Supersonic Turbulent Boundary Layer Separated by a Forward Facing Step," AIAA Journal, Vol. IV, No. 8., Aug. 1972.
- A14. Kuehn, D. M., "Turbulent Boundary-Layer Separation Induced by Flares on Cylinders at Zero Angle of Attack," NASA TRR-117.
- A15. Korst, H. H., "A Theory for Base Pressures in Transonic and Supersonic Flow," J. of Applied Mechanics, Dec. 1956.
- A16. Page, R. H., and Korst, H. H., "Non-Isoenergetic Compressible Jet Mixing with Consideration of its Influence on the Base Pressure Problem," presented at the Fourth Midwestern Conference on Fluid Mechanics, Purdue 1955.

- A17. Korst, H. H., Page, R. H., and Childs, M. E., "A Theory for Base Pressures in Transonic and Supersonic Flow," ME TN 392-2, OSR-TN-55-39, U of Illinois, March 1955.
- A18. Dahm, T. J., "A Comprehensive Analytical Procedure for the Performance Prediction of Rocket Thrust Vector Control with Gaseous Secondary Injection," Aerotherm Report 67-11, 1967.
- A19. Brower, W. B., "Leading-Edge Separation of Laminar Boundary Layers in Supersonic Flow", J. of the Aerospace Sciences, Dec. 1951.
- A20. Moretti, G. "Inviscid Flow Field Past a Pointed Cone at an Angle of Attack. Part I" GASL Tech. Report 577, Dec. 1965.
- A21. Mueller, T. J., "Determination of the Turbulent Base Pressure in Supersonic Axisymmetric Flow," J. Spacecraft, Jan. 1968.